Photoionization and vibrational spectroscopy of sodium doped water clusters

Dissertation

zur Erlangung des mathematisch-naturwissenschaftlichen Doktorgrades
„Doctor rerum naturalium“
der Georg-August-Universität Göttingen

im Promotionsprogramm Chemie
der Georg-August University School of Science (GAUSS)

vorgelegt von
Christoph Wilhelm Hansjörn Ralf Dierking
aus Aachen

Göttingen, 2019

Betreuungsausschuss

PD. Dr. Thomas Zeuch
Abteilung Physikalische Chemie II, Institut für Physikalische Chemie, Georg-August-Universität Göttingen

Prof. Dr. Alec M. Wodtke
Abteilung Physikalische Chemie I, Institut für Physikalische Chemie, Georg-August-Universität Göttingen

Mitglieder der Prüfungskommission

Referent: PD. Dr. Thomas Zeuch
Abteilung Physikalische Chemie II, Institut für Physikalische Chemie, Georg-August-Universität Göttingen

Korreferent: Prof. Dr. Alec M. Wodtke
Abteilung Physikalische Chemie I, Institut für Physikalische Chemie, Georg-August-Universität Göttingen

Weitere Mitglieder der Prüfungskommission

Prof. Dr. Burkhard Geil
Abteilung Biophysikalische Chemie, Institut für Physikalische Chemie, Georg-August-Universität Göttingen

Dr. Sebastian Kruss
Nachwuchsforschungsgruppe Nanobiotechnologie, Institut für Physikalische Chemie, Georg-August-Universität Göttingen

Prof. Dr. Götz Eckold
ABteilung Physikalische Chemie fester Körper, Institut für Physikalische Chemie, Georg-August-Universität Göttingen

Prof. Dr. Philipp Vana
Abteilung Makromolekulare Chemie, Institut für Physikalische Chemie, Georg-August-Universität Göttingen

Tag der mündlichen Prüfung: 8. Februar 2019

Abstract

The intermolecular interactions of water molecules and the resulting phase transitions of macroscopic water govern many important processes in earth's atmosphere. Spectroscopy on clusters has proven to be a powerful tool to study molecular aggregates in detail and can be used to investigate the phase transitions on a molecular scale. Moreover, experiments on these systems provide benchmark data for testing molecular simulations.

In this work, pure water clusters are produced via supersonic expansions and subsequently doped with sodium atoms. Size-selection is achieved by means of photoionization time-of-flight mass spectrometry. In previous studies the resulting neutral $Na(H_2O)_n$ clusters were characterized by their ionization threshold energies. In contrast to this, the photoionization efficiency curves in the photon energy range of $2.7 - 5.4\,\mathrm{eV}$ are obtained in this work. It is found that the photoionization efficiency is saturated at $4.1\,\mathrm{eV}$ for all cluster sizes with $n \geq 9$. For smaller clusters the saturation point is a cluster size dependent property. The experimental photoionization efficiency curves of small clusters ($n = 2, 3, 4, 5$, and 7) are compared to predicted curves from ab initio molecular dynamics simulations, for which the energies were computed via the DFT functionals BLYP or LC-ωPBE with the 6-31++g** basis set. The predictions do not satisfactorily reproduce the photoionization efficiency curves for all cluster sizes. Nevertheless, the comparison of the photoionization efficiency curves with the calculated ionization energies reveals the presence of several isomers for each cluster size.

Vibrational spectra of sodium doped water clusters can be obtained by introducing an IR laser to the setup. The resonant absorption of IR photons facilitates the ionization of clusters by the UV laser, as long as the UV laser is operated at photon energies below the saturation point of the photoionization efficiency curve. Previous studies showed that this increase is closely related to the cluster temperature. This work shows that for UV photon energies close to the ionization threshold of $3.2\,\mathrm{eV}$ approximately 90% of the clusters can contribute to the IR-induced signal gain. Previous spectra of large sodium doped clusters are found to be distorted at long delay times between IR and UV pulse and at large photon fluxes. Measurements of the laser delay and photon flux dependency indicate that the distortion is caused by IR-induced evaporation from the clusters, which reduces the temperature of these. A detailed analysis of the spectra shows that only amorphous clusters are affected by this. The evaporation effect leads to an exponential decay of the IR-induced signal enhancement with a rate constant of $10^7 - 10^8\,\mathrm{s}^{-1}$. Size-selective, vibrational spectra of $Na(H_2O)_n$ clusters with reduced distortion for a broad range of cluster sizes are obtained for the first time in this work. An analysis of these spectra and a comparison to FTIR spectra and to the spectra obtained at high photon fluxes indicate the coexistence of amorphous and crystalline clusters in the molecular beam at certain cluster sizes.

Spectral features are tested as indicators for the amorphous-to-crystalline transition in clusters. It is found that the intensity of the dangling OH peak could be

linked to the physical state of the clusters. An increasing relative spectral intensity at $3200\,\mathrm{cm}^{-1}$ was found to be a more robust criterion to conclude the presence of crystalline clusters. Based on this, the smallest crystalline cluster obtainable in the experiment is found to be at $n = 90 \pm 10$. A comparison of this result to predictions from molecular simulations relying on empirical force fields reveals that predictions based on the TTM2-F potential are satisfactory whereas other theoretical methods fail.

Contents

1 Introduction **1**

2 Applied methods and scientific context **5**

2.1 Experimental techniques 5

2.1.1 Supersonic expansions 5

2.1.2 Mass spectrometry 7

2.1.2.1 Ionization methods 7

2.1.2.2 Time-of-flight mass spectrometry 9

2.1.2.3 Detectors 11

2.2 Cluster preparation 11

2.2.1 Cluster formation in supersonic expansions 12

2.2.2 The pickup approach 14

2.2.3 Fragmentation 15

2.3 Sodium water clusters 17

2.3.1 The sodium water reaction in clusters 17

2.3.2 Hydrated electrons 19

2.3.2.1 Experimental characterization approaches 19

2.3.2.2 Isomers of anionic water clusters 21

2.3.2.3 Isomers of sodium water clusters 23

2.4 Spectroscopy of water clusters 24

2.4.1 Size-selective cluster detection 24

2.4.2 Water molecule binding motifs 26

2.4.3 Probing physical states of water clusters 28

2.4.4 IR-assisted photoionization of $Na(H_2O)_n$ 32

3 Setup **35**

3.1 Cluster beam apparatus 35

3.1.1 Cluster source 35

3.1.2 Pickup cell . . . 36
3.1.3 Mass spectrometer . . . 37
3.1.4 Pumping system . . . 39
3.2 Laser system . . . 40
3.2.1 Nd:YAG pump laser . . . 40
3.2.2 Laservision IR-OPO/OPA . . . 40
3.2.3 Continuum Panther Ex OPO . . . 42
3.2.4 Sirah Cobra Stretch dye laser . . . 43
3.3 Mass detection and data processing . . . 44

4 Single photon ionization of $Na(H_2O)_n$ clusters 47
4.1 Experimental method . . . 47
4.2 Experimental results . . . 47
4.3 Comparison of experimental and theoretical results . . . 54
4.3.1 Computational methods . . . 54
4.3.2 Results . . . 55
4.3.2.1 $Na(H_2O)_2$ . . . 55
4.3.2.2 $Na(H_2O)_3$ . . . 58
4.3.2.3 $Na(H_2O)_{n=4,5,7}$ . . . 61
4.4 Conclusion . . . 65

5 Vibrational spectroscopy of $Na(H_2O)_n$ clusters 67
5.1 Introductory remarks . . . 67
5.2 Temporal signal dependence . . . 67
5.3 Pulse energy dependence . . . 76
5.4 Time-resolved spectroscopy of $Na(H_2O)_n$ clusters . . . 79
5.4.1 Spectra at high-E_{IR} conditions . . . 79
5.4.2 Spectra at low-E_{IR} conditions – vibrational spectra of $Na(H_2O)_n$ with reduced distortion . . . 86
5.5 Detecting crystalline clusters via vibrational spectroscopy . . . 90
5.5.1 Broadening of the bonded OH absorption peak . . . 91
5.5.2 Signal of the free OH oscillators . . . 95
5.6 Conclusion . . . 102

6 The smallest water ice I cluster - Revisited 105
6.1 Introductory remarks . . . 105

6.2 Experimental results . . . 106
6.2.1 Vibrational spectra . . . 106
6.2.2 Signal of the free OH oscillators . . . 110
6.3 Comparison to other methods . . . 112
6.4 Conclusion . . . 116

7 Conclusion and Outlook **119**
7.1 Single photon ionization of $Na(H_2O)_n$ clusters . . . 119
7.1.1 Conclusion . . . 119
7.1.2 Outlook . . . 120
7.2 Vibrational spectroscopy of $Na(H_2O)_n$ clusters . . . 121
7.2.1 Conclusion . . . 121
7.2.2 Outlook . . . 123
7.3 Experimental approach . . . 125

A Appendix **127**
A.1 Experimental results . . . 127
A.2 Modified pickup cell top . . . 130
A.3 Correction of the pressures of the old manometer . . . 131
A.4 List of chemicals and gases . . . 132
A.5 List of abbreviations . . . 133

Bibliography **135**

1 Introduction

The influence of water on earth and its atmosphere is omnipresent and of unequivocal importance to the whole planet's energy budget and thus its habitability. Phase transitions of water are of crucial importance for atmospheric processes on earth: Evaporation of water and subsequent condensation of water vapor on sulfate clusters leads to the formation and growth of aerosol particles, which results in the formation of clouds.[1–3] Therefore, the presence of liquid water is considered to be a mandatory criterion for the presence of life in earth-like environments and great effort is put into the observation of water on extraterrestrial objects.[4–7] But also crystalline water droplets play an important role in the atmosphere. Their formation in polar stratospheric clouds at very low temperature during polar winter[8] causes the formation of molecular chlorine from two reservoir species on the surface of crystalline, µm-sized droplets: $ClONO_2 + HCl_{(ads)} \longrightarrow Cl_2 + HNO_{(ads)}$.[9,10] This ultimately results in the formation of the ozone hole in polar spring after photolysis of Cl_2.

Aside from these fundamental contributions of water to earth's atmospheric chemistry and physics, water itself is of scientific interest due to its several anomalies.[11] Since the macroscopic properties arise from the microscopic structure of the intermolecular hydrogen bond network, the development of model potentials describing water in its various configurations has been subject of research for several decades.[12] In order to test and evaluate the quality of such models, experimental benchmarks are required, which have to be sensitive to the hydrogen bond network structure. Vibrational spectroscopy has shown to be a suitable technique as the hydrogen bonded OH stretching vibrations are a sensitive probe to the underlying interactions. As bulk characteristics were observed in clusters of a variety of sample systems,[13–15] and these molecular aggregates can be studied in detail—and often with precise size-resolution—the spectroscopy of clusters is a promising approach to unravel the emergence of bulk phenomena on a microscopic scale.[14,16] Since the size-selective measurement of vibrational spectra of water clusters in the atmosphere cannot cur-

rently be accomplished,[17,18] they are prepared under well-defined laboratory conditions,[19–21] for instance in molecular beams from supersonic expansions.[22] This technique produces clusters of several sizes and therefore requires subsequent mass separation, which is routinely carried out by means of electric or magnetic fields for charged water clusters.[20,23–26] In contrast to this, the separation of neutral clusters is challenging. Small neutral clusters with up to ten water molecules can be mass-separated via scattering in crossed molecular beams.[27] However, larger, neutral, pure water clusters cannot be studied by this method. An alternative approach extends the experimentally accessible range of cluster sizes by the addition of chromophores to the clusters and subsequent photoionization, followed by size selection of the produced ions. Via chromophores such as phenol[28,29] or earth-alkaline[30] or alkali metal atoms[31–33] the detectable range of neutral clusters can be extended to hundreds of constituents.[34,35] The excess energy of the resonance enhanced multi photon ionization (REMPI) scheme applied to the phenol doped clusters can result in the evaporation of up to 6 water molecules and therefore is not entirely size-selective.[28,29] A combination of this REMPI scheme with vibrational spectroscopy that is based on infrared multi photon dissociation (IRMPD) is limited to the larger clusters of a given cluster distribution and requires adjustment of the cluster distribution if other clusters sizes are to be investigated.[29] In contrast to the phenol method, photoionization of alkali metal doped water clusters is considered to be free of fragmentation if performed close to the ionization threshold.[34,36,37]

Sodium doping is a suitable technique for the detection of pure, nm-sized particles and clusters of several compounds, like water,[38] ammonia,[38–40] alcohols,[41–43] toluene,[44] propane,[44] dimethylether,[40] acetic acid,[45] and rare gases.[46] Therefore sodium doping has been applied as a reference technique to study the fragmentation of clusters caused by other ionization methods.[34,47,48] Besides the capability to detect neutral aggregates, neutral and charged sodium doped water clusters offer insights into the topics of reactivity of sodium on water, sodium solvation, and hydrated electrons and therefore have been the subject of many computational studies, see [49–61] and references cited therein. While the threshold ionization energy of atomic sodium is 5.139 eV,[62] it decreases with the number of attached water molecules until it reaches a constant value of 3.17 ± 0.05 eV for $Na(H_2O)_{n\geq 4}$.[38] Early experimental and theoretical work aimed to characterize neutral sodium water clusters in terms of this quantity.[38,60,61,63] However, these studies are further complicated by the likely presence of several isomers for each cluster size.[16,64–68] Since

recent experimental evidence points to the presence of several isomers of sodium doped water clusters in molecular beams, which are not responsible for the observed threshold ionization energies,[40,68–71] one goal of this work is to probe the isomer distribution of $Na(H_2O)_n$ clusters by means of single photon ionization. The obtained ion yield curves—also referred to as photoionization efficiency curves[13]—are compared to results from molecular dynamics simulations[72] and to the photoelectron spectrum of a $Na(H_2O)_n$ cluster distribution.[40] In addition, an upper limit of the fraction of clusters which are probed by the vibrational spectroscopic approach developed by Steinbach and Buck[36] (see e.g. references [36, 37, 71]) can be obtained. For the results of this study and a comparison to theoretical predictions on $Na(H_2O)_n$ clusters provided by the group of Prof. Petr Slavíček (Department of Physical Chemistry of the University of Chemistry and Technology Prague) see Chapter 4.

Since the vibrational frequencies are a suitable probe for the hydrogen bond strengths, vibrational spectroscopy has proven to be a powerful tool to resolve the structure of hydrogen bonded networks.[16,73–80] The vibrational spectra of size-selected sodium doped water clusters can be obtained by a special fashion of IR action spectroscopy, which will be explained in Section 2.4.4. The approach requires two lasers: an UV laser with fixed UV wavelength and a tunable IR laser. As the setup has recently been equipped with a new UV laser system, which provides smaller pulse length than the previous, the delay time dependent IR signal can be measured. Therefore, in this work, the influence of the delay between the two lasers and the IR laser pulse energy on the IR-UV signal is tested. The aim of this is to understand why the vibrational spectra of crystalline $Na(H_2O)_n$ clusters[71] differ from those obtained via IRMPD of both $La^{3+}(H_2O)_n$[81] and those obtained via Fourier transform infrared (FTIR) spectroscopy of pure water nanodroplets.[21] This question can be answered by time-resolved vibrational spectroscopy of $Na(H_2O)_n$. The corresponding results are shown in Chapter 5.

Water ice nucleation in the atmosphere is a heterogeneous process in almost every case. Most recently, it could be studied on the microscopic scale via experimental[82] and computational methods.[83] However, how many water molecules are required to form crystalline clusters with ice I cores remains uncertain. Several experimental studies indicate that the resulting range of cluster sizes for which a transition from liquid-like to crystalline clusters occurs is around $n_{\text{transition}} = 100-900$.[19,20,71,81,84–86] Theoretical studies with empirical model potentials, which differ in the parameteri-

zation of the water monomer, indicate that the smallest cluster size for which crystalline clusters are stable is $n = 90$,[87] 137,[88] or 293.[16,89] Vibrational spectroscopy of $Na(H_2O)_n$ clusters, formed via supersonic expansions with subsequent sodium attachment, showed that the cluster size for which crystalline cores are observed depends on the expansion conditions.[37,86,90] Therefore, another aim of this work is to change the expansion conditions in a way that the liquid-crystal transition can be observed at smaller cluster sizes than previously reported (references [37, 71, 86]). This then allows a direct comparison to the theoretical predictions and is therefore used to assess which of the existing theories is accurate enough to correctly predict the transition from amorphous to crystalline clusters. The results of this project are shown in Chapter 6.

2 Applied methods and scientific context

In order to study sodium doped water clusters experimentally, the combination of several techniques and components is required. This chapter will give a brief overview on the experimental background of these. Moreover, studies on water clusters as well as the properties of $Na(H_2O)_n$ clusters will be described.

2.1 Experimental techniques

2.1.1 Supersonic expansions

Adiabatic expansions of gaseous samples along strong pressure gradients produce molecular beams with well-defined velocity distributions, which are mandatory for many experimental approaches as they yield control over the kinetic energy of the molecules in well directed beams.[91] Sample flow velocities that exceed the local speed of sound are obtained, hence the term supersonic expansions. The Mach number Ma is defined as the ratio of flow velocity v and local speed of sound c_s. For effusive expansions sample beams with $Ma \leq 1$ are present, for supersonic expansions $Ma > 1$.[91]

One condition to achieve an efficient energy redistribution during an expansion of a sample substance from an oven with temperature T_0 and pressure p_0 through an orifice is the occurrence of many collisions during the expansion process.[91]

The high number of collisions in the vicinity of the nozzle as a required condition for supersonic expansion can be expressed in terms of the dimensionless Knudsen number Kn as the ratio of the gas molecule's mean free path λ_m and the orifice diameter d_0:[92,93]

$$Kn = \frac{\lambda_m}{d_0} \tag{2.1}$$

If $Kn \ll 1$, λ_m is small compared to d_0, efficient collisional cooling of the expanded gas phase is provided.[93] The resulting narrow velocity distribution originates from these three or more body collisions in the vicinity of the orifice.[91]
As the effective cross sections for energy redistribution follow the trend $\sigma_{\mathrm{trans}\rightarrow\mathrm{trans}} > \sigma_{\mathrm{rot}\rightarrow\mathrm{trans}} > \sigma_{\mathrm{vib}\rightarrow\mathrm{trans}}$, the translational energy in the expansion direction results mainly from the translational and rotational degrees of freedom of the initial conditions.[91]
The maximum terminal velocity of the adiabatically expanded gas $v_{\mathrm{beam,max}}$ can be estimated from the balance of the enthalpies $H_{0,1}$ before (index 0) and after passing the nozzle (index 1), see page 17 in [94].

$$H_1 + \frac{1}{2} v_{\mathrm{beam},1}^2 = H_0 \tag{2.2}$$

with

$$v_{\mathrm{beam},1}^2 = 2(H_0 - H_1) = 2 \int_{T_1}^{T_0 \gg T_1} c_p^* \mathrm{d}T \tag{2.3}$$

Here T_0 denotes the reservoir temperature, T_1 the temperature of the expanded gas and c_p^* the mass-related, average heat capacity of a mixed gas. For an ideal gas mixture and with the approximations $c_p^*(T) = \text{const.}$ and $T_0 \gg T_1 \rightarrow 0$ follows

$$v_{\mathrm{beam,max}} = \sqrt{2 c_p^* T_0} = \sqrt{2 T_0 \frac{\sum_i x_i c_{p,i}}{\sum_i x_i M_i}} \tag{2.4}$$

with the molar fraction x_i, molar mass M_i, and the molar specific heat $c_{p,i}$ of each component and the expression

$$c_p^* = \frac{\bar{c_p}}{\bar{M}} = \frac{\sum_i x_i c_{p,i}}{\sum_i x_i M_i} \tag{2.5}$$

Relation 2.4 shows that $v_{\mathrm{beam,max}}$ depends on the reservoir temperature T_0 and the molecular mass of the gas constituents M_i. This illustrates the possibility of tuning the velocity of seeded molecular beams.[94] Stein[95] showed that cooling rates can exceed $10^{10}\,\mathrm{K\,s^{-1}}$ and can be tuned as follows: While the maximum cooling rate increases with T_0, it decreases with the molecular weight and the degrees of freedom of the expanded gas, and for increasing nozzle diameters d_0. An increase of the reservoir pressure results in an improved cooling of the sample.[37,76]
The velocity distribution function in the direction of the molecular beam axis around

the mean velocity $\bar{v}$ resulting from the supersonic expansion can be written as

$$f(v) = v^3 \left(\frac{m}{2k_\mathrm{B}T_\mathrm{axis}}\right)^{\frac{3}{2}} \exp\left[-\frac{m}{2k_\mathrm{B}T_\mathrm{axis}}(v-\bar{v})^2\right] \tag{2.6}$$

with the the Boltzmann constant k_B and T_axis accounting for the width of the distribution around $\bar{v}$.[91,92,96,97]

As the gas expands from an orifice along a pressure gradient, collisions with residual gas molecules in the vacuum chamber result in a boundary of the jet expansion where the local particle density is higher.[98] Reflections of molecules and atoms from this boundary layer interfere with each other at certain points along the molecular beam axis and cause another region with higher particle densities, which is called the Mach disk. For circular nozzles the distance x_disk of the first Mach disk from the orifice depends on the pressure ratio of reservoir and vacuum via[99]

$$x_\mathrm{disk}/d_0 = 0.67 \cdot \left(\frac{p_0}{p_\infty}\right)^{\frac{1}{2}} \tag{2.7}$$

Here, d_0 denotes the nozzle diameter, p_∞ the background pressure, and p_0 the oven pressure. In order to not perturb the expanded, cooled sample by the collisional heating in the Mach disk area, a skimmer can be placed in the molecular beam axis before the Mach disk.[100,101]

2.1.2 Mass spectrometry

Mass selection of charged species can be performed via a variety of mass spectroscopic methods (in the following MS). These techniques have in common that they exploit the interaction of electrical charges with electric or magnetic fields in order to achieve size separation with respect to the mass per charge ratio $\frac{m}{z}$. All mass spectrometers include three major parts, which are often operated at high vacuum conditions: An ion source where the investigated sample is ionized, a mass analyzer separating the species of different mass-to-charge ratios, and a detector, which converts the mass-resolved ions into detectable voltage pulses.[102]

2.1.2.1 Ionization methods

In ion sources, the ions are either formed from neutral species (e.g. by electron impact ionization (EI) or photoionization) or by suitable sample inlet approaches

(e.g. electrospray ionization, ESI). The ionization techniques are described either as soft or hard ionization techniques, depending on the resulting extent of fragmentation.[102]

Size-selection of weakly bound clusters formed over a wide range of cluster sizes by means of mass spectroscopic methods requires the abundance of charged species. While charged water clusters can be directly produced from electrospray ionization during the expansion from a capillary,[25] other approaches produce neutral water clusters via supersonic expansions and afterwards ionize or dope the clusters with chromophores for later ionization.[20,29,31,36] While electron impact ionization (EI) may be the most common ionization technique, it has been demonstrated to promote extensive fragmentation of hydrogen bonded clusters[34,48] and rare gas cluster held together by van der Waals interactions.[46]

As photoionization techniques can yield less fragmented cluster ions, several of these were applied to neutral water clusters. Single photon ionization of pure water clusters by vacuum-ultraviolet (VUV) radiation leads to fragmentation according to the following scheme[103,104]

$$\begin{aligned}(H_2O)_n + h\nu &\rightarrow \left[H_2O^+(H_2O)_{n-1}\right]^\ddagger + e^- \\ &\rightarrow H^+(H_2O)_{n-1-m} + {}^\bullet OH + m \cdot H_2O + e^-\end{aligned} \tag{2.8}$$

As the energy release due to the proton transfer reaction (around 1 eV) leads to the loss of only a few water molecules due to the large enthalpy of evaporation, it has been concluded by Litman et al.[47] that the water cluster decay due to the proton transfer after VUV ionization is negligible for clusters with a large number of constituents. For water clusters, the second reaction step in equation 2.8 can be suppressed in mixed clusters of argon and water by a fast evaporation of weakly bound carrier gas constituents from the aggregates. Thus, unprotonated, cationic water clusters of $(H_2O)_n{}^+$ type can be produced.[103,104]

The application of resonance enhanced multi photon ionization (REMPI) requires the presence of suitable electronic states. In order to reduce the effect of these relaxation processes, ultrashort laser pulses can be used. For pure water clusters a (3+1)-REMPI scheme has been reported to be applicable for $(H_2O)_{n>10}$.[105] In order to reduce immediate fragmentation picosecond laser pulses of 355 nm radiation were used. The obtained products were $H^+(H_2O)_n$ clusters.[105]

All of the above-mentioned approaches share the relatively high ionization energy of

the water clusters ($\geq 11\,\mathrm{eV}$[103,104]) that has to be put up by the ionizing radiation. Another way to achieve photoionization is to reduce the ionization energy by forming mixed clusters of water with a chromophore. These methods can use phenol,[29] alkali metal atoms,[31–33] or alkaline earth metals[30] in order to provide soft ionization methods for water clusters which do not require VUV radiation. While the excess ionization energy of the photoionization process is large enough to evaporate up to six water molecules from a phenol water cluster,[28,29] the ionization of alkali metal doped clusters is often considered to be fragmentation-free if performed close to the ionization threshold energy[106]—also referred to as appearance ionization energy[106,107] (in the following aIE).

2.1.2.2 Time-of-flight mass spectrometry

The idea of a TOF instrument has been reported by Stephens in 1946.[108] Since then, TOF mass analyzers have become widely used and appreciated for their unlimited $\frac{m}{z}$ size range,[102,109] which makes TOF-MS suitable for the study of weakly-bound clusters with hundreds to thousands of constituent molecules.[34,110]
The mass separation in a TOF mass spectrometer is achieved by acceleration of equally charged species with different masses m to different terminal velocities v by conversion of the potential energy E_{el} of a charge $q = z \cdot e$ within an electric field with the electric potential difference U_{a_0} to kinetic energy E_{kin}.[102]

$$E_{\mathrm{kin}} = E_{\mathrm{el}} \tag{2.9}$$

$$\frac{m \cdot v^2}{2} = z \cdot e \cdot U_{a_0} \tag{2.10}$$

The time-of-flight along a drift region of length l_{drift} depends on the mass-to-charge ratio $\mathrm{s}\frac{m}{z}$.

$$t_{\mathrm{drift}} = \frac{l_{\mathrm{drift}}}{\sqrt{2 \cdot e \cdot U_{a_0}}} \sqrt{\frac{m}{z}} \tag{2.11}$$

Relation 2.11 describes t_{drift} assuming a well-defined ionization location a_0 and an infinitesimally short ionization time. In reality, the ions with the same $\frac{m}{z}$-ratio arrive at different flight times at the detector due to three major broadening processes:

I The ions are formed in the same place but at different times (limited by temporal width of the ionization incident, e.g. laser pulse duration).[93,102,111]

II Ions with equal initial velocities are formed in different positions a_0 and are accelerated to different velocities due to different voltages U_{a_0} (e.g. due to an unfocused laser beam).[93,102,111]

III Ions with different initial velocities are formed in the same place (often negligible as the kinetic energies due to the acceleration stage can be orders of magnitude higher than the initial kinetic energies).[93,102,111]

These broadening processes[I] can be compensated by a dual-stage linear TOF instrument with tunable voltages by applying low extraction voltages and high acceleration voltages.[111,113] The plane perpendicular to the molecular beam direction where all ions of equal $\frac{m}{z}$ pass through simultaneously is called space focus. Its condition is an independence of the overall flight time on the ionization position a_0 within the ion source and can be expressed as:[112,113]

$$\frac{\partial t_{\mathrm{TOF}}}{\partial a_0} = 0 \tag{2.12}$$

While the first-order space focus within a single electric field ion source is fixed, it's position can be varied in a dual-stage ion source.[112–114]
In order to improve the temporal separation of ions of different $\frac{m}{z}$-values, a reflecting electric field, called reflectron or ion-mirror, is used.[115] The spatial spread of the ions with the same $\frac{m}{z}$-ratio after passing the space focus is compensated by the reflectron as ions with higher velocity dive deeper into the repelling electric field and thus reside longer within the reflectron than ions with lower velocity.[111,114] Afterwards, the ions are guided towards the detector by the reflectron and a second space focus is present at the same distance from the reflectron as the initial space focus.[114] This is the position where the detector should be placed, since the temporal resolution is optimized in the sense of space focusing and ion mass separation is enhanced due to the increased drift length and time-of-flight.[114]
Besides the benefits stated above, a reflectron allows for the detection of metastable species that decay on a µs timescale. These long-timescale fragmentations—also referred to as post-source decay (PSD)—take place in the drift tube between ion source and reflectron. The formed fragment ions (daughter ions) have the same

[I] Note that two further broadening processes exist: 1. Ions can fragment and the parent ion signal is broadened by contributions of daughter ions.[112] In this case the TOF-to-mass calibration of the parent ions is not applicable for the daughter ions.[103] 2. Equally charged ions repel each other and can therefore broaden the TOF signal.

velocity as their unfragmented parent ions.[103,114,116] As the kinetic energies of the daughter ions are smaller than those of their parent ions, they dive less deeply into the repelling electric field of the reflectron and can therefore be detected at different flight times than the parent ions.[103,114]

2.1.2.3 Detectors

In the detector, impacting ions with the same $\frac{m}{z}$ ratios are converted into an electron pulse, which is enhanced by several orders of magnitudes via several secondary electron emission steps. Common detectors are channeltrons and multichannel plates (MCP, also referred to as microchannel plates).[117,118] In order to increase the electron pulse intensity two to three MCPs can be stacked.[117] In addition, MCPs applied with a phosphor screen anode and a charged-coupled device camera can be used to obtain the spatial resolution of the impacting charges.[102,119]

2.2 Cluster preparation

Clusters can be synthesized by any technique which provides a supersaturated gas phase. Some methods for cluster production are Knudsen effusion, aggregation of gas molecules within a flow regime, atom or cluster extraction from surfaces via laser ablation or impact of charged species, supersonic expansions (see e.g. reference [97]), ESI ion sources,[25] and homogeneous, reactive in situ production of species with low volatility.[3].

In effusive beams, physical properties like the velocity distribution of the particles in the beam resemble those in the reservoir. They yield low particle sizes due to the low cooling rates[94] and can be applied to attach molecules and atoms to preformed clusters in crossed beam arrangements.[31,120]

Gas aggregation sources feed monomer units into a stationary or flowing cooling gas, which results in nucleation and cluster growth.[97] In collisional cooling cells, investigation of the aggregates is possible, e.g. via FTIR spectroscopy.[19] Extraction of monomers and clusters from surfaces can be achieved through irradiation with laser beams or impacts of charged particles.[97]

In contrast to some of the aforementioned methods, supersonic expansions can produce large particles with diameters in the range of several nanometers[21,34] while providing high particle fluxes and cooling rates exceeding $10^7\,\mathrm{K\,s^{-1}}$.[94,95]

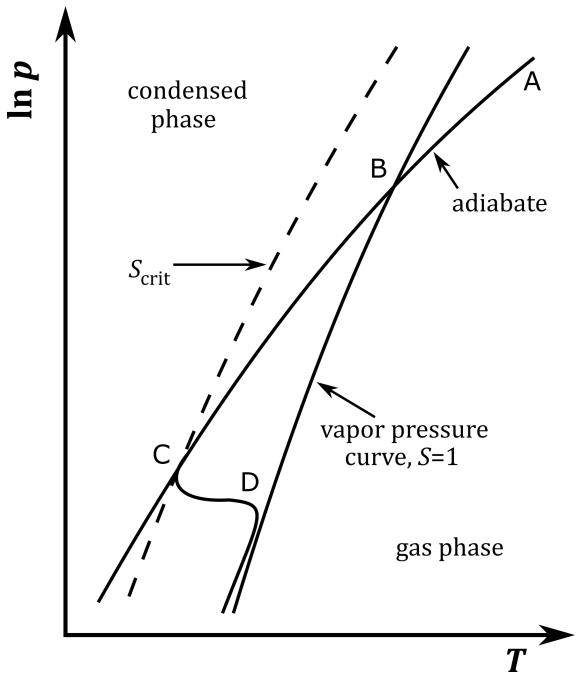

Figure 2.1: Schematic p-T-diagram illustrating the cluster formation by supersonic expansion of water vapor along the adiabate $\overline{\text{ABC}}$. The vapor pressure curve is shown as solid line. The dashed line marks the supersaturation required for the formation of stable nuclei. Figure taken from [97] and adapted by permission from Springer Nature Customer Service Centre GmbH: Springer-Verlag Berlin Heidelberg, Clusters of atoms and molecules by H. Haberland. Copyright (1994).

2.2.1 Cluster formation in supersonic expansions

The nucleation of gas phase molecules to clusters requires a supersaturated gas phase. This can be achieved by supersonic expansions as these provide large cooling rates and therefore high nucleation rates. In a macroscopic, thermodynamic point of view, the cluster formation results from an supersonic expansion. The adiabate of an expansion in a p-T-diagram is shown in Figure 2.1 by the line from point A to C.[97] As the warm gas at point A is expanded along a pressure gradient to lower p-values, it reaches the crossing point with the vapor pressure curve at B. Further adiabatic cooling results in supersaturation without cluster formation until, at C, the supersaturation reaches a critical value and stable nuclei form. The subsequent condensation leads to a temperature increase and the deviation of the system's properties from the initial isentrope.[22] After the release of the condensation enthalpy, the formed clusters are cooled by evaporation of monomers and by collisions with the carrier gas in the vicinity of the nozzle, which results in a decreasing temperature, see point D in Figure 2.1.[97] Nevertheless, the former adiabatic limit cannot be reached because of the decreasing number of collisions.[21,86]

A fundamental aspect of cluster formation from regimes with high monomer concentrations is a resulting broad cluster size distribution, which follows a log-normal distribution for small and large clusters.[34,110,121–125] The log-normal distribution function is given as

$$f(n) = \frac{1}{n\sigma\sqrt{2\pi}} \exp\left(-\frac{(\ln(n)-\mu)^2}{2\sigma^2}\right) \tag{2.13}$$

with the cluster size n and the distribution parameters μ and σ.[126] Whereas the cluster growth by condensation only would results in an exponentially decreasing cluster size distribution,[127] condensation and coagulation are responsible for the formation of large clusters following a log-normal distribution.[3,127] For the intermediate case, exhibiting a bimodal cluster distribution,[34,127] Bobbert et al.[34] concluded that two different coagulation processes are present: While the smaller clusters are formed by addition of smaller clusters to the initial nuclei, the large cluster fraction results from coagulation of larger clusters.

In supersonic expansions, the log-normal cluster size distribution can be tuned by adjustment of the partial pressures of the sample and the seeding gas in the reservoir: An increase of the seeding gas backing pressure was shown to result in larger clusters.[34,127] This can be explained by an increased cooling rate leading to a minimized evaporation from the clusters as the enthalpy of condensation does not heat the clusters to evaporative ensemble conditions. Consequently, an increase of the nozzle temperature at otherwise identical conditions shifts the cluster size distribution to smaller cluster sizes.[34]

An attempt to estimated the average cluster size $\bar{n}$ for several expansion conditions was made by Hagena for atomic clusters by a unified scaling law with a "reduced scaling parameter" Γ^*.[128] The mean cluster size of the terminal cluster distribution can be estimated via[128]

$$\bar{n} = \mathrm{c}_1 \cdot \left(\frac{\Gamma^*}{1000}\right)^{\mathrm{c}_2} \tag{2.14}$$

with

$$\Gamma^* = \frac{\Gamma}{\Gamma_{\mathrm{ch}}} = \frac{N_0 d_{\mathrm{eq}}^{q} T_0^{\frac{q}{4}-1.5}}{r_{\mathrm{ch}}^{q-3} T_{\mathrm{ch}}^{\frac{q}{4}-1.5}} \tag{2.15}$$

with the monomer density in the reservoir N_0, the equivalent nozzle diameter for

conical nozzles $d_{eq} = d_0/\tan(\alpha)$ (d_0 being the orifice diameter and α the opening angle), the nozzle temperature T_0, q as parameter that has to be determined experimentally, the scaling factor Γ, and the two characteristic parameters r_{ch} and T_{ch}. For sodium doped water clusters these parameters and the constants c_1 and c_2 were determined to be $r_{ch} = 3.19\,\text{Å}$, $T_{ch} = 5684\,\text{K}$, $q = 0.643 \pm 0.63$, $c_1 = 2.63 \pm 0.45$, and $c_2 = 1.872 \pm 0.066$.[34] Equation 2.14 illustrates that large reduced scaling parameters ($\Gamma^* > 1000$) are required to form clusters with many constituent molecules.[128] Aside from the sheer cluster size distribution, the investigation of the isomer composition and population for each cluster size is of growing interest. In this context the formation of mixed rare gas alkali metal water clusters[64] and vibrational spectroscopy of small sodium doped water clusters[68] showed to be promising approaches to exploit the presence of several isomers for a given cluster size.

2.2.2 The pickup approach

The measurement of cluster size distributions requires size-selective mass spectrometry methods which are ideally fragmentation free. One way to overcome harsh ionization conditions, which often lead to fragmentation, is the doping of clusters with chromophores in order to access softer ionization conditions. This pickup of atoms, molecules or small clusters to larger clusters can be achieved through two approaches: by crossing the initial molecular beam with an effusive beam or by passing it through a gas cell, also referred to as scattering cell or pickup cell. The first technique was developed in the Scoles group in order to attach SF_6 to Ar-clusters.[120] Crossed beam pickup approaches have also been used to introduce alkali metals[31,34,63,129] and alkaline earth metals[30,130] to hydrogen-bonded clusters. The use of a gas cell for pickup experiments instead provides a volume with dopant density in order to increase the pickup probability for each passing cluster and thus the mixed cluster production.[34,127,131,132]

Due to the conservation of momentum, small host clusters can be deflected by dopant species or the uptake of these.[133] This can lead to intensity losses in the experiment. Consequently, the host cluster's momentum should be significantly higher than the dopant's, which is provided by the use of large host clusters. If each pickup event is independent of the amount of dopants already captured by a cluster, the probability for the pickup of k dopants can be expressed as a Poisson distribution. This was shown to be consistent with observed abundances of pickup products.[134–138] The pickup probability according to the Poisson distribution function can be calculated

via

$$P(k,N) = \frac{(l_{\text{pickup}} N \sigma_{\text{pickup}})^k}{k!} \cdot \mathrm{e}^{-l_{\text{pickup}} N \sigma_{\text{pickup}}} \tag{2.16}$$

for a pickup cell with the length l_{pickup}, a dopant gas number density N, the number of captured dopant units k, and the pickup cross section σ_{pickup}.[134,135,137,139]
As the pickup probability $P(k,N)$ depends on the pickup cross section σ_{pickup}, the detected cluster size distribution is not necessarily equal to the initial cluster distribution since smaller clusters should have a smaller σ_{pickup} than larger clusters and are prone to deflection upon doping.
An attempt to correct for the capture efficiency of sodium atoms by ammonia clusters and for the detection efficiency over a broad size range was made by Schläppi et al.:[35] While sodium gas density and the cluster size affected the efficiency of pickup of at least one sodium atom, the sticking efficiency and the photoionization efficiency were assumed to be constant for all cluster sizes. The doping process and subsequent photoionization with 4.66 eV photons was found to lead to the loss of only few molecules per cluster, which can be negligibly small for larger clusters compared to their cluster size.[45,47,140] Compared to ionization methods such as EI and VUV photoionization, photoionization of sodium doped clusters was concluded to be mostly fragmentation free for photons energies below 5 eV.[46–48]
Despite the inability of mixed cluster detection of N_2O and NO_3^- containing particles[141,142] due to intra-cluster reactions, a variety of sodium doped clusters such as benzene,[35] water,[42] methanol,[42] ethanol,[42] 2-aminoethanol,[139] acetic acid,[140] dimethyl ether,[40] ammonia,[39] and rare gases[46] have been produced and detected.

2.2.3 Fragmentation

When clusters are formed, it is important to provide efficient cooling, as a high internal energy destabilizes the cluster. Isolated clusters can reduce their internal energy only by unimolecular decay. This decomposition can occur in two different ways: by the evaporation of monomers or by fission of the initial cluster.[97,143]

$$\mathrm{M}_n \longrightarrow \mathrm{M}_{n-1} + \mathrm{M} \tag{2.17}$$

$$\mathrm{M}_n \longrightarrow \mathrm{M}_{n-x} + \mathrm{M}_x \tag{2.18}$$

The energy balance for the evaporation of a monomer from a M_n cluster is[97,144]

$$E_{\mathrm{int},n} = E_{\mathrm{int},n-1} + E_{\mathrm{diss},\,n} + E_{\mathrm{kin,vib,rot,el}} \tag{2.19}$$

with the internal energies of the parent cluster $E_{\mathrm{int},n}$ and the daughter cluster $E_{\mathrm{int},n-1}$, the dissociation energy $E_{\mathrm{diss},\,n}$ for the separation of a monomer from the cluster, and the total energy of the monomer $E_{\mathrm{kin,vib,rot,el}}$. The energy loss of the evaporating cluster is $E_{\mathrm{diss},\,n} + E_{\mathrm{kin,vib,rot,el}}$ per evaporated monomer. As the internal energy per monomer unit of the cluster decreases due to the evaporation and the evaporation rate coefficient is a function of the internal energy of a cluster, the evaporation rate constant for subsequent evaporation is lower. This is why the evaporative ensemble theory[144–147] assumes that the rate coefficient for subsequent monomer evaporation from a cluster, that has already evaporated at least one monomer, is proportional to the reciprocal time since the beginning of the decay process.[147] This explains why clusters formed at elevated temperatures and in the absence of large cooling rates are metastable and decay on the µs timescale.[23,145]

As a cluster's total heat capacity increases with n, larger clusters at evaporative ensemble conditions cool less efficiently by a single evaporation incident and therefore tend to evaporate more molecules.[23,144] This cluster size dependency was shown in the decreasing abundance of parent ions due to metastable decay on a µs timescale:[23] While the $H^+(H_2O)_n$ parent ion abundance for $n = 290$ was halved and resulted in the evaporation of one to three monomers, 80% of parent ions with $n = 100$ did not decay. The clusters showing this significant monomer evaporation were formed by a corona discharge at ambient air and tempered within a feed-through capillary ($T_{\mathrm{capillary}} = 26 - 60°\mathrm{C}$).[23]

But at which temperatures are evaporative ensemble conditions present in isolate water clusters? The cluster temperatures of an evaporative ensemble were estimated by Klots[147] via the expression

$$\frac{RT}{E_{\mathrm{evap,bulk}}} = 0.04 \tag{2.20}$$

for evaporation on timescales of tens of microseconds. The evaporative ensemble temperature for water clusters obtained from this simple relation with the bulk molar evaporation energy ($E_{\mathrm{evap,bulk}} = 44.0\,\mathrm{kJmol^{-1}}$[148]) is around 210 K. In contrast to this, the investigation of the fragmentation ratio vs. the initial cluster temperature showed that evaporative ensemble temperatures of charged water clusters

range from 136 ± 6 K for $(H_2O)_{48}^-$ and 144 ± 6 K for $(H_2O)_{118}^-$ [149] to 163 ± 2 K for $H^+(H_2O)_{n=60-79}$. [150]

In order to prevent evaporative ensemble conditions, seeded supersonic expansions can be performed, reducing the cluster temperatures below the critical temperatures: Modelling of the droplet formation kinetics and the transport processes for coexpansions of neon and water vapor by Gimelshein et al. [86] have shown that the clusters can be cooled to temperatures of 100 K in the apparatus described in Chapter 3. [86] Comparison of simulated and experimental $Na(H_2O)_n$ cluster distributions showed sufficient agreement for $n \geq 50$. From this was concluded that fragmentation of the clusters—due to the pickup of a sodium atom and the subsequent photoionization with 3.2 eV photons—is negligible for sufficiently larger clusters which are ionized close to their ionization threshold. [36,71]

An experimental tool to study the mechanistic aspects of fast fragmentation processes is the measurement of the kinetic energy of an ejected fragment. [138,151] It was recently shown through this method that collisions of an argon atom with a $H^+(H_2O)_{n=4-8}$ cluster results in fragments, of which only a fraction follows the Maxwell-Boltzmann velocity distribution. [151] The observation of fragments deviating from the Maxwell-Boltzmann velocity distribution was concluded to indicate fast evaporation of a monomer before the energy redistribution within the cluster could occur.

2.3 Sodium water clusters

2.3.1 The sodium water reaction in clusters

The addition of a sodium atom to a water cluster does not result in an explosive reaction as is known for bulk sodium and bulk liquid water at ambient conditions. The crucial differences of the molecular beam experiment to the bulk reaction are the cooled and thus solid-like behaving water aggregates and the control of the number of collisions between the water clusters and the dopant species. [129,152] In a pioneering experiment, the group of Hertel demonstrated the possibility of forming $Na(H_2O)_n$ clusters from atomic sodium and water clusters with the pickup technique. [31] Single collision conditions in a crossed beam experiment of Na_m and $(H_2O)_k$ yield only products of $Na(H_2O)_n$ type, [129] whereas in experiments with pickup conditions al-

lowing several collisions of Na or Na_2 with pure water clusters $Na_{1-4}(H_2O)_n$ [63,131] and $Na(NaOH)_{2,4,6}(H_2O)_n$ were formed.[152,153] For the former species an odd/even oscillation of the ionization energies has been deduced from the observation that clusters with even numbered sodium stoichiometry were observed only at high UV photon energies of $4.43 - 4.66\,eV$.[63,131,152] The formation of the sodium hydroxide containing species requires multiple collisions of a water cluster with sodium atoms or dimers, as the underlying reaction mechanism consists of at least two collision induced reaction steps.[54,152,153] Buck and Steinbach proposed a two step mechanism for the formation of $Na(NaOH)_2(H_2O)_n$:[153]

$$Na + (H_2O)_{n+x+y} \longrightarrow Na(H_2O)_{n+y} + x\,H_2O \tag{2.21}$$

$$Na_2 + Na(H_2O)_{n+y} \longrightarrow Na(NaOH)_2(H_2O)_n + H_2 + (y{-}2)\,H_2O \tag{2.22}$$

The clusters' internal energy increase due to the sodium pickup process is reduced by evaporation of water molecules ($x = 2 - 3$).[129] In a subsequent collision of the stable sodium doped water cluster with Na_2, several products are formed: molecular hydrogen, water molecules, and a cluster of $Na(NaOH)_2(H_2O)_n$ type, see reaction 2.22.

Molecular dynamic simulations by Mundy et al.[54] supported this mechanism and allowed to subdivide the second step into three reactions:[54,152]

$$Na_2 + Na(H_2O)_{n+2} \longrightarrow Na_3(H_2O)_{n+2} \tag{2.23}$$

$$Na_3(H_2O)_{n+2} \longrightarrow Na(NaH)(NaOH)(H_2O)_{n+1} \tag{2.24}$$

$$Na(NaH)(NaOH)(H_2O)_{n+1} \longrightarrow Na(NaOH)_2(H_2O)_n + H_2 \tag{2.25}$$

The sodium dimer addition to the $Na(H_2O)_{n+2}$ cluster by charge separation in Na_2 to yield $Na^{\delta+}$ and $Na^{\delta-}$ is followed by NaH and NaOH formation. The explanation for this reaction to occur therefore is as follows:[54,152] The sodium dimer is polarized by the water cluster and the partially negatively charged sodium atom of the dimer extracts a proton from a water molecule with the resulting hydroxide anion forming NaOH with a partially positively charged sodium atom. The NaH formation was determined to be the rate determining reaction step[54] and could also be interpreted as an insertion of a sodium atom in a OH bond.[154] Dissociation of another water molecule due to the reactive hydride yields molecular hydrogen and a second NaOH. This mechanism explains the formation of even numbered amounts of NaOH

within the product clusters due to the stoichiometry needed to form molecular hydrogen.[54,131,152,153] The energy released upon NaOH formation should lead to the evaporation of H_2O or NaOH constituents. Since only even numbered amounts of NaOH were observed, it was concluded that water molecules are weaker bound to the cluster than NaOH.[131] Triply sodium doped clusters of $Na_3(H_2O)_{n=1-4}$ type were concluded to be the precursors to the reaction described above.[131]
Computational studies indicate that the direct sodium hydroxide formation via

$$Na_2 + (H_2O)_n \longrightarrow (NaOH)_2(H_2O)_{n-2-x} + H_2 + x\,H_2O \tag{2.26}$$

is less probable in molecular beam experiments. The reason is, that the formation of a $Na_2(H_2O)_{6,8}$ cluster, in which the sodium atoms have different charges, does not occur likely but can be increased by an asymmetric charge distribution as found in $Na(H_2O)_n$ clusters.[155] Moreover, the hydrolysis of the sodium atom can be easily catalyzed by $(NaCl)_2$ clusters,[156] which indicates that it could be catalyzed for instance by other species such as solvated electrons or a third sodium atom as proposed by Mundy et al.[54] and Steinbach and Buck.[152]

2.3.2 Hydrated electrons

The applicability of sodium atoms as chromophores for the detection of weakly bound clusters is related to the decrease of the ionization energy due to the formation of solvated electrons and has been observed for mixed sodium solvent clusters.[106] The hydrated electron has been concluded to be an important reaction step for the formation of sodium hydroxide on ice[69] or the explosive reaction of a potassium-sodium alloy with bulk water.[157]

2.3.2.1 Experimental characterization approaches

Solvated, delocalized electrons in clusters are characterized by their ionization energies, which can be determined by two experimental approaches:

1. The measurements of ionization efficiency curves. When the normalized ion yield (IY) is plotted against the photon energy, the ionization threshold energy (also referred to as appearance ionization energy,[106,107] aIE) can be obtained as the baseline intercept from steepest gradient extrapolation.[13,70]

2. Photoelectron spectroscopy (PES), where the electron's kinetic energy is mea-

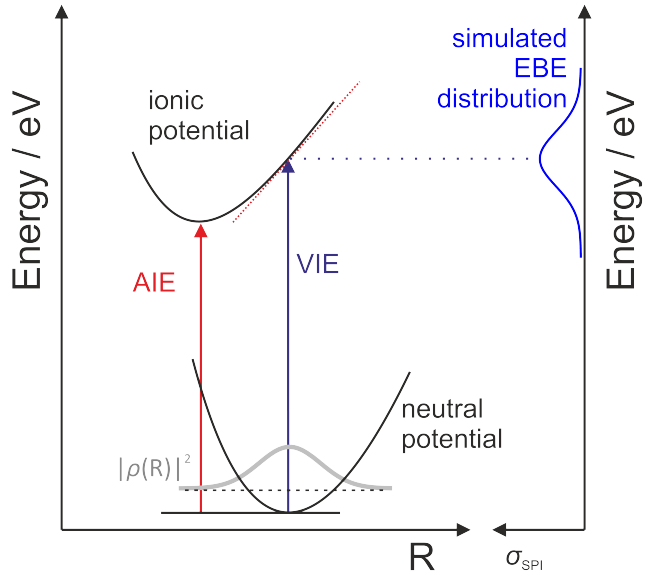

Figure 2.2: Schematic diagram illustrating the difference between adiabatic and vertical ionization energy (AIE and VIE)[13] and the calculation of EBE distributions via the reflection principle in terms of a distribution of single photon ionization cross sections (σ_{SPI}).[158–160] The ground state probability function of the neutral cluster $|\rho(R)|^2$ is reflected at the ionic potential, which is assumed to exhibit an almost linear slope around $R_{e,neutral}$.[159] Figure inspired by references [13, 158, 159].

sured and the electron binding energy (EBE) can be determined as the difference of the photon energy and the kinetic energy of the electron.[13,40,63,70] In PES spectra the whole distribution of ionization energies up to the photon energy used for ionization is obtained.

In order to understand the connection between these measured properties and the ionization process of a cluster the terms of adiabatic and vertical ionization energies are used. The adiabatic ionization energy denotes the energy difference of the ground state energies of a neutral and an ionic cluster, see Figure 2.2. The vertical ionization energy corresponds to the energy difference of the neutral and the ionic cluster in the same configuration. If the ionic and the neutral cluster have differing minimum energy structure, the VIE is larger than the adiabatic ionization energy.[13]
While the aIE of IY curves is often assumed to correspond to the adiabatic ionization energy, the IY curve ranges to ionization energy values above the VIE.[13] Peaks in PES spectra are interpreted as vertical ionization energies.[26,67,161] If an IY curve is

interpreted as an integrated PES-analogue spectrum, the VIE might be determined from the maximum position of the first derivative of the IY curve.[13,107,162,163] Then the VIE corresponds to the inflection points of the IY curve.
Which of the two experimental approaches is applicable depends on the charge of the investigated species. PES provides the ionization energy distribution for all cluster sizes[67] and is widely used on anionic clusters as they are easily size separable.[13,106] For neutral clusters, the use of PES yields size-unselective data.[40] In contrast to this, the measurement of IY curves can provide size-selectivity as the mass separation is achieved after the ionization step.
The VIE is calculated as the energy difference between the neutral potential and the ionic potential. However, many experimental methods such as PES or photoionization efficiency curves obtain broad peaks and therefore do not sharply probe the VIE but a distribution of ionization energies.[13] These can be simulated by means of a convolution of the ground state probability function $|\rho(R)|^2$ and the ionic potential.[158–160] The simulated EBE distribution therefore resembles a reflection of $|\rho(R)|^2$ on the ionic potential close to internuclear distance of the neutral state's equilibrium position $R_{\mathrm{e,neutral}}$, see Figure 2.2.

2.3.2.2 Isomers of anionic water clusters

Since anionic $(H_2O)_n^-$ clusters are a suitable model system for studying the properties of the hydrated electron, they were already investigated in great detail, see e.g. references [26, 67, 149, 161, 167]. The vertical ionization energies of $(H_2O)_n^-$ clusters—determined as peak positions in photoelectron spectra—decrease almost linearly with $n^{-1/3}$ for each isomer class, see red and black open symbols in Figure 2.3. This indicates that the VIE depends on the interactions of all H_2O constituents and that the cluster geometry might converge for $n \to \infty$ towards spherical shape.[106] The isomers with higher VIE were assigned to internally solvated electrons, those with lower VIE to isomers where the excess electron resides at the cluster surface.[106]
The ionization energies of solvated electrons in bulk water[164–166] are shown at $n^{-1/3} = 0$. The bulk ionization energy values determined by PES measurements of internally solvated electrons in liquid jets ($3.3 - 3.6\,\mathrm{eV}$[164–166,168]) are matched by extrapolations of the VIE from $(H_2O)_n^-$ clusters with internally solvated e_{hydr}^-, which were assigned as isomer class I, see [106] and references cited therein. The VIE of surface bound hydrated electrons in larger clusters of isomer class II with

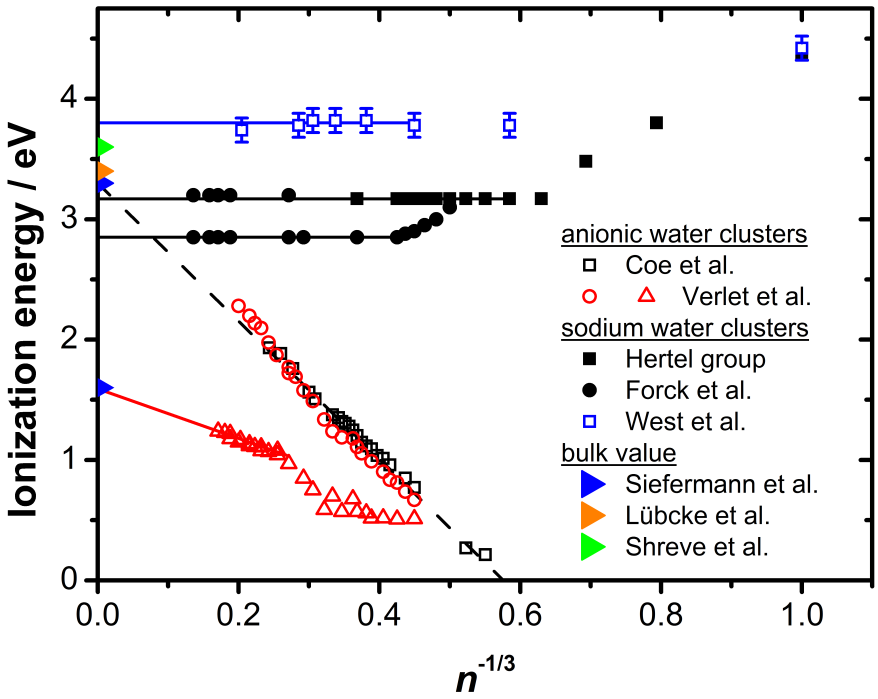

Figure 2.3: Comparison of appearance ionization energies of $Na(H_2O)_n$ clusters (black filled symbols)[38,70] and the VIE of $Na(H_2O)_n$ clusters (open blue squares[40]) and the VIE of $(H_2O)_n^-$ clusters (black open squares[161], red circles and triangles[67]) as determined from peaks of photoelectron spectra with ionization energies of bulk solvated electrons. The EBEs of solvated electrons in bulk water (blue[164], orange[165], and green[166]) are shown at $n^{-1/3} = 0$. The dashed black line is the extrapolation of Coe et al.[161] The solid lines are extrapolations from the corresponding data. Figure taken from reference [106] and modified.

$n \geq 50$ extrapolate to a bulk value of 1.6 eV,[67] which is in agreement with the value of hydrated electrons in the vicinity of a liquid jet surface suggested by Siefermann et al.[164] (note that this value is still debated as it could not be reproduced by other groups[169]), see open triangles and solid red line in Figure 2.3. The extrapolations to bulk values are suitable for larger clusters in which the VIE of the two isomer classes of $(H_2O)_n^-$ appear to scale with the spatial distribution of the electron density and no structural transitions with increasing cluster size occurs.[67] For clusters with $n = 11 - 35$ a third isomer class with ionization energies of around 0.25 eV was reported.[67] The abundance ratio of the three isomer classes has been shown to strongly depend on the seeding conditions as the surface electron isomer abundance is promoted by expansion conditions providing colder clusters.[67]

In conclusion, the extensive study of size-selected photoelectron spectra[26,67,161,167]

of $(H_2O)_n^-$ and their evolution upon variation of the cluster temperatures provided a detailed understanding of the isomer distribution and of the properties of the isomer classes.

2.3.2.3 Isomers of sodium water clusters

Size-unresolved photoelectron spectroscopy has been applied to sodium doped water clusters.[40] The onset of the peak was determined to be in the range of $3.2 - 3.4\,\text{eV}$ and the peak position of the distribution of ionization energies was found to be at $3.8 \pm 0.1\,\text{eV}$, see blue open squares in Figure 2.3. In order to obtain size-selective ionization energies, photoionization with tunable UV lasers was applied to determine the aIE of $Na(H_2O)_n$ clusters from photoionization efficiency curves in which the detected ion yield was plotted against the photon energy.[63,70] It was found that, when a sodium atom is added to a hydrogen bonded cluster, the ionization threshold energy decreases from $5.139\,\text{eV}$ for atomic sodium[62] to cluster size and constituent dependent values.[42,63,70,106,139] A comparison of the appearance ionization energies for different cluster sizes shows that small clusters with $n \leq 4$ show a decreasing aIE with increasing n, whereas clusters with $n \geq 4$ have a constant aIE of $3.17 \pm 0.05\,\text{eV}$,[38,63], see black filled squares in Figure 2.3. This aIE has been assigned to clusters from the so-called isomer class I.[70,71,106] Other alkali metal dopants yield constant aIE values in the range of $3.12 - 3.18\,\text{eV}$ for clusters with $n \geq 4$.[32,33] Mg and Ca doped water clusters have an aIE for $n \geq 9$ or $n \geq 8$ of $3.18\,\text{eV}$.[30] The levelling off of the aIE has been interpreted to be caused by the completion of the first solvation shell.[30,32,33,63,70]

Although the high-n aIE of $M(H_2O)_n$ clusters is close to the value for internally solvated electrons in bulk water around $3.3\,\text{eV}$ from Siefermann et al.[164] and Tang et al.[168], it is not linked to the abundance of internally solvated electrons, but to the attractive interaction between the hydrated electron and the M^+ counterion, as the hydrated electron in $Na(H_2O)_n$ clusters was shown to reside on the surface.[70] In different OH containing solvents such as methanol, this interpretation persists.[41,42,106] For sodium water clusters it was shown that a second isomer class with a lower aIE than isomer class I exists. Its aIE values decrease to a high-n limit of $2.8\,\text{eV}$ for $n \geq 15$ (and therefore $n^{-\frac{1}{3}} \leq 0.41$),[70] see black filled dots in Figure 2.3. Molecular dynamics simulations suggested that the isomer classes I and II differ in the spatial separation of Na^+ and e_{hydr}^-:[70] in both cases the sodium was solvated in terms of coordination by several water molecules and the electron was shown to reside on

the cluster surface. The separation of Na^+ and ${e_{hydr}}^-$ is governed by the position of the sodium cation within the clusters. It can be solvated on the cluster surface or within the cluster interior. The former case corresponds to isomer class I configuration while the latter was assigned to isomer class II.[70] For isomer class II, the separation of Na^+ and ${e_{hydr}}^-$ is larger than in isomer class I. This results in a weakened attractive interaction of the two charges and therefore in a more loosely bound electron.[70] Consequently, the structural properties of the sodium cation and the hydrated electron were referred to as solvent separated ion pair ${Na_{aq}}^+ + {e_{hydr}}^-$ for isomer class II and contact ion pair ${Na_{aq}}^+ \cdots {e_{hydr}}^-$ for isomer class I.[70]
The discovery of $Na(H_2O)_n$ clusters with a higher degree of $Na^+ - {e_{hydr}}^-$ separation by Forck et al.[70] supports the results of Kim et al.[69] where the presence of solvated electrons was concluded to be a mandatory step for the formation of the products NaOD and solvent separated Na^+ and OD^- in a surface reaction of sodium atoms and ice. Here it was found, that Na^+ was solvated within the surface film while OD^- was located at the surface.[69]
An increase in the photoionization efficiency curve of $Na(H_2O)_{45-450}$ for photon energies larger than 3.7 eV has been mentioned by Pradzynski et al.[71] They concluded the presence of a third isomer class, for which the neutral sodium atom is attached to the cluster surface.
Most experimental studies focused on the size selective determination of the aIE of $Na(H_2O)_n$ clusters. Unfortunately, this approach and interpretation cannot observe other isomers than those with the lowest ionization energy and neglect other isomers that can be present. This is further indicated by IR-spectroscopic results on $Na(H_2O)_3$[68] and the photoelectron spectrum of $Na(H_2O)_n$ clusters[40] as both studies reveal that isomers with higher ionization energies are present.

2.4 Spectroscopy of water clusters

2.4.1 Size-selective cluster detection

As molecular aggregates can be produced in a variety of size ranges, matching investigation techniques are needed. Small $(H_2O)_{n=2-5}$ clusters can be investigated via standard vibrational spectroscopy methods. The clusters can be prepared in jet expansions or matrices and the observed peaks can be assigned to distinct isomers by a comparison to vibrational frequencies calculated by means of high-level

quantum chemical methods.[75,76,170] Scattering of clusters with a crossed helium beam achieves size resolution in terms of spatially separating clusters with different masses due to the conservation of momentum.[171,172] This method is capable to size-resolve clusters with up to 10 molecules.[27] Size-selectivity of the water clusters with $n > 10$ can up to now only be achieved by mass spectroscopic (MS) methods, which require charged sample substances. Within the field of MS-assisted studies on water clusters, several sample preparation techniques are used:

- electrospray ionization from charged capillaries to yield ionic cluster such as $H^+(H_2O)_n$[79] or $[M(H_2O)_n]^{z+}$ ($M = Ce, Eu, La, Na, Ca, {SO_4}^{2-}, I^-$),[25,173]
- gas aggregation sources combined with pulsed gas discharges to form $H^+(H_2O)_n$ clusters,[26,174]
- threshold ionization of pure water clusters,[103]
- formation of pure water clusters from supersonic expansions and subsequent chromophore labelling of the clusters with e.g. phenol,[29,175] alkali metals,[31–33] alkaline earth metals,[30] or attachment of electrons[67,77,161] to obtain ${(H_2O)_n}^-$.

As positive charges such as La^{3+} influence the morphology of the network of hydrogen bonds within a water cluster,[81] the vibrational spectra of these can differ from those of neutral water clusters. Despite this, the major advantage of charged clusters as sample species is the possibility to modify the sample properties such as the cluster temperature in temperated ion traps.[81]
Threshold ionization of pure water clusters leads to the above-mentioned formation of protonated water cluster,[103,104] see Equation 2.8. Unprotonated, cationic water clusters (${(H_2O)_n}^+$) are accessible via threshold photoionization of mixed rare gas water clusters by VUV radiation.[103,104]
If threshold ionization with VUV radiation is not accessible, chromophores can be introduced into the hydrogen bond network either by coexpansions with the water vapor or via pickup arrangements. Phenole is a suitable dopant as it can be integrated into the cluster by its hydroxyl group and and is ionizable via REMPI by 275 nm photons. Unfortunately, the excess energy can lead to evaporation of up to six water molecules.[29]
The methods described in this section so far are suitable to measure vibrational spectra by means of infrared multi photon dissociation spectroscopy. In contrast to this, neutral alkali metal water clusters can be examined by a special kind of

action spectroscopy. In this method both an IR and an UV laser are used. An increase of the ion yield for a certain cluster size n is observed if the IR radiation is resonant with the absorption frequency of the clusters. This effect and the proposed underlying mechanism[43,71] are described in Section 2.4.4.

2.4.2 Water molecule binding motifs

The IR spectrum of water vapor in the gas phase at ambient conditions shows multiple peaks assignable to rovibrational transitions. These originate from the population of many rotational states of the asymmetric rotor. Collisional cooling in supersonic expansions efficiently reduces the population of rotationally excited states[91] and thus simplifies the spectrum.[76] The vibrational frequencies of the water molecule's fundamental transitions are $1595\,\mathrm{cm}^{-1}$ (bending vibration), $3657\,\mathrm{cm}^{-1}$ (symmetric stretching in H−O bond direction), and $3756\,\mathrm{cm}^{-1}$ (asymmetric stretching vibration).[148]

When the water molecule forms a hydrogen bond with a suitable hydrogen atom donor or acceptor site, the molecule's OH-bonds are weakened. This can be monitored by vibrational spectroscopy methods as the band positions are down-shifted to lower vibrational frequencies by up to several hundreds of cm^{-1}.[176] Due to the cooperativity of hydrogen bonds, the aforementioned spectral shift depends on the surroundings of the affected OH-oscillator.[16] The hydrogen bond topology of a specific water molecules with its neighboring water molecules is denoted in terms of binding motifs, which abbreviate how many hydrogen atoms the molecule accepts (A) or donates (D). The spectral ranges in which the water molecule motifs absorb radiation are summarized in Table 2.1. The binding motifs are illustrated in Figure 2.4 for an isomer of the $(H_2O)_{11}$ cluster. For larger clusters the spectral regions cannot be assigned unambiguously to the molecular environments as the spectral regions where the motifs absorb overlap.[16]

Molecules that serve once as a hydrogen donor and once as acceptor are denoted DA. Water molecules of this type are present in neutral water clusters with 3 to 5 water molecules, for which ring type structures are observed.[75,176] The spectra of these clusters exhibit well separated peaks in the OH-stretch region and can be interpreted by means of high-level quantum chemical calculations which circumvents the lack of mass resolution.[75,76] As the cluster size increases, the interpretation of experimental spectra in terms of the assignment of distinct isomers to certain peaks is complicated by an increasing number of low energy isomers that can contribute

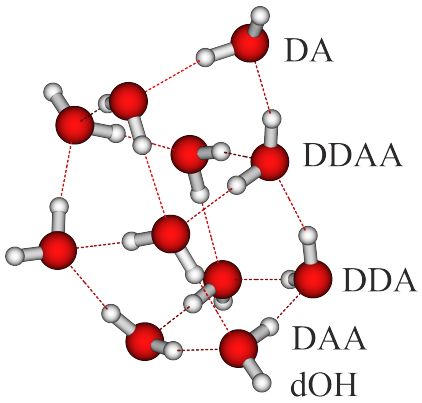

Figure 2.4: Structure of the $(H_2O)_{11}$ cluster predicted by the TTM2.1-F potential as published by Kazachenko and Thakkar;[177] reproduced from numerical data.

Table 2.1: Band positions of OH-stretch vibrational transitions of the binding motifs mentioned in Section 2.4.1. The values for DA bound molecules are taken from reference [176] as cited in [75]. The values for three- and four- coordinated water molecules are taken from [19, 71, 81, 178] for larger clusters and from [27] for small clusters with $n = 8 - 10$.

motif	DA[75,176]	DAA	DDAA	DDA	dOH	ref.
$\tilde{\nu}$/ cm^{-1}	3533 ($(H_2O)_3$) 3401 ($(H_2O)_4$) 3355 ($(H_2O)_5$)	≤ 3100 $3000 - 3150$	3400 (amorphous) 3220 (ice)	$3520 - 3600$ $3500 - 3600$	3703 ≈ 3700	[178] [27] [19, 81]

to the spectra.[68,76,179] A prominent example for this is the water hexamer: For $n = 6$, three low energy isomers exist: a trigonal prism, a book-like cluster, and an isomer referred to as "cage" (Pérez et al.[179]).[179,180] In addition to these, a ring-type isomer can be observed if the water cluster is grown in a helium droplet which prevents the formation of three-dimensional isomers.[181] $(H_2O)_6$ thus marks the cluster size where the transition from almost two-dimensional to three-dimensional clusters occurs.[179,182] In case of the latter, the clusters contain water molecules of DDA and DAA type. Only water molecules which donate less than two hydrogen bonds exhibit free OH oscillators, also referred to as dangling OH bonds (dOH). The geometry of $(H_2O)_{n=7-9}$ clusters is based on the cubic, D_{2d} symmetric water octamer and obtained by removal or addition of a water molecule.[27,74,87,183] While the minimum energy structure of $(H_2O)_{10}$ is often predicted to be a petagonal prism structure,[27,87] a cube with two opposing, DA bridged edges was concluded from experimental vibrational spectra.[27,74]

In larger clusters, molecules of DDAA type (double donor and double acceptor) are abundant.[79,87,177,178,184] These DDAA motifs were shown to dominate the vibra-

tional spectra of clusters with tens to hundreds molecules.[19,21,29,37,71,106,185,186] Due to the sensitivity of the OH stretch frequency to its environment, the large number of constituents, and the resulting large number of normal modes of the hydrogen bonded cluster, a broad spectral feature around $3400\,\mathrm{cm}^{-1}$ for DDAA type molecules is observed.[71] If the cluster's interior resembles the structure of an ice phase, the cooperativity is maximized, which results in a downshift of the maximum absorption from $\tilde{\nu} \approx 3400\,\mathrm{cm}^{-1}$ to $\tilde{\nu} \approx 3220\,\mathrm{cm}^{-1}$.[16,19,21,71,81,187] Note that both peak positions are sensitive to the temperature.[19,187]

For sodium doped clusters the motif nomenclature (DA, DAA, DDA, DDAA) can be extended to account for interactions of the water molecules with the sodium atom and the solvated electron. The direct coordination of the sodium atom by a water oxygen atom is denoted as C, whereas the interaction of H atoms with the delocalized electron are expressed by an e.[188] While the vibrational spectra of low-IE sodium water clusters can be dominated by contributions from these interactions[188] the possibility of non-destructive sodium capturing, producing clusters in which the hydrogen bond network remains nearly unchanged, has also been reported.[37,68,71]

2.4.3 Probing physical states of water clusters

Bulk water has 17 known ice phases which differ by their crystal lattice structures and their proton order.[189,190] The two at pressures up to 1 bar thermodynamically stable phases relevant to the experiments—hexagonal ice Ih and cubic ice Ic—, other ice phases are produced at high pressure conditions of bulk samples or by removal of guest atoms from clathrates. Ih and Ic cannot be distinguished from their IR absorption spectra.[191] Their lattice structures differ by the stacking order of tetrahedrally coordinated DDAA water molecule layers; Ih has the stacking order $[ABABAB]_\infty$ whereas Ic has $[ABCABC]_\infty$ order.[192] When supercooled water clusters crystallize, they can form cubic ice clusters[193] or an ice phase best described as a stacked mixture of Ih and Ic.[88,194]

A standard technique to observe phase transitions in bulk samples is differential scanning calorimetry, which measures the amount of energy that is consumed in order to reach a certain temperature. Von Issendorff et al. developed an analogous method to apply on isolated, size-selected clusters.[149,150,195] They investigated phase transitions in $H^+(H_2O)_n$ and $(H_2O)_n{}^-$ clusters by measuring the ratio of metastable decay after collisional heating.[149,150] While this technique can determine at which temperature a phase transition occurs, it does not yield a direct feedback on the

cluster's structure or physical state. In contrast to this, the physical states of water clusters can be probed by means of electron diffraction[84,193,196], neutron diffraction[190] or FTIR spectroscopy.[19,21,187]

Figure 2.5 shows the FTIR spectra of µm-sized water droplets at 273 K, 240 K, and 235 K, top black traces.[187] While the two spectra at higher temperatures are similar to each other and correspond to liquid and supercooled water, the spectrum of ice I droplets at 235 K is of entirely different shape: The peak position is downshifted to 3260 cm^{-1} and the intensity at 3400 cm^{-1} decreased.[187] Note that the peak position in the IR spectrum of ice particles is affected by the temperature of the droplets and can be described by a linear shift of 0.2 $cm^{-1}K^{-1}$ between 20 K and 240 K and $3220 - 3260\,cm^{-1}$.[19,21] The peak maximum of ice at around 3250 cm^{-1} was suggested to result from excitation of an in-phase, asymmetric vibration of DDAA water molecules in crystalline geometries,[197] which was concluded to cause a large transition dipole moment.[16]

Vibrational spectroscopy of sodium doped water clusters[86] and $La^{3+}(H_2O)_n$ clusters[81] showed the presence of crystalline clusters for $n = 140 - 550$. However, the limiting cluster size for the presence of crystalline clusters is still unclear. Estimates for the answer to this question were provided by molecular dynamics simulations of several groups. In a pioneering computational chemistry study on the presence of ice-like clusters by Buch et al.,[16] they revealed how the vibrational spectra change with cluster size and physical state. With growing cluster size, the amount of water molecules in arrangements similar to strained and unstrained crystal lattices increases, which results in a gradual shift of the peak maximum from $n = 123$ to $n = 931$,[16] see blue traces in Figure 2.5. A broad vibrational spectrum for $n = 293$ results from a strained ice-like hydrogen bond network within the cluster. For larger clusters with $n = 600$ and 931, spherical clusters with crystalline cores and an amorphous cluster surfaces were predicted to yield spectra resembling the spectrum of crystalline water droplets in shape, but with a peak position below 3200 cm^{-1}.[16] The shoulder around 3280 cm^{-1} has been concluded to originate from DDAA molecules in tilted tetrahedral coordination.[16]

The predicted cluster structures and the vibrational spectra were generated by Kazimirski and Buch[89] and Buch et al.[16] as follows: Bulk cubic ice structures were used as initial geometries for several molecular dynamics simulations with the empirical TIP4P potential with energies corresponding to temperatures of $100 - 200$ K, which guaranteed the population of several minima of the potential energy surface.

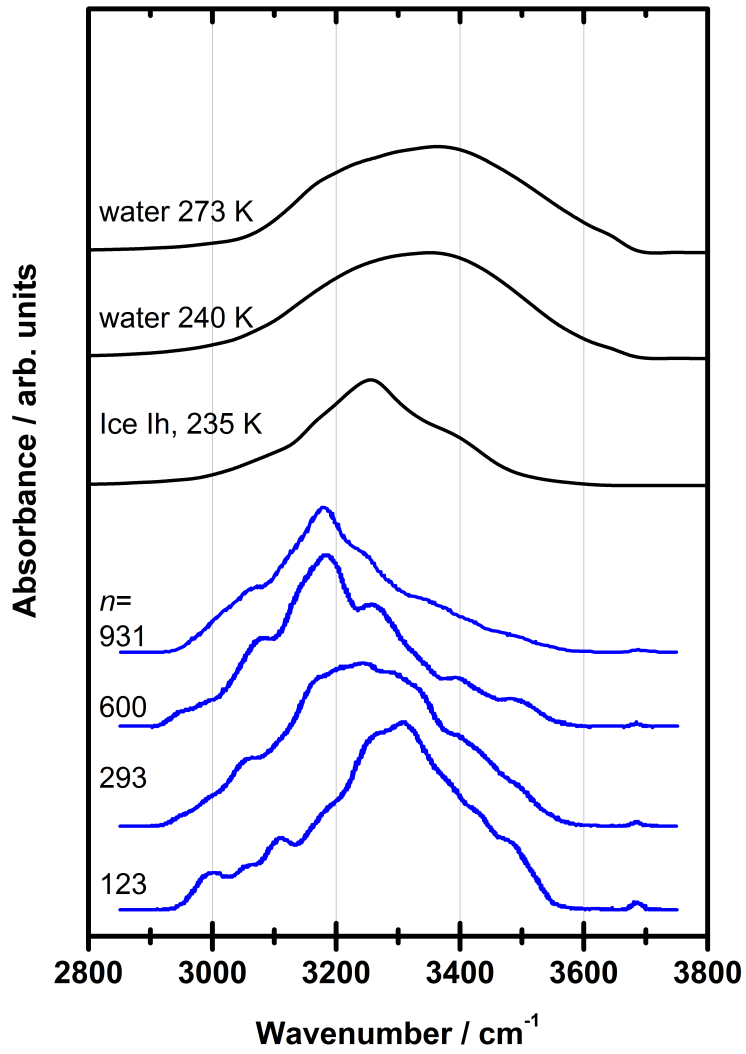

Figure 2.5: Vibrational spectra of water droplets and clusters: Black traces: IR spectra of µm sized water droplets at different temperatures of liquid and supercooled water, and ice. Data reproduced from numerical data of reference [187]. Blue traces: calculated vibrational spectra of $(H_2O)_n$ clusters with $n = 931, 600, 293, 123$. Spectra taken from reference [16].

The temperature range $130 - 160\,\mathrm{K}$ lead to a satisfying exploration of the potential energy surface while the low energy isomers were still predominantly populated.[16] While the ice-like geometries of larger cluster survived the MD simulations, they were lost for smaller clusters. In a proceeding simulation, the structures for $n \leq 293$ obtained from the MD simulations underwent a Monte-Carlo optimization scheme in order to optimize the hydrogen positions for the found oxygen atom network and thus improve the accuracy of the dOH positions.[16] The resulting spectra for $n = 123$, 293, 600, and 931 (see blue lines in Figure 2.5) were calculated for structures reoptimized via the EMP potential. The hydrogen bonds were treated as interactions of two oscillating dipoles oscillating in the direction of the OH bond and the frequency shift was assumed to steadily decrease with increasing electric field strength along the OH bond.[16]

The work of Buch et al.[16] showed the formation of improved crystal lattices with growing cluster size by comparison of only few cluster sizes (123, 293, 600, 931) since the modelling of all cluster sizes would have been too computationally expensive. Bandow and Hartke[87] examined the cluster size range $n \leq 150$ by using the TTM2-F potential for the optimization of ice Ic, ice Ih, and ice VI cutouts.[II] They found that approximately 25% of the molecules of a $n = 145$ cutout remained in their original ice Ic position. This indicates the presence of a crystalline core covered by an amorphous surface, which is in agreement with the geometries suggested by Buch et al.[16] By comparing the energy per molecule of the optimized ice cutouts with that of amorphous clusters obtained via a global optimization algorithm, it was concluded that $n \approx 90$ could be a lower limit for the presence of crystalline clusters.[87]

An entirely different approach does not aim to describe all atoms of each water molecule but treats the whole molecules as a quasi-atom with preferentially tetrahedral connectivity.[198] This mW (monatomic water) called potential has been used to simulate the crystallization of bulk water[198,199] and the crystallization of water clusters.[88] It showed a coexistence of Ic and Ih in crystalline clusters in molecular dynamics simulations with fixed cooling rates.[88] For clusters with 417–13824 molecules a ratio of Ic to Ih of around 2.5 was observed[88] which is close to the value of 1.8–2.5 observed in MD simulations with the mW potential of crystallized bulk water.[200] In simulations with $T = 150\,\mathrm{K}$, the smallest clusters which crystal-

[II] The TTM2-F potential is considered to be more accurate than TIP4P, but also more expensive.[87]

lized in the simulations of Johnston and Molinero contained 137 water molecules. These also showed a crystalline core and a distorted surface.[88] As for $n = 137$ and $n = 159$ less than 50% of the molecules were in a crystal-like environment, Johnston and Molinero[88] concluded that crystalline clusters with $n \approx 100$ are unlikely to form ice I type crystal cores.
The three different potentials TIP4P, TTM2-F, and mW result in different minimum cluster sizes for which crystallization is observed. From this, the necessity of size-resolved experimental methods probing the physical state of the clusters arises. With the aforementioned spectral peak shift due to the presence of crystalline cluster cores, vibrational spectroscopy appears to be a suitable technique.

2.4.4 IR-assisted photoionization of $Na(H_2O)_n$

The sodium pickup approach has been first applied to water clusters by the Hertel group[31] and is now an established tool for the measurement of cluster size distributions.[34,35,37,43,47,48,71,86,184] The extension of this technique towards vibrational spectroscopy of mixed sodium water clusters was developed by Steinbach and Buck.[36] Previous experiments on sodium solvent interactions, with HO-R solvents using the apparatus (with several modifications) are described in references [36, 37, 41–43, 68, 70, 71, 90, 93, 106, 139, 178, 184, 188]. The proposed mechanism of the action spectroscopic approach for the generation of size selected vibrational spectra has been discussed in references [43, 68, 71].
The ion yield of $Na(H_2O)_n{}^+$ from photoionization of $Na(H_2O)_n$ shows a surprising breadth, see Figure 2.6 (a). Forck et al.[70] determined the ionization threshold energies by extrapolation to the abscissa as 2.8 eV for isomer class II and 3.2 eV for isomer class I,[70] which is in agreement with the value from the Hertel group.[38,63] As the ion signal still increases for photon energies higher than 3.7 eV, the abundance of a third isomer class was assumed, in which the sodium atom is located on the cluster surface.[71] Predicted ionization energy distributions of the sodium-methanol system indicate that the population of low-IE isomers increases with increasing temperature.[43] This finding has been assumed to be similar in the sodium water case.[71]
While the IY curve of sodium solvent clusters can be measured with a tunable UV light source, the measurement of vibrational spectra requires an UV and an IR laser.[70] For sodium methanol clusters it has been shown that IR-induced action spectra of sodium doped clusters can be measured in two ways: As a signal enhancement if the UV photon energy is close to the aIE, or as a signal depletion if

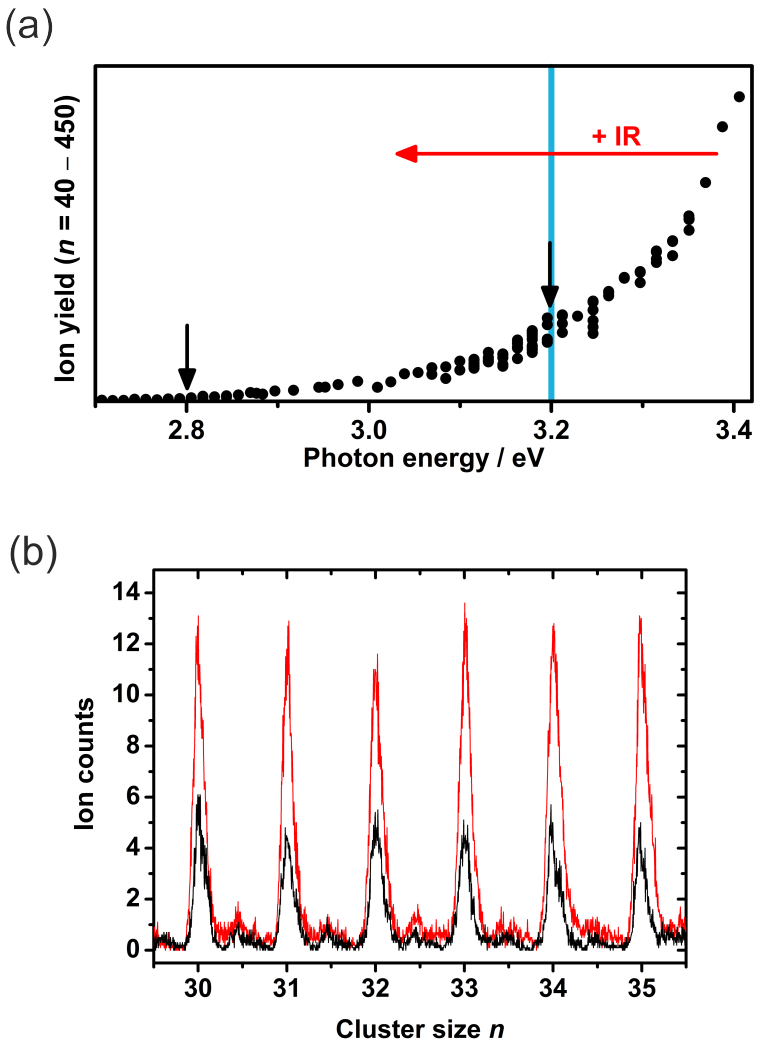

Figure 2.6: Enhanced photo ion yield by vibrational excitation:
(a) Ion yield of $Na(H_2O)_n^+$ cluster vs. photon energy of ionizing radiation. The blue line marks the ionization wavelength used in the IR-UV experiment. The black arrows mark the ionization threshold energies of the isomer classes I (3.2 eV) and II (2.8 eV).[70] The red arrow indicates the influence of IR radiation on the detected ion yield. Figure taken from [71] and modified. Reprinted with permission from AAAS.
(b) Excerpt of mass spectra taken at the same expansion conditions but with different ionizing conditions: The black mass spectrum results from ionization with 3.22 eV photons, whereas the red mass spectrum was measured with an IR-laser ($\tilde{\nu} = 3400\,\mathrm{cm}^{-1}$) exciting the clusters prior to ionization by 3.22 eV photons.

the photon energy is well above the aIE.[41,43] In the first case, the enhanced ion signal is caused by a change of the isomer distribution upon vibrational excitation of the clusters.[43,71] This corresponds to an IR-induced solvation of the sodium atom.[71] To be more precise, the IR-induced signal gain observed for a UV photon energy of 3.2 eV is caused by transformation of clusters with higher ionization energies to clusters with IE$\leq$ 3.2 eV, see Figure 2.6 (a). The obtained vibrational spectra therefore originate from isomers with an exterior and mostly unsolvated sodium atom and from those of isomer class I.[71]

The applied near-threshold ionization by 3.2 eV photons should minimize fragmentation.[106] This is in agreement with the finding that the cationic species and the neutral species with low ionization energies were predicted to have similar geometries.[51,60] Consequently, if neutral low-IE clusters are ionized by radiation near their threshold ionization energy, the resulting cationic clusters should not contain large amounts of excess energy and therefore should not fragment.[106]

The lower panel of Figure 2.6 shows a significant increase for the detected ion yield of $Na(H_2O)_{n=30-35}{}^+$ after IR-assisted ionization. This demonstrates that the signal increase from clusters which undergo the sodium solvation transition outlined above—and would not be detected without the IR excitation—is much larger than the loss due to IR-induced fragmentation. The small peaks in the mass spectra of panel (b) of Figure 2.6 were shown to correspond to multiply sodium doped cluster products of $Na(NaOH)_2(H_2O)_l$ type[153] and not to $Na(H_2O)_n{}^{2+}$ as a second ionization step of $Na(H_2O)_n{}^+$ clusters is not accessible by 3.2 eV photons. For $Na(CH_3OH)_n$[43] and $Na(H_2O)_n$[139,184] it was concluded that fragmentation can be suppressed by near-threshold ionization as exceptionally stable clusters are present in the molecular beam.[43,139,184] Therefore, the fragmentation of metastable clusters as a cause for the presence of the small peaks in the mass spectra obtained at photon energies of 3.22 eV is unlikely.

From a comparison of the signal gain spectra of large sodium doped water clusters with IR photodissociation spectra of phenol water clusters and cationic sodium water clusters the comparability of the three methods wa deduced.[71,90] For clusters larger than $n \geq 19$ the similarity of the data with those from other chromophore-based methods has lead to the conclusion of only a small pertubation of the hydrogen bond network due to the sodium atom.[71,90] These characteristics make IR-assisted photoionization of alkali water clusters a promising sample to obtain size-selective vibrational spectra of large water clusters.

3 Setup

In this chapter, the cluster beam machine used in this work will be presented. Its design[46,201] and ionoptics[202] were developed and constructed in the Buck group at the Max-Planck-Institut für Dynamik und Selbstorganisation in Göttingen. Over the last two decades several modifications were added: an effusive beam for pickup experiments,[201] a gas cell for pickup experiments,[127] an optical parametric oscillator / optical parametric amplifier (OPO/OPA) IR laser system,[180] a double pickup cell,[93] replacement of the IR laser system,[139] an UV/Vis OPO laser system,[90] and an UV/Vis dye laser.[90] The latest changes are minor adjustments to the hardware components of the pickup cell to simplify their repair and a change of the laser pulse sequence for the measurement of vibrational spectra.[203,204]

3.1 Cluster beam apparatus

The apparatus consists of three separated chambers in order to achieve pressures of 10^{-6} mbar in the TOF mass spectrometer by means of differential pumping and to simplify repairs. These compartments will be called expansion chamber, pickup chamber, and detection chamber in the following.

3.1.1 Cluster source

Cluster formation is achieved by continuous supersonic expansion of water vapor seeded in different carrier gases from a conical nozzle with a length of 2 mm, and an opening angle α of 20°.[93,188] While a diameter of $d = 63\,\mu m$ was reported previously,[93,188] recent observations showed that the nozzle flange has altered as now the orifice is of irregular, nearly elliptic shape with a mean diameters of around 75 µm.[205] The nozzle is attached to an oven, which can be partly filled with a sample substance and where the seeding gas is directly applied to the gas phase above the sample filled in. The nozzle can be separately heated to prevent it from clogging. Spatial adjustment of the oven-nozzle-compartment is possible in three directions:

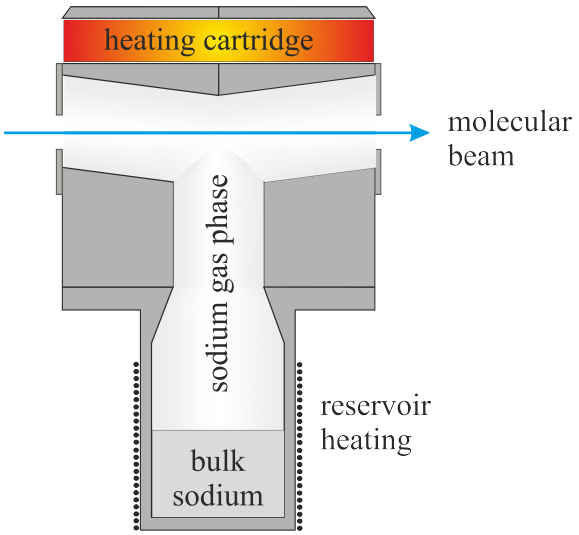

Figure 3.1: Schematic cross section of the pickup cell. An engineering drawing of the new upper part can be found in the appendix in Figure A.5. The design follows the one presented by Steinbach[127] and Dauster.[93] Figure taken from [93] and modified.

one along the flow direction of the molecular beam and the other two perpendicular to it.

3.1.2 Pickup cell

The sodium pickup cell is located in the pickup chamber. Its design and dimensions follow the one presented by Steinbach[127]and Dauster,[93] see Figure 3.1. Recently, it has been partly equipped with heating cartridges instead of the former tungsten wire heating to simplify future repairs. The engineering drawing can be found in the appendix in Figure A.5 on page 130.

In the given sodium gas cell design, bulk sodium is stored in the lower part of the pickup cell, see Figure 3.1. Heating of this reservoir allows the control of the sodium vapor pressure. To minimize dopant condensation in the upper part of the cell, this part is heated separately. Two apertures with 5 mm diameter let the molecular beam pass through the pickup cell onto the detection chamber. Typical sodium vapor pressures used in the experiment range from 10^{-3} Torr to 10^{-4} Torr. These can be estimated with the Antoine equation determined by Buck and Pauly; $\log_{10}(p/\mathrm{Torr}) = 8.08 - \frac{5479}{T/\mathrm{K}}$.[206]

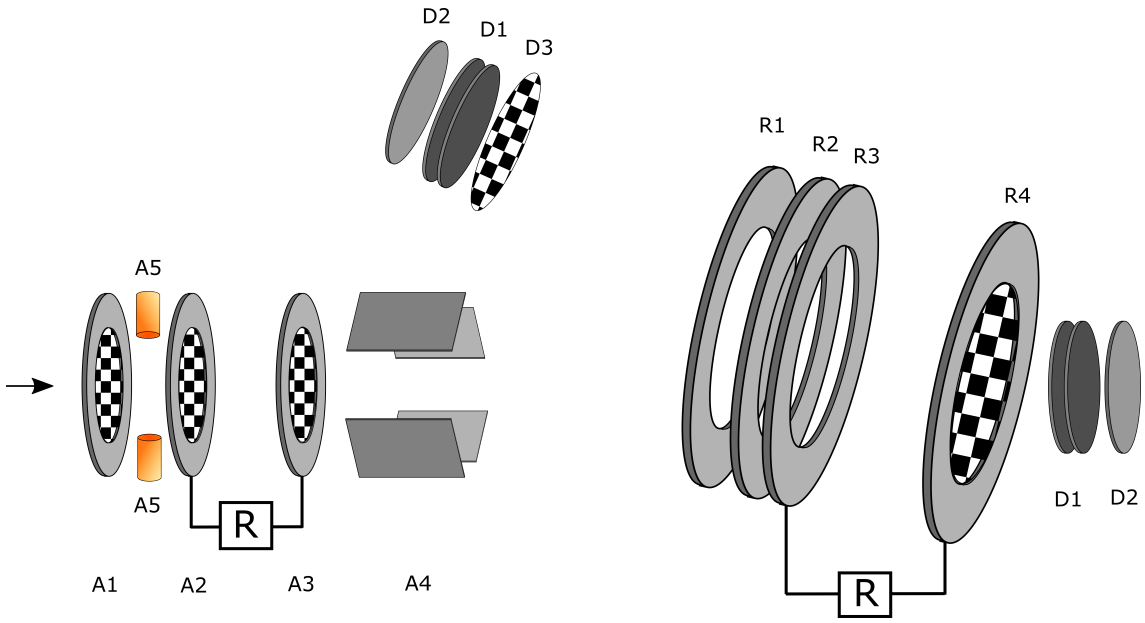

Figure 3.2: Schematic diagram of the mass spectrometer. The direction of the incoming molecular beam is indicated by the arrow. [R] marks resistors connecting several steel plates. Grids are indicated by checkered patterns. For the applied voltages see Table 3.1. Figure taken from reference [207] and modified.

A1 – entrance plate	R1 – entrance plate	D1 – Chevron MCP
A2 – cation extraction plate	R2 – brake field	D2 – signal anode
A3 – end of acceleration stage	R3 – correction field	D3 – re-acceleration grid
A4 – deflection field	R4 – repeller plate	
A5 – copper bolt		

3.1.3 Mass spectrometer

A schematic overview of the mass spectrometer is shown in Figure 3.2. The voltages applied to the different electrical components are listed in Table 3.1. The mass spectrometer consists of three parts. In the first part, the ion source, sodium doped clusters are photoionized, extracted from the ionization zone, accelerated in the direction of the reflectron, and deflected by few degrees with respect to the direction of the molecular beam of the neutral species. The clusters are ionized in the center of the ionization zone, which is between the copper bolts A5 and the steel aperture plates A1 and A2 (90% transmission) that are limiting the extraction field, see Figure 3.2. Subsequently, the cluster cations pass a nearly homogeneous electric acceleration field with several steel aperture plates until they pass the exit plate A3 at the end of the acceleration stage. In order to simplify the alignment of the reflectron, two deflection fields (A4) are located behind the Wiley-McLaren[113] dual-stage acceleration fields (A1 to A3) of the ion source.

The reflectron[115] follows a Wiley-McLaren design[113] and consists of an electric

Table 3.1: Voltages applied to the mass spectrometer shown in Figure 3.2.

part	component in Fig. 3.2	voltage in V
ion source	A1	1210
	A2	1000
	A3	0
	A4	25 and 50
	A5	1090
reflectron	R1	0
	R2	619
	R3	753
	R4	1740
detector	D1 (front)	-1900 ± 100
	D1 (rear)	-40
	D2	0
	D3	-250

field to slow the clusters down (between R1 and R2 in Figure 3.2) and a nearly homogeneous electric field, where the reflection of the cluster takes place (R3 to R4).[202,208] Only the last steel plate has a grid whereas the rest of the reflectron is gridless in order to increase the transmittance of ions through the reflectron.[209] Another advantage of the gridless reflectron is a narrow outgoing ion beam as the gridless entrance has the same effect as an electrostatic lens.[202,210] Therefore the reflectron guides the cations towards the detector which is located above the rear end of the acceleration stage. The overall drift lengths in the apparatus is 1820 mm.[188] If the reflectron is not used, the ions can pass through it and reach a detector located in linear position.

Both detectors are Chevron-type multichannel plate (MCP) arrangements (D1) operated with metal signal anodes (D2). In front of the detector for the reflected beam a grid with 50% transmission is placed in order to achieve a higher detection sensitivity for larger clusters by fragmenting them and re-accelerating the resulting smaller species in the direction of the MCP.[90,201]

3.1.4 Pumping system

In order to achieve pressures that are low enough to not perturb the ion signal in the TOF mass spectrometer by collisions with residual gas, differential pumping is applied. The expansion chamber and the pickup chamber are separated by a skimmer with a diameter of approximately 0.6 mm. The pickup chamber and the detection chamber are separated by a valve with 5 mm diameter.
Whereas the expansion chamber and the pickup chamber are each pumped by an oil diffusional pump, the detection chamber with the mass spectrometer is pumped by a turbomolecular pump. The oil diffusional pump of the expansion chamber is operated with two backing pumps: a roots pump and a rotary vane pump. The backing pumps for the pickup and the detection chamber are rotary vane pumps. A list of the used pumps is provided in Table 3.2.

Table 3.2: List of the pumps used in this work. Table taken from [90] and modified.

chamber (resulting pressure)	brand and model	pump type	flow rate
expansion chamber (10^{-4} mbar)	Leybold D60A[I]	rotary vane	60 $m^3 \cdot h^{-1}$
	Leybold D65BCS[II]	rotary vane	65 $m^3 \cdot h^{-1}$
	Leybold-Heraeus E150[II]	rotary piston	150 $m^3 \cdot h^{-1}$
	Balzers WKP500[I]	roots	500 $m^3 \cdot h^{-1}$
	Alcatel RSV[II,III]	roots	375 $m^3 \cdot h^{-1}$
	Leybold DI6000[I]	oil diffusional	$\leq$ 6000 $L \cdot s^{-1}$
pickup chamber (10^{-5} mbar)	Leybold D16B	rotary vane	16 $m^3 \cdot h^{-1}$
	Diffstak 100/300	oil diffusional	300 $L \cdot s^{-1}$
detection chamber (10^{-6} mbar)	Leybold D16B	rotary vane	16 $m^3 \cdot h^{-1}$
	Pfeiffer TMU260[I]	turbomolecular	220 $L \cdot s^{-1}$
	Pfeiffer TPH270[II]	turbomolecular	270 $L \cdot s^{-1}$

[I] first choice of expansion chamber pump system
[II] alternative pump
[III] two identical pumps

3.2 Laser system

The measurements of vibrational spectra and of photoionization efficiency curves require tunable lasers in the mid-IR and in the UV range. While dye lasers are only tunable within the limits of the used laser dye and can require time consuming adjustments when the spectral range is changed, an OPO provides a broader accessible spectral range of coherent radiation.
The setup used in this work is equipped with two Nd:YAG (neodynium doped yttrium aluminium garnet, Nd:$Y_3Al_5O_{12}$) lasers,[211,212] which are used to optically pump a Sirah Cobra-Stretch dye laser[213] or a Continuum Panther Ex-OPO[214], and an LaserVision IR-OPO/OPA system.[215] These lasers have been described in detail in the theses of Dr. R. M. Forck[139] and Dr. C. C. Pradzynski[90] and shall only be introduced briefly in the following.

3.2.1 Nd:YAG pump laser

In the present Nd:YAG lasers (Continuum Powerlite 8000 and Continuum Powerlite 9010) Q-switching is achieved by means of a Pockel's cell.[139,211] The temporal uncertainty of the laser pulse emission for external triggering is $\leq 1\,\mathrm{ns}$ at FWHM pulselengths of $7-8\,\mathrm{ns}$.
The Continuum Panther Ex-OPO and the Sirah Cobra-Stretch dye laser are pumped by the third harmonic generation of the 1064 nm pulse from the Continuum Powerlite 9010. The pump beam pulse energies used were in the range of $350-400\,\mathrm{mJ}$ for the Panther Ex OPO and up to 350 mJ for the Sirah dye laser. The IR-OPO/OPA system was pumped by 550 mJ pulses of 1064 nm radiation provided by the Continuum Powerlite 8000 pump laser.

3.2.2 Laservision IR-OPO/OPA

The LaserVision OPO/OPA system provides mid-IR radiation in the range between $2500\,\mathrm{cm^{-1}}$ and $4508\,\mathrm{cm^{-1}}$.[215] A beam splitter divides the Nd:YAG fundamental laser beam by reflecting a third of the intensity. The reflected beam passes trough a $\lambda/2$-plate tilting its polarization plane by $45°$.[215] This tilted pump beam is fed into a KTP type II doubler crystal to yield 532 nm radiation that is coupled into an OPO resonator after it has been separated from the residual 1064 nm beam. The OPO resonator contains two counter-rotating KTP type II crystals and supplies

the 1064 nm pumped OPA with radiation from its idler in the wavelength range of 1.350 µm to 2.218 µm ($7407 - 4508\,\mathrm{cm}^{-1}$).[215] Difference frequency generation of the OPO idler beam and the Nd:YAG beam in the OPA KTA type II crystals yields mid-IR photons in the range between $2500\,\mathrm{cm}^{-1}$ and $4508\,\mathrm{cm}^{-1}$ (5 µm to 2.218 µm).[215] Wavenumbers as low as $2000\,\mathrm{cm}^{-1}$ can be reached but with very low pulse energies. In the range of $2800\,\mathrm{cm}^{-1} - 3560\,\mathrm{cm}^{-1}$ pulse energies of up to 14 mJ – 15 mJ were accessible, for $3560\,\mathrm{cm}^{-1} - 3800\,\mathrm{cm}^{-1}$ strong fluctuations in the measured pulse energy occurred due to absorption by water vapor in the laboratory air, see right panel of Figure 3.3.

The spectral linewidth of the mid-IR beam was $1.7\,\mathrm{cm}^{-1}$ for seeded and $3.7\,\mathrm{cm}^{-1}$ for unseeded operation of the Nd:YAG pump laser.[215] Calibration of the system against gaseous HCl (300 mbar in a 20 cm cuvette) and the rotational-vibrational absorption lines of water vapor in the laboratory air showed a constant spectral offset over the whole tuning range.

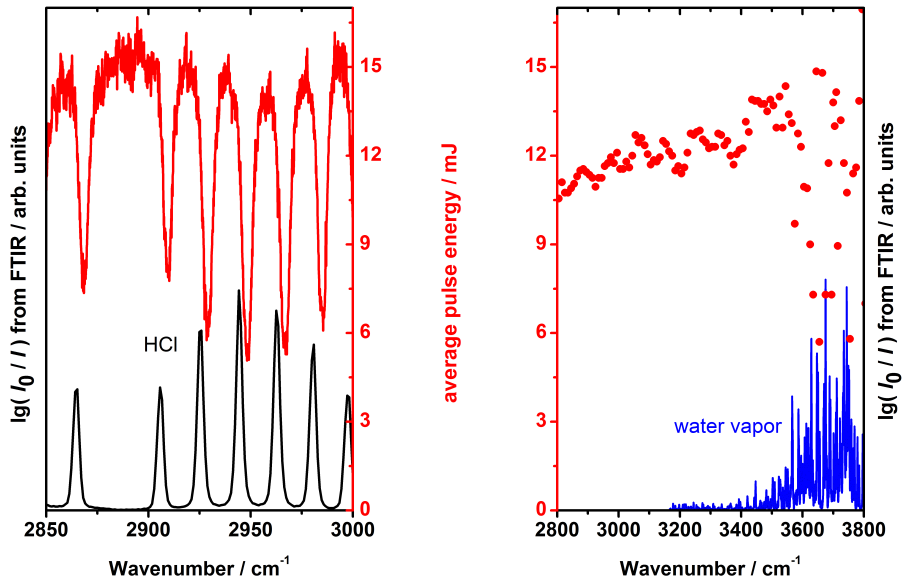

Figure 3.3: Left: Comparison of FTIR spectrum of gaseous HCl (black) with the IR-laser pulse energies measured behind the same cuvette (red). Note the offset between the ro-vibrational transition peaks obtained from FTIR spectrometer and the IR-Laser system of $4\,\mathrm{cm}^{-1}$. Right: Average IR laser pulse energies of 11th April 2017 and 12th April 2017 (red dots). The fluctuations of the laser pulse energy are caused by water vapor in the laboratory air, a water vapor FTIR spectrum for ambient conditions is shown for comparison (blue).

3.2.3 Continuum Panther Ex OPO

The Panther Ex OPO generates UV to NIR light in the range of $205 - 2550\,\text{nm}$ with a gap at 355 nm and is pumped by the third harmonic generation of the Powerlite 9010 Nd:YAG laser (355 nm, $350 - 400\,\text{mJ}$, FWHM $= 7 - 8\,\text{ns}$). The broad range of accessible radiation results from several possible output beams (signal, idler, doubled signal, or double idler) and cannot be straight-forwardly used for scanning over the whole tuning range.[214]

The 355 nm pump beam is injected into the OPO resonator after being collimated by a telescope consisting of a plano-convex and a plano-concave lens.[214] The orientation of these lenses within their mount is of crucial importance as an erroneously aligned plano-concave lens can lead to damage of the OPO-BBO type II crystal due to focussing of a retro-reflected pump beam with a focus in the vicinity of the crystal. If this lens is installed correctly, the focussed reflected beam can be observed between the two lenses of the telescope.

The OPO resonator includes an long-pass filter in order to be operated in a singly resonant mode by only injecting the idler and pump beam reflections back into the BBO crystal.[214] By absorbing the reflected signal beam but re-injecting the idler beam, the lasing from the OPO resonator should be more stable and the OPO output beams—signal and idler—should have smaller linewidths compared to the re-injection of both signal and idler.[214] The spatial offset of the beams due to OPO crystal rotation is corrected by a counter-rotating quartz crystal right after passing the output mirror of the resonator. Signal and idler are separated by a pair of dichroic mirrors directing the beams to different output positions of the laser housing.

If a wavelength below 410 nm is required, a standard 90° prism is placed before the set of dichroic mirrors to guide both, signal and idler beam, to a pair of counter-rotating BBO frequency doubling crystals (type I).[214] Here, the second harmonic of the injected, vertically polarized beam is generated at phase-matching conditions. The BBO crystals do not cover the same spectral range but their ranges overlap for 260 nm radiation.[214] As signal and idler beam have different polarizations, a $\lambda/2$-plate has to be placed in front of the crystals. A rotatable Pellin-Broca prism separates the pump beam (signal or idler) from the generated UV beam (second harmonic of signal or idler).[214]

Table 3.3: Panther Ex OPO specifications.[214]

beam	wavelength range	energy	linewidth
pump	355 nm	400 mJ	–
signal (unseeded)	410 − 710 nm	70 mJ (450 nm)	$< 5\,\mathrm{cm}^{-1}$
signal (seeded)	410 − 710 nm	85 mJ	$< 2.5\,\mathrm{cm}^{-1}$
doubled signal (unseeded)	205 − 355 nm	7 mJ (260 nm)	$< 5\,\mathrm{cm}^{-1}$
doubled signal (seeded)	205 − 355 nm	10 mJ (260 nm)	$< 4\,\mathrm{cm}^{-1}$

3.2.4 Sirah Cobra Stretch dye laser

The Sirah Cobra-Stretch is a dye laser supplying radiation from 370 − 760 nm with a linewidth of 0.0027 nm, that is limited by the build-in grating (2400 lines / mm).[213] Pumping with vertically polarized 355 nm or 532 nm radiation pulses at a repetition rate of 10 Hz is provided by the second harmonic generation (SHG) or third harmonic generation (THG) of the Continuum Powerlite 9010 laser. Pump pulse energies with up to 400 mJ are tolerated.[213] The output energies used in the experiments were in the range of 3 − 10 mJ.

Second harmonic generation of the dye laser output in a BBO crystal supplies radiation in the range 280 − 450 nm. As this process requires a collimated beam with a homogeneous beam profile, an amplifier cuvette with a capillary design was used.[90,213] The spatial beam offset resulting from the BBO crystal rotation is corrected by a counter-rotating quartz-crystal. The dye laser beam and its second harmonic generation are spatially separated by means of a stage with four Pellin-Broca prisms.

The laser dyes used in this work and their specifications are listed in Table 3.4.

Table 3.4: Properties of the used laser dyes.[213]

dye name	solvent	λ_{pump}	$\lambda_{\mathrm{output}}$	max. efficiency
Exalite 389	1,4-dioxane	355 nm	382 − 392 nm	16%
Pyridine 1	ethanol	532 nm	667 − 720 nm	21%
Pyridine 2	ethanol	532 nm	691 − 751 nm	20%
DCM	ethanol	532 nm	602 − 660 nm	28%

3.3 Mass detection and data processing

A voltage pulse from clusters impacting on the MCP detector is assigned to a specific time-of-flight within a multiple event time detection system (FAST ComTec GmbH, P7887 multiscaler).[90,216] As the voltage pulses have widths of few ns, 32 channels with widths of 250 ps were binned to 8 ns channels. The voltage amplitude detection threshold was adjusted such that the highest possible ion count rates were measured and the ratio of cluster signal and noise counts was not lowered due to increased noise generation.

In order to reliably determine the peak positions and integration borders of cluster peaks in the mass spectra, a summed mass spectrum was generated.[203] In this spectrum the peak positions of $Na(H_2O)_n{}^+$ were determined as follows: After binning the ion counts in 200 ns segments, the first peak maximum was determined. For this purpose the peak of the $Na(H_2O)_4{}^+$ cluster was used. The subsequent peak position of $Na(H_2O)_5{}^+$ was found by the definition of a peak threshold level of 91% of the peak height of the previous signal for the next 200 ns bin.[203] As the cluster peaks are separated by few µs, this 9% lowering of the peak threshold level was applied several consecutive times resulting in a exponential decay with increasing peak separation ($0.91^{(x_{\mathrm{bin}}-x_{\mathrm{bin},n=4})}$). Further peak positions were determined via the same approach, but starting from the beforehand determined cluster peak. The aim of this approach was to neglect low-intensity mass peaks between the peaks of $Na(H_2O)_n{}^+$ in the mass calibration procedure.[203] These small clusters (see Figure 2.6 on page 33 at cluster sizes 30.5, 31.5, ...) are a product of multiple sodium doping in the pickup cell and belong to $Na(NaOH)_2(H_2O)_l{}^+$ clusters.[152,153]

After the rough determination of cluster peak positions was completed, the peak maxima and the peak integration borders were re-evaluated by fitting Gaussian peak profiles around the ranges of the determined peak positions.[203] The resulting mass calibration has been tested against a series of mixed phenol ethanol clusters ionized via REMPI with 275 nm photons, see Figure 3.4. As the time of flight is proportional to the square root of the mass-to-charge ratio ($t_{\mathrm{TOF}} \propto \sqrt{m/z}$), the peaks for large clusters ($n > 100 - 120$) cannot be resolved properly and overlap until only a broad, log-normal shaped peak is observed.[34,90,127] The mass calibration for this region is based on the proper determination of the cluster masses in the range of separated signal peaks. Based on the relation $t_{\mathrm{TOF}} \propto \sqrt{m/z}$ the two calibration parameters c (a constant) and t_0 (the flight time of an ion with zero mass) can be

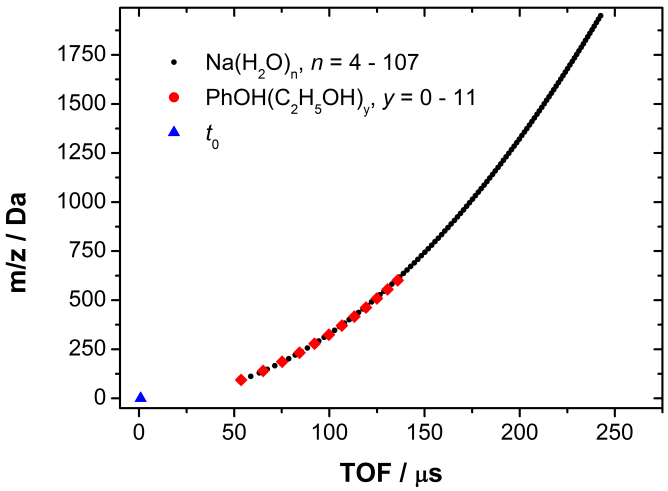

Figure 3.4: Peak position of $Na(H_2O)_n{}^+$ and phenol ethanol clusters. The parameter t_0 was obtained from the mass calibration of the $Na(H_2O)_n{}^+$ clusters via equation (3.4).

introduced [93,139]

$$\frac{m_n}{z_n} = \frac{m_n}{1} = \frac{(t_n - t_0)^2}{c} \tag{3.1}$$

and calculated from the position of two cluster peaks with known masses m_n and charges $z_n = 1$ via

$$t_0 = \frac{m_1 t_2 - m_2 t_1 + \sqrt{m_1 m_2} \cdot |t_2 - t_1|}{m_1 - m_2} \tag{3.2}$$

and

$$c = \frac{(t_1 - t_0)^2}{m_1} \tag{3.3}$$

or from a quadratic regression from the peak positions [203] via

$$\frac{m}{z} = \frac{1}{c} t_{\mathrm{TOF}}^2 - \frac{2t_0}{c} \cdot t_{\mathrm{TOF}} + \frac{t_0^2}{c} \tag{3.4}$$

If the two calibration parameters are known, the TOF can be transferred to a mass scale. The cluster size n, denoting the number of water molecules of the mixed

sodium water clusters, is then obtained via

$$n = \frac{m_n - m_{\mathrm{Na}}}{m_{\mathrm{H_2O}}} \tag{3.5}$$

Here, m_{Na} refers to the atomic weight of sodium and $m_{\mathrm{H_2O}}$ to the molecular weight of water. m_n denotes the masses of cluster peaks obtained from the mass calibration of the time-of-flight mass spectra.
In order to measure two mass spectra simultaneously—a reference spectrum with only the UV laser used for ionization and a mass spectrum from IR-UV double resonance experiments—, a 10 ms TTL pulse with 5 Hz repetition rate (in the following TAG) was fed into the P7887 multiscaler to yield the assignment of the detected pulses to the correct mass spectrum.[203,204] This TAG pulse was generated in a logic box whenever both Nd:YAG pump lasers, for the UV laser and the IR laser, were Q-switched. As the IR-OPO/OPA's pump laser Q-switch was operated at halved frequency of the UV laser's pump laser, spectra of photoionized clusters with and without IR excitation could be measured simultaneously. The delay time Δt between the laser pulses was adjustable in the range between -50 ns and tens of µs and is defined as[203]

$$\Delta t = t_{\mathrm{UV}} - t_{\mathrm{IR}} \tag{3.6}$$

The laser pulse times t_{UV} and t_{IR} were determined as rising slopes of the laser pulse as detected by a photodiode (Electro-Optics Technology, Inc., Silicon PIN Detector ET-2000) and observed on an oscilloscope (Tektronix, TDS 744A).

4 Single photon ionization of $Na(H_2O)_n$ clusters

In this chapter, the results from a single photon ionization study on sodium doped water clusters are presented. The photon energy dependent ion yield of small sodium water clusters is compared to the results from ab initio molecular dynamics simulations provided by the group of Prof. Petr Slavíček from the Department of Physical Chemistry of the University of Chemistry and Technology Prague. Most of the results of this chapter were published in a joint publication, reference [72].

4.1 Experimental method

All experiments were conducted with the apparatus described in Section 3. Pure water clusters were formed by skimmed, rare gas-seeded, supersonic expansions from a conical nozzle. Sodium doping was achieved in a pickup cell. The $Na(H_2O)_n$ clusters were ionized by UV light in the energy range of $2.7 - 5.4\,\mathrm{eV}$ from either the Continuum Panther Ex OPO or the Sirah Cobra Stretch dye laser. The measured mass spectra were corrected for the laser pulse energies and the number of laser shots.

4.2 Experimental results

Sodium water clusters can be ionized by UV photons over a broad range.[70] Changing the UV photon energy from 3.1 eV to 4.1 eV results in mass spectra which differ mainly in signal intensity and only slightly in the position of the mean cluster size, see Figure 4.1. Both mass spectra show peaks from $Na(H_2O)^+_{n=4-80}$ and only small peaks interjacent to the peaks of the $Na(H_2O)_n$ cluster series. As mentioned above, these small peaks correspond to byproducts of the doping process.[131,152] Therefore, no ion signal is observed from multiply charged cluster cations, or daughter ions

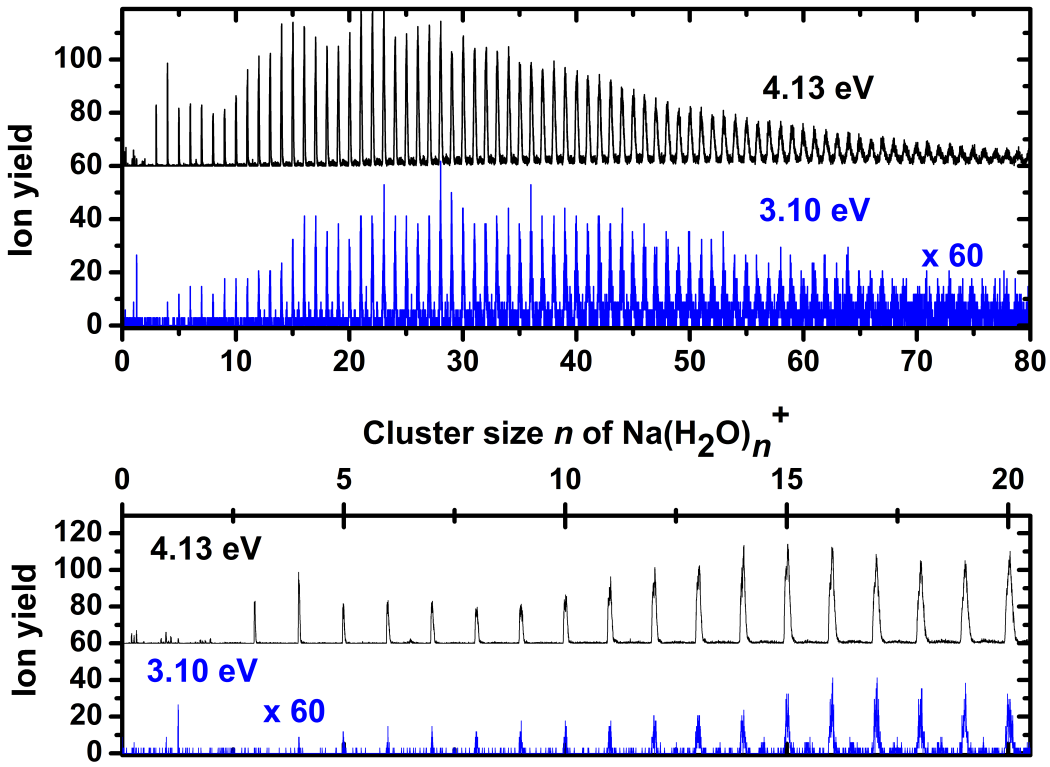

Figure 4.1: Mass spectra of $Na(H_2O)_n^+$ clusters measured at different photoionization wavelengths. The clusters were formed in He seeded expansions with 1.4 bar water vapor at a stagnation pressure of 2.1 bar and a nozzle temperature of 160 °C. The spectra taken at 4.1 eV were offset by +60 counts. The spectra at 3.1 eV were multiplied by 60 to give comparable peak heights.

resulting from post-source decay.[43,103] The peak at $n = 1.3$ in the low IE spectrum of Figure 4.1 corresponds to dimeric sodium (Na_2). Comparison with the 4.1 eV spectrum shows that the detected cluster distribution is not drastically shifted towards smaller cluster sizes if higher photoionization energies are used. From this can be concluded that monitoring the integrated mass signal (in the following ion yield, IY) while the photoionization wavelength is tuned may result in size-selective ion yield curves, especially at low photon energies. These could be a measure for the isomer population of each cluster size.

Figure 4.2 displays the IY vs. photon energy curves for $Na(H_2O)_n^+$ with $n = 2, 3, 10, 30$ and 70. Each IY spectrum shows similar features: A region without ion signal at low photon energies, a broad signal increase, and a saturation of the ion signal. The transitions between these regions show a strong size dependence for $n = 2 - 9$, as indicated by the IY curves of $n = 2$ and $n = 3$ shown in panel a) of Figure 4.2.[72] The appearance ionization energy values of isomer class I as deter-

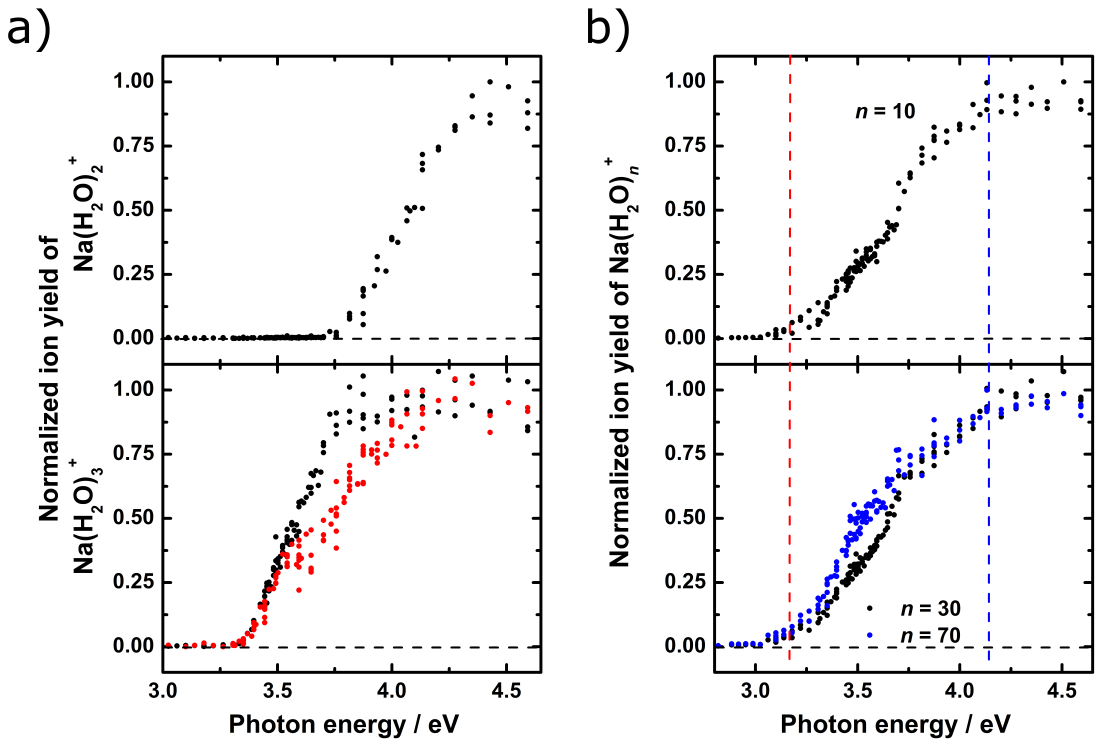

Figure 4.2: Ion yields of $Na(H_2O)_n^+$ with $n = 2$ and 3 (panel a)), and $n = 10, 30$, and 70 (panel b)) plotted vs. the photon energy. The expansion conditions underlying the black and blue data were the same as for the mass spectra in Figure 4.1. Panel a): The red points for $Na(H_2O)_3^+$ are from Ar seeded expansions of 0.7 bar water vapor at $p_{stag} = 1.8 \pm 0.1$ bar at $T_{nozzle} = 100\,°C$. Panel b): The red dashed line at 3.2 eV marks the aIE of isomer class I.[38,70] The blue dashed line marks the value of 4.1 eV at which the IY of $Na(H_2O)_{n>9}$ clusters is saturated. Data taken from [72].

mined by Hertel et al.[38,63] can be extrapolated from these data. However, for $n = 3$ an aIE of 3.35 ± 0.05 eV is observed, which is slightly lower than the 3.48 ± 0.06 eV reported previously.[63]

The photon energy at which the IY curve is saturated (in the following called saturation ionization energy, sIE), differs for small clusters but reaches a constant value of 4.1 ± 0.1 eV for $n \geq 9$. This resulting constant value is shown as blue dashed line in panel b) of Figure 4.2. The aIE for $n \geq 4$ of isomer class I (3.2 eV[38,70]) is shown as a red dashed line in Figure 4.2.

The IY curve of $n = 2$ shows the first ion signal around 3.75 eV, which is well above the aIE of cluster with $n > 2$. In addition, the ion signal of $Na(H_2O)_2^+$ is detected when the IY curve of $Na(H_2O)_3^+$ formed in He seeded expansions is saturated. From this follows that over a large range of ionization energies (3.35 eV to 3.75 eV)

no signal of $Na(H_2O)_2^+$ is generated due to fragmentation of larger clusters or water molecule ejection from $n = 3$. A possible reason for this could be the kinetic trapping of cationic $Na(H_2O)_n^+$ clusters, as observed for $Li^+(H_2O)_{n=3,4}Ar$ by Rodriguez and Lisy.[64]

Both $n = 2$ and $n = 3$ show a spectral width of $0.5 - 0.6\,eV$ for the IY increase with He as the seeding gas.[72] If the seeding gas is changed to Ar (red dots in IY curve for $n = 3$ in panel a) of Figure 4.2), the photoionization spectrum of $n = 3$ shows a step around 3.6 eV and thus has three inflection points. This step points to the presence of several isomers differing in their ionization energies.[217] The IY is saturated at higher energies and has only reached half of its normalized intensity at 3.7 eV, where the sIE is reached for He-seeded conditions.[72] This increased sIE indicates by the presence of isomers with higher ionization energies. This is in agreement with the results from an IR-spectroscopic study, where high-IE isomers were formed at argon-seeded expansion conditions.[68] No significant seeding effects on the IY curves of other cluster sizes have been observed.[72]

The aIE and sIE for several cluster sizes are shown in Figure 4.3. Clusters with $n \geq 9$ have a constant sIE of $4.1 \pm 0.1\,eV$, which persists for clusters containing hundreds of water molecules. From the work of Forck et al.[70] a further spread of the photoionization spectrum is known as clusters with an aIE below 3.2 eV are abundant for $n \geq 9$ whose aIE levels off at 2.8 eV for $n \geq 15$. However, the fraction of clusters with an aIE below 3.2 eV contributes to only a few percent of the intensity in the photoionization spectrum.[72]

At photon energies above 3.2 eV, only subtle changes of the photoionization spectrum are observed for larger clusters, see panel b) of Figure 4.2. While the aIE of isomer class I and the sIE are constant for $n \geq 9$, a change in the curvature of the IY curve is observed for cluster sizes between $n = 30 - 70$: The IY gradient is shallower above 3.5 eV and steepest below 3.5 eV for $n = 70$, whereas the IY curve of $n = 30$ has its steepest gradient around $3.5 - 3.7\,eV$. The transition from one curvature shape to the other occurs gradually and in the cluster size range of $n = 50 - 60$ the shift of the steepest gradient to below 3.5 eV is observed. This cluster size region has been of interest in recent studies as fluctuations of both ion yield and EBE were observed for $(H_2O)_n^-$ clusters,[26] as well as a strong size dependency of the predicted thermodynamic stability of $(H_2O)_n$ from several model potentials,[177] and cluster size specific peak position shifts of the dOH peak.[178]

A comparison of the sIE of this work[72] with the data from photoelectron spectra[40]

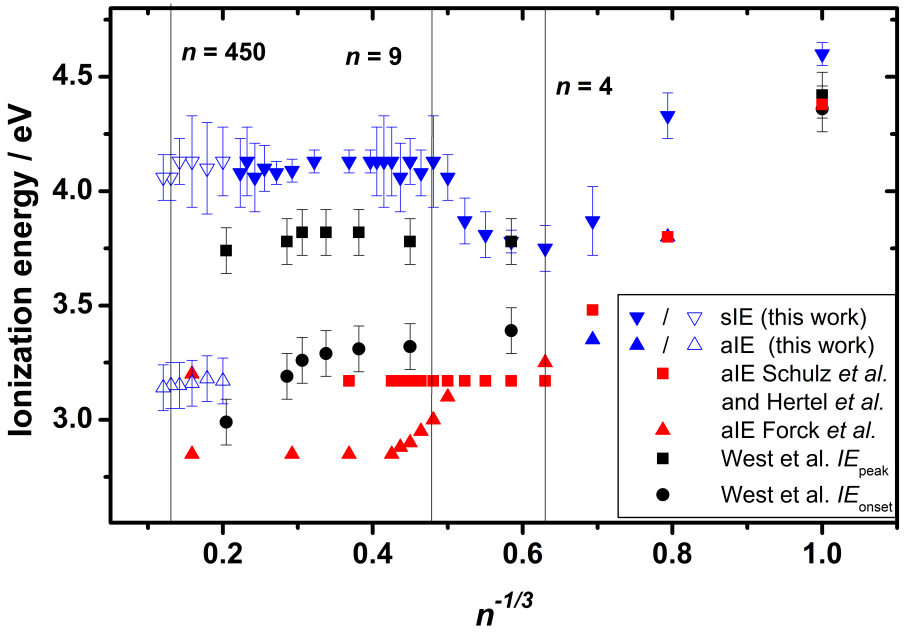

Figure 4.3: Comparison of the experimental results for $Na(H_2O)_n$ clusters in terms of aIE and sIE of this work (blue triangles) with the aIE for isomer class I (red squares)[38,63] and II (red triangles)[70] and the onset IE and peak IE of photoelectron spectra[40] (black points and squares). The filled blues triangles refer to He seeded expansions of 1.4 bar water vapor at a stagnation pressure of 2.1 bar. The open blue triangles refer to He seeded expansions of 2.7 bar water vapor at reservoir pressures of 3.7 bar. Figure taken from [72] and modified.

and the aIE of isomer classes I[38,63,70] and II[70] is shown in Figure 4.3. When comparing sIE and aIE of several cluster sizes, starting from $n = 1$ both decrease with increasing size until $n = 4$. While the aIE reaches the constant value for isomer class I,[38,63] the sIE does not remain constant with cluster size but increases again until $n = 9$. Surprisingly, a constant sIE is reached for cluster sizes for which the emergence of isomer class II with aIE < 3.2 eV has been reported.[70] For $n \geq 15$, the sIE and the aIE of isomer classes I and II remain constant, even for clusters beyond hundreds of water molecules. The obtained sIE for larger clusters indicates that the third isomer class of $Na(H_2O)_n$ clusters assumed by Pradzynski et al.[71] indeed exists.

In contrast to the results from size-selective IY curves, photoelectron spectra of neutral $Na(H_2O)_n$ clusters cannot provide size-selectivity.[40] In order to compare the obtained PES results—onset ionization energies and PES peak positions—to the size-selective data, they are shown at the average cluster sizes of the distributions

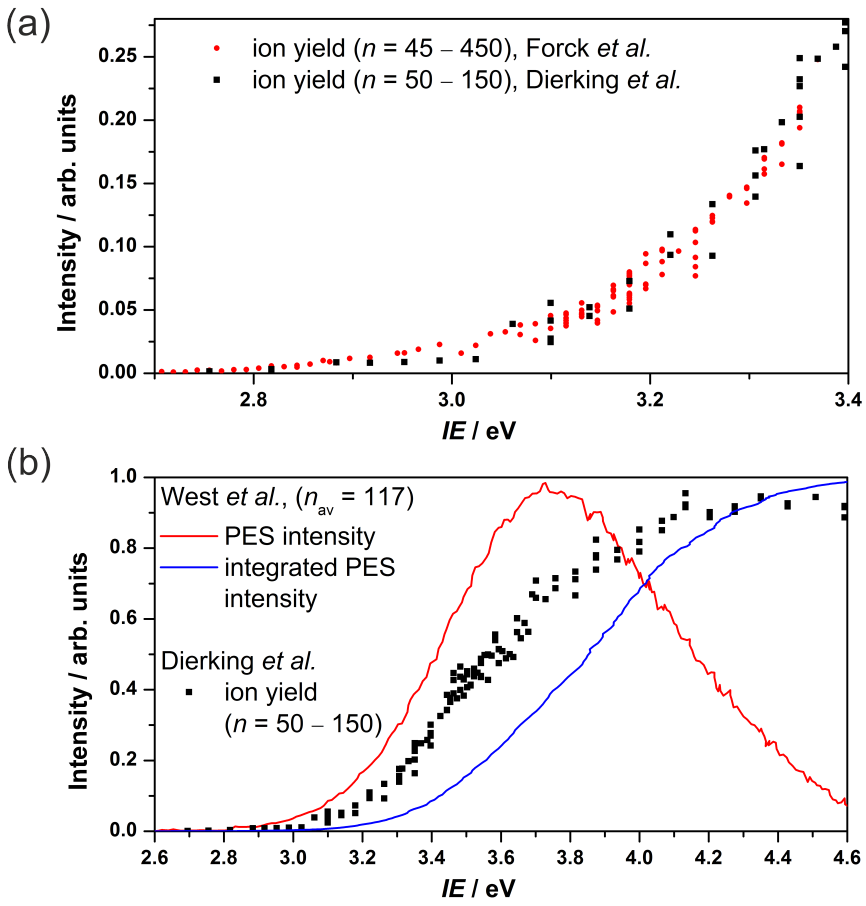

Figure 4.4: Comparison of measured IY curve (black squares) with the data of Forck et al.[70] (red dots) and West et al.[40] (red and blue traces in panel (b)). Panel (a): Comparison of the previously examined low energy part of the photoionization spectrum with the previous IY curve[70,71] (data taken from [71], reprinted with permission from AAAS). The data are scaled such that they are similar at 3.37 eV.
Panel (b): Normalized PES intensity (red trace, data taken from [40]) and integrated PES intensity (blue trace).

contributing to the PES signal, see Figure 4.3. As the expansion conditions had to be changed in order to obtain different cluster distributions, the cluster temperatures and isomer distributions are likely to have changed as well. This may explain the decreasing onset ionization energies from the photoelectron study, see black dots in Figure 4.3. The peak ionization energies remained nearly constant at around 3.8 eV.[40] Both properties stated by West et al.,[40] onset and peak ionization energies, are in the range between aIE and sIE observed in this work.
To compare the IY data from this work with that of Forck et al.[70] for $n = 45 - 450$ and the PES data from West et al.[40] for $\bar{n} = 117$, the mass signal was averaged over the cluster size range $n = 50 - 150$. The IY curves of this work and the low-IE

part of the photoionization spectrum of Forck et al.[70] are in very good agreement in the range $2.7 - 3.4\,\mathrm{eV}$. Both show the very low abundance of isomer class II, see panel (a) of Figure 4.4. These IY curves indicate that approximately 10% of the clusters are ionized by 3.22 eV radiation. A direct comparison of the PES spectrum of West et al.[40] with the normalized ion yield curve shows that the PES peak position (3.74 eV) is close to the IE value of halved ion yield around 3.6 eV, see panel (b) of Figure 4.4. The integrated photoelectron spectrum (blue trace) is similar to the IY curve presented in this work: Both exhibit a sigmoid shape with a beginning signal around $3.0 - 3.2\,\mathrm{eV}$ and a broad distribution of ionization energies. While the IY curve reaches a constant value at 4.1 eV, the photoelectron spectrum and the normalized, integrated photoelectron intensity indicate that about 20% of the $Na(H_2O)_n$ clusters have ionization energies above 4.1 eV. This suggests that fragmentation is likely to occur in the high energy part of the photoionization spectrum. As no details on the seeding conditions during the cluster preparation are stated by West et al.,[40] the question, whether the discrepancy in the levelling off positions of the IY curve and the integrated photoionization spectrum arises from different seeding conditions or fragmentation of the clusters in the IY measurements, remains unanswered.

Another possible cause of the PES intensity at higher photon energies could be the contribution of small water clusters with $n = 1$ and 2. These cluster sizes show ionization energies between 3.8 eV (aIE of $Na(H_2O)_2$[63]) and 4.6 eV (sIE of $Na(H_2O)$[72]). Considering the spread of the cluster distribution, these two cluster sizes should contribute to less than 1% of the PES spectrum of West et al.[40]

Despite the high-IE discrepancy, both experimental data indicate a broad distribution of ionization energies, which suggests that $Na(H_2O)_n$ clusters with unsolvated sodium atoms are present in the cluster distribution[71] and more abundant than the formerly published isomer classes I and II. In terms of isomer classes, this indicates the presence of a further isomer class, which has not been observed in the purely aIE-focused studies.[38,70] In addition, both techniques reveal that at least 90% of the clusters feature ionization energies above 3.2 eV, which is of special interest for the application of the spectroscopic technique introduced by Steinbach and Buck[36] and further developed by the Zeuch group.[37,43,68,71,106,178,184]

4.3 Comparison of experimental and theoretical results

Introductory remarks

In order to use the obtained photoionization efficiency curves as a simulation target for predictions of ab initio theory and in order to evaluate the suitability of IY curves for probing the isomer population of water clusters, an existing cooperation with the Slavíček group from University of Chemistry and Technology Prague was re-activated and the results were published in [72]. While the experimental data for this comparison were measured in Göttingen, the computational work was done by the group of Prof. Petr Slavíček in Prague. For detailed information on the computational methods see [72] and references cited therein. A brief description is given below.

4.3.1 Computational methods

For small sodium water clusters ($Na(H_2O)_{n=2-5,7}$) the minimum energy isomers were determined by means of density functional theory (DFT) methods.[72] The basis set 6-31++g** was used employing three different DFT functionals, namely BMK[218] (a method with hybrid functionals), LC-ωPBE[219] (range-separated hybrid functionals), and BLYP[220] with an included empirical dispersion correction (general gradient approximation type functionals, GGA). The calculated minimum energy values of $Na(H_2O)_2$ and $Na(H_2O)_3$ were compared to values from CCSD(T)/aug-cc-pVTZ calculations.[72] As the BMK functional was able to reproduce the CCSD(T) energy ordering of the isomers of $Na(H_2O)_{2,3}$ and the CCSD(T) ionization energies the best, it was constantly used during the MD simulations for the calculation of the ionization energy and the gyration radius r_g, a measure for the delocalization of the solvated electron.

In order to compare the goodness of the predictions from computationally efficient GGA functionals (namely the BLYP functional), which typically favor higher solvation of the sodium atom, and range-separated hybrid-functionals (in this case LC-ωPBE), where the exact exchange energy is taken stronger into account with increasing interaction distance,[72], the predicted ionization energy distributions were compared to the obtained IY curves. In these MD simulations, the ionization energy distribution is determined by a convolution of the neutral cluster's ground state

probability function and the potential of the cationic cluster, which is also referred to as reflection principle,[158–160] see Figure 2.2 on page 20. For the calculation of the ionization energy distribution of $Na(H_2O)_n$ in the range probed by the experiment, only the ejection of the sodium 3s electron needs to be taken into account, as the energy required for its ejection is well below those of all other electrons within the cluster.[72]

The integrated ionization energy distributions from ab initio MD simulations mimicking thermal equilibrium and relying on the forces determined from energies obtained via the BLYP or the LC-ωPBE functional are compared to the IY curve of $Na(H_2O)_2{}^+$ in Section 4.3.2.1 and to the IY curve of $Na(H_2O)_3{}^+$ in Section 4.3.2.2. Integrated ionization energy distributions for $n = 4, 5$ and 7 from the isomer distribution obtained via forces from the BLYP functional are compared to the corresponding IY curves in Section 4.3.2.3.

4.3.2 Results

4.3.2.1 $Na(H_2O)_2$

For $n = 2$, three low energy isomers were found, see Table 4.1: a structure where a singly coordinated (SC) sodium atom is attached to an intact water dimer with a calculated IE of 4.03 eV, a cluster with doubly coordinated sodium and a hydrogen bond between the two water molecules (DC, 3.92 eV), and a cluster where both water molecules only coordinate the sodium atom (FS, 3.64 eV).[72] The energy ordering from CCSD(T), BMK, and LC-ωPBE suggests the structure with singly coordinated sodium atom attached to an intact water dimer to be the global minimum isomer.[72] In contrast to this, BLYP yields a different ordering of the isomers. This is most likely connected to the self-interaction error in the BLYP method which favors higher coordination of the sodium atom.[72]

Figure 4.5 shows the experimental data (black dots), the vertical ionization energies of the calculated isomers (dashed lines), and the integrated ionization energy distributions predicted from the BLYP and the LC-ωPBE functionals at 50 K and 200 K (blue and red traces). The experimental data indicate that the photoionization spectrum is dominated by the SC isomer, as the inflection point is above 4 eV.[72] The LC-ωPBE data are in good agreement with this, see lower panel of Figure 4.5. BLYP predicts the population of the DC and the FS isomers. While the experimental data indicates the presence of the DC isomer, the population of

Table 4.1: Minimum energy structures of $Na(H_2O)_2$ with their energies from CCSD(T)/aug-cc-pVTZ and the DFT methods BMK/6-31++g**, LC-ωPBE/6-31++g**, and BLYP/6-31++g**, and the ionization energies determined from the BMK method. Data and structures taken from [72].

structure	abbreviation	E / eV CCSD(T)	BMK	LC-ωPBE	BLYP	IE / eV
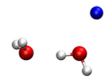	SC	0	0	0	0	4.03
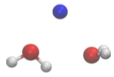	DC	0.028	0.002	0.022	−0.129	3.92
	FS	0.095	0.116	0.093	−0.097	3.64

the FS structure is not supported by the experiment. This inconsistency with the experiment has been concluded to be a result of the intrinsic self interaction error of the BLYP method, which results in the favoring of fully solvated species and thus a possibly erroneous energy ordering. [72]

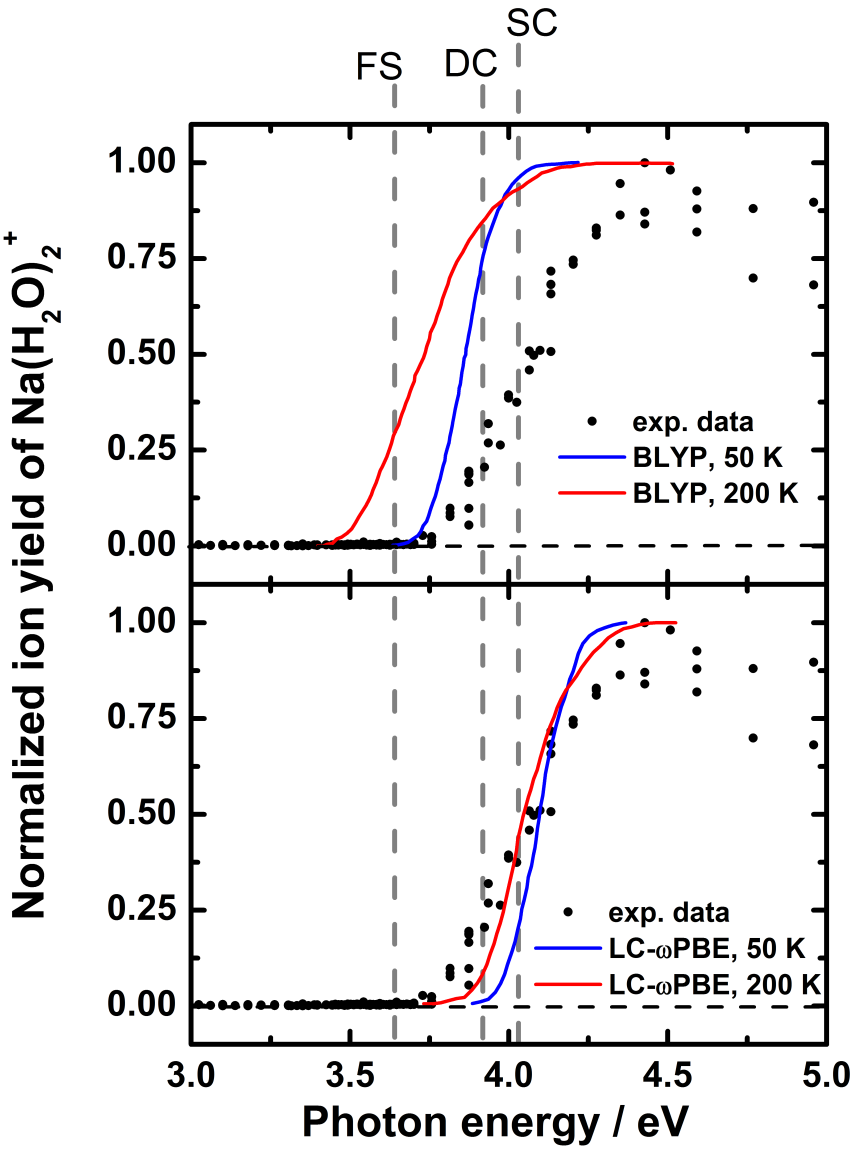

Figure 4.5: Comparison of the measured ion yield curve (black) and the integrated ionization energy distributions (lines) from BLYP (upper panel) and LC-ωPBE functional (lower panel) at different temperatures (see legend) for $n = 2$. The calculated ionization energies of the isomers shown in Table 4.1 are indicated as dashed grey lines. Figure taken from [72] and modified.

4.3.2.2 $Na(H_2O)_3$

Five low energy isomers of $Na(H_2O)_3$ were found,[72] see Table 4.2: a cluster in which the sodium atom is doubly coordinated and forms a square with the hydrogen bonded water molecules (S, 3.95 eV), a similarly square shaped isomer with a singly coordinated sodium atom (S2, 4.35 eV), a tetrahedral isomer structure where the sodium atom is attached to a cyclic water trimer with weakened hydrogen bonds compared to the pure cyclic water trimer (T, 3.67 eV), a trigonal cluster with a fully solvated sodium atom and no hydrogen bonds between the water molecules (Tr, 3.59 eV), and an isomer where the sodium atom is doubly coordinated and the third water molecule is hydrogen bonded to the cluster (DCHB, 3.80 eV). The CCSD(T) energy ordering of the isomers is matched by the BMK energies. As the error of the DFT method and the calculated energies are both in the range of 0.1 eV, the energies calculated via LC-ωPBE are still in rough agreement with the CCSD(T) energies. BLYP predicts a different energy ordering of the isomers.
Forck et al.[68] already described the isomers S and S2. In addition they found an isomer with a topology similar to DCHB but with slightly different geometry, and an intact cyclic water trimer isomer for which the sodium atom is singly coordinated. Their calculated vertical ionization energies for S, S2, and the DCHB analogous isomer are in agreement with those obtained in this work. The calculated ionization energy of the intact cyclic trimer with a singly coordinated sodium atom was 4.19 ± 0.17 eV.[68]
The experimental ion yield curve for the helium-seeded expansion conditions shows a saturation of the ion signal at 3.8 eV and an inflection point at around 3.6 eV, see black dots in Figure 4.6. With regard to the calculated ionization energies, this appears to exclude the presence of the two most stable isomers (S and S2) with calculated ionization energies of 3.95 eV and 4.35 eV,[72] as well as the presence of the isomer containing an intact cyclic water trimer of Forck et al.[68] In the case of the argon-seeded expansion conditions, the IY curve indicates the population of high-IE isomers as it levels off at significantly higher photon energies than in the helium-seeded case, see red dots in Figure 4.6.[72] The low-IE range is similar in both cases. A comparison of the experimental IY curve from argon-seeded expansions and the ionization energies calculated with the BMK functional could indicate the presence of the S isomer. It is noted that a vibrational spectroscopic study of Forck et al.[68] demonstrated that a sodium doped cyclic water trimer is present in expansion conditions as used in this work. This isomer likely contributes to the high ionization

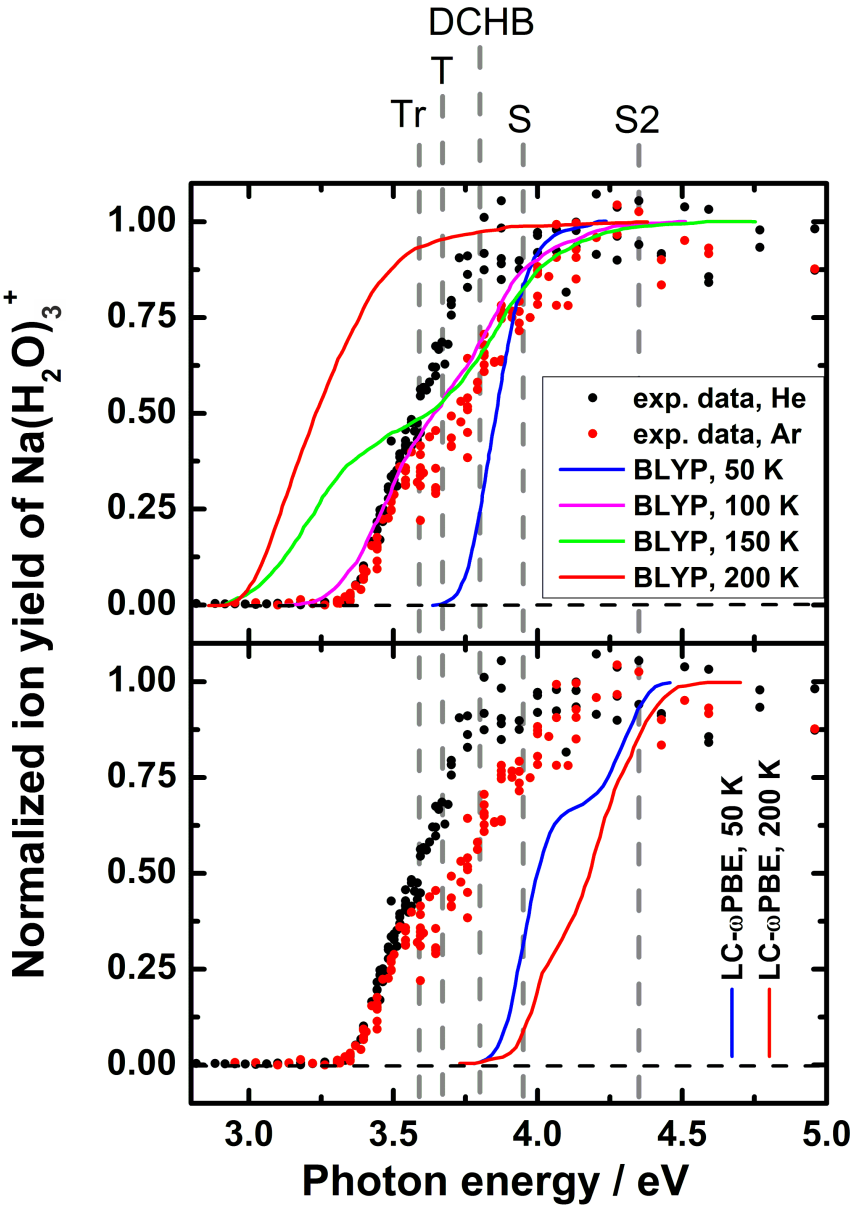

Figure 4.6: Comparison of the measured ion yield (black and red points, as in Figure 4.2) and the integrated ionization energy distributions (lines) from ab initio molecular dynamics based on the BLYP (upper panel) and the LC-ωPBE functional (lower panel) at different temperatures for $n = 3$. The calculated ionization energies are indicated as dashed grey lines. Figure taken from [72] and modified.

Table 4.2: Minimum energy isomers of $Na(H_2O)_3$ with their energies obtained from CCSD(T)/aug-cc-pVTZ and the DFT methods BMK/6-31++g**, LC-ωPBE/6-31++g**, and BLYP/6-31++g**, and the ionization energies determined via the BMK method. Data and structures taken from [72].

structure	abbreviation	E / eV CCSD(T)	BMK	LC-ωPBE	BLYP	IE / eV
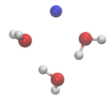	S	0	0	0	0	3.95
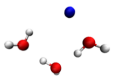	S2	0.010	0.034	−0.004	0.133	4.35
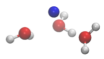	T	0.087	0.079	0.133	0.012	3.67
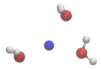	Tr	0.166	0.155	0.083	0.030	3.59
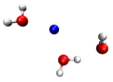	DCHB	0.175	0.181	0.158	0.030	3.80

energy part of the IY curve due to its high IE and was concluded to be formed due to kinetic trapping of the cyclic water cluster arrangement during the pickup process.[68] The kinetic trapping of this high-energy isomer during the pickup process might be caused by formation of mixed water argon clusters,[64,103] from which the Ar atoms could quickly evaporate during the pickup process.[103,139] Since the applied simulations did not consider the isomer detected by Forck et al.,[70] the high-IE range may not be described correctly by the simulations. Aside from this, the comparison of the experimental data with the predicted isomers is complicated by the uncertainty of the VIE calculated with the BMK functional (approximately 0.24 eV[218]) and the strong effect of the (even partial) sodium solvation on the IE.[70,72]

According to the ionization energy distributions obtained from the LC-ωPBE level of theory, the two isomers S and S2 should be dominant, whereas the isomers with lower ionization energies should not be present, see solid lines in bottom panel of Figure 4.6.[72] The resulting integrated ionization energy distributions do not match the experimental data as they are at too high energies. Therefore, the LC-ωPBE functional can be concluded to predict the isomer population and thus the ionization energy distribution of $Na(H_2O)_3$ unsatisfactorily.[72]

Surprisingly, the BLYP functional is in good agreement with the experimental data

and can reproduce the two step IY curve if the MD simulation temperature is set to 100 K. Tuning the temperature in the MD simulations in the range of $50 - 200$ K indicates that the low IE isomers are gradually populated with increasing temperature.[72] This is in agreement with ionization energy distributions of sodium doped methanol clusters calculated at the MP2/6-31++g** level of theory.[43] At high temperatures the increased population of low IE isomers is indicated and most likely over-exaggerated by the BLYP results due to its favoring of structures with a high degree of sodium solvation.[72]

As the BLYP method showed a poor agreement for the $Na(H_2O)_2$ cluster, it is clear that the data for $n = 3$ are only well described due to error compensation:[72] While the self-interaction error leads to favoring of isomers with a fully solvated sodium atom, the non-corrected zero point energy promotes the population of isomers with lower sodium coordination. These errors appear to compensate such that the presence of several isomers is predicted, which is in agreement with the experimental data, see Figure 4.6. For $Na(H_2O)_2$ this error compensation does not occur for the singly coordinated sodium cluster as the self interaction error dominated.[72]

Despite this error compensation and the erroneous energy ordering of the isomers, the results of the BLYP MD simulation may provide a qualitative explanation for the IR action spectroscopic approach previously applied for the generation of vibrational spectra of $Na(H_2O)_n$ clusters:[37,68,71,90] A higher temperature can lead to the population of isomers with a higher degree of sodium and electron solvation and therefore a lower IE. From this follows that high-IE isomers can be transferred to low-IE species upon IR excitation. This is in agreement with predicted IE distributions of sodium doped methanol clusters.[43]

4.3.2.3 $Na(H_2O)_{n=4,5,7}$

The energy hypersurface becomes more complex with increasing cluster size. Unfortunately, the DFT-based energies of these cluster could not be validated by CCSD(T) calculations.[72] The calculated energies and geometries of the most stable isomers for $n = 4, 5, 7$ are listed in Table 4.3.

For $n = 4$, the global minimum found with the BMK and LC-ωPBE functional is an intact cyclic water tetramer with an attached, singly-ccordinated sodium atom (4i1, 4.26 eV).[72] In the other isomers found (4i2, 4i3, and 4i4), the sodium atom is coordinated by several water molecules, which results in ionization energies of $3.48 - 3.60$ eV. The calculated ionization energies of these three isomers are within

Table 4.3: low energy isomers of $Na(H_2O)_{n=4,5,7}$. The energies were obtained from DFT calculations at the BMK/6-31++g**, LC-ωPBE/6-31++g**, and BLYP/6-31++g** level of theory. The ionization energies were determined via the BMK method. Data and structures taken from [72].

structure	abbreviation	E / eV BMK	LC-ωPBE	BLYP	IE / eV
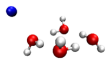	4i1	0	0	0	4.26
	4i2	0.031	0.172	−0.143	3.48
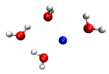	4i3	0.045	0.136	−0.147	3.51
	4i4	0.050	0.182	−0.150	3.60
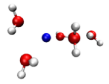	5i1	0	0	0	3.52
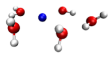	5i2	0.003	0.040	-	3.57
	5i3	0.003	0.031	−0.017	3.74
	5i4	0.078	0.112	−0.036	3.47
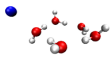	5i5	0.087	−0.033	0.318	4.26
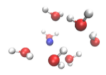	7i1	0	0	0	3.69
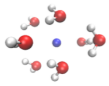	7i2	0.033	0.014	0.145	3.82
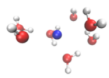	7i3	0.036	0.024	0.029	3.52
	7i4	0.059	0.030	−0.010	3.41
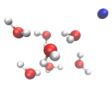	7i5	0.098	0.061	0.300	3.92

the range of the breadth of the experimental ion yield increase, see top panel of Figure 4.3. Again, the BLYP energy ordering of the isomers differs from the one obtained with the BMK and the LC-ωPBE functional. The experimental IY curve levels off at around 3.75 eV and features a step around 3.6 eV, see top panel of Figure 4.7.[72] The second step indicates the presence of clusters isomers with higher IE. The difference of the predicted ionization energy distribution and the experimental

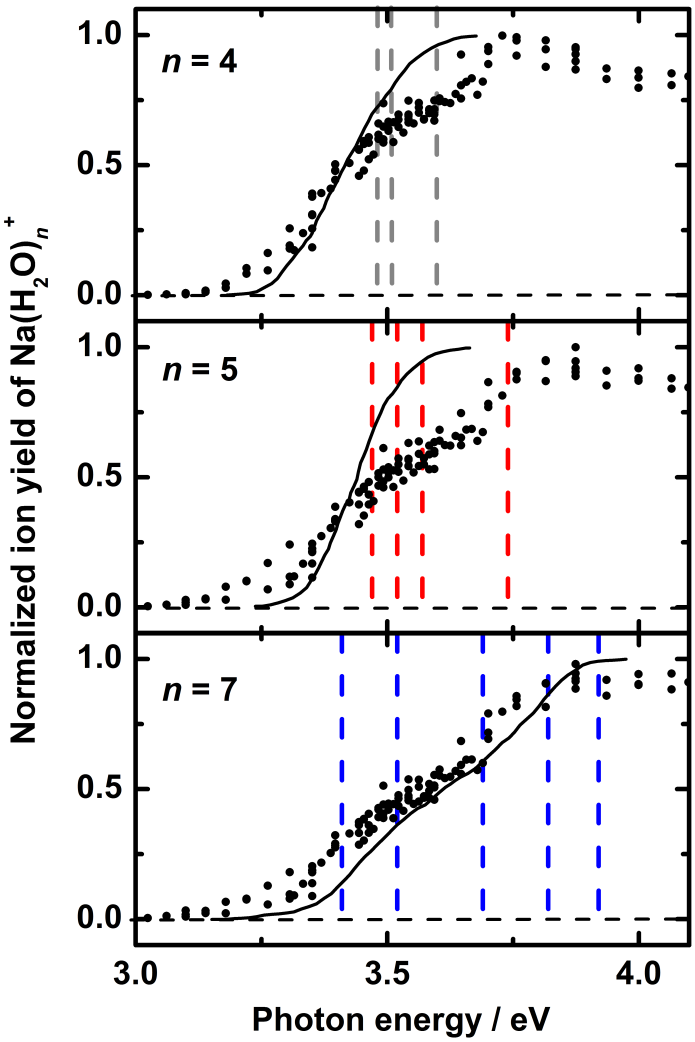

Figure 4.7: Comparison of the experimental ion yields of $Na(H_2O)_{n=4,5,7}^+$ (points) and the predicted ionization energy distributions of $Na(H_2O)_{n=4,5,7}$ (solid lines) from BLYP level MD simulations at 50 K. The calculated IE of the isomers are indicated by dashed lines. Figure taken from reference [72] and modified.

data in the range of this step has two possible reasons: either kinetic trapping of high-IE isomers, which has been concluded to be responsible for the abundance of high-IE isomers of $Na(H_2O)_3$,[68] or the favoring of isomers with a higher degree of solvation by the BLYP method.[72]
In the case of $n = 5$, the experimental IY curve (black dots in middle panel of Figure 4.7) indicates the presence of the calculated cluster isomers 5i1, 5i2, 5i3, and 5i4 based on their calculated IE (depicted as red dashed lines).[72] The integrated ionization energy distribution (calculated from the isomer distribution obtained in simulations with the BLYP functional) shows a discrepancy to the experimental data: The experimental ion yield levels off at 3.8 eV whereas the MD result indicates the sIE to be at 3.6 eV. As in the case of $n = 4$, it can be speculated that the deviation of experiment and theory is caused either by the presence of kinetically trapped high-IE isomers of $Na(H_2O)_n$—in which the sodium atom is not fully solvated—in the experiment, or by the favoring of structures with a solvated sodium atom by the BLYP functional.[72]
For $n = 7$, the experimental ion yield is well described by the simulated ionization energy distribution, see bottom panel of Figure 4.7. The sIE is equal for the BLYP MD simulation at 50 K and the experiment and the two step structure of the spectrum is reproduced. Both curves are in agreement with the calculated ionization energies of the isomers 7i1, 7i2, 7i3, and 7i4. The ionization energy of isomer 7i5 is in the range of the observed experimental sIE and is therefore less likely to be present. The crucial difference between the clusters with seven water molecules to clusters with less than 6 molecules is the presence of three-dimensional hydrogen bonded networks.[74,76,87,179] The agreement of the experimental data and the predicted ionization energy distribution indicates that in the hydrogen bond network of the pure water clusters could partly survive the sodium doping process in sufficiently large clusters and lead to high-IE cluster.[72] The high-IE isomers are populated in the BLYP simulation despite the favoring of solvated structures by this method. It has to be noted that the calculated isomers of $Na(H_2O)_7$ are within a Gibbs energy range of less than 0.1 eV, which may not be covered by the accuracy of the simulation method.[72]

4.4 Conclusion

Photoionization efficiency curves of $Na(H_2O)_n$ clusters have been compared to a size-averaged photoelectron spectrum,[40] the previously reported low energy part of the photoionization efficiency curve of larger clusters,[70,71] and the integrated ionization energy distributions from ab initio MD simulations.[72]

The measured ion yield curves all show sigmoidal curves for which the appearance ionization energy, the saturation ionization energy, and the curve shape depend on cluster size.[72] The experimental data reproduces the previously reported aIE values.[38,63,70] An exception is the aIE of $Na(H_2O)_3$ for which a new, lower value of 3.35 ± 0.05 eV was determined.[72] The saturation ionization energy reaches a constant value of 4.1 eV for clusters with $n \geq 9$. The photoionization spectrum of $Na(H_2O)_2$ is free of signal resulting from fragmentation of larger clusters for photon energies up to 3.75 eV. Fragmentation cannot be ruled out for higher photon energies. The comparison of the photoelectron spectrum of West et al.[40] indicates that up to 20% of the photoelectron intensity results from cluster with ionization energies above 4.1 eV. As the cluster temperatures could not be measured or controlled in both experiments, the influence of the cluster temperature on the ionization energy distribution[68,72] or fragmentation in the high-IE range could be reasons for the discrepancy of both experimental studies.

Clusters with $n \geq 9$ show a broad distribution of ionization energies, which proves the presence of more than the two isomer classes as determined from measurements in the low-IE range[63,70] and demonstrates the high abundance of clusters with higher ionization energies. This is also indicated by the PES measurements of West et al.[40] It was found that the large fraction of clusters with IE > 3.2 eV—approximately 90% of the clusters—can contribute to signal gains in the IR-assisted vibrational spectroscopy approach outlined in Section 2.4.4.

Only for $n = 3$ a strong seeding gas effect on the detected photoionization efficiency curve was observed. The observed population of high-IE isomers is in agreement with the presence of kinetically trapped high-IE isomers which were observed in a previous work.[68] Ab initio molecular dynamics simulations for $Na(H_2O)_3$ with energies calculated from the BLYP functional add a qualitative explanation of the influence of the cluster temperature on the IY curve and thus the IR-assisted photoionization of $Na(H_2O)_n$ clusters:[72] higher cluster temperatures increase the population of low-IE isomers. This is in agreement with the calculated temperature dependence

of ionization energy distributions for $Na(CH_3OH)_n$ [43] and the proposed IR-induced solvation of a sodium atom attached to a water cluster. [71]

Although the calculated ionization energy distributions from the BLYP level of theory were able to match the experimental data for $n = 3$ and $n = 7$, they failed at other cluster sizes ($n = 2, 4, 5$), see Section 4.3. LC-ωPBE assisted MD simulations showed satisfactory agreement with the experimental data only for $n = 2$. To overcome the lack of a computationally efficient method which describes the isomer population of sodium water clusters found in experiments, the experimental data presented here and in reference [72] may serve as a reference dataset for further theoretical development as they provide size-selective ion yield curves over a broad range of cluster sizes and ionization energies, including clusters with only few water molecules. [72]

5 Vibrational spectroscopy of $Na(H_2O)_n$ clusters

5.1 Introductory remarks

Sodium doping has recently been used for the size-selective measurement of vibrational spectra of clusters over a wide range of cluster sizes.[36,37,43,68,71,106,178,184,188] In all of these studies, the ionizing UV radiation was provided by an excimer pumped dye laser with a pulse length of 28 ns and the delay time between IR and UV pulse was set to $\Delta t = 80$ ns, as it was reported to yield an optimal signal enhancement if photoionization was performed at a photon wavelength of 400 nm.[36,188] After replacement of the excimer pump laser by an Nd:YAG pump laser, the FWHM pulse lengths were reduced to $7-8$ ns.[90] This, together with the detection scheme stated in Section 3.3 (and described in detail in the master's thesis of Sabine Wolff[203]), enables the investigation of the delay time dependence of the signal gain resulting from the action spectroscopic mechanism outlined in Section 2.4.4.
The experimental work of this section is partly reported in the bachelor's thesis of Daniel Becker.[221] The first time-dependent measurements with the modified setup are reported in the master's thesis of Sabine Wolff.[203]

5.2 Temporal signal dependence

Δt denotes the temporal delay between the two laser pulses and is defined as follows[203]

$$\Delta t = t_{\mathrm{UV}} - t_{\mathrm{IR}} \tag{5.1}$$

t_{UV} and t_{IR} are the starts of the laser pulses determined with a photodiode with sub-ns resolution (Electro-Optics Technology, Inc., Silicon PIN Detector ET-2000)

and an oscilloscope (Tektronix, TDS 744A). The temporal uncertainty of Δt from this procedure is 2 ns. A negative delay corresponds to photoionization prior to vibrational excitation, whereas a positive delay denotes that the laser pulse of the IR laser irradiates the cluster beam before the UV laser pulse.[203] Due to the two laser pulse lengths and the temporal uncertainty of Δt, an overlapping of the pulses occurs at around $-10 < \Delta t < +10$ ns.

The mass spectra measured at different delay times show significant differences, see Figure 5.1. The mass spectra shown in black are obtained from clusters which were only irradiated by the UV laser pulse. These spectra are a reference to study the effect of the IR laser pulse on the cluster distribution. The mass spectra shown in red are obtained using IR and UV laser simultaneously. For a delay time $\Delta t = -10$ ns, low-IE $Na(H_2O)_n$ clusters (IE $\leq$ 3.22 eV) are ionized before vibrational excitation by an IR laser pulse occurs. The change in the mass spectrum with regard to the UV reference mass spectrum results from the vibrational excitation of $Na(H_2O)_n{}^+$ cations. The used IR frequency of $\tilde{\nu} = 3400\,\mathrm{cm}^{-1}$ is close to the broad absorption maximum of amorphous, liquid-like clusters.[16,20,37,71] Therefore, the successive absorption of multiple photons from 10 mJ laser pulses is very likely to occur, also since the laser pulse duration (8 ns) is several orders of magnitude larger than the intermolecular vibrational relaxation (IVR, few ps[222,223]). The heated cationic clusters fragment, which results in a mass spectrum that shows higher abundances for clusters with $n \leq 150$ and lower abundances for $n \geq 200$, see top panel of Figure 5.1. This laser pulse detection sequence corresponds to IR multi photon dissociation (IRMPD) of $Na(H_2O)_n{}^+$.

For positive delay times, where the clusters are first exposed to the IR pulse and are ionized afterwards, a signal increase is observed for all clusters sizes at short delay times, see middle panel of Figure 5.1. The signal gain is a cluster size dependent quantity, compare e.g. ion yield gains for $n = 30 - 50$ and $n \geq 250$. In contrast to the mass spectrum obtained at $\Delta t = -10$ ns, no depletion is observed for the large cluster sizes of the cluster distribution. This indicates that the abundance increase due to the action spectroscopic mechanism outlined above is larger than the cluster fragmentation shown for $\Delta t = -10$ ns.

Increasing the delay time to $\Delta t = +200$ ns results in a higher IR-induced signal gain with regard to the UV reference but a lower ion yield than obtained in the $\Delta t = +10$ ns IR-UV mass spectrum. However, the ion signal of $n \geq 450$ clusters is similar to the UV reference, so no IR-induced signal depletion is observed. A possible

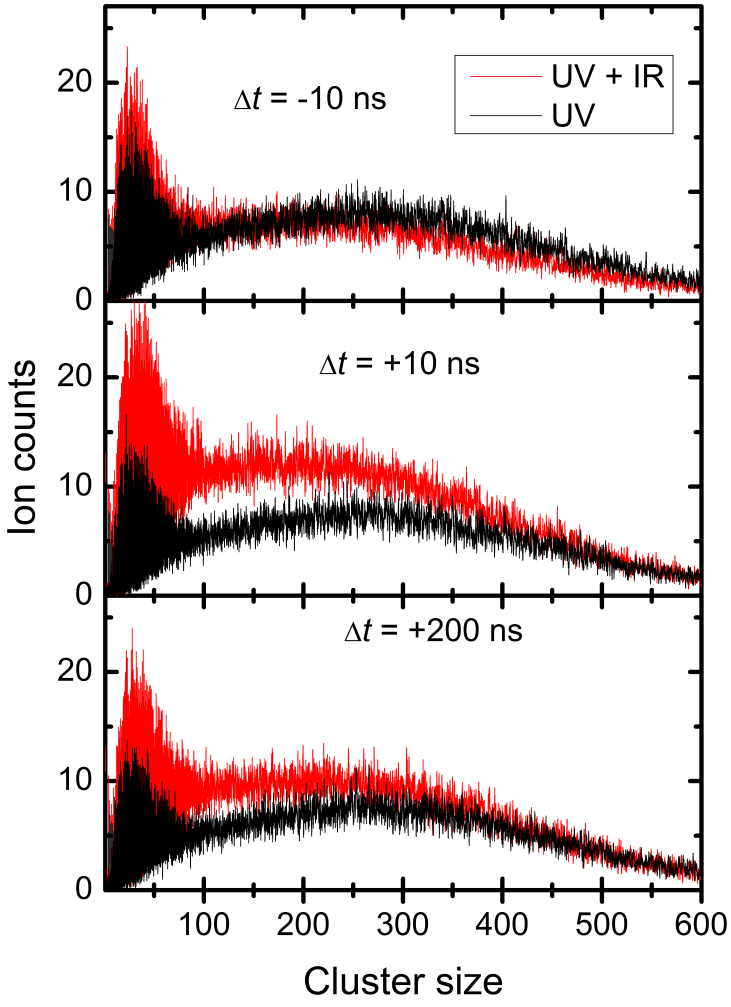

Figure 5.1: Comparison of mass spectra from ionization conditions differing only in Δt. The black traces correspond to single photon ionization by 385 nm photons, the red traces to ion signal from irradiation of the clusters with both IR ($\tilde{\nu} = 3400\,\mathrm{cm}^{-1}$) and UV laser pulse ($\lambda_{\mathrm{UV}} = 385\,\mathrm{nm}$). The delay times applied are $-10\,\mathrm{ns}$, $+10\,\mathrm{ns}$, and $+200\,\mathrm{ns}$. The helium-seeded supersonic expansions were performed with 2.7 bar water vapor and $p_{\mathrm{stag}} = 3.7 \pm 0.1$ bar.

reason for this observation is that the depletion from IRMPD and the signal gain due to IR excitation balance out in this case.
The changes of the mass spectra with Δt shown in Figure 5.1 suggest to study the temporal evolution of the IR signal gain in more detail. Panel (a) of Figure 5.2 shows the IR-induced signal gain as a function of the delay time Δt for the IR frequencies $\tilde{\nu} = 3200\,\mathrm{cm}^{-1}$ (black squares) and $\tilde{\nu} = 3400\,\mathrm{cm}^{-1}$ (red squares) for the cluster size range $n = 50 - 450$. These frequencies were chosen since they are close to the absorption peaks of crystalline and amorphous clusters.[16,20,37,90] Since individual mass peaks of clusters with $n > 100$ are not resolved and in order to reduce the noise in the IR-induced signal, several cluster sizes are binned in the following. Both signal gain curves show a similar trend with four different regions:[221]

I $\Delta t \leq -10\,\mathrm{ns}$, a constant depletion of the signal from the largest clusters and a correspondingly tilted mass spectrum caused by IRMPD of $Na(H_2O)_n^+$ cluster cations;

II $-10\,\mathrm{ns} < \Delta t \leq 5\,\mathrm{ns}$, a sharp rise of the ion gain with a maximum at $\Delta t = 5 - 10\,\mathrm{ns}$;

III $5\,\mathrm{ns} \leq \Delta t \leq 2.5\,\mu\mathrm{s}$, a decreasing signal gain;

IV $\Delta t > 2.5\,\mu\mathrm{s}$ (not shown), a constant value of 0, as the IR-pumped clusters have flown out of the UV-probed ionization volume.

The observation in region IV and the linear contribution to the signal decay of region III are related to the velocity of the molecular beam and the laser beam diameter as the clusters that have been irradiated by the IR pulse are no longer present in the volume probed by the UV laser pulse. This is reasonable since the mean beam velocity for the applied seeding conditions (2.7 bar water vapor, 3.7±0.1 bar stagnation pressure, He seeded) has been determined to be $\bar{v}_{\mathrm{beam}} = (1.19 \pm 0.07) \cdot 10^3\,\mathrm{m/s}$ and therefore the clusters travel only about 0.24 mm in 200 ns which corresponds to less than 10% of the laser beam diameter ($\sim 3\,\mathrm{mm}$).
The constant depletion for large clusters at $\Delta t \leq -10\,\mathrm{ns}$ (region I) is caused by IRMPD of cationic clusters, compare the corresponding mass spectrum in Figure 5.1. The resulting change of the cluster distribution can also be shown by plotting the signal gain values of cluster size ranges for $\Delta t \leq -10\,\mathrm{ns}$ as shown in panel (b) of Figure 5.2. This tilting was observed for several UV photon energies for a cluster distributions producing smaller clusters, see Figure A.1 in the appendix.

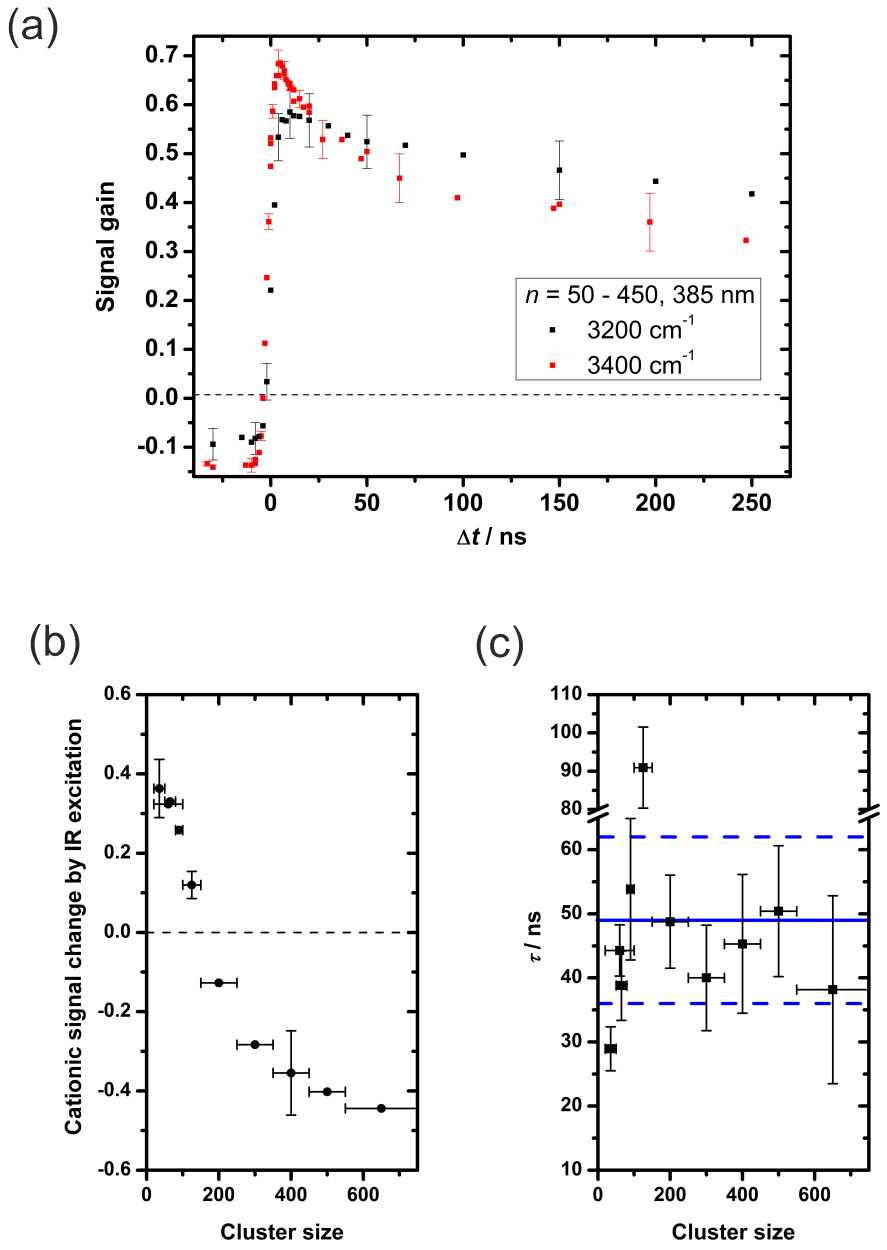

Figure 5.2: (a) Δt-dependence of the ion signal gain for $\tilde{\nu} = 3200\,\mathrm{cm}^{-1}$ (black squares) and $\tilde{\nu} = 3400\,\mathrm{cm}^{-1}$ (red squares) of the cluster size range $n = 50 - 450$ for $Na(H_2O)_n$ clusters ionized by 385 nm photons.
(b) Relative signal change upon IR irradiation ($\tilde{\nu} = 3400\,\mathrm{cm}^{-1}$, $\Delta t \leq -10$ ns) of cationic clusters for several cluster size ranges of the cluster distributions shown in Figure 5.1. The binned cluster sizes are marked by the abscissa error bars.
(c) Exponential decay coefficients τ determined from regressions for which the flyout of vibrationally excited clusters was accounted for by adding a linear function to the mono-exponential regression function (black dots). The blue lines mark the average exponential decay lifetime $\bar{\tau} = 49 \pm 13$ ns that is obtained if the flyout of IR-irradiated clusters is neglected and the signal gain data in the range of $\Delta t = 10 - 150$ ns are considered for the mono-exponential regressions; data taken from [221].

The sharp rise of the signal gain in region II is related to the temporal overlap of the two lasers and thus occurs on a shorter timescale than the laser pulse lengths.[203] This signal gain is caused by the mechanism stated in Section 2.4.4 and originates an IR-induced solvation of the sodium atom.[71] This is consistent with the shift of the ionization energy distribution towards smaller ionization energies with increasing temperature.[43,72] The fast signal increase is completed within a delay time interval of $12 - 16\,\mathrm{ns}$ and was observed for all IR frequencies tested that provide resonant vibrational excitation of larger water clusters.[203,221] The breadth of this signal increase is similar to the temporal laser pulse widths and therefore the underlying process cannot be temporally resolved with the present setup.
The decrease of the signal gain for $5\,\mathrm{ns} \leq \Delta t \leq 2.5\,\mu\mathrm{s}$ depends on the IR frequency as shown in the top panel of Figure 5.2. The ion yield at an IR excitation of $3200\,\mathrm{cm}^{-1}$ shows a steady, almost linear decrease, while at $3400\,\mathrm{cm}^{-1}$ a convolution of the linear decrease with an exponential decrease is observed for all cluster sizes. The linear signal decay is related to the molecular beam velocity, as it ends at around $\Delta t = 2.5\,\mu\mathrm{s}$ when any IR-irradiated clusters have moved beyond the ionization volume. The exponential contribution to the signal decrease indicates a unimolecular process that reduces the fraction of low-IE clusters with regard to the signal gains obtained at around $\Delta t = 5\,\mathrm{ns}$. The first order character of the signal decay was shown in the bachelor's thesis of Daniel Becker.[221] For the exponential signal decrease, the lifetime τ was determined from a fitting function which consisted of a linear function and an exponential decay term:

$$I(\Delta t \geq 5\,\mathrm{ns}) = I_1 + m \cdot \Delta t + I_2 \cdot \exp\left(-\frac{\Delta t}{\tau}\right) \tag{5.2}$$

Here, $I(\Delta t \geq 5\,\mathrm{ns})$ corresponds to the IR-induced signal gain, I_1, I_2 and m to constants, Δt to the delay time between the laser pulses, and τ to the lifetime of the exponential decay. The obtained τ is in the range of $20 - 100\,\mathrm{ns}$, see panel (c) in Figure 5.2, and corresponds to rate constants of $5 \cdot 10^7 - 1 \cdot 10^8\,\mathrm{s}^{-1}$. If determined from the raw signal gain data in the range of $\Delta t = 10 - 150\,\mathrm{ns}$ with a standard exponential decay fitting function, similar τ values are obtained,[221] see blue lines in Figure 5.2 (c). A correlation between τ and the cluster size is not observed.
The exponential signal decrease can only be observed if the UV photon energy is lower than the sIE of $4.1 \pm 0.1\,\mathrm{eV}$, as reported in Section 4. For photon energies of $4.27\,\mathrm{eV}$, a constant IR-induced shift of the mass spectra to smaller cluster sizes—

independent of Δt—is obtained, see Figure A.2 on page 128 in the appendix.
The mechanism causing the sharp signal rise is rather well understood, see Section 2.4.4: The resonant absorption of IR photons leads to an increase of the cluster temperature[43,72] and therefore to an increased population of low-IE isomers with a higher degree of solvation of the sodium atom.[71] While the linear part of the signal gain decrease is caused by the flyout of vibrationally excited clusters, the exponential decrease indicates that the temperature of the vibrationally excited clusters decreases with increasing Δt due to the high temperature sensitivity of the sodium atom solvation.[43] Since the clusters in the molecular beam can be considered to be isolated due to the high vacuum conditions in the mass spectrometer, a temperature decrease is most likely obtained by ejection of constituents from the clusters. As sodium doped water clusters are present, the exponential decay of the signal gain can therefore be caused by ejection of the sodium atom from vibrationally excited clusters

$$\mathrm{Na(H_2O)}_n{}^* \rightarrow \mathrm{Na} + \mathrm{(H_2O)}_{n-\mathrm{z}} + z\,\mathrm{H_2O} \tag{5.3}$$

or by evaporation of monomeric or oligomeric water

$$\mathrm{Na(H_2O)}_n{}^* \rightarrow \mathrm{Na(H_2O)}_{n-\mathrm{x}} + x\,\mathrm{H_2O} \tag{5.4}$$

$$\mathrm{Na(H_2O)}_n{}^* \rightarrow \mathrm{Na(H_2O)}_{n-\mathrm{y}} + \mathrm{(H_2O)}_y \tag{5.5}$$

If the evaporation of the sodium atom from the cluster occurs on the observed timescale it should be observable via the sodium atom signal as this should increase with τ. The Δt dependence of the sodium ion signal is shown in Figure 5.3. At negative delay times the Na^+ signal is not affected by the IR laser pulse. For positive delay times a constant Na^+ ion signal increase is obtained; but an increase of the Na^+ ion yield with increasing Δt for $\Delta t \geq 5\,\mathrm{ns}$ is not observed. Therefore it can be concluded that the exponential decay of the IR-induced signal gain does not originated from the ejection of sodium atoms from the clusters as stated by equation 5.3.
The equations 5.4 and 5.5 correspond to water monomer evaporation and cluster fission. Which of these processes is present cannot be distinguished by the present experiment. Both processes yield smaller sodium water clusters. However, a corresponding tilting of the mass spectra to smaller cluster sizes has not been observed with increasing delay time. Also, no fragment cluster size was observed that would

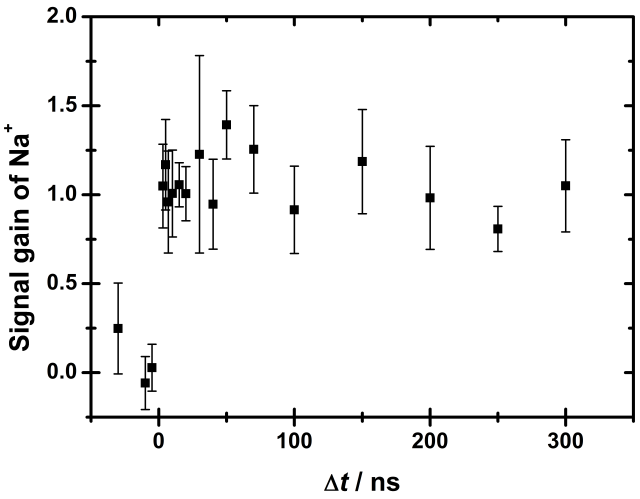

Figure 5.3: Delay time dependent ion signal of Na^+ for irradiation by IR photons with $\tilde{\nu} = 3400\,\mathrm{cm}^{-1}$.

correspond to $Na(H_2O)_{n-x/y}$ and which's ion signal increases with increasing delay time in the range $5\,\mathrm{ns} \leq \Delta t \leq 200\,\mathrm{ns}$. With regard to the temperature dependence of the ionization energy distribution [43,72] and the evaporative ensemble theory [144,146,147] an explanation for the observations could be as follows: As the clusters are heated by the IR laser pulse with $\tilde{\nu} = 3400\,\mathrm{cm}^{-1}$ and populate low IE isomers, which are ionizable by the 3.22 eV UV laser pulse, a fraction of these IR-heated low IE clusters is cooled by evaporation of water molecules or ejection of small clusters within the observed timescale. The cooled clusters may then form isomers with higher ionization energies which are not probed by the experiment at photon energies of 3.22 eV (385 nm).

Surprisingly, the exponential decrease is observed for vibrational excitation by radiation at $\tilde{\nu} = 3400\,\mathrm{cm}^{-1}$ but not for $3200\,\mathrm{cm}^{-1}$, see Figure 5.2 (a). This difference could be related to the absorption cross sections of the clusters for the two IR frequencies. [21] As the presence of crystalline $Na(H_2O)_n$ clusters was shown for $n \geq 275 \pm 25$ at similar expansion conditions at the present setup by Pradzynski et al., [71] a comparison of the Δt-dependent signal gain obtained at $\tilde{\nu} = 3200\,\mathrm{cm}^{-1}$ for amorphous and for crystalline clusters is possible, see Figure 5.4: In the case of amorphous clusters ($n = 20 - 100$) a slight exponential decay for $\Delta t \geq 12\,\mathrm{ns}$ is observed, whereas the signal of large crystalline clusters ($n = 350 - 450$) [71] remains constant. The fraction of the exponentially decaying signal gain observed for $n = 20 - 100$ is smaller than observed for irradiation with $\tilde{\nu} = 3400\,\mathrm{cm}^{-1}$ photons,

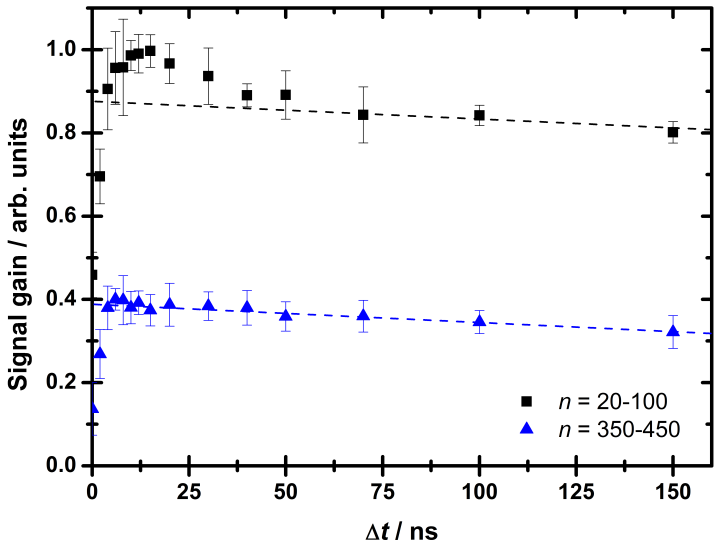

Figure 5.4: Delay time dependent signal gain after $3200\,\mathrm{cm}^{-1}$ irradiation for amorphous clusters ($n = 20 - 100$, black squares) and crystalline clusters ($n = 350 - 450$, blue triangles). The dashed lines are linear extrapolations from the data of $\Delta t = 75 - 250\,\mathrm{ns}$. Water vapor (2.7 bar) was expanded with He at a reservoir pressure of 3.7 bar. The clusters were ionized by 385 nm photons.

which should be due to the smaller absorption cross section of amorphous clusters for $\tilde{\nu} = 3200\,\mathrm{cm}^{-1}$, see e.g. Section 2.4.3. For crystalline clusters with $n = 350 - 450$ no exponential decay is observed and the obtained signal gain is stable. These crystalline clusters therefore appear to be less prone to an IR-induced signal decrease if excited by $3200\,\mathrm{cm}^{-1}$ radiation. This can be explained by a melting transition the cluster can undergo and which results in an upshift of the absorption maximum from $3250\,\mathrm{cm}^{-1}$ to $3400\,\mathrm{cm}^{-1}$.[224] As the absorption cross section of the thus formed clusters is significantly lower at $\tilde{\nu} = 3200\,\mathrm{cm}^{-1}$ than that of the crystalline clusters,[21,187,225] the absorption of further photons should be reduced. This transformation is likely to occur as the energy required to melt crystalline clusters is far smaller than the one needed for the evaporation of water molecules[21] and the melting transition was shown to occur within 10^2 ps for superheated bulk ice.[224] The observed decay of the signal gain corresponds to a decreasing fraction of low-IE clusters and therefore could indicate a decreasing temperature of the clusters.[43,72] As these aggregates are isolated in vacuum, the most probable way to reduce a cluster's internal energy is the loss of water molecules,[144] which is not directly probed by the present setup. In the following the observed exponential decay lifetimes for the

are compared to that observed for the evaporation of water molecules from charged water clusters: With regard to the obtained rate coefficients ($k_{\mathrm{decay}} = 10^7 - 10^8\,\mathrm{s}^{-1}$, corresponding to $\tau = 10 - 100\,\mathrm{ns}$), it is apparent that these differ significantly from the rate constants of internal vibrational relaxation ($10^{12}\,\mathrm{s}^{-1}$),[223] black-body infrared dissociation of water clusters (around $10^1\,\mathrm{s}^{-1}$),[25,226] and the dissociation rate coefficients observed for the decay of metastable water cluster ions ($10^4\,\mathrm{s}^{-1}$).[227] Simulations of Caleman and van der Spoel on the evaporation of isolated water particles containing few ions are in agreement with the timescales found in this work:[228] They found that the number of monomer units in the clusters decreased with a lifetime of $30 - 50\,\mathrm{ns}$ for $Na_4^+(H_2O)_n$ clusters ($n = 212$ and $n = 508$) with initial temperatures of 275 K.[228] Additionally, they showed that not only monomer evaporation but also cluster fission can contribute to decreasing the cluster size for positively charged clusters. Moreover, it was found that the cluster temperature of evaporating, pure water droplets decreases to around 215 K,[229] which is close to the value estimated by Klots.[147] In order to reach cluster temperatures of 275 K in the molecular beam several photons have to be absorbed by each cluster.[III] This could be possible within the experimental parameters, as IVR occurs in the ps timescale and thus 3 orders of magnitude faster than the temporal IR laser beam length and pulse energies of ca. 10 mJ were used, providing 10^{20} photons per laser pulse. In addition, several vibrational modes contribute to the peak absorption of large clusters.[16]

5.3 Pulse energy dependence

In this section, the delay-dependent IR-induced signal gain is characterized in terms of the IR laser pulse energy E_{IR}. The laser pulse energy was adjusted by tuning the OPA stage 1064 nm pump beam attenuator of the LaserVision OPO/OPA system such that spatial and temporal beam alignment remained unchanged.[215]
Figure 5.5 shows the IR-induced signal gain for three cluster size regions ($n = 40-50$, $250 - 300$, and $400 - 450$) at four different ionization conditions. The IR-assisted ionization has been performed with $\Delta t = 12\,\mathrm{ns}$ (filled symbols) and 200 ns (open symbols) and the frequency of the IR laser radiation was set to $\tilde{\nu} = 3200\,\mathrm{cm}^{-1}$ (black) or $3400\,\mathrm{cm}^{-1}$ (red).

[III] $n_{\mathrm{photon}} = 12$ for a cluster containing 100 water monomers, $n_{\mathrm{photon}} = 61$ for a cluster containing 500 water monomers. These values were estimated with a specific heat per water molecule of $2.5 \cdot 10^{-4}\,\mathrm{eV\ K}^{-1}$,[71,149] initial cluster temperatures of 70 K,[37] and IR photon energies of 0.42 eV corresponding to $3400\,\mathrm{cm}^{-1}$.

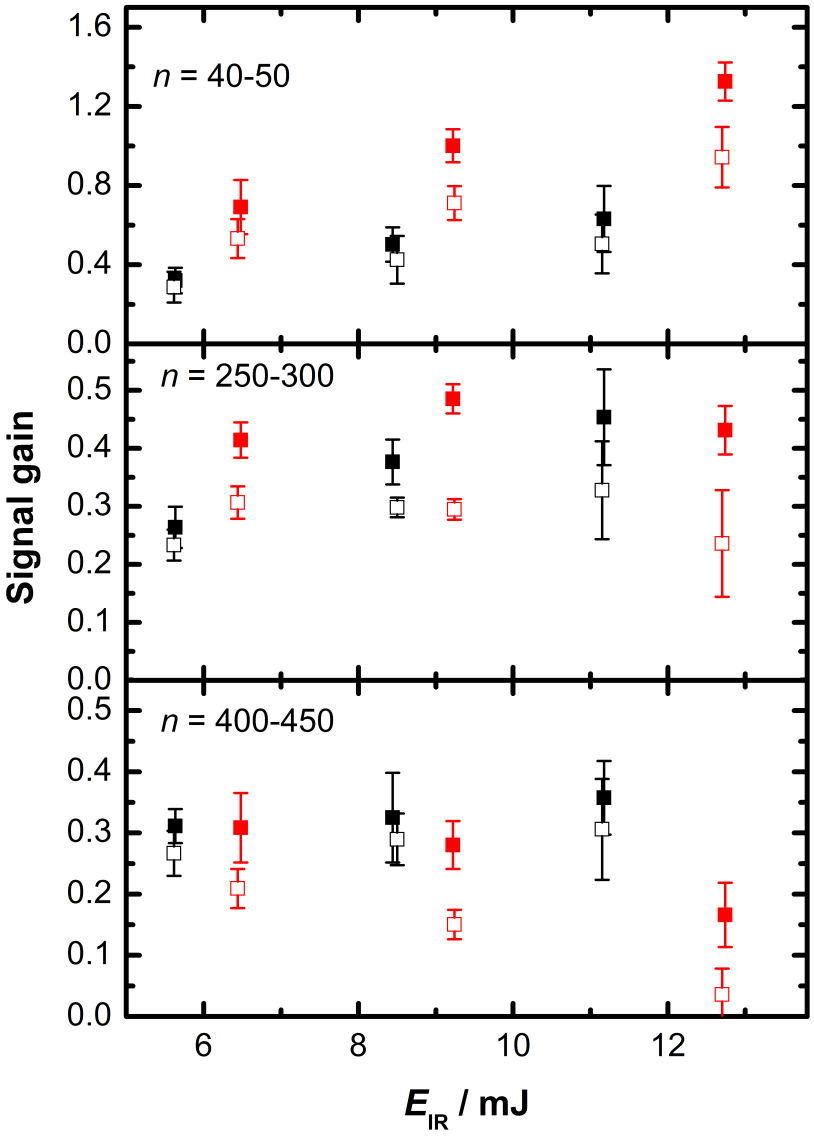

Figure 5.5: Dependence of the IR-induced signal gain on the IR laser pulse energy, E_{IR}, for the cluster size ranges $n = 40-50$, $250-300$, and $400-450$. Signal gains from $3200\,\mathrm{cm}^{-1}$ radiation (black points) and $3400\,\mathrm{cm}^{-1}$ (red) were measured at $\Delta t = 12\,\mathrm{ns}$ (filled squares) and 200 ns (open squares). Water vapor (2.7 bar partial pressure) has been expanded at a stagnation pressure of 3.7 ± 0.1 bar with He seeding.

The upper panel of Figure 5.5 shows the signal gain for $n = 40 - 50$. Clusters in this size regime correspond to amorphous, drop-like structures.[87,89,177,178] All four datasets are consistent with a linear dependence of the signal gain on the pulse energy. The signal gain for vibrational excitation by $3400\,\mathrm{cm}^{-1}$ photons is larger than for excitation by $3200\,\mathrm{cm}^{-1}$ radiation, which is in agreement with the corresponding absorption cross sections of amorphous clusters.[71] An increase in the delay time results in a decrease of the signal gain, which is more pronounced for excitation at $3400\,\mathrm{cm}^{-1}$. The signal gain ratio of excitation at $3400\,\mathrm{cm}^{-1}$ and $3200\,\mathrm{cm}^{-1}$ appears to remain constant over the IR laser pulse energy range presented here.

For $n = 250 - 300$, the signal gain increases linearly for excitation at $3200\,\mathrm{cm}^{-1}$. Irradiation with $3400\,\mathrm{cm}^{-1}$ photons yields a signal saturation and a stronger decay of the signal with increasing Δt and E_{IR}. So, the signal gain intensity behaves differently for $\tilde{\nu} = 3200\,\mathrm{cm}^{-1}$ and $3400\,\mathrm{cm}^{-1}$ and therefore might indicate the presence of two distinctly different types of cluster. Note that for $\mathrm{Na(H_2O)}_n$ with $n = 250 - 300$ an increasing signal gain around $3200\,\mathrm{cm}^{-1}$ has been reported and assigned to the presence of crystalline clusters formed at similar expansion conditions.[71]IV

For $\mathrm{Na(H_2O)}_n$ clusters with $n = 400 - 450$—for which the presence of crystalline clusters was also reported at similar cluster preparation conditions[37,71]—the E_{IR}-dependent data for excitation at $3200\,\mathrm{cm}^{-1}$ and at $3400\,\mathrm{cm}^{-1}$ show different trends: Vibrational excitation at $3400\,\mathrm{cm}^{-1}$ causes a decreasing signal for both $\Delta t = 12\,\mathrm{ns}$ and $200\,\mathrm{ns}$ with increasing E_{IR}. This could indicate that successive absorption of multiple photons causes the E_{IR}-dependent decrease.[110] In contrast to this, the IR-induced signal gain for excitation at $3200\,\mathrm{cm}^{-1}$ remains nearly unchanged with increasing E_{IR} and is only slightly reduced with increasing Δt. This is consistent with the temporal evolution of the $3200\,\mathrm{cm}^{-1}$ data shown in the previous section and could indicate a coexistence of crystalline and amorphous clusters.

Comparing the E_{IR}-dependence of the signal gain for excitation at $3400\,\mathrm{cm}^{-1}$ for small ($n = 40 - 50$) and large ($n = 400 - 450$) clusters, it is observed that it decreases with increasing E_{IR} for the large cluster fraction but increases for the small clusters. If the signal of smaller clusters would increase at the expense of the ion signal of larger clusters, it should increase with increasing delay time. This is not observed as the IR-induced signal decreases with increasing Δt for all cluster sizes

IV The barometer used by Pradzynski[90] and Forck[139] was observed to measure erroneous reservoir pressures. I suppose that this defect persisted for a long time and therefore I chose a reservoir pressure of $p_{\mathrm{stag}} = 3.7 \pm 0.1\,\mathrm{bar}$ instead of 3.9 bar (see Figure A.6 on page 131 in the appendix) in order to obtain expansion conditions comparable to those in [71].

and IR laser pulse energies. Therefore, it can be concluded that the exponential decay of the Δt-dependent signal gain does not cause an IR-induced tilting. The difference in the energy dependence between excitation at $3200\,\mathrm{cm}^{-1}$ and $3400\,\mathrm{cm}^{-1}$ shown in Figure 5.5 may indicate the coexistence of crystalline and amorphous clusters at large cluster sizes. This is consistent with the interpretation of the delay time dependence of the signal gain shown above: While the amorphous clusters tend to evaporate water molecules or eject fragments more easily,[230] the signal of crystalline clusters remains less affected. This could be due to a change of the absorption spectrum caused by a crystalline-to-amorphous melting transition,[224] which should reduce the absorption cross section of melting clusters at $3200\,\mathrm{cm}^{-1}$ and therefore could prevent heating to evaporative ensemble conditions.

5.4 Time-resolved spectroscopy of $Na(H_2O)_n$ clusters

Since the IR-induced signal gain depends on Δt, E_{IR}, and $\tilde{\nu}$ the necessity for cluster size and delay time-resolved vibrational spectra is apparent. These were measured for $\Delta t = 12\,\mathrm{ns}$ and $200\,\mathrm{ns}$ with high or low E_{IR} at otherwise identical experimental conditions. The clusters were formed in helium-seeded supersonic expansions of $2.7\,\mathrm{bar}$ water vapor at a stagnation pressure of $3.7 \pm 0.1\,\mathrm{bar}$ and ionized by $3.22\,\mathrm{eV}$ photons. The IR laser pulse energies were in the range of $E_{\mathrm{IR}} = 8 - 15\,\mathrm{mJ}$ for $\tilde{\nu} = 2800 - 3550\,\mathrm{cm}^{-1}$. The spectral resolution was $10\,\mathrm{cm}^{-1}$. An exception was made in the range of the dangling OH oscillator (dOH) peak around $3700\,\mathrm{cm}^{-1}$ where mass spectra were measured every $5\,\mathrm{cm}^{-1}$.

5.4.1 Spectra at high-E_{IR} conditions

The normalized signal gain spectra of various cluster size ranges for $\Delta t = 12\,\mathrm{ns}$ and $200\,\mathrm{ns}$ at high-E_{IR} conditions are shown in Figures 5.6 and 5.7. In all spectra, a broad absorption pattern and a well separated peak around $3700\,\mathrm{cm}^{-1}$ are observed. The latter corresponds to the absorption of dOH oscillators, the broad signal gain peak in the range of $2900 - 3600\,\mathrm{cm}^{-1}$ to bonded OH oscillators, see Section 2.4.2. The gradually downshifting peak position of the bonded OH peak with increasing cluster size is typically assigned to a transition from amorphous (see spectra for $n \leq 150$) to crystalline clusters ($n \geq 300$)[37,71,81] and can be caused by either a growing fraction of crystalline clusters[21] or an increasing crystallinity within the

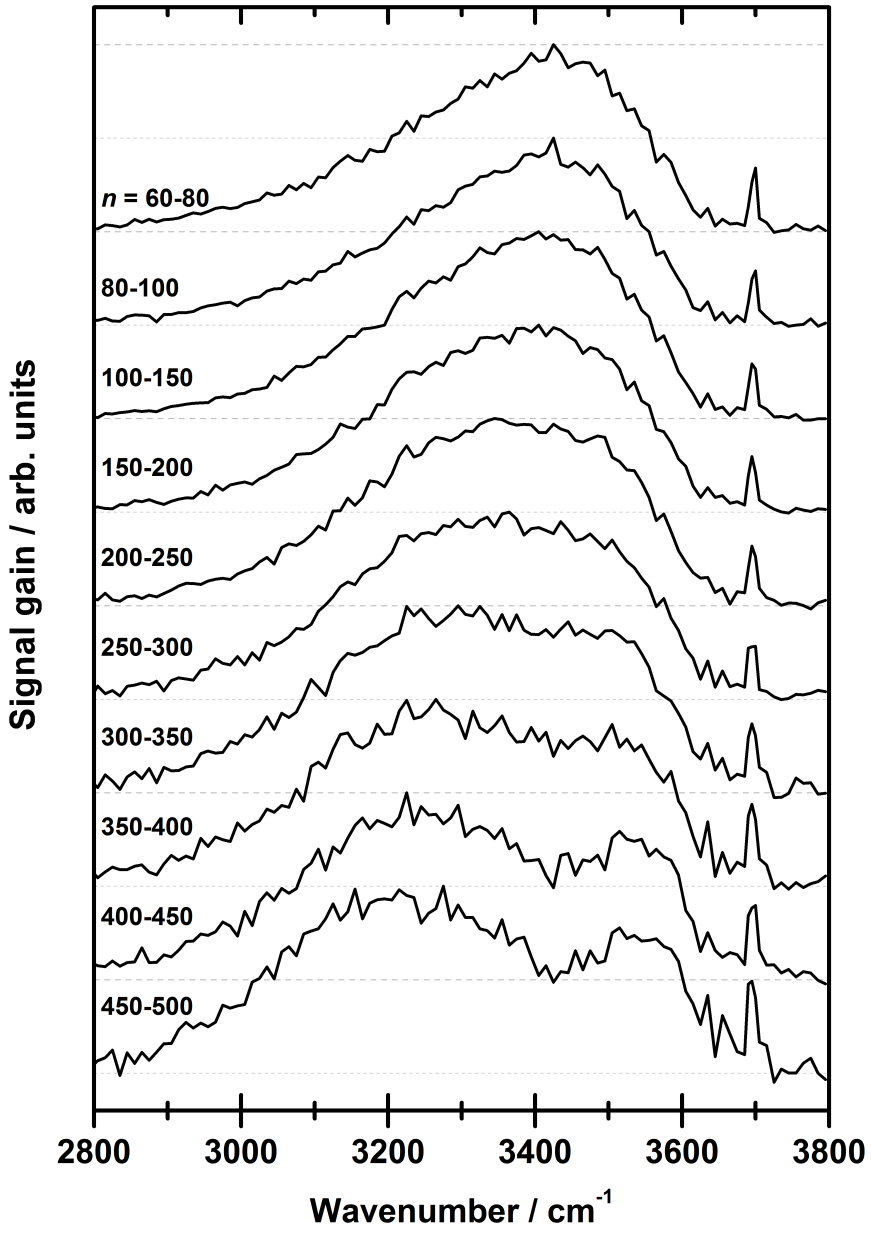

Figure 5.6: Normalized vibrational spectra of $Na(H_2O)_n$ clusters. The spectra were measured at $\Delta t = 12\,\text{ns}$ and are averaged from three scans at identical experimental parameters.

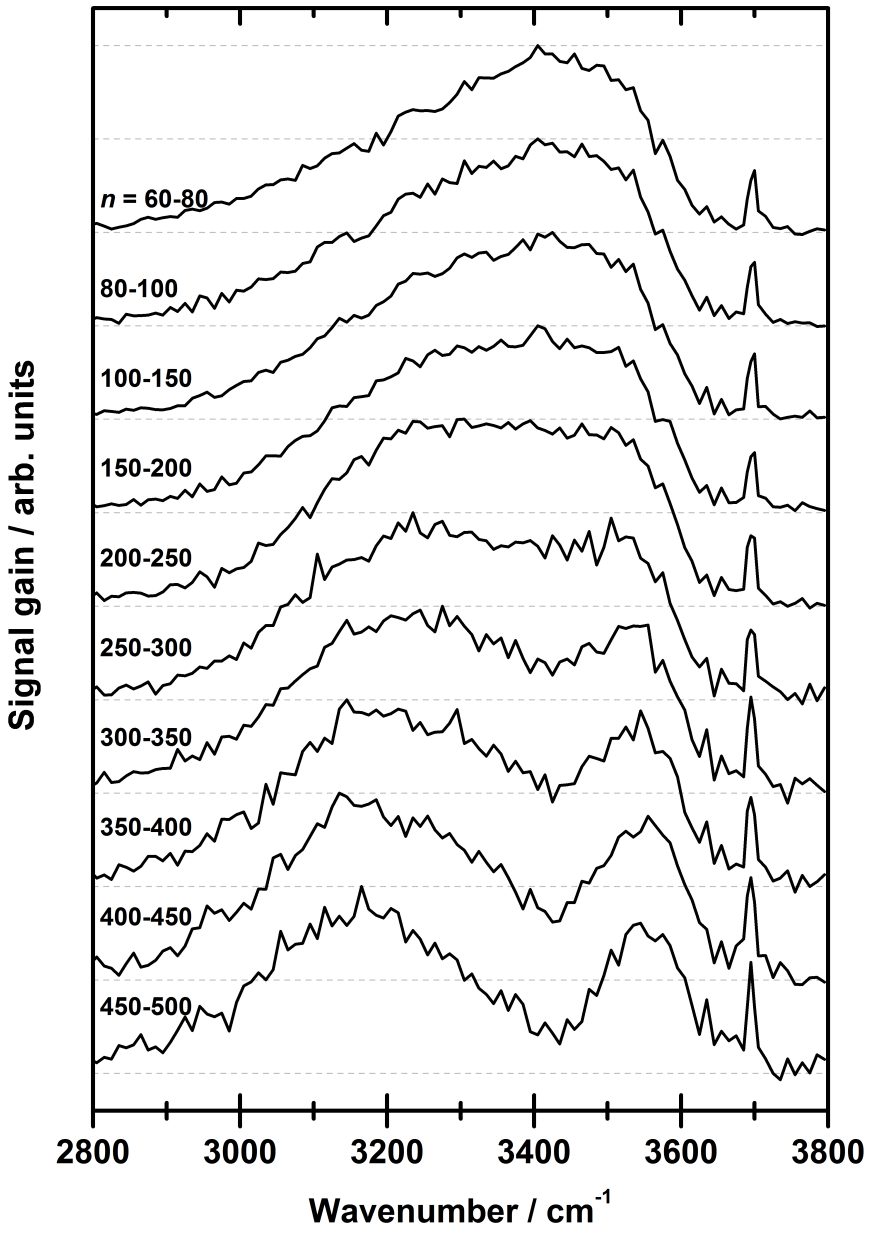

Figure 5.7: Normalized vibrational spectra of $Na(H_2O)_n$ clusters measured at $\Delta t = 200\,\text{ns}$. All other experimental parameters are identical to those used for the measuring the spectra of Figure 5.6.

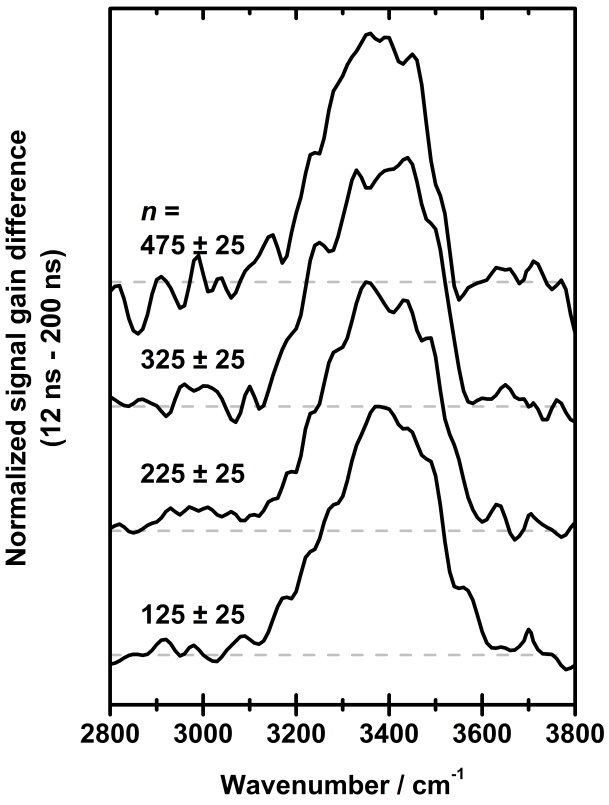

Figure 5.8: Difference spectra of the unscaled vibrational spectra with $\Delta t = 12\,\text{ns}$ and the corresponding spectra measured with $\Delta t = 200\,\text{ns}$. The difference spectra were smoothed by a threefold applied weighted average of adjacent data points (25%-50%-25%) and normalized to the maximum intensity. The grey dashed lines mark the baselines. The spectra are each offset by 0.5 for clarity.

clusters.[16]

The vibrational spectra measured at $\Delta t = 12\,\text{ns}$ and 200 ns for $\text{Na}(\text{H}_2\text{O})_{n=60-500}$ are strikingly similar regarding the observed shift of the maximum intensity from $3400\,\text{cm}^{-1}$ to $3200\,\text{cm}^{-1}$ with increasing cluster size, see Figures 5.6 and 5.7. At around $3400\,\text{cm}^{-1}$ a decreasing intensity with increasing cluster size is observed. This broad dip is more pronounced in the spectra taken at 200 ns, and is therefore related to the Δt-dependent decay of the IR-induced signal gain described above. In order to test if only amorphous clusters are affected by the decay, a spectrum of the decaying species is required. The raw, unscaled spectra of the 200 ns dataset are subtracted from the 12 ns spectra, which yields difference spectra, see Figure A.3 on page 128 in the appendix. Normalized difference spectra are shown in Fig-

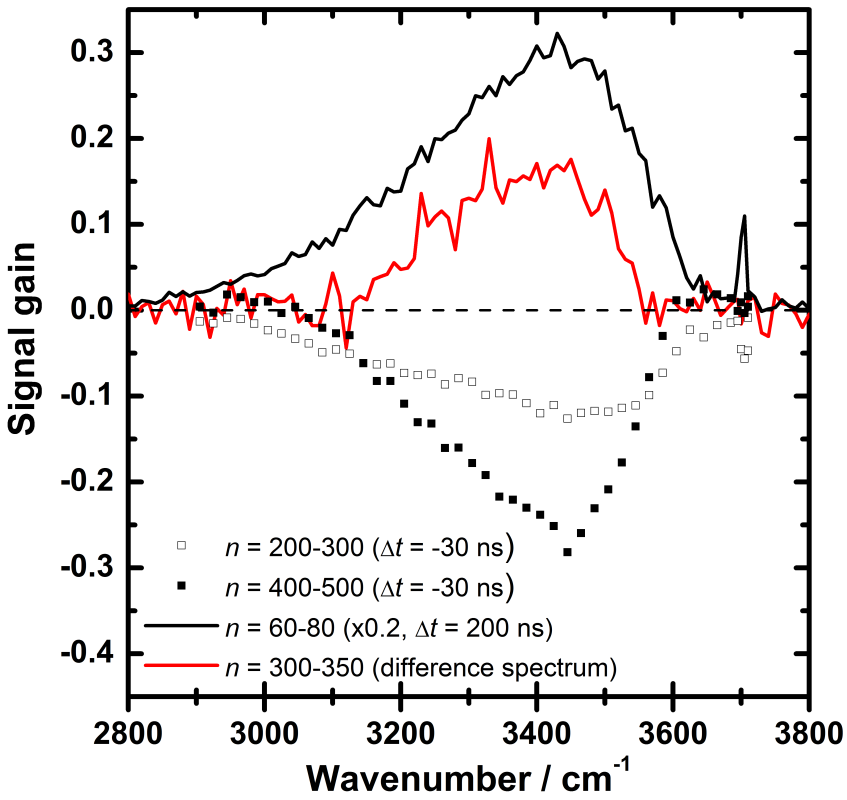

Figure 5.9: Comparison of the difference spectrum of the delay times 12 ns and 200 ns (shown in red), the signal gain spectrum of $n = 60 - 80$ (black, scaled by 0.2, $\Delta t = +200$ ns), and the depletion spectra of $n = 200 - 300$ and $n = 400 - 500$ of $Na(H_2O)_n^+$ cluster cations ($\Delta t = -30$ ns, open and filled black squares). All clusters were ionized with a photon energy of 3.22 eV.

ure 5.8. These spectra were smoothed by a threefold application of a weighted average of 25%-50%-25% type in order to reduce the noise and highlight the robust signal. The difference spectra show that the spectral response of the decaying species is similar for all cluster sizes, see Figure 5.8. The component corresponding to the decaying signal has a broad intensity peak between $\tilde{\nu} = 3180\,\mathrm{cm}^{-1}$ and $3560\,\mathrm{cm}^{-1}$ with a maximum at around $3400\,\mathrm{cm}^{-1}$. While the peak position corresponds to that of amorphous clusters[37,71] the overall peak shape is different, see Figure 5.9. The signal gain spectrum of amorphous $Na(H_2O)_{n=60-80}$ clusters has signal intensity over a broader range of IR frequencies than the obtained difference spectra. The crucial difference between the difference spectrum (red in Figure 5.9) and the signal gain spectrum measured at $\Delta t = 200$ ns (black) is the reduced in-

tensity at frequencies related to surface bound water molecules ($\tilde{\nu}_{\mathrm{DAA}} \leq 3150\,\mathrm{cm}^{-1}$, $\tilde{\nu}_{\mathrm{DDA}} = 3550-3630\,\mathrm{cm}^{-1}$, $\tilde{\nu}_{\mathrm{dOH,DAA}} \approx 3700\,\mathrm{cm}^{-1}$; see Section 2.4.2) in the difference spectrum.

A comparison of the depletion spectra of cluster cations generated from neutral clusters with IE $\leq 3.22\,\mathrm{eV}$ and the temporal difference signal of the signal gain spectra is also given in Figure 5.9. The spectrum of $\mathrm{Na(H_2O)}^+_{n=200-300}$ is similar to spectra of amorphous clusters. For larger cluster sizes the depletion spectrum is similar to the difference spectrum, with low intensity of surface bound molecules. Both spectra of the cationic clusters indicate that they belong to amorphous clusters. Whether the depletion spectra are caused by monomer evaporation or cluster fission cannot be determined from this experiment. Note that IRMPD of $(\mathrm{H_2O})_n$ revealed that fragmentation can occur by ejection of cluster fragments with at least up to 9 molecules.[230,231]

The difference spectrum and the depletion spectrum of the larger cations have narrowed bonded-OH peak shapes compared to the signal gain spectrum of amorphous clusters but in agreement with the peak position of amorphous clusters. From this can be deduced that the decay occurs if the absorption of several photons by a cluster occurs.

From the data presented above, it can be concluded that the signal gain spectra measured at $\Delta t = 12\,\mathrm{ns}$ and 200 ns (see Figures 5.6 and 5.7) are distorted in the range of the peak position of amorphous clusters due to the a decay of the IR-induced signal gain, which corresponds to a decreasing fraction of clusters with a solvated sodium atom. Vibrational spectra of $\mathrm{Na(H_2O)}_n$ clusters at $\Delta t = 80\,\mathrm{ns}$ and lower IR laser pulse energies ($E_{\mathrm{IR}} = 5-10\,\mathrm{mJ}$) were obtained by Pradzynski et al.[71] Figure 5.10 shows these spectra, which were presented in [71, 90]. All spectra show at least one broad peak in the region of bonded OH-stretch oscillators and a small peak around $3700\,\mathrm{cm}^{-1}$, corresponding to the vibration of the dangling OH;[16,19,20,71] and therefore are in agreement with those presented in this work. The spectra were smoothed ten times by a weighted three-point average (25%-50%-25%).[90] For $n \leq 250$, the peak position is around $3400\,\mathrm{cm}^{-1}$. The maximum intensity of larger clusters with $n \geq 300$ is shifted to $\tilde{\nu} < 3300\,\mathrm{cm}^{-1}$. A transition between these two cases occurs at $n = 275 \pm 25$ and was therefore assigned as the "onset of crystallization" (Pradzynski et al.[71]), see red spectrum in Figure 5.10. In this spectrum the peak position is slightly downshifted and an increasing intensity at around $3200\,\mathrm{cm}^{-1}$ is observed when compared to the spectra of amorphous clusters. The spectra assigned to amor-

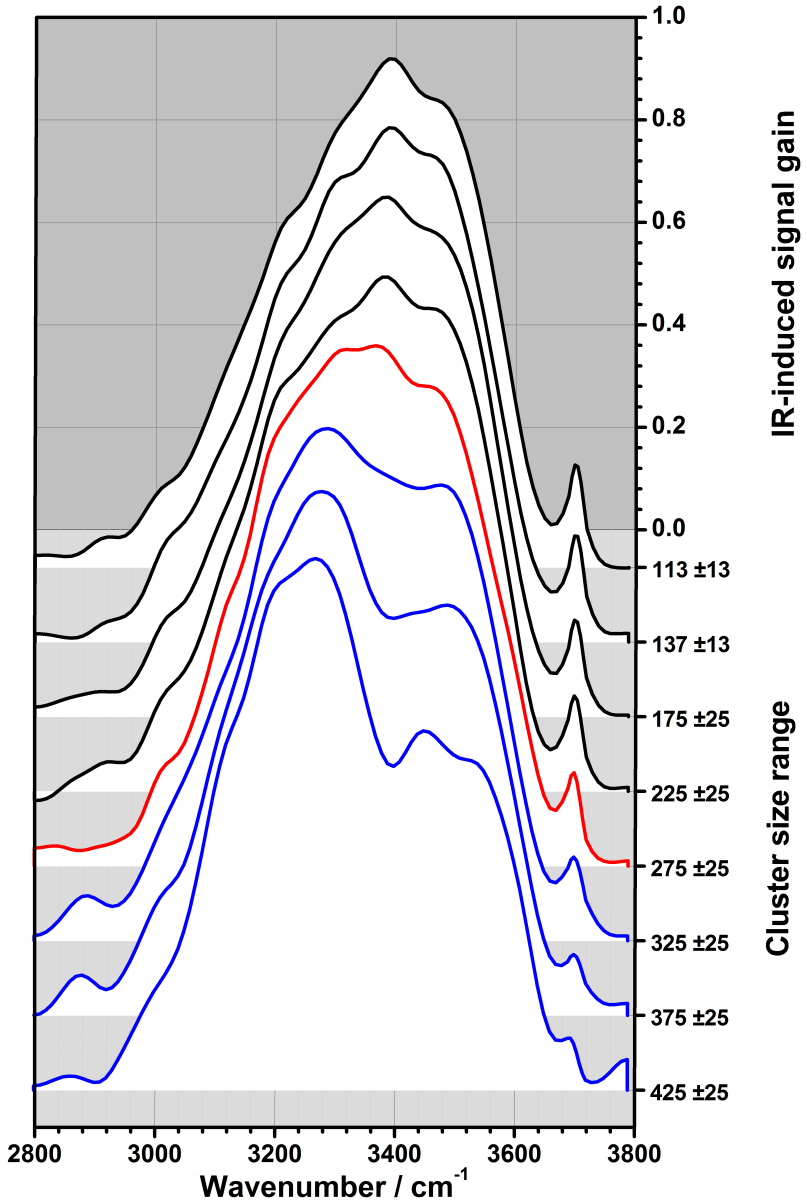

Figure 5.10: Spectra of $Na(H_2O)_n$ clusters. The spectra were measured at the following conditions: $\Delta t \approx 80\,\text{ns}$, $\lambda_{UV} = 390\,\text{nm}$ (3.18 eV), 2.7 bar water vapor seeded with He at $p_{\text{stagnation}} = 3.9 \pm 0.1\,\text{bar}$. The red trace marks the spectrum of $Na(H_2O)_{275\pm25}$, the smallest cluster size range Pradzynski et al.[71] concluded to indicate the presence of crystalline clusters. Black spectra were assigned to the presence of amorphous clusters, blue spectra to the presence of crystalline clusters.[71] Data taken from references [71]. Reprinted with permission from AAAS.

phous clusters are shown as black traces and the spectra with gradually downshifted absorption maxima are shown in red and blue. The spectra of large cluster sizes from Pradzynski et al.[71] feature a slight dip at $3400\,\mathrm{cm}^{-1}$ and therefore are still affected by the decay stated above, see blue traces in Figure 5.10. However, the depletion is reduced compared to the spectra shown in Figures 5.6 and 5.7. In all three cases, the signal at $3200\,\mathrm{cm}^{-1}$ is rather robust and the downshift occurs in the cluster size range of $n = 200 - 300$. Therefore it can be concluded that the signal gain around $3200\,\mathrm{cm}^{-1}$ indicates the abundance of crystalline clusters in all cases. In agreement to this, the decaying signal influences the spectra for $\tilde{\nu} \leq 3200\,\mathrm{cm}^{-1}$ only marginally, see Figure 5.8.
Differences between the spectra of Pradzynski et al.[71] and the spectra of this work can be caused by several reasons: With regard to the Δt used, the spectra of Pradzynski et al.[71] are an intermediate case whereas the used IR laser pulse energies were lower ($E_{\mathrm{IR}} = 5 - 10\,\mathrm{mJ}$).[90] Possible changes of the expansion conditions —either in terms of different backing pressures in the expansion chamber or in terms of a miscalibrated barometer in the seeding line— could have affected the cooling rate in the supersonic expansion. Besides these differences, the more recent spectra were measured with an improved signal-to-noise ratio, which should result from the new measurement mode[203] as well as the higher ion signal in the mass spectra used during the measurements of this work, which was at least a factor of 3 higher than that of Pradzynski et al.[71]

5.4.2 Spectra at low-E_{IR} conditions – vibrational spectra of $Na(H_2O)_n$ with reduced distortion

The results shown in Sections 5.2, 5.3, and 5.4.1 revealed that the signal gain spectra of large $Na(H_2O)_n$ clusters are distorted. The signal gain spectra indicate the decay of amorphous clusters, depending on Δt and the IR pulse energy. From this follows that pure signal gain spectra of $Na(H_2O)_n$ could be obtained in the limit of short delay times and reduced IR pulse energies.
Figure 5.11 shows spectra measured at the same expansion conditions as the spectra shown in Section 5.4.1, but with different IR laser pulse operation parameters ($\Delta t = 12\,\mathrm{ns}$, $E_{\mathrm{IR}} = 5 - 8\,\mathrm{mJ}$ instead of $10 - 15\,\mathrm{mJ}$). At even lower IR laser pulse energies, the Δt-dependent reduction of the signal gain was minimized, but test measurements indicated rather noisy vibrational spectra. Therefore measuring spectra

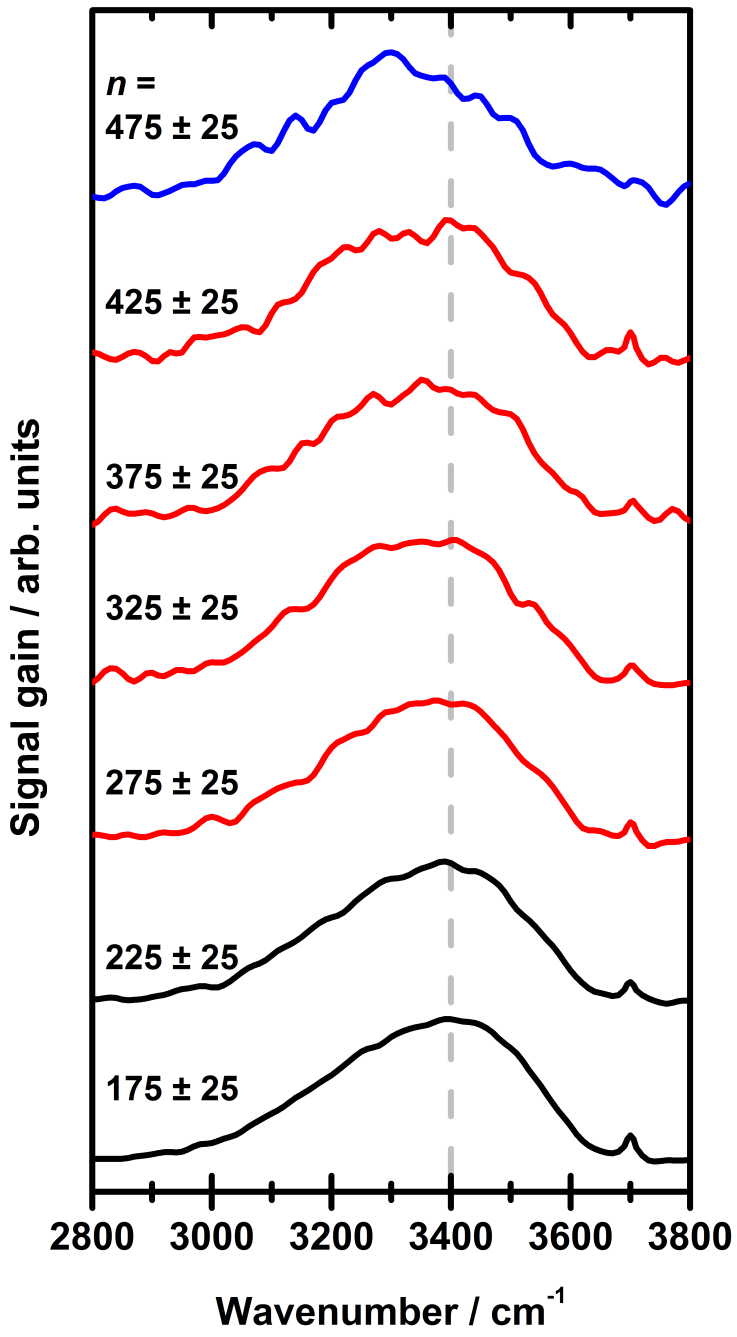

Figure 5.11: Vibrational spectra of $Na(H_2O)_n$ with reduced distortion; $\Delta t = 12\,\mathrm{ns}$, $E_{\mathrm{IR}} \approx 6\,\mathrm{mJ}$. The spectra were smoothed three times by a weighted three-point average of a 25%-50%-25% type.

at $E_{IR} = 5 - 8\,mJ$ showed to be a compromise as the decay was not to strong compared to larger pulse energies (see Figure A.4 on page 129 in the appendix) and sufficiently large ion count rates were obtained. The vibrational spectra were smoothed by threefold application of a weighted average of 25%-50%-25% type.
For all spectra, again, a broad absorption in the absorption range of hydrogen bonded water molecules and an isolated peak around $3700\,cm^{-1}$ are observed. While the spectra of $n = 175 \pm 25$ and 225 ± 25 indicate the abundance of amorphous clusters (black traces in Figure 5.11), a gradual downshift of the peak absorption occurs for larger cluster sizes. Spectra with broadened peaks and a slight downshift of the maximum intensity are now obtained for a broad range of cluster sizes ($n = 250 - 450$, red traces). The spectrum for $n = 475 \pm 25$ (blue trace) has a peak around $3300\,cm^{-1}$. This distortion-free spectrum of $Na(H_2O)_{475\pm25}$ is strikingly different from those shown in Section 5.4.1. The major differences are the peak position of bonded OH oscillators ($3300\,cm^{-1}$ instead of around $3200\,cm^{-1}$), no dip around $3400\,cm^{-1}$ and no second peak around $3500 - 3600\,cm^{-1}$, compare for instance Figures 5.11 and 5.7.
The shape of the spectra with reduced distortion of $Na(H_2O)_n$ with $n = 250 - 450$ resembles the predicted spectrum of $n = 293$ from Buch et al.[16], compare red spectra of Figure 5.11 with blue spectrum for $n = 293$ in Figure 2.5. Their calculated crystalline cluster isomers were composed of crystalline cluster cores and amorphous-like cluster surfaces.[89] For larger cluster a larger fraction of water molecules was predicted to be in ice-like geometries. Therefore the predicted spectrum for $n = 600$ exhibits a further downshift of the peak position and a narrowed peak shape. The experimental, spectra with reduced distortion for $n = 250-450$ and for $n = 450-500$ are similar to those calculated by Buch et al.[16] but the predicted spectra appear to be offset compared to the experimental spectra by more than $100\,cm^{-1}$. Whereas the calculated spectra of [16] originated from clusters containing water molecules in crystalline and amorphous arrangements, the results in Sections 5.2, 5.3, and 5.4.1 appear to indicate that two different types of clusters are present at sufficiently large cluster sizes. This is also indicated by the FTIR spectra of Manka et al.,[21] who showed that vibrational spectra in the transition region of liquid to crystalline particles, red and orange traces in Figure 5.12, can be reproduced by a combination of the liquid (blue trace) and the crystalline spectrum (middle black trace). The FTIR spectrum shown in orange corresponds to a fraction of ice I of 55%, whereas the red spectrum corresponds to 10% of ice I. Comparing these spectra to the spectrum

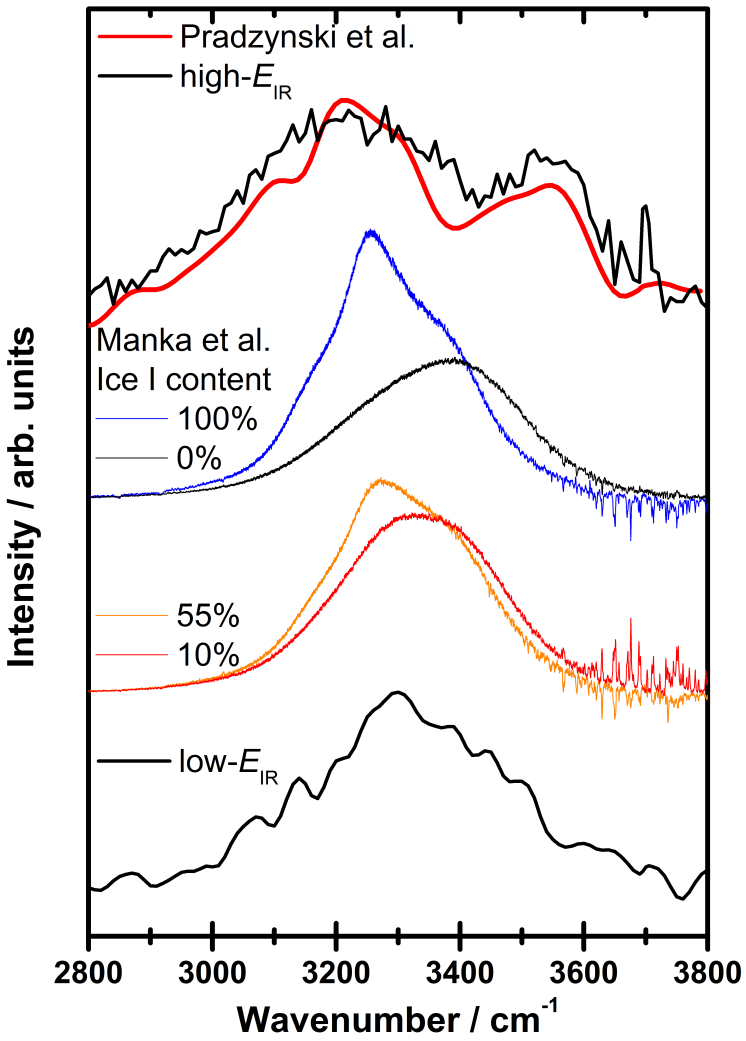

Figure 5.12: Comparison of the spectrum with reduced distortion for $n = 475 \pm 25$ (bottom spectrum) with the FTIR spectra of $\bar{d} = 5.8\,\mathrm{nm}$ water droplets of Manka et al.[21] at various temperatures (upper and lower middle spectra, the spectra were provided by Prof. Barbara Wyslouzil and were published in reference [21]), the vibrational spectrum of $n = 475 \pm 25$ obtained at high-E_{IR} conditions (top spectrum, black) and the corresponding spectrum of Pradzynski et al.[71] (top spectrum red, spectrum taken from [71]).

obtained at low-E_{IR} conditions (bottom black trace) indicates that the low-E_{IR} spectrum corresponds to a signal gain spectrum with contributions from amorphous and crystalline clusters.
The high-E_{IR} spectrum for $n = 475 \pm 25$ (top black trace) and the spectrum of Pradzynski et al.[71] are distorted around $3400\,\mathrm{cm}^{-1}$ due to the decay shown above. Compared to these, the low-E_{IR} spectrum appears to provide a better comparability to IR spectra from other methods, see Figure 5.12. However, in the high-E_{IR} spectra the peak of the crystalline clusters is more dominant, which is consistent with the E_{IR}-dependence of the IR-induced signal gains.

5.5 Detecting crystalline clusters via vibrational spectroscopy

The liquid-to-crystalline phase transition of water can be observed via vibrational spectroscopy methods due to the well separated peak positions of ice I ($\tilde{\nu}_{\mathrm{peak,\,ice\,I}} \approx 3250\,\mathrm{cm}^{-1}$) and amorphous water ($\tilde{\nu}_{\mathrm{peak,\,amorphous}} \approx 3400\,\mathrm{cm}^{-1}$).[187,224] Since the vibrational spectra of size-selected clusters show a gradual transition from amorphous clusters to crystalline clusters with increasing cluster size, the determination of the minimum cluster size required for the formation of stable crystalline nuclei is of ongoing interest.[37,71,81] Possible indicators for this onset of crystallization are:

(I) a broad intensity increase at around $3200\,\mathrm{cm}^{-1}$—also observed as intensity increase for $\tilde{\nu} \leq 3400\,\mathrm{cm}^{-1}$—, which leads to a slightly downshifted bonded OH peak position compared to the spectra of amorphous clusters,[71] or

(II) a downshift of the dangling OH peak by $3 - 4\,\mathrm{cm}^{-1}$.[232]

In this Section, these indicators are used for the interpretation of the spectra of $Na(H_2O)_n$ clusters shown above and discussed with respect to their suitability to provide reliable results. Therefore, the cluster preparation conditions for $Na(H_2O)_n$ clusters were kept constant whereas the IR-UV detection scheme was varied in terms of Δt and E_{IR}.
The smallest cluster size range of each set of spectra that indicates the presence according to indicator (I) is referred to in the following as n_{onset}. Aside from this, the dOH peaks for different cluster sizes are studied by means of Gaussian lineshape fitting in order to test if indicator (II) is applicable or if other dOH peak charac-

teristics correlate with the presence of crystalline clusters. These two approaches, indicators (I) and (II), are further examined in the Sections 5.5.1 and 5.5.2.

5.5.1 Broadening of the bonded OH absorption peak

An increasing intensity for $\tilde{\nu} \leq 3400\,\mathrm{cm}^{-1}$—coinciding with a beginning downshift of the peak position of bonded water molecules—has been concluded to indicate the presence of the smallest crystalline $Na(H_2O)_n$ clusters present in broad cluster distributions.[71] As seen in the previous Section 5.4.2, the spectra of large clusters with $n = 475 \pm 25$ are distorted if obtained with high IR laser pulse energies. However, the spectra in the cluster size region where the onset of crystallization is observed may appear to be not that strongly affected by this distortion. Therefore, in this Section the obtained spectra from high and low-E_{IR} are compared to determine how the observed onset cluster size is affected by the detection scheme.

Pradzynski et al.[71] concluded that a growing fraction of H_2O molecules in crystalline environment within the clusters' interior leads to a gradual downshift of the peak absorption, compare spectra of $n = 225 \pm 25$ and $n = 275 \pm 25$ in upper panel of Figure 5.13. A further increase of the cluster size leads to a downshift of the maximum intensity to $3290\,\mathrm{cm}^{-1}$ for $n = 325 \pm 25$ (blue trace). With further increasing cluster size, a dip around $3400\,\mathrm{cm}^{-1}$ was observed.[71] This was also shown for the spectra of large $Na(H_2O)_n$ clusters obtained at high-E_{IR} conditions, see Figures 5.6 and 5.7 on pages 80 and 81. Considering the results shown in Section 5.4.1, this dip evidently originates from the signal decay of amorphous clusters.

The IRMPD spectra of $La^{3+}(H_2O)_n$ clusters tempered to 133 K from Cooper et al.[81] are shown in the lower panel of Figure 5.13. Here, the transition from amorphous to crystalline clusters is a function of the cluster size, too. The transition region, indicated by broadened spectra and peak positions in the range of $\tilde{\nu} = 3300 - 3400\,\mathrm{cm}^{-1}$, is not as narrow as in the dataset of Pradzynski et al.[71] and ranges from $n = 150 - 350$, see reference [81]. Both sets of spectra in Figure 5.13 show a downshift of the maximum absorption with increasing cluster size. As the IRMPD spectra from Cooper et al.[81] show no distortion caused by the applied detection scheme but the signal gain spectra of $Na(H_2O)_n$ do, the reliability of n_{onset} for this sample system shall be investigated in the following.

The vibrational spectra of $Na(H_2O)_n$ clusters of this work obtained at high-E_{IR} conditions are similar to those of Pradzynski et al.[71] with respect to the smallest cluster size range for which the presence of crystalline clusters is concluded, see Figure 5.14

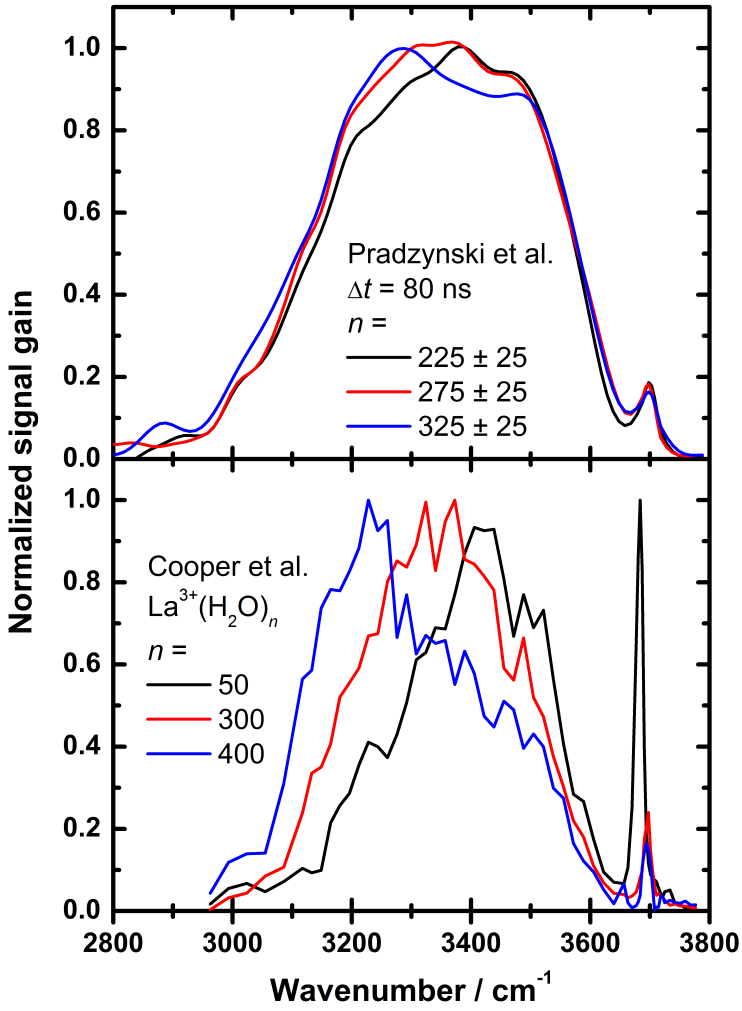

Figure 5.13: Spectra of $Na(H_2O)_n$ clusters (upper panel)[71,90] and $La^{3+}(H_2O)_n$ clusters (lower panel)[81] showing a red-shift of the maximum absorption with increasing cluster size. The spectra of $Na(H_2O)_n$ were taken from references [71]. The spectra of $La^{3+}(H_2O)_n$ were provided by Richard Cooper, Ph.D., and were published in reference [81].

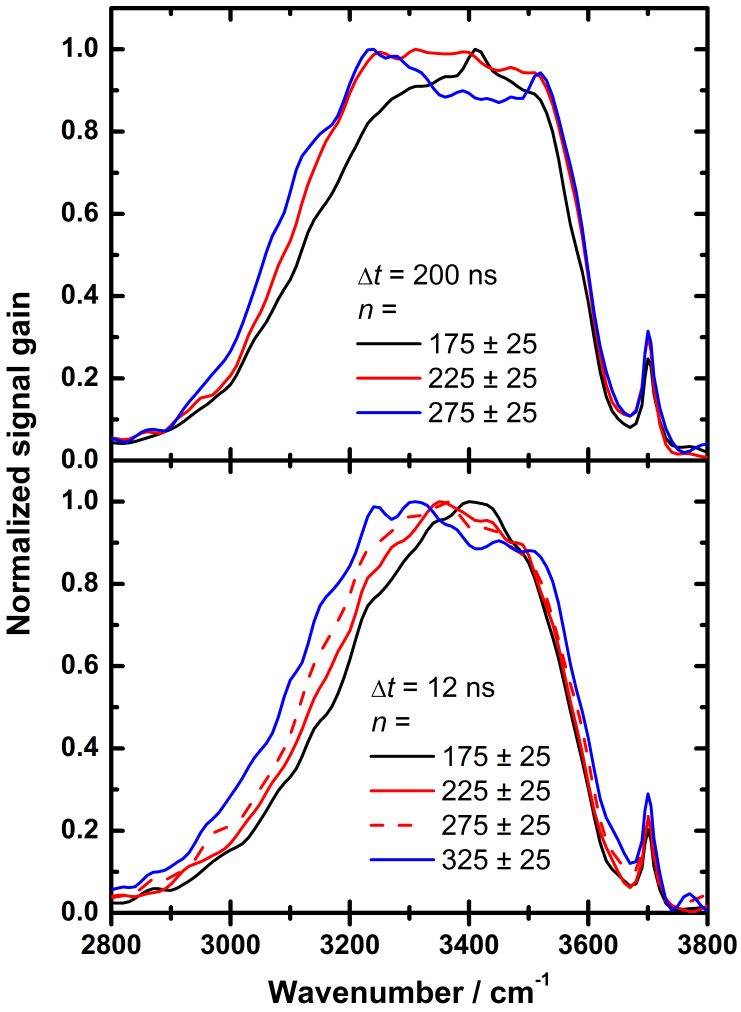

Figure 5.14: Spectra of $Na(H_2O)_n$ clusters measured at $\Delta t = 12\,ns$ and $200\,ns$, see Section 5.2 or reference [221]. The spectra show a down shift of the maximum absorption with increasing cluster size similar to the spectra of Figure 5.13. The spectra were smoothed three times to reduce the noise level and normalized in order to highlight the shift of the maximum intensity.

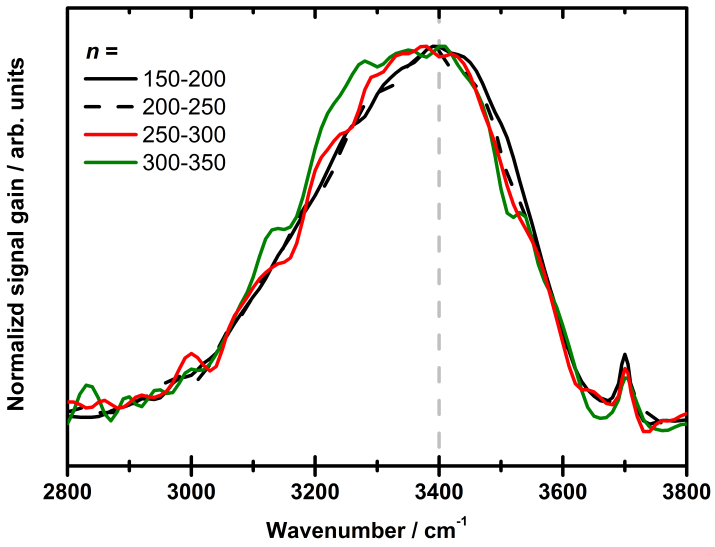

Figure 5.15: Spectra with reduced distortion for $n = 150 - 350$. The spectra were smoothed three times by a weighted three-point average of 25%-50%-25% type.

and compare to Figure 5.13. Evaporation from amorphous clusters was concluded to reduce the cluster temperature and thus the amount of low-IE clusters in which the sodium atom is solvated. This causes an increasing distortion of the spectra of clusters with $n \geq 300$ due to a broad dip around $3400\,\mathrm{cm}^{-1}$ on the timescale of tens of nanoseconds, see Section 5.2. The spectra presented in Figure 5.14 were measured at 12 ns and 200 ns. Consequently, the spectra with $\Delta t = 200\,\mathrm{ns}$ deviate from those with shorter delay times as the signal decay shown above has progressed farther and thus causes a plateau-like shape of the spectra, contrast both blue or both red spectra in Figure 5.14. Despite this distortion of the spectra, the transition from amorphous to crystalline clusters is observed in the same cluster size region $n = 175 \pm 25 \rightarrow n_{\mathrm{onset}} = 225 \pm 25$, which is close to the cluster size with a beginning crystallization determined by Pradzynski et al.[71] and shown in the upper panel of Figure 5.13 ($n = 225 \pm 25 \rightarrow n_{\mathrm{onset}} = 275 \pm 25$).

The onset of crystallization can also be concluded from the vibrational spectra with reduced distortion by an increasing signal gain intensity for $\tilde{\nu} \leq 3400\,\mathrm{cm}^{-1}$ and a gradual shift of the peak position, see Figure 5.15: The spectrum of $n = 175 \pm 25$ (black trace) resembles the spectra of amorphous clusters. The gradual peak shift due to an intensity increase below $3400\,\mathrm{cm}^{-1}$ with increasing cluster size is observed for $n = 225 \pm 25 \rightarrow n_{\mathrm{onset}} = 325 \pm 25$. The spectrum for $n = 325 \pm 25$, green trace

in Figure 5.15, shows an increased signal intensity in for $\tilde{\nu} \leq 3400\,\mathrm{cm}^{-1}$ and therefore indicates the presence of crystalline clusters.[71] The spectrum of $n = 275 \pm 25$ exhibits a broadened and slightly downshifted bonded OH peak which may also indicate the onset of crystallization.[71] From this can be concluded that application of indicator (I) to the vibrational spectra with reduced distortion indicates the presence of crystalline clusters for $n_{\mathrm{onset}} = 250 - 350$ and therefore at slightly larger cluster size ranges than observed in the spectra obtained at high-E_{IR} conditions.
The major difference of the spectra shown in Figures 5.14 and 5.15 is that the spectra with reduced distortion show much larger contributions of amorphous clusters. This can be explained by the E_{IR} dependency of the IR-induced signal gain for clusters in this cluster size regime: For larger clusters the signal gain obtained at $\tilde{\nu} = 3200\,\mathrm{cm}^{-1}$ appears to be not saturated whereas it is for $3400\,\mathrm{cm}^{-1}$, see Figure 5.5 on page 77 in Section 5.3. From this can be concluded that an increasing laser pulse energy E_{IR} leads to an increasing IR-induced ion signal for $\tilde{\nu} = 3200\,\mathrm{cm}^{-1}$ but not for $3400\,\mathrm{cm}^{-1}$. Based on this it could be deduced that—at high-E_{IR} conditions—the intensity related to crystalline clusters is increased relative to the signal gains obtained for amorphous clusters.
In conclusion, the cluster size range for which the presence of crystalline clusters is concluded from vibrational spectra can depend on the detection scheme, namely the IR laser pulse parameters Δt and E_{IR}. All applied detection schemes indicate that crystalline clusters are present for the cluster size range $n = 275 \pm 25$, but an estimate of the uncertainty of this value including at least on adjacent cluster size appears to be reasonable.
In contrast to this, the cluster size for which the peak absorption is downshifted close to the peak position of ice I, n_{crystal}, is affected by the detection scheme to a larger extent.

5.5.2 Signal of the free OH oscillators

Peaks of the dOH stretch vibration from the spectra of $\mathrm{Na}(\mathrm{H_2O})_n$ clusters measured in this work are shown in Figure 5.16. The spectral resolution in the range of the dOH peak was $5\,\mathrm{cm}^{-1}$, the bandwidth of the used IR laser system[215] $3.7\,\mathrm{cm}^{-1}$. The signal gain data were normalized to the integrated intensity in the range $2800 \leq \tilde{\nu} \leq 3150\,\mathrm{cm}^{-1}$. This range was chosen as it is neither distorted by the exponential decay shown above, see Figure 5.8 on page 82, nor did the IR pulse energy fluctuate due to IR absorption of water vapor in the laboratory air, which is

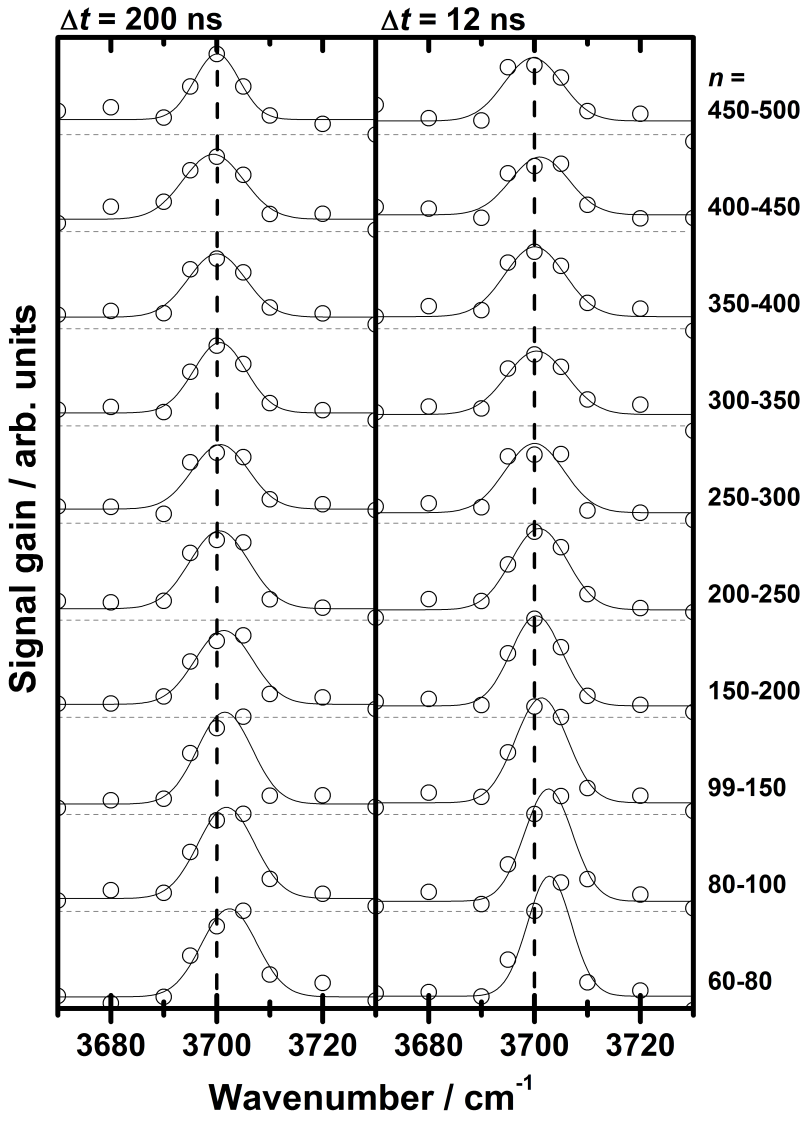

Figure 5.16: Spectra of Figures 5.6 and 5.7 scaled to the same integrated intensity for $2800 \leq \tilde{\nu} \leq 3150\,\mathrm{cm}^{-1}$. The offset between the spectra is +0.05. The dashed lines show the corresponding baselines. The solid lines are the fitted Gaussian peak profiles. The black dashed lines mark $\tilde{\nu} = 3700\,\mathrm{cm}^{-1}$.

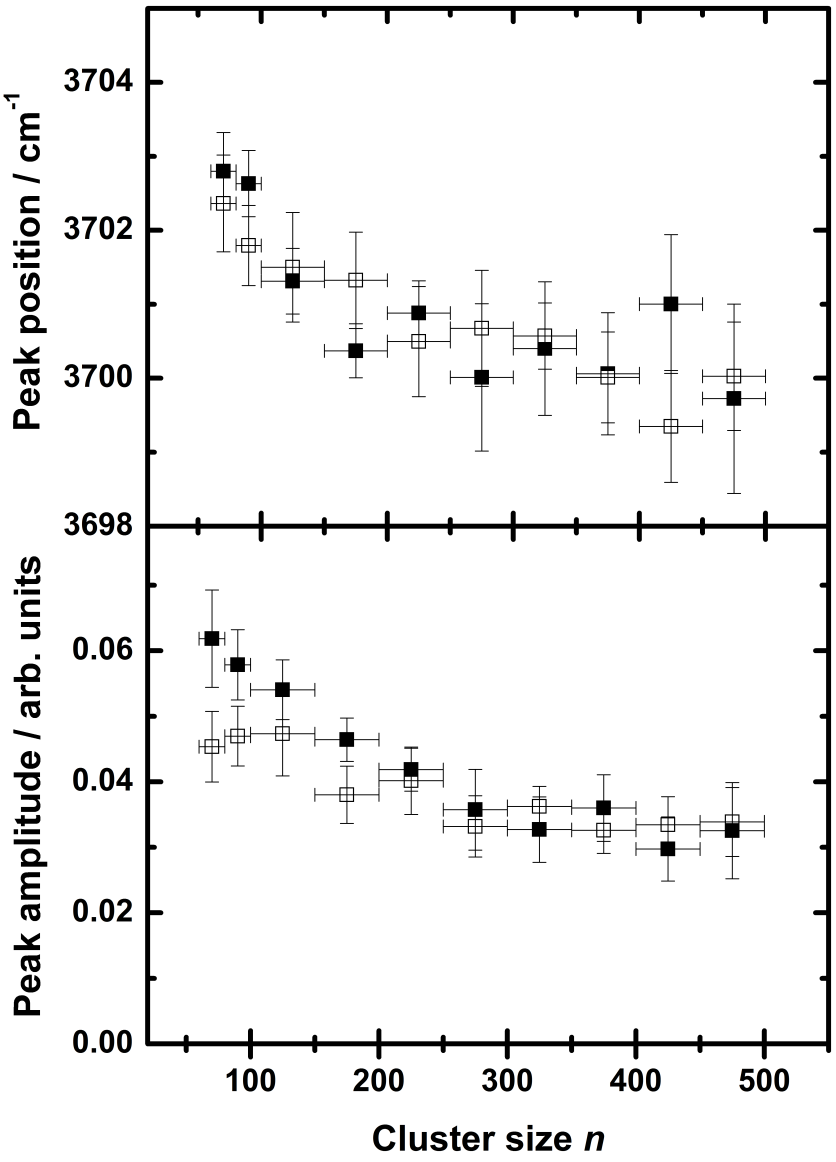

Figure 5.17: The dOH peak positions $\tilde{\nu}_{\mathrm{dOH}}$ and the peak amplitude as determined by Gaussian lineshape fitting, see Figure 5.16. The filled symbols correspond to data obtained at $\Delta t = 12\,\mathrm{ns}$, open symbols to those obtained at $\Delta t = 200\,\mathrm{ns}$. The abscissa error bars correspond to the margins of the binned cluster size ranges, the ordinate error bars to the standard errors obtained from the fitting procedure.

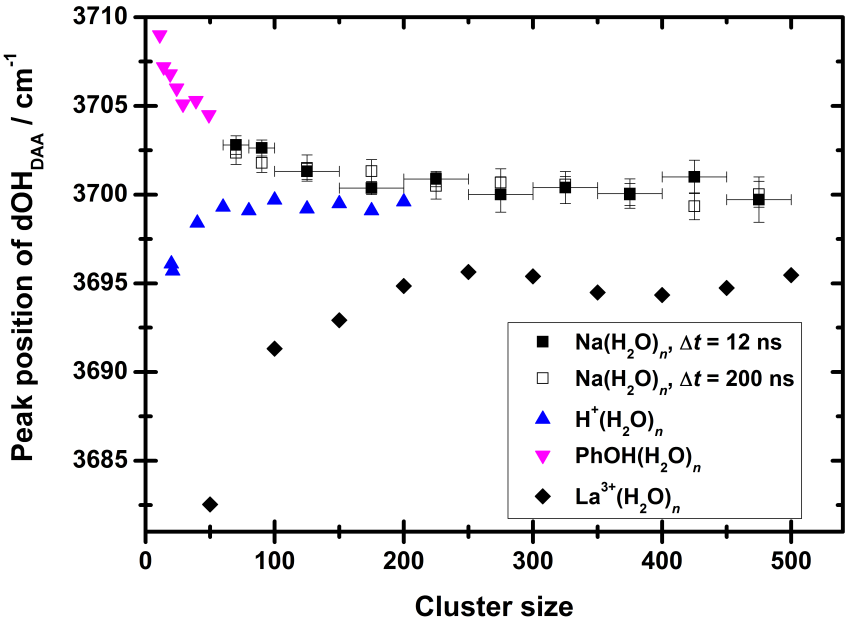

Figure 5.18: Comparison of the dOH peak positions of chromophore or charge labelled water clusters. Squares: data of this work for $Na(H_2O)_{n=60-500}$ (see Figure 5.17). Pink triangles: neutral phenol water clusters $PhOH(H_2O)_{n=11-49}$.[29] Blue triangles: protonated water clusters $H^+(H_2O)_{n=20-200}$.[20] Black diamonds: $La^{3+}(H_2O)_{n=50-500}$ clusters.[81] Figure inspired by reference [20].

the case in the high energy part of the spectrum, compare right panel in Figure 3.3 on page 41. For both delay times of $\Delta t = 12\,\text{ns}$ and 200 ns, the dOH band appears to be downshifted by a few cm^{-1} with increasing cluster size: Whereas the point with highest intensity is at $3705\,\text{cm}^{-1}$ for $n \leq 100$, it is downshifted with increasing cluster size, see Figure 5.16. Gaussian lineshape regressions were applied in order to give estimates on cluster size related properties such as a gradual cluster size dependent shift of $\tilde{\nu}_{\text{peak}}$.[20,29]

The measured signal gains are shown as circles in Figure 5.16. The solid lines are Gaussian lineshape regressions obtained via OriginPro 8.5G (OriginLab, Northampton, MA) obeying the formula

$$I(\tilde{\nu}) = I_0 + A \exp\left(-\frac{(\tilde{\nu} - \tilde{\nu}_{\text{peak}})^2}{2w^2}\right) \tag{5.6}$$

Here, $I(\tilde{\nu})$ marks the signal gain intensity, I_0 an offset, A the peak amplitude, $\tilde{\nu}_{\text{peak}}$ the peak position, and w the width parameter of the Gaussian lineshape. The rela-

tion between w and the FWHM of the peak is given as $w = \mathrm{FWHM}/(2\sqrt{\ln(4)})$. The obtained dOH peak positions and the peak amplitudes are shown in Figure 5.17. The peak position for spectra measured at 12 ns and at 200 ns decreases from $3703\,\mathrm{cm}^{-1}$ for $n = 70 \pm 10$ to $3700\,\mathrm{cm}^{-1}$ for $n \geq 275 \pm 25$. The dOH peak position and the peak amplitude appear to level off for $n \geq 250$. Note that the presence of crystalline clusters has been concluded in this cluster size range from the spectra of the bonded OH oscillators, see Section 5.5.1 and [71].

A comparison of the dOH peak positions from the spectra of $PhOH(H_2O)_n$,[29] $H^+(H_2O)_n$,[20] and $La^{3+}(H_2O)_n$[81] clusters shows that the dOH peak position is a cluster size dependent property for a variety of water clusters and levels off to constant values for each cluster type, see Figure 5.18. The values for $PhOH(H_2O)_n$ were taken from reference [29], those of $H^+(H_2O)_n$ from [20]. The peak positions of $La^{3+}(H_2O)_n$ from Cooper et al.[81] were determined from Gaussian regressions of spectra, which were scaled via the same routine as applied to the spectra of $Na(H_2O)_n$. The spectra were provided by Richard Cooper, Ph.D.

Neutral $PhOH(H_2O)_{n\leq 49}$ and $Na(H_2O)_{n\leq 225\pm 25}$ clusters show a decreasing peak position with increasing cluster size. This downshift with increasing cluster size reveals a weakening of the dOH bond, which is caused by strengthened hydrogen bonds and the coinciding decrease of electron density in the vicinity of the oxygen atoms in larger clusters.[29] For protonated water clusters the peak position levels off around $3699 - 3700\,\mathrm{cm}^{-1}$ but starts at lower wavenumbers for smaller clusters.[20] The dOH peak position of $La^{3+}(H_2O)_n$ clusters increases with cluster size and levels off at around $3695\,\mathrm{cm}^{-1}$ for $n \leq 200$. The difference of the high-n values could be linked to the long range influence of the trivalent metal cations' charge.[25] Since the peak position of $M^z(H_2O)_n$ clusters with 250 water molecules decreases almost linearly for charges with $z = -2$ to $+3$, the polarity of the ion has been concluded to affect the cluster's whole hydrogen bond network.[25]

With the peak position data presented here and considering those of $H^+(H_2O)_n$ and $La^{3+}(H_2O)_n$ clusters, none of these nm-sized aggregates showed a downshift of the peak position of $3 - 4\,\mathrm{cm}^{-1}$ as observed by Devlin and Buch[232] for larger particles[V] of cubic ice and of amorphous water. A possible explanation is, that the crystalline clusters of this work are rather low in abundance and that their dOH signal is strongly overlapped with the dOH peak of amorphous clusters. With regard to the spectral resolution of the $Na(H_2O)_n$ data of this work ($5\,\mathrm{cm}^{-1}$) and the

[V] The average particle diameter was in the range of 20 nm (approximately 10^5 molecules).[232]

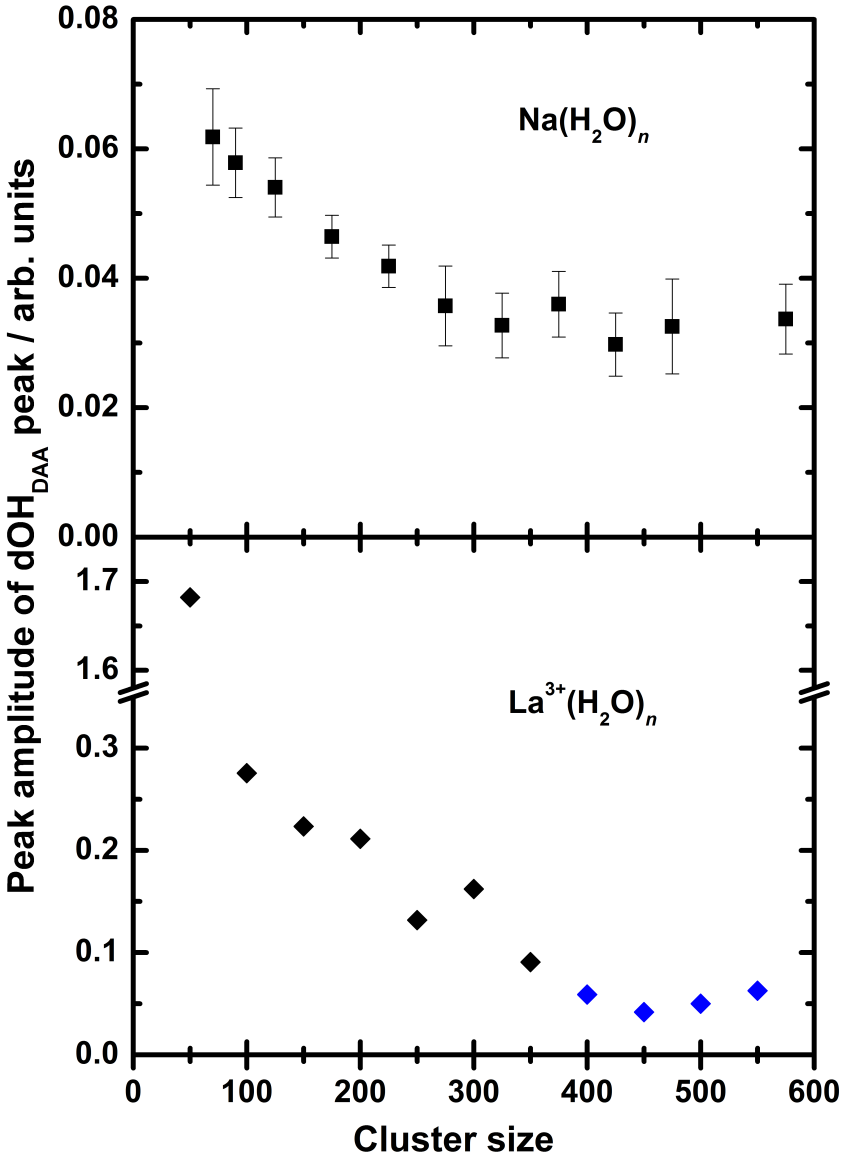

Figure 5.19: Amplitude of the dOH peak of $Na(H_2O)_n$ (Δt = 12 ns, upper panel) and $La^{3+}(H_2O)_n$ [81] (lower panel). Blue diamonds refer to spectra of crystalline clusters from Cooper et al. [81]

spectral width of the IR laser ($3.7\,\mathrm{cm}^{-1}$ [215]), it has to be admitted that a study with improved spectral resolution and reduced laser bandwidth may show the peak shift observed by Devlin and Buch [232] for the transition from amorphous to crystalline water aerosol.

The peak amplitude parameter A of the dOH peaks as obtained by the Gaussian regression decreases with increasing cluster size for the scaled 12 ns data until it reaches a constant value of $A = 0.03 - 0.04$ for $n \geq 275 \pm 25$, see lower panel of Figure 5.17. The data of $\Delta t = 200\,\mathrm{ns}$ deviate from the 12 ns case: While the constant A value for $n \geq 275 \pm 25$ is reproduced, lower amplitudes are observed for $n \leq 225 \pm 25$. The quasilinear amplitude decrease observed in the 12 ns data is not present for $\Delta t = 200\,\mathrm{ns}$. Nevertheless, the A values obtained from the spectra measured with $\Delta t = 200\,\mathrm{ns}$ appear to be larger for $n < 275 \pm 25$ than for $n \geq 275 \pm 25$. The amplitude parameters obtained for $Na(H_2O)_n$ at $\Delta t = 12\,\mathrm{ns}$ and $La^{3+}(H_2O)_n$ clusters are shown in Figure 5.19. For the $La^{3+}(H_2O)_n$ clusters, which were tempered to 133 K, [81] the amplitude shows a linear decrease for $n = 100 - 400$. For larger clusters, which show a peak absorption around $3220\,\mathrm{cm}^{-1}$ and are therefore fully crystalline, [81] the amplitude remains constant. This indicates that the constant amplitude parameter correlates with the presence of crystalline clusters. From this can be deduced, that the constant amplitude parameter found for $Na(H_2O)_n$ clusters may also indicate the presence of crystalline clusters, which is in agreement with the obtained n_{onset}.

If the ratio of dOH peak intensity and the integrated intensity of bonded OH oscillators is a suitable measure for the ratio of surface and volume of a spherical cluster, the dOH amplitude should decrease with increasing cluster size. While this is observed for smaller amorphous clusters, A levels off for $Na(H_2O)_{n\geq250}$ and $La^{3+}(H_2O)_{n\geq400}$ in the cluster size ranges for which the presence of crystalline clusters has been concluded, see Figure 5.19. The spectra were normalized to the same integrated intensity in the range of $\tilde{\nu} = 2800 - 3150\,\mathrm{cm}^{-1}$ and the amplitude A therefore corresponds to the intensity ratio of the dOH peak and this low-frequency range for hydrogen bonded OH oscillators. For a transition from liquid-like to crystalline clusters, the intensity in the range of $2800 - 3150\,\mathrm{cm}^{-1}$ increases as ice-like clusters exhibit a shoulder at around $3100\,\mathrm{cm}^{-1}$. [19,187] and due to an increase of the integrated absorptivity of crystalline clusters compared to amorphous clusters. [225] Considering this, the constant amplitude values indicate an increasing dOH peak intensity in crystalline clusters. From this can be concluded that the amplitude of

the peak of free OH oscillators might be a probe for the presence of crystalline water clusters. In order to validate or refute this hypothesis a detailed study on the dOH peak with higher spectral resolution and a significantly improved signal-to-noise ratio is required.

5.6 Conclusion

The temporal evolution of the IR-induced ion gain was shown to be as follows: At negative delay times, which corresponds to photoionization prior to IR irradiation, a shift of the mass spectrum towards smaller cluster sizes is observed, which is caused by the decomposition of cationic clusters. A sharp signal increase is observed when the laser pulses overlap, provided that the photon energy of the ionizing radiation does not exceed the sIE of $Na(H_2O)_n$ clusters of 4.1 eV. For $\Delta t > 5$ ns, an exponential decay of the signal—corresponding to the fragmentation of amorphous clusters—is observed for all cluster sizes for excitation by 3400 cm^{-1} photons. Excitation by 3200 cm^{-1} photons shows a similar decay only for small, amorphous clusters whereas the signal of larger clusters is stable. The E_{IR} dependence of the IR-induced ion yield gain indicates that the signal gains obtained at $\tilde{\nu} = 3400\,cm^{-1}$ and 3200 cm^{-1} are not caused by the same species of clusters at cluster sizes large enough to form crystalline clusters.

The vibrational spectra obtained at high-E_{IR} conditions reveal that those of Pradzynski et al.[71] deviate from the spectra of pure water ice droplets and $La^{3+}(H_2O)_n$ clusters due to a distortion by the decaying amorphous component. Spectra with reduced distortion can be obtained with reducing the IR laser pulse energy. These spectra are signal gain spectra of crystalline and amorphous water clusters and—along with the Δt and E_{IR}-dependence of the signal gain—indicate the coexistence of these two cluster types for certain sizes. In addition, the spectra with reduced distortion can resemble those obtained in an FTIR study on the crystallization behavior of water nanodroplets in Laval nozzles.[21]

The cluster size ranges for which the presence of crystalline clusters were concluded are listed in Table 5.1. The cluster size for which the peak position of bonded OH oscillators is downshifted to $\tilde{\nu} \leq 3300\,cm^{-1}$ is $n_{crystal}$. n_{onset} is the cluster size for which a broadening of the bonded OH peak—coinciding with a beginning downshift of the bonded-OH peak absorption to $\tilde{\nu} \leq 3400\,cm^{-1}$—is observed by comparison to the spectra of smaller, amorphous clusters. The cluster size for which the dOH

Table 5.1: Cluster size ranges for which a beginning crystallization is observed in terms of the spectra interpretation of Pradzynski et al.,[71] $n_{\text{transition}}$, cluster sizes ranges for which the maximum absorption peak is downshifted to $\tilde{\nu}_{\text{peak}} \leq 3300\,\text{cm}^{-1}$, n_{crystal}, and the cluster size range for which the scaled dOH amplitude reaches a constant value, $n_{\text{dOH amplitude}}$ for each set of spectra from identical expansion conditions. The data for $\Delta t = 80\,\text{ns}$ are from references [71, 90].

Δt / ns	E_{IR} / mJ	$n_{\text{transition}}$	n_{crystal}	$n_{\text{dOH amplitude}}$
80	$5-10$	275 ± 25	325 ± 25	–
12	$8-15$	$200-300$	325 ± 25	275 ± 25
200	$8-14$	225 ± 25	275 ± 25	275 ± 25
12	$5-8$	$250-350$	475 ± 25	–

peak amplitude remained constant with further increasing cluster size is denoted $n_{\text{dOH amplitude}}$.

The vibrational spectra measured in this work show that crystallization sets in for the cluster size range $n = 200-300$ if the determined n_{onset} are considered, see Table 5.1. The smallest cluster size range for which a rising intensity in the vibrational spectra of $Na(H_2O)_n$ clusters is observed for $\tilde{\nu} < 3400\,\text{cm}^{-1}$, is around $n \approx 275 \pm 25$ for all variations of Δt and E_{IR}. At high-E_{IR} conditions n_{onset} is downshifted by up to two adjacent cluster size discs compared to the conditions with lower E_{IR}. Larger deviations are observed for the cluster size for which the peak position observed in the vibrational spectra of $Na(H_2O)_n$ is downshifted to $\tilde{\nu} \leq 3300\,\text{cm}^{-1}$ and therefore close to the range of the peak position of crystalline clusters, n_{crystal}.

If the noise level of the vibrational spectra was low enough to detect the dOH peak around $3700\,\text{cm}^{-1}$, a Gaussian lineshape was fitted to the data. The peak positions appear to level off at larger cluster sizes to around $3699-3700\,\text{cm}^{-1}$, which is consistent with the observations from protonated water clusters.[20] The obtained amplitudes of the dOH peaks, scaled to the integrated signal gains for $\tilde{\nu} = 2800-3150\,\text{cm}^{-1}$, decrease with increasing cluster size until they level off for $n \geq 250$. Note that the presence of crystalline clusters was concluded for this cluster size, see n_{onset} in Table 5.1. As the intensity in the spectral range used for the scaling of the dOH part of the spectra increases if crystalline clusters are present, the constant amplitude of the dOH peak should increase similarly in order to obtain constant values. A similar behavior is observed for the dOH peak of the spectra of $La^{3+}(H_2O)_n$ clusters from Cooper et al.:[81] the amplitude parameter levels off as soon as crystalline clusters are observed in the spectral range of bonded OH oscillators. Since the bonded-OH part of these IRMPD spectra is not distorted and

can be considered to resemble the spectra of crystalline clusters, this constant peak amplitude can be concluded to correlate with the presence of crystalline clusters. From this follows for the $Na(H_2O)_n$ clusters that crystalline clusters are likely present for $n \geq 275 \pm 25$, which is in agreement with the obtained $n_{\text{transitions}}$. Furthermore, this shows that Pradzynski et al.[71] determined the onset of crystallization via n_{onset} correctly despite the rather long delay time they used and the distortion present in their vibrational spectra of large cluster sizes.

6 The smallest water ice I cluster - Revisited

6.1 Introductory remarks

How many water molecules are required in a cluster to form a microscopic ice-analogue? This question has been addressed in several computational[16,87–89] and experimental studies.[19–21,71,81,84] Predictions from molecular dynamics simulations with empirical potentials showed that crystalline clusters can be present for $n = 293$,[16,89] $n = 137$,[88] or $n \geq 90$.[87] The experimental results from vibrational spectroscopy methods and electron diffraction indicate a broad range over hundreds of cluster sizes for the onset of crystallization. Most of these experimental studies cannot reliably rank the computational studies[16,87,88] with respect to the accuracy of their predictions as the applied experimental techniques either lack size-resolution[19,21,84,230] or the cluster sizes investigated exceeded those from the predictions.[71,81] In contrast to these, Mizuse et al.[20] concluded the presence of partly crystalline $H^+(H_2O)_n$ clusters with $n \geq 100$ from IRMPD spectra. This appears to be in agreement with the predictions of Bandow and Hartke.[87]

In experiments on $Na(H_2O)_n$ clusters, the presence of crystalline clusters can be tuned by the expansion conditions:[37,86,90] while an increase of the stagnation pressure leads to larger crystalline clusters, a change of the carrier gas from helium to heavier atoms along with a reduction of the stagnation pressure results in smaller crystalline clusters.[37,90] The estimated terminal cluster temperatures appear to correlate inversely with n_{onset}.[37] In helium-seeded expansion conditions crystalline clusters were obtained for $n_{\text{onset}} = 275 \pm 25$ with $T_{\text{cluster}} \approx 70\,\text{K}$, see Chapter 5 and [37, 71].

In this chapter, IR spectra of $Na(H_2O)_n$ clusters formed in argon-seeded expansions are presented and compared to previously reported cluster size ranges of crystalline clusters from experiments and simulations. The choice of the expansion condi-

tions was inspired by a previous work on the identification of low-energy isomers of $Na(H_2O)_{20}$.[184]
The vibrational spectra discussed in this chapter were measured with $0.2 - 0.3$ bar water vapor at a stagnation pressure of 1.05 ± 0.10 bar. The ionization parameters were $\Delta t = 100$ ns, $E_{IR} = 10 - 14$ mJ, and $\lambda_{UV} = 385$ nm. The high-E_{IR} conditions were applied in order to obtain an improved signal-to-noise ratio despite the low ion count rates in the argon-seeded expansions.

6.2 Experimental results

6.2.1 Vibrational spectra

Vibrational spectra of $Na(H_2O)_{n=60-300}$ clusters from argon-seeded expansions are shown in Figure 6.1. Noise reduction was performed by binning several cluster sizes and by threefold smoothing with a weighted average of a 25%-50%-25% type. The spectral trends are equal to those shown and discussed in Section 5.4.1 for the helium-seeded expansion: All spectra show a broad peak in the range of $2800 - 3650\,cm^{-1}$ and a single isolated peak around $3700\,cm^{-1}$.
Since a rather long delay time ($\Delta t = 100$ ns) and high IR pulse energies ($E_{IR} = 10 - 14$ mJ) were used, the decay of amorphous, liquid-like clusters causes a depletion of the IR induced signal gain for larger clusters at around $\tilde{\nu} = 3400\,cm^{-1}$, see Figure 6.1. The onset signal of crystalline clusters is indicated by a broadened, slightly downshifted maximum intensity of the bonded OH peak position from $\tilde{\nu}_{peak,bonded\ OH} = 3430\,cm^{-1}$ for the cluster size range $n = 70 \pm 10$, black trace, to $\tilde{\nu}_{peak,bonded\ OH} \leq 3400\,cm^{-1}$ for $n \geq 90 \pm 10$, red trace. This coincides with an intensity increase for $\tilde{\nu} \leq 3400\,cm^{-1}$.
Some of the spectra of Figure 6.1 are compared to each other in Figure 6.2. The spectrum for $n = 60 - 80$ (black solid line) indicates that these clusters are amorphous. With increasing cluster size an increase of the intensity between $3100\,cm^{-1}$ and $3400\,cm^{-1}$ is observed. While the spectra of the cluster size ranges $n = 80 - 100$ and $n = 100 - 150$ (red solid and red dashed lines) show a shift of the maximum absorption to $3300 - 3400\,cm^{-1}$ compared to $n = 60 - 80$, a further increase of the cluster size leads to a shift of the intensity maximum to around $3250\,cm^{-1}$ for $n = 150 - 200$ (blue). In order to further refine the cluster size range for which the onset of crystallization can be observed, smaller cluster size bins were generated.

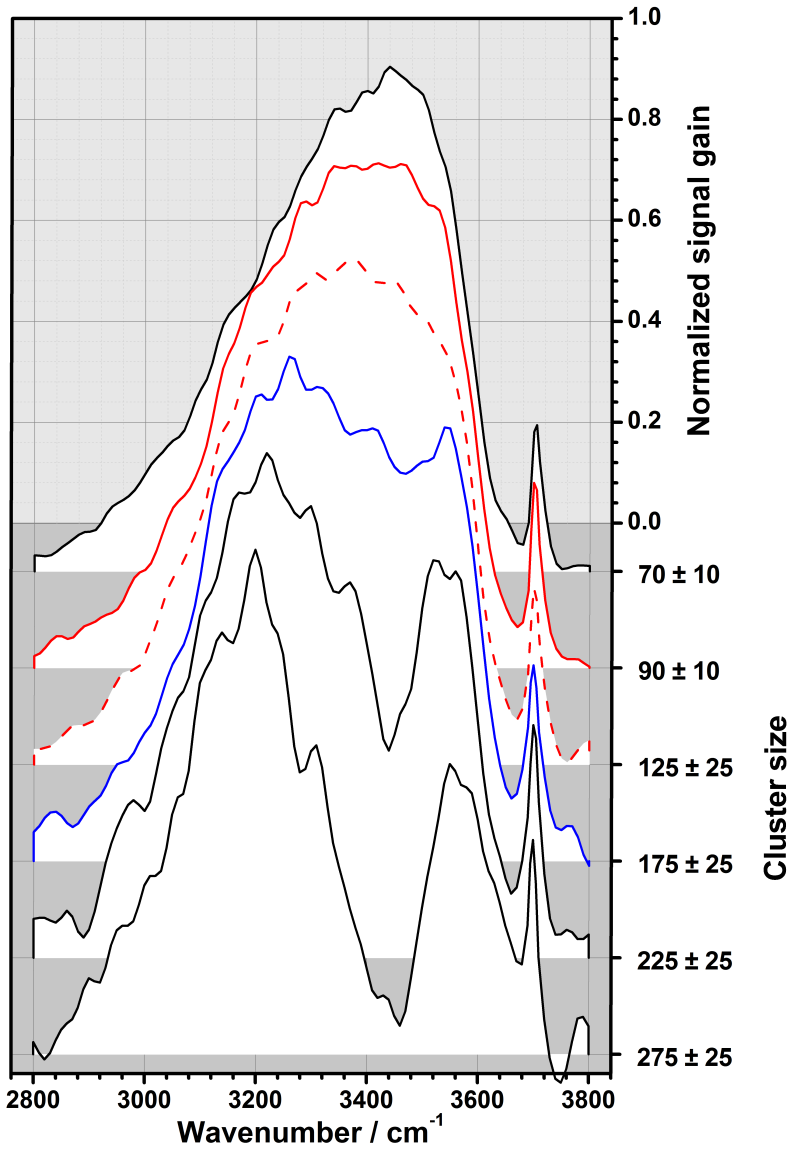

Figure 6.1: Normalized vibrational spectra of $Na(H_2O)_n$ clusters. Water vapor ($0.2 - 0.3$ bar) was coexpanded with Ar at a reservoir pressure of 1.05 ± 0.10 bar. The spectra were smoothed three times by a weighted three-point average of 25%-50%-25% type.

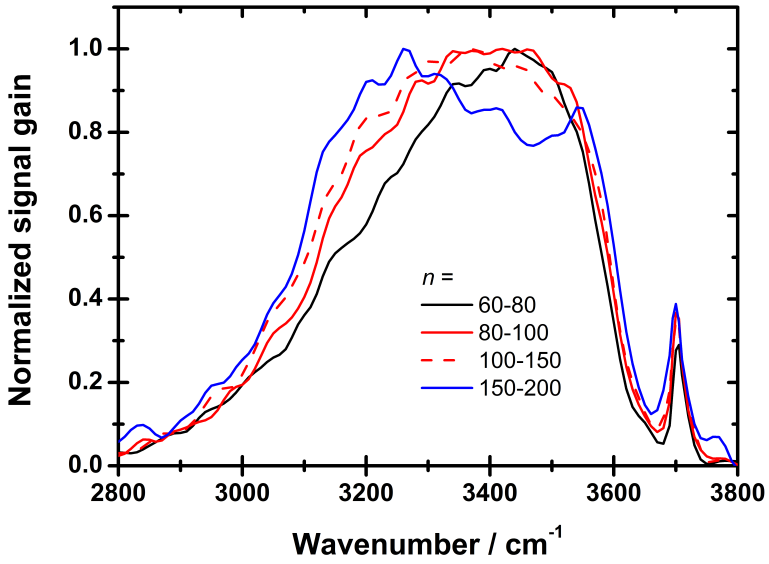

Figure 6.2: Spectra of $Na(H_2O)_n$ clusters with $n = 60 - 200$. The spectra were smoothed three times in order to reduce the noise and to highlight the shift of the maximum intensity.

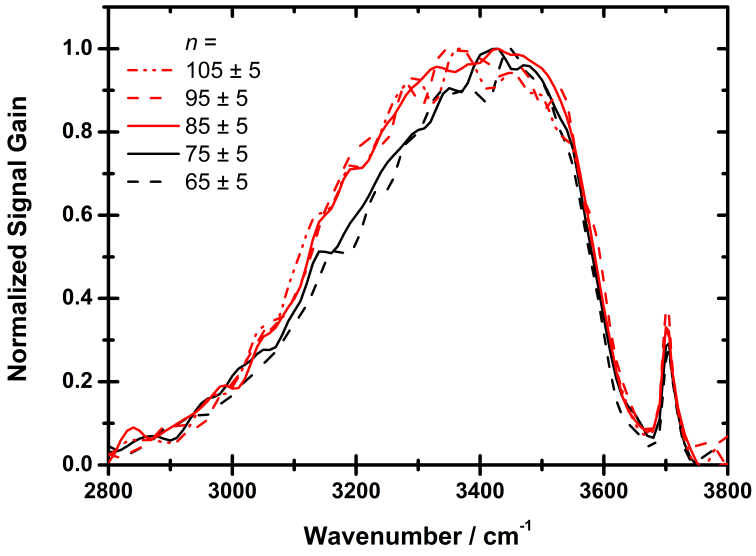

Figure 6.3: Vibrational spectra of $Na(H_2O)_{n=60-110}$. The spectra of $n = 65 \pm 5$ and $n = 75 \pm 5$ are shown as black and dashed black line, those of $n = 85 \pm 5$, 95 ± 5, and 105 ± 5 as solid red line, dashed red line, and red dot-dashed line. The spectra were smoothed three times by a weighted three-point average of 25%-50%-25% type.

The thus obtained spectra are shown in Figure 6.3. The spectra for $n = 65 \pm 5$ and $n = 75 \pm 5$ (black traces) resemble those of amorphous clusters with a peak position in the range of $\tilde{\nu} = 3400 - 3450\,\mathrm{cm}^{-1}$. The red spectra of $n = 80 - 110$ deviate from these due to an intensity increase for $\tilde{\nu} < 3400\,\mathrm{cm}^{-1}$. This signal increase indicates that the presence of crystalline clusters can be shifted to clusters with as few as $n = 85 \pm 5$ water molecules. Since the signal increase remains approximately constant for $n = 80 - 110$, it may also be concluded that the fraction of crystalline clusters does not increase steadily in this size regime.
These spectra were obtained at high-E_{IR} conditions, the size range of the estimated lower bound n_{onset} can be estimated to be $n_{\mathrm{onset,\ Ar}} = 90 \pm 10$ instead of 85 ± 5.
As the amorphous to crystalline transition occurs at significantly smaller cluster sizes than observed for the helium-seeded case, see Section 5.5.1, and the n_{onset} is affected by the applied expansions conditions and the resulting cluster temperature,[37] the experimental parameters of both expansions should be examined, see Table 6.1:

Table 6.1: Experimental parameters of the helium-seeded and argon-seeded expansion.

seeding gas	He	Ar
$p_{\mathrm{stagnation}}$ / bar	3.7 ± 0.1	1.05 ± 0.10
$p_{\mathrm{v,\,H_2O}}$ / bar	2.7	$0.2 - 0.3$
T_{nozzle} / K	413	343
$\bar{n}$	$240 - 245$	105

Whereas the cluster temperatures cannot be measured in the present setup, a comparison of the experimental parameters allows a qualitative estimate of the temperature obtained in the argon-seeded conditions relative to helium case; for which $T_{\mathrm{clu}} \approx 70\,\mathrm{K}$ was concluded.[37] While a reduction of the water vapor fraction should decrease the cluster temperature,[86] the reduction of the reservoir pressure reduces the cooling rate in the supersonic expansion and therefore increases the cluster temperature. An increased nozzle temperature at constant reservoir pressure shifts the cluster distribution to smaller cluster sizes[34,86] but was shown to not strongly affect the terminal cluster temperature.[86] Moreover, the use of a heavier seeding gas results in lower cooling rates.[95] These points support the hypothesis of Buck et al.,[37] which states that smaller crystalline clusters are observed at higher cluster temperatures. In conclusion, the cluster temperature obtained from the argon-seeded expansion conditions should exceed that observed by Gimelshein et al.[86] for neon-seeded expansions;[37] $T_{\mathrm{cluster,\,Ar}} > 100\,\mathrm{K}$. This is further supported by slightly

increased decay rate constants observed for the Ar-seeded expansion conditions.[205] Mizuse et al.,[20] who also concluded the presence of crystalline clusters for $n \geq 100$, estimated their cluster temperatures to be $T_{\text{cluster}} \approx 150 - 200\,\text{K}$. Note that these temperatures are in the range of the evaporative ensemble conditions concluded by Schmidt and von Issendorff.[150] In addition, the pickup process[VI][72] and the vibrational excitation by IR irradiation influence the cluster temperature.[71]

6.2.2 Signal of the free OH oscillators

Panel a) of Figure 6.4 shows the dOH part of the spectra of water clusters formed in argon-seeded supersonic expansions. With increasing cluster size, an intensity increase below $3705\,\text{cm}^{-1}$ (dashed line) is observed, which results in a down-shift of the maximum absorption to $3700\,\text{cm}^{-1}$. In addition, the dOH peaks of larger cluster sizes appear to be broader than those of smaller clusters, compare for instance the spectrum of $n = 30 \pm 10$ or $n = 50 \pm 10$ to $n = 150 \pm 10$.

Gaussian lineshape regressions are applied to the data of $3680 - 3740\,\text{cm}^{-1}$ in order to observe changes of the dOH peak with increasing cluster size. Panel b) shows the obtained fit parameters for regressions which do not exceed the arbitrarily chosen threshold of the Pearson's χ^2 parameter, $\chi^2_{\text{thres}} \leq 1 \cdot 10^{-5}$. The obtained peak parameters are presented in Panel b) of Figure 6.4.

With increasing cluster size, the obtained dOH peak position decreases steadily from $3705\,\text{cm}^{-1}$ for $n = 20 - 30$ to around $3700\,\text{cm}^{-1}$ for $n \approx 150$. For clusters sizes larger than $n = 160$, the peak position does not appear to be further down-shifted. If too few cluster sizes are binned, deviations from this behavior arise. For larger clusters with $n \geq 150$, the noise level of the spectra increases, which results in $\chi^2_{\text{thres}} > 1 \cdot 10^{-5}$ or scattering fit parameters, compare top trace for $n = 170 \pm 10$ in panel a) of Figure 6.4 and the data for $n \geq 150$ in panel b). The gradual decrease of the peak position has similarly been observed for $H^+(H_2O)_n$ and $PhOH(H_2O)_n$ clusters.[20] It is partly in agreement with the results from the helium-seeded expansion conditions, see Section 5.5.2, as now the dOH peak position does not level off at n_{onset} but decreases further. This steady decrease of $\tilde{\nu}_{\text{dOH}}$ therefore might allow the conclusion that the peak position is determined by the cluster size in the size range below $n \leq 170$. In addition, the presence of disordered clusters, consisting of annealed smaller clusters as proposed by Lengyel et al.[233] can be ruled out, as these should be observable by

[VI] MD simulations (BLYP/6-31+g*) of the Slavíček group showed that the temperature of a $(H_2O)_{15}$ cluster can increase by up to 80 K because of the pickup of an Na atom.[72]

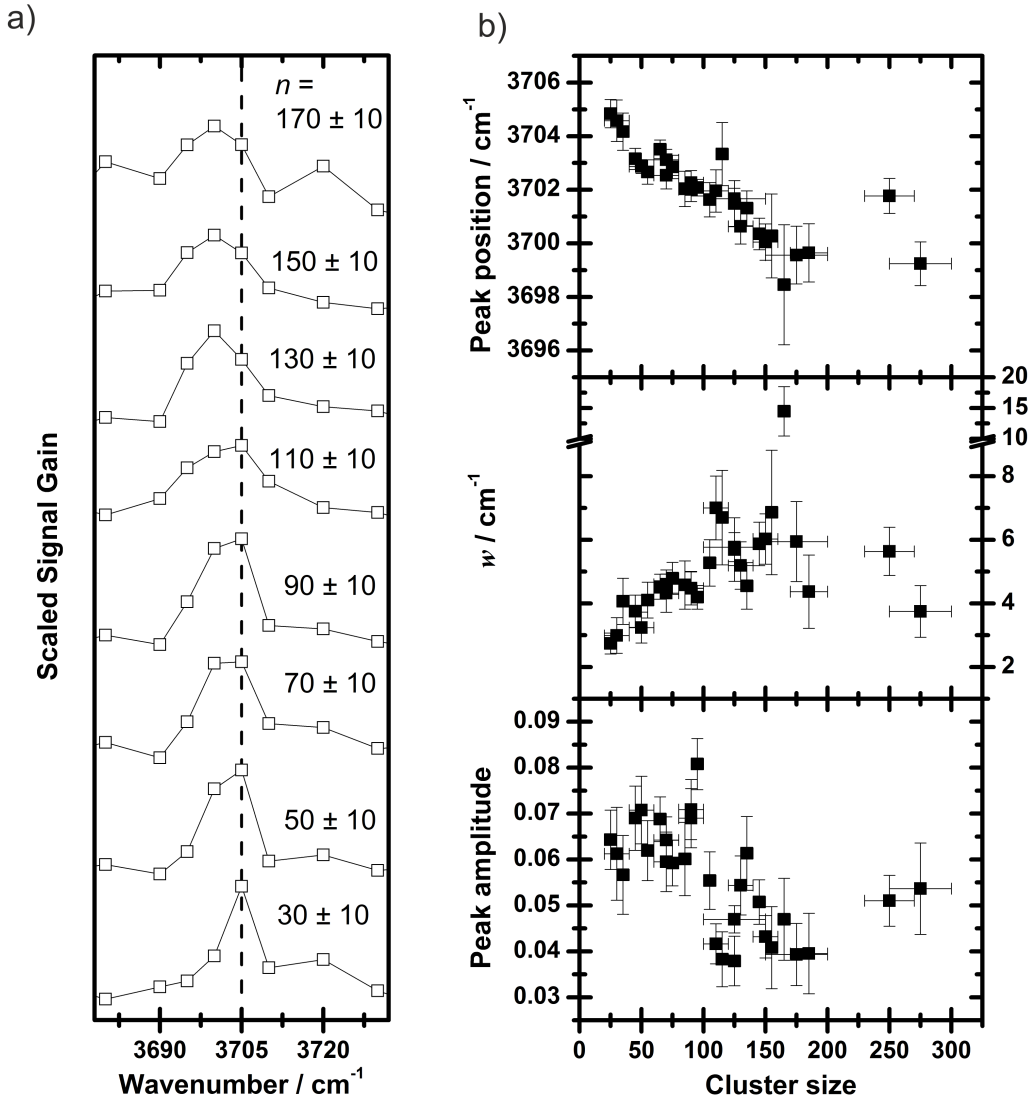

Figure 6.4: Panel a): Peak of the unbound OH oscillators from the argon seeded conditions. The signal gain was scaled to the integral of the spectral range of $2800 - 3150\,\mathrm{cm}^{-1}$. The dashed line marks $3705\,\mathrm{cm}^{-1}$. The spectra were offset for clarity.
Panel b): The resulting fit parameters from Gaussian lineshape regression applied to the data for $3680 - 3740\,\mathrm{cm}^{-1}$ for several cluster size ranges. From top to bottom: Peak position $\tilde{\nu}_{\mathrm{peak}}$, linewidth parameter w, and peak amplitude parameter A.

an up-shift of the dOH peak position with increasing cluster size.
The Gaussian peak width parameter w increases with cluster size for $n \leq 100$. For larger cluster sizes, the width parameter may level off, however, the obtained values of w are scattered in the range of $4 - 15\,\mathrm{cm}^{-1}$. The indicated broadening of the dOH peak could be caused by the increasing number of low energy isomers with each cluster size. For large clusters this could also indicate the presence of crystalline clusters, which might have a slightly downshifted dOH peak position.[232] However, the scattering of the data shows that a detailed investigation of the dOH peak with a significantly improved signal-to-noise ratio is required as the goodness of obtained fitting results is limited by the noise level of the experimental data, especially for large cluster sizes with $n \geq 100$. This could be reduced in future investigations on this spectral range by a better spectral resolution, which is only limited by the IR laser bandwidth in seeded operation ($1.7\,\mathrm{cm}^{-1}$ [215]).
In contrast to the data from He-seeded expansions taken at short delay times or the IRMPD spectra of $La^{3+}(H_2O)_n$ clusters from Cooper et al.,[81] the amplitude parameter A obtained for clusters from argon-seeded supersonic expansions shows no linear decrease for smaller cluster sizes, compare Figure 5.19 on page 100 in Chapter 5, but rather resembles the data of He-seeded expansions with $\Delta t = 200\,\mathrm{ns}$. In the bottom panel of Figure 6.4 b) a general trend such as a continuous increase or decrease cannot be made out, nevertheless, the A values for $n > 105$ scatter around $A = 0.045$ while those of $n < 105$ scatter around 0.065 and thus may subtly decrease similar to the ones observed above. This is close to the cluster size range $n_{\mathrm{onset}} = 90 \pm 10$ for which crystalline clusters were concluded to contribute to the vibrational spectra, see Section 6.2.1. Note that for both expansion conditions, helium-seeded (see Chapter 5) and argon-seeded (this chapter), the amplitude parameter appears to reach a constant, lower value at slightly larger clusters sizes than the corresponding n_{onset}, which has been concluded from an intensity increase in the range of $\tilde{\nu} < 3400\,\mathrm{cm}^{-1}$ for spectra obtained at high-E_{IR} conditions.

6.3 Comparison to other methods

Since the cluster size $n_{\mathrm{onset}} = 90 \pm 10$, for which the presence of crystalline clusters has been concluded, is remarkably small, it is compared to the smallest crystalline cluster sizes observed in several experiments and to predictions from theory in the following. The cluster sizes of the obtained or concluded crystalline clusters as well

Table 6.2: Comparison of cluster size ranges for which a crystalline clusters are observed in experimental and computational studies. The table is structured from top to bottom as follows: the data obtained in this work, data from similar or other size-selective experiments, size-unresolved experiments on $(H_2O)_n$, predictions from theory.

species	technique	$n_{\text{transition,crystal}}$	T_{cluster} / K	ref.
$Na(H_2O)_n$	see Section 2.4.4	90 ± 10 [Ar,a]	> 100	this work
		175 ± 25 [Ar,b]		Chapter 6
$Na(H_2O)_n$	see Section 2.4.4	225 ± 25 [He1,a]	~ 70	this work
		275 ± 25 [He1,b]		Chapter 5
$Na(H_2O)_n$	see Section 2.4.4	$200 - 300$ [He2,a]	~ 70	this work
		325 ± 25 [He2,b]		Chapter 5
$Na(H_2O)_n$	see Section 2.4.4	$250 - 450$ [He3,a]	~ 70	this work
		475 ± 25 [He3,b]		Chapter 5
$Na(H_2O)_n$	see Section 2.4.4	~ 140 [b]	100	[86]
$Na(H_2O)_n$	see Section 2.4.4	275 ± 25 [a]	70	[71, 90]
		325 ± 25 [b]		
$Na(H_2O)_n$	see Section 2.4.4	475 ± 25 [b]	50	[37, 90]
$La^{3+}(H_2O)_n$	IRMPD	400 [b]	133	[81]
		$150 - 350$[a]		
$H^+(H_2O)_n$	IRMPD	100	$150 - 200$	[20]
$(H_2O)_n$	IRMPD	630 [c]	–	[230, 231]
$(H_2O)_n$	FTIR	$4.2 \cdot 10^3$ [d]	161.2	[21]
$(H_2O)_n$	FTIR	$5.1 \cdot 10^2$ [d]	$5.2 - 6.3$	[19]
$(H_2O)_n$	FTIR	~ 500	100	[85]
$(H_2O)_n$	e^--diffraction	$230 - 900$	180 ± 20	[84]
$(H_2O)_n$	CNT	130 [d]	150	[234]
$(H_2O)_n$	MD (mW)	137	150 [e]	[88]
$(H_2O)_n$	MD (TIP4P)	293	–	[16, 89]
$(H_2O)_n$	MD (TTM2-F)	$\gtrsim 90$	–	[87]

[Ar] Ar seeded expansion conditions, see Section 6.2.1; $\Delta t = 100\,\text{ns}$, $E_{\text{IR}} = 10 - 14\,\text{mJ}$.
[He1] He seeded expansion conditions, see Chapter 5; $\Delta t = 200\,\text{ns}$, $E_{\text{IR}} = 8 - 14\,\text{mJ}$.
[He2] He seeded expansion conditions, see Chapter 5; $\Delta t = 12\,\text{ns}$, $E_{\text{IR}} = 8 - 15\,\text{mJ}$.
[He3] He seeded expansion conditions, see Chapter 5; $\Delta t = 12\,\text{ns}$, $E_{\text{IR}} = 5 - 8\,\text{mJ}$.
[a] Indicated by intensity increase for $\tilde{\nu} = 3130 - 3320\,\text{cm}^{-1}$, referred to as n_{onset} above.
[b] Indicated by a peak position of H-bonded OH oscillators below $3300\,\text{cm}^{-1}$, referred to as n_{crystal}.
[c] Concluded from a small peak at $3200\,\text{cm}^{-1}$ by Andersson et al.[230]
[d] Number of water molecules estimated via the temperature dependence of the density of liquid water aerosol as in reference [21].
[e] Temperature for isothermal crystallization. The melting temperature of spontaneously crystallized clusters was $170 \pm 9\,\text{K}$. The melting temperature of a corresponding Ih cluster is slightly lower ($162 \pm 5\,\text{K}$).

as the applied techniques are listed in Table 6.2.
The spectra of $Na(H_2O)_n$ from argon-seeded supersonic expansions indicate the presence of crystalline clusters for $n = 90 \pm 10$. This value is based on an intensity increase for $\tilde{\nu} \leq 3400\,cm^{-1}$ with a coinciding slight downshift of the peak maximum of bonded OH oscillators and is observed by comparison to the spectra of smaller, amorphous clusters. The thus determined cluster size which's spectrum showed contributions from crystalline clusters has been denoted as n_{onset} above. The cluster size for which the bonded OH peak is downshifted to $\tilde{\nu} \leq 3300\,cm^{-1}$ has been referred to as $n_{crystal}$ and is larger than n_{onset} in every set of spectra.
With regard to the previous work on the crystallization of $Na(H_2O)_n$ cluster, the obtained value of $n_{transition,\,Ar} = 90 \pm 10$ marks a new lowest cluster size for which crystalline clusters were observed in the present apparatus, see Table 6.2. The cluster temperature should follow the trend proposed by Buck et al.,[37] and therefore exceed 100 K.
For pure water clusters, $(H_2O)_n$, a rough estimate of the critical particle size required for the crystallization of water droplets was obtained by Zasetsky et al.[234] via classical nucleation theory (CNT). They calculated a critical cluster diameter of 2 ± 1 nm for the homogeneous crystallization at 150 K.[VII] Electron diffraction of nm-sized water clusters with estimated cluster temperatures of 180 ± 20 K showed the presence of cubic ice for cluster distributions with an approximated mean cluster size of $\bar{n} \approx 900$ but not for $\bar{n} \approx 230$. From this Torchet et al.[84] concluded the onset of crystallization to occur in between these cluster sizes. FTIR spectra of $(H_2O)_n$ clusters formed in supersonic expansions or collisional cooling cells with $T_{cluster} \leq 190$ K indicate a smallest cluster size for crystalline clusters to be around $\bar{n} = 400 - 500$.[19,21,85] Andersson et al.[230] obtained vibrational spectra by detecting fragments of the IRMPD of $(H_2O)_n$ cluster distributions. They concluded the presence of crystalline clusters for $\bar{n} \sim 630$ from a small peak around $3200\,cm^{-1}$ [230] and based on a comparison to calculated spectra of cluster surfaces of crystalline clusters.[16,231]
Size-selective vibrational IRMPD spectra of charged water clusters such as $H^+(H_2O)_n$ [20] and $La^{3+}(H_2O)_n$ [81] partly resemble bulk spectra. For the protonated clusters with estimated cluster temperatures of $150 - 200$ K the presence of crystalline clusters was concluded for $n \geq 100$.[20] In contrast to this, the $La^{3+}(H_2O)_n$ clusters were

[VII] This corresponds to a critical cluster with $n \approx 130^{+310}_{-110}$ if estimated via the liquid water density as in reference [21].

tempered to 133 K in an ion trap.[81] While spectra with $n \geq 400$ show a peak around 3200 cm^{-1} and thus indicate the presence of crystalline clusters,[81] a broad cluster size regime with spectra exhibiting broadened bonded OH peaks is observed ($n_{onset} = 150 - 350$). Since the La^{3+} cation has a strong impact on the hydrogen bond network it can disturb the formation of a crystalline core.[81] Therefore, it was concluded that the spectra of the smaller clusters in this cluster size regime can be affected by the trivalent cation in terms of an intensity increase at lower wavenumbers, see reference [25]. This charge-induced distortion of the spectra was found to be small for singly charged ions such as Na^+ and I^-,[25] and negligible for protonated water clusters.[20]

In conclusion, of the aforementioned experimental studies on the smallest clusters indicating the presence of crystalline clusters, only in the work of Mizuse et al.[20] the presence of crystalline clusters was concluded for size ranges comparable to this work's $n_{transition,\ Ar} = 90 \pm 10$.

Since the smallest cluster size required for the formation of a crystalline core has been of interest for computational chemists,[16,87–89] the present result can be used to assess the suitability of the approaches to this task. Due to the large cluster sizes, empirical potentials (TIP4P[235] and TTM2-F[236]) or simplifying descriptions of the water molecules (mW potential[198]) were used in these studies.

Buch et al. investigated the stability of cubic ice in molecular dynamics simulations with the TIP4P potential in the temperature range $T = 100 - 200$ K for $n = 123, 293, 600, 931$ and observed that crystalline cores persisted for $n = 293, 600$, and 931.[16,89] For $n = 123$ the crystallinity of the input geometries was lost. With regard to the aforementioned result ($n_{transition,\ Ar} = 90 \pm 10$) it can be concluded, that the MD simulations with the computationally efficient TIP4P potential do not satisfactorily predict the crystallization behavior of water clusters in the experimentally observed size range.

Johnston and Molinero[88] performed MD simulations with the mW potential, which treats each water molecule as a single atom preferentially residing in a tetrahedral coordination environment. They found that the formed crystalline cores consist of a mixture of cubic and hexagonal ice. In isothermal crystallization simulations at $T = 150$ K they showed that clusters with 137 and 159 molecules could form crystalline cores. Since the 137-mer formed a metastable crystal core, Johnston and Molinero[88] speculated that clusters with 100 waters could not form ice-like cores. Comparing this finding to the experimental result stated above it can be concluded

that the mW potential with the temperatures of reference [88] does not yield a correct lower bound for the smallest crystalline cluster.
Bandow and Hartke developed an algorithm for the exploration of minimum energy cluster structures and used the TTM2-F potential[236] for the energy calculations of the water cluster energies.[87] A comparison of energies of clusters formed by their approach with those of clusters from relaxed spherical cutouts of bulk cubic and hexagonal ice revealed that the energies of the relaxed ice cutouts are similar to the obtained minimum energy isomers of amorphous, spherical clusters from the structure finding algorithm for $n \geq 90$. Based on this Bandow and Hartke stated that the cluster size $n = 90$ could be a lower limit for the presence of clusters with ice-like cores. With regard to the results of Mizuse et al.[20] and especially those presented in this chapter the conclusion of Bandow and Hartke appears to be justified. However, with regard to the large number of empirical and semiempirical potentials taylored for the description of intermolecular water-water interactions[12] and the observed temperature ranges in which water clusters can crystallize,[21,37,81] the value of $n_{\text{onset}} = 90 \pm 10$ as a lower limit for the presence of crystalline clusters will likely be refined in future investigations.

6.4 Conclusion

Vibrational spectra of sodium water clusters formed via argon seeded supersonic expansions and the pickup of sodium atoms are measured and interpreted concerning the presence of crystalline clusters. Spectra in the cluster size range $n = 80-110$ exhibit an intensity increase for $\tilde{\nu} < 3400\,\text{cm}^{-1}$ compared to the spectra of $n = 60-80$. From this follows that the previously reported smallest cluster size of crystalline clusters with $n_{\text{onset}} \approx 140$ for sodium water clusters[37,86] has to be refined to $n_{\text{onset}} = 90 \pm 10$.
The obtained $n_{\text{transition, Ar}} = 90 \pm 10$ was used to assess the suitability of three computational chemistry methods—references [16, 87, 88]—regarding their ability to correctly predict the presence of crystalline clusters. It was found that the predicted cluster sizes from the computationally efficient, empirical TIP4P potential[16] and the atomistic mW potential[88] are not in agreement with the smallest crystalline cluster size n_{onset} found in this work. Energies of amorphous and crystalline clusters for $n \geq 90$ calculated via the empirical TTM2-F potential indicate that crystalline clusters are isoenergetic to amorphous clusters in this size range.[87] This is in agree-

ment with the experimental observation of crystalline clusters for $n = 90 \pm 10$.
Gaussian lineshape regressions of the dOH peak indicate a gradual decrease of the peak position for $n \leq 170$. This levelling off positions does not correlate with the presence of crystalline clusters concluded from a broad intensity increase around $\tilde{\nu} = 3200\,\mathrm{cm}^{-1}$ in the bonded OH part of the vibrational spectra compared to the spectra of smaller cluster sizes. As this indicator was concluded to robustly indicate the presence of crystalline clusters and the regression parameter $\tilde{\nu}_{\mathrm{peak}}$ shows no clear correlation to the crystallinity in clusters, it may be concluded from the presented data that it is no reliable indicator for the presence of crystalline clusters. The width parameter of the peak profiles increases steadily for $n \leq 100$, for larger clusters the data scatter strongly and thus allow no estimate. The peak amplitude parameter A appears to indicate the presence of crystalline clusters as it is downshifted to smaller values for $n > 105$, which is close to the cluster size range of $n_{\mathrm{onset}} = 90 \pm 10$ and therefore in agreement with the corresponding observation of Section 5.5.2. However, a detailed investigation on the dOH peak, studying the peak parameters with a higher spectral resolution and an improved signal-to-noise ratio, is required to validate the concluded sensitivity of A to the presence of crystalline clusters.
The only experimental work that concluded the presence of crystalline clusters for $n \geq 100$ is that of Mizuse et al.[20] With regard to the inverse correlation of cluster temperature and observed n_{onset} concluded by Buck et al.,[37] the work of Mizuse et al.[20] and the results of this work are in qualitative agreement. Note that this indicates that evaporative ensemble conditions should be present.[147,150] Despite this, no post source decay has been observed for $\mathrm{Na}(\mathrm{H_2O})_n$ clusters.

7 Conclusion and Outlook

7.1 Single photon ionization of $Na(H_2O)_n$ clusters

7.1.1 Conclusion

The single photon ionization experiments indicate that the ionization energy distributions of $Na(H_2O)_n$ clusters with $n = 9 - 500$ do not differ strongly with cluster size and seeding conditions, see Chapter 4 and reference [72]. The obtained ion yield curves[72] are in agreement with the appearance ionization energies (aIE, also referred to as ionization threshold energies) reported by Hertel et al.[38] and the low-IE part of the photoionization spectrum as published by Forck et al.[70] An exception from this is found for $Na(H_2O)_3$, for which a slightly lower aIE is obtained (3.35±0.05 eV instead of 3.48±0.06 eV). Fragmentation of larger clusters to $Na(H_2O)_2{}^+$ at photon energies below 3.75 eV is not observed. Therefore, measuring photoionization efficiency curves is suitable to probe the distribution of ionization energies via the IY curve as an analogue to the integrated distribution of ionization energies. For photon energies larger than 3.75 eV, fragmentation cannot be ruled out. The possibility of fragmentation in the high photon energy part of the obtained IY curves is indicated by a comparison with the photoelectron spectrum of $Na(H_2O)_n$ clusters, where a fraction of clusters has higher ionization energies than the photon energy at which the photoionization efficiency curve is saturated.[40] The ionization energy at which the IY curves are saturated (in this work referred to as saturation ionization energy, sIE) is shown to be a cluster size-dependent property for $n \leq 9$. It reaches a constant value of 4.1 ± 0.1 eV for $n \geq 9$, which persists for clusters with up to hundreds of water molecules. The IY curves indicate that up to 90% of the $Na(H_2O)_n$ clusters can contribute to the IR-induced signal gain if the clusters are ionized by 3.22 eV radiation.

The comparison of the measured IY curves with predicted integrated ionization energy distributions from ab initio molecular dynamics simulations, which rely on the

energy calculations from the functionals BLYP and LC-ωPBE with the 6-31++g** basis set, shows only qualitative agreement.[72] These methods were chosen in order to reduce the costs of the computations. In the BLYP case, good agreement of some of the predicted ionization energy distributions with the experimental data was obtained for $n = 3$ and 7. The presence of high-IE isomers indicated by the experimental data for the cluster sizes $n = 4$ and 5 was not matched by the calculated IE distributions, but the low-IE part of the photoionization spectrum was. For $n = 2$ the experimental data were not matched by the BLYP based prediction, but by the IE distribution obtained from simulations relying on the LC-ωPBE functional. Since the MD simulations with the BLYP functional are in better agreement with experimental data of the larger cluster sizes, the presence of a substantial error compensation of missing zero point energy correction and a missing self interaction error compensation is apparent.[72] The BLYP based predictions for $n = 3$ provide a qualitative picture for the IR-induced enhanced ion signal: with increasing temperature low-IE isomers are increasingly populated.[72] This is in agreement with predicted ionization energy distributions of sodium doped methanol clusters.[43]
It was found that the energy ordering of the isomers and the ionization energies calculated via the BMK functional are in agreement with the results from CCSD(T) calculations.[72] More sophisticated quantum chemical methods might better reproduce the isomer distribution observed in the molecular beam experiment.

7.1.2 Outlook

The IY curves for $n = 3$ are affected by the applied seeding conditions and therefore indicate that the obtained photoionization spectrum could depend on the cluster temperature. In order to validate this, photoionization efficiency curves or photoelectron spectra of IR-heated clusters are required. The then obtained EBE distributions should be shifted to smaller ionization energies for clusters which were heated by IR-excitation.[43,71,72] When applying photoelectron spectroscopy (PES) and mass spectrometry to the $Na(H_2O)_n$ clusters simultaneously, two types of measurements are possible depending on the number of ionization incidents per laser pulse. At ion count rates larger than $1\frac{\text{ion count}}{\text{laser pulse}}$ the detected electron signal cannot be correlated to distinct cluster sizes[237] and therefore only represents the overall photoelectron spectrum of the whole cluster distribution.[40] This can be circumvented by reducing the pulse energy of the ionizing laser beam in order to perform photoelectron photoion coincidence (PEPICO) spectroscopy.[237] The benefit of the

obtained data would be that photoelectron spectra could be measured for distinct cluster sizes and the influence of the IR excitation on the IE distributions is observed for these. Aside from this, size-selective PES and PEPICO could be possible control experiments regarding the question whether the sIE correctly marks the saturation of ionization energies.

7.2 Vibrational spectroscopy of $Na(H_2O)_n$ clusters

7.2.1 Conclusion

Delay time and IR pulse energy dependence of the IR-induced signal gain

Contrary to several previous studies[37,43,68,71,178,184] in which the IR spectra of sodium doped clusters were measured using a constant delay time of $\Delta t = 80\,ns$ and high-E_{IR} conditions,[188] the influence of these two parameters on the IR-induced signal gain are now examined in detail. The IR-induced solvation process of the sodium atom[71] occurs at short delay times and cannot be time-resolved with the given setup.

IR-induced signal gains are observed for all cluster sizes if the clusters are irradiated by an IR laser pulse prior to photoionization. With increasing delay time, an exponential decay of the signal gain with a rate coefficient of $10^7 - 10^8\,\mathrm{s}^{-1}$ occurs for all cluster sizes. In contrast, the mass spectra of cationic $Na(H_2O)n^+$ clusters show a slightly decreasing ion intensity for larger clusters and an slightly increasing intensity at smaller masses, indicating IR-induced fragmentation. This suggests that the clusters cooled by evaporation of monomers cannot be probed by 3.22 eV photons as they have higher ionization energies due to the high temperature sensitivity of the solvation of the sodium atom.[43,72] The observed lifetimes are in agreement with those from simulations on the evaporation from large ${Na_4(H_2O)_n}^{4+}$ clusters at 275 K.[228] Cluster temperatures in this range can only be obtained in the experiment if several IR photons are absorbed by each cluster. This absorption of multiple photons is further indicated by the IR laser pulse energy dependence of the IR-induced signal gain. While the IR-induced signal gains increase with E_{IR} for small, amorphous clusters for excitation at $3400\,\mathrm{cm}^{-1}$ as well as $3200\,\mathrm{cm}^{-1}$, they differ for larger cluster sizes. For these, the IR-induced signal remains more stable for excitation at $3200\,\mathrm{cm}^{-1}$ than for excitation at $3400\,\mathrm{cm}^{-1}$, where a decrease with increasing pulse energy is observed. Difference spectra taken at different delay times

demonstrate that the decaying component corresponds to amorphous clusters for all cluster sizes. This indicates the coexistence of crystalline and amorphous clusters for larger cluster sizes. As the signal gain spectra of larger clusters show the presence of crystalline clusters, this signal from amorphous clusters observed for the same cluster sizes indicates the coexistence of crystalline and amorphous clusters in the molecular beam experiment. In addition, spectra with a reduced distortion, measured at small Δt and reduced E_{IR}, show that mixed signal gain spectra which are a convolution of the spectra of crystalline and amorphous clusters can be obtained. These are similar to spectra obtained via FTIR spectroscopy of freezing nm-sized particles.[21]

Probing crystalline water clusters

Vibrational spectroscopy is a suitable technique for studying whether large water clusters are crystalline or amorphous.[16,187] The commonly used indicator of an amorphous-crystalline transition is a downshift of the peak position of the bonded OH oscillators from $3400\,\mathrm{cm}^{-1}$ to $3250\,\mathrm{cm}^{-1}$.[20,21,71,81] For vibrational spectroscopy on $\mathrm{Na}(\mathrm{H_2O})_n$ clusters, the Δt- and E_{IR}-dependencies of the IR-induced signal gains demonstrate that the spectra measured at high E_{IR}- and long Δt-conditions of Pradzynski et al.[71] are distorted by a dip at around $3400\,\mathrm{cm}^{-1}$ at high-E_{IR} conditions. A suitable indicator for the onset signal of crystalline clusters was found to be the increase of the IR intensity around $3200\,\mathrm{cm}^{-1}$ and a coinciding down-shift of the bonded-OH peak position to $\tilde{\nu}_{\mathrm{peak}} < 3400\,\mathrm{cm}^{-1}$ for a given cluster size. This requires the comparison to the spectra of smaller, amorphous clusters. This indicator was shown to be rather independent of the applied IR-excitation conditions as the presence of crystalline clusters is observed at similar cluster sizes in spectra obtained at high-E_{IR} and low-E_{IR}. Therefore, this indicator was applied for the interpretation of spectra formed in argon-seeded expansion conditions. For these, the presence of crystalline clusters is concluded for $n = 90 \pm 10$ via the increased intensity around $3200\,\mathrm{cm}^{-1}$ from a comparison to smaller cluster sizes. This is the first experimental indication for the presence of crystalline water clusters with less than 100 water molecules and was therefore used to assess molecular dynamics simulations[16,87–89] regarding their ability to predict the smallest crystalline cluster size correctly. The simulations with the TTM2-F[87] potential give a more accurate estimate than those relying on the TIP4P[16,89] potential or the mW[88] model.
The isolated peak of the dOH motif peak was fitted by Gaussian lineshape regres-

sions in order to study which peak characteristic of this surface-located motif is affected by a crystalline hydrogen bond network within the clusters. The spectra of $La^{3+}(H_2O)_n$ from Cooper et al.[81] were used as a reference and suggest that the amplitude of the dangling OH oscillator could be a possible indicator for the presence of crystalline clusters, whereas the dOH peak position appears to be dominated by the cluster size.

7.2.2 Outlook

Time-resolved vibrational spectroscopy of $Na(H_2O)_n$ clusters

In order to study the kinetics of the IR-assisted sodium solvation, which leads to the observed signal gains,[71] laser pulse lengths on the order of femtoseconds are required to resolve the IVR of the pumped vibrational mode on a picosecond timescale.[222,223] As the temperature of an IR-heated cluster decreases with each evaporation step and the evaporation rate constant depends on the cluster temperature, the exponential decay lifetime increases with each consecutive evaporation step.[144] Therefore, the measurement of vibrational spectra at different delay times might allow the detection of stable isomers. Figure 7.1 shows the vibrational spectra of $Na(H_2O)_{20}$ measured at delay times $\Delta t = 12\,\text{ns}$ (red trace) and 200 ns (black trace) and the calculated spectrum of a $(H_2O)_{20}$ isomer consisting of three face-sharing pentagonal prisms[184] (blue trace).[VIII] The peaks at $3140\,\text{cm}^{-1}$ and $3300\,\text{cm}^{-1}$ in the experimental spectrum measured with $\Delta t = 12\,\text{ns}$ (red trace) indicate the presence of this isomer. The experimental spectrum taken at long delay times ($\Delta t = 200\,\text{ns}$, black trace) shows that these peaks are not persistent for all ionization conditions. This can be caused by IR-induced isomerization or by evaporation of larger clusters on the timescale of $10^1 - 10^2\,\text{ns}$. Based on the present data it cannot be resolved which of the two processes dominates.

With regard to the broad distribution of ionization energies of sodium water clusters,[40,72] the measurement of vibrational spectra at different UV wavelengths could lead to the structural assignment of further cluster isomers at smaller cluster sizes by a comparison of depletion and signal gain spectra.[43,68]

[VIII] It was shown in reference [184] that the dominant peaks of this isomer's vibrational spectrum persists upon sodium attachment.

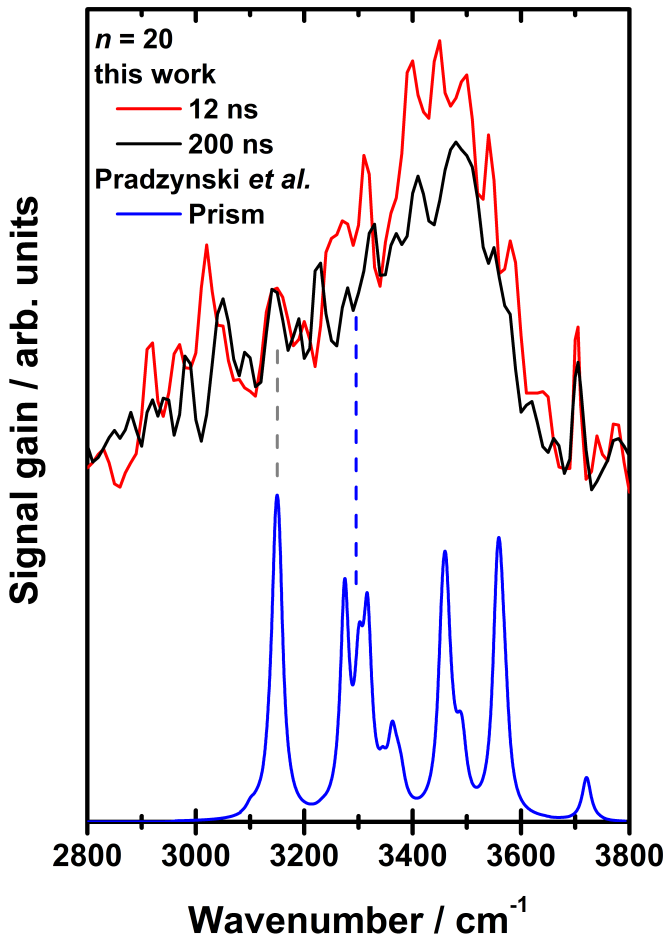

Figure 7.1: Comparison of unscaled vibrational spectra of $Na(H_2O)_{20}$ from He-seeded expansion conditions (2.7 bar water vapor, $p_{stag} = 3.7$ bar, $\lambda_{UV} = 385$ nm) measured at different delay times with the calculated spectrum of the edge-sharing pentagonal prism isomer of $(H_2O)_{20}$. The calculated spectrum (calculated with MP2/aug-cc-pVDZ) was taken from reference [184].

Crystalline clusters

For sodium water clusters formed in argon-seeded expansions the transition from amorphous to crystalline clusters was observed at significantly smaller cluster sizes than previously reported. This change towards smaller cluster sizes is likely related to a reduced cooling rate in the nozzle. Unfortunately, neither the cluster temperature nor the cooling rate can be quantified or measured in the present experiment.

As the rate coefficient of the IR-induced evaporation could increase with increasing cluster temperatures, the decay coefficient could be a suitable probe to determine relative cluster temperatures for several expansion conditions. Measurements on the delay time dependence of the IR-induced signal gain for the applied Ar-seeded expansions conditions appear to indicate a higher evaporation rate coefficient than for the He-seeded conditions.[205] This might support the hypothesis that the cluster temperatures are higher in the Ar-seeded case, which should also be related to the significantly smaller reservoir pressures used and thus the smaller cooling rates. Note that the cluster temperature is further increased by the sodium doping process and the IR excitation. Therefore, further investigations are necessary to clarify the importance and quantify the influence of the cooling rate on the cluster size for which crystalline clusters are observable.
The presence of crystalline clusters with $n = 90 \pm 10$ water molecules was observed in the argon-seeded expansions and this result can be used to assess predictions from molecular simulations. A comparison with calculated spectra based on the cluster structures from the MB-pol potential[238–240] appears to be promising with regard to its capability of reproducing experimental vibrational spectra of bulk ice.[241]
A detailed study on the dangling OH peak[204] may validate whether the amplitude parameter is a suitable probe for the presence of crystalline clusters. In addition, this investigations could clarify for which cluster size a down-shift of the dOH peak position upon crystallization is present.[232]
The coexistence of amorphous and crystalline clusters is only possible in a certain temperature range.[66] A detailed study on the molecular beam composition for neon-seeded expansions may allow to determine the temperature range in which crystalline clusters and amorphous clusters coexist by means of a simulation of the cluster formation process and by simulations of the temperature profile within the nozzle[86] where the amorphous and crystalline clusters are formed.[21,86]

7.3 Experimental approach

In order to obtain a molecular beam with higher sample densities at higher seeding gas fractions, the expansion can be modified by replacing the continuous beam source with a pulsed nozzle arrangement, e.g. an Even-Lavie valve,[242] with a larger nozzle diameter.
The sodium doping technique has been used to detect a variety of clusters.[35,46,47,106]

However, it has limitations which still need to be investigated. A major challenge is the extension towards further sample systems and to resolve whether the detected cluster distributions are subjected to post source decay of the formed ions: While metastable fragmentation of $Na^+(CH_3OH)_6$ was observed as a daughter ion peak between the peaks of $Na^+(CH_3OH)_5$ and $Na^+(CH_3OH)_6$,[43] no such interjacent peaks were observed for the sodium water clusters in the present apparatus so far. In order to study the post source decay of large clusters which cannot be size-resolved by the present apparatus, a mass gate—a pulsed electric field allowing only a small cluster size range to pass through—can be installed between ion source and reflectron and could be suitable to obtain information on the metastable decay of large clusters.[186] An extension of the sodium doping technique towards an ensemble of organic compounds in various oxidized states as obtained from combustion or gas phase ozonolysis might open up the field of reaction monitoring for the sodium doping technique.

A Appendix

A.1 Experimental results

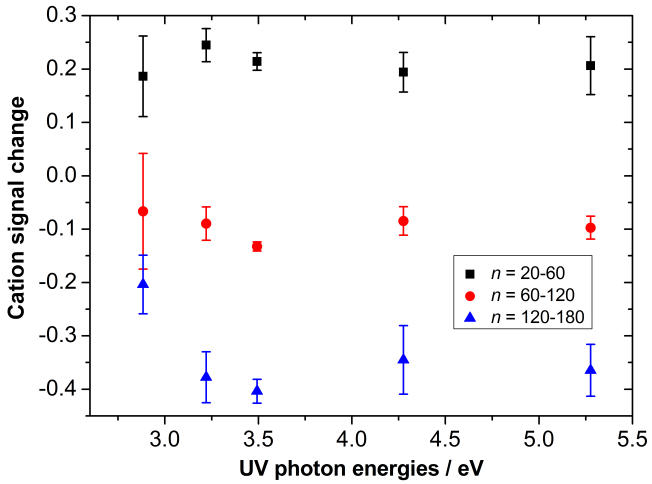

Figure A.1: Change of the detected ion yield of $Na(H_2O)_n^+$ cations upon irradiation with 3400 cm^{-1} photons after the ionization from UV photons with different energies. Water vapor (1.4 bar) was coexpanded with helium as carrier gas at as reservoir pressure of $p_{stag} = 1.9$ bar.

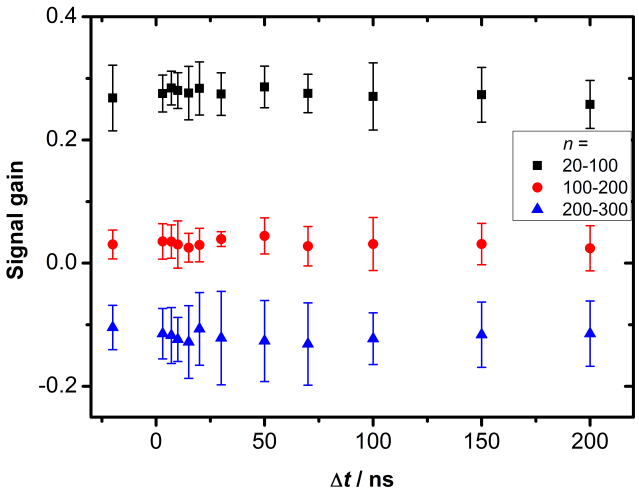

Figure A.2: Time dependent signal gain vs. Δt at $\lambda_{UV} = 290\,\text{nm}$. He-seeded water vapor (1.4 bar) was expanded at a stagnation pressure of 1.9 bar.

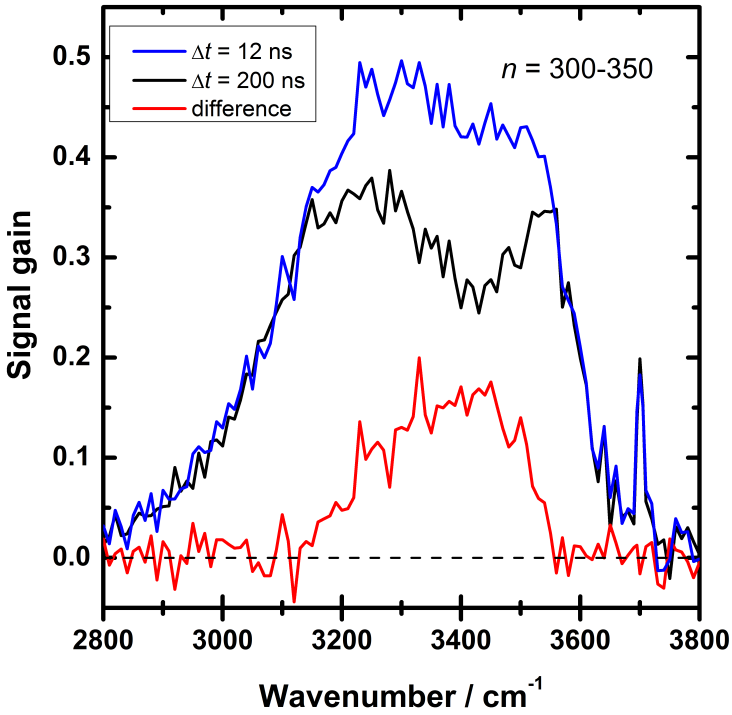

Figure A.3: Vibrational spectra taken at $\Delta t = 12\,\text{ns}$ (blue) and 200 ns (black) for the cluster size range $n = 300 - 350$ from the raw, unscaled data and the corresponding difference spectrum (red). The signal gain spectra (black and blue) were obtained by averaging of three scans from identical experimental conditions.

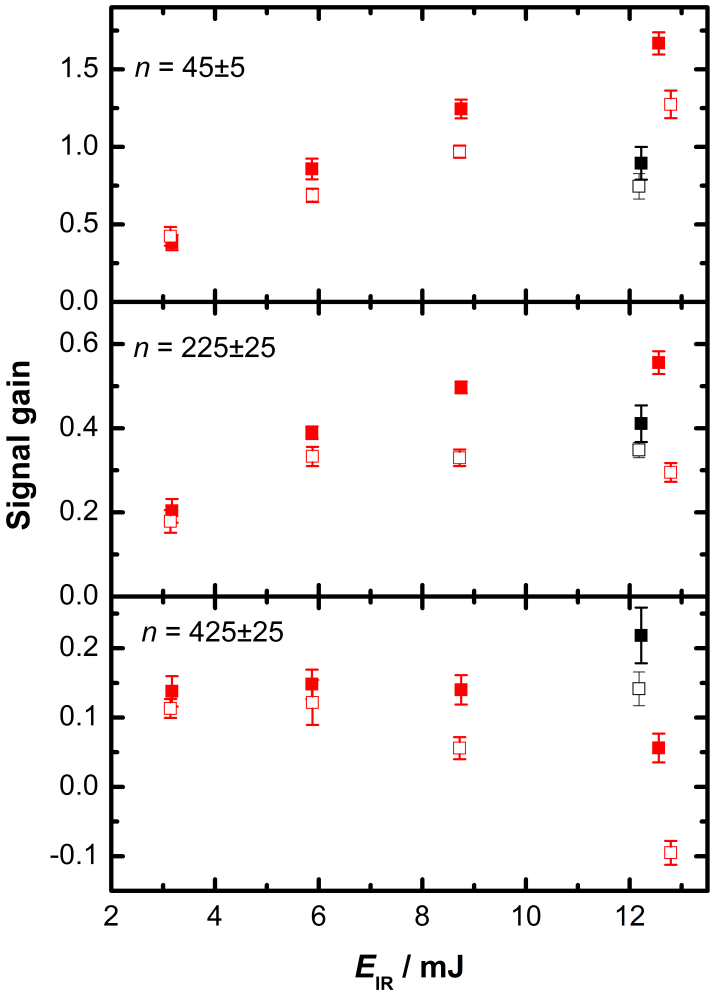

Figure A.4: Dependence of the IR-induced signal gain on E_{IR} for $\tilde{\nu} = 3200\,\mathrm{cm}^{-1}$ (black square) and $3400\,\mathrm{cm}^{-1}$ (red square) obtained at $\Delta t = 12\,\mathrm{ns}$ and $200\,\mathrm{ns}$ obtained from 10 consecutive scans.
Water vapor (2.7 bar) was expanded with He at a reservoir pressure of 3.7 bar. The clusters were ionized by 385 nm photons. The expansion chamber backing pressure was lower than in the data shown in Section 5.3 and the IR photon flux was increased due to a different position of a focusing lens.

A.2 Modified pickup cell top

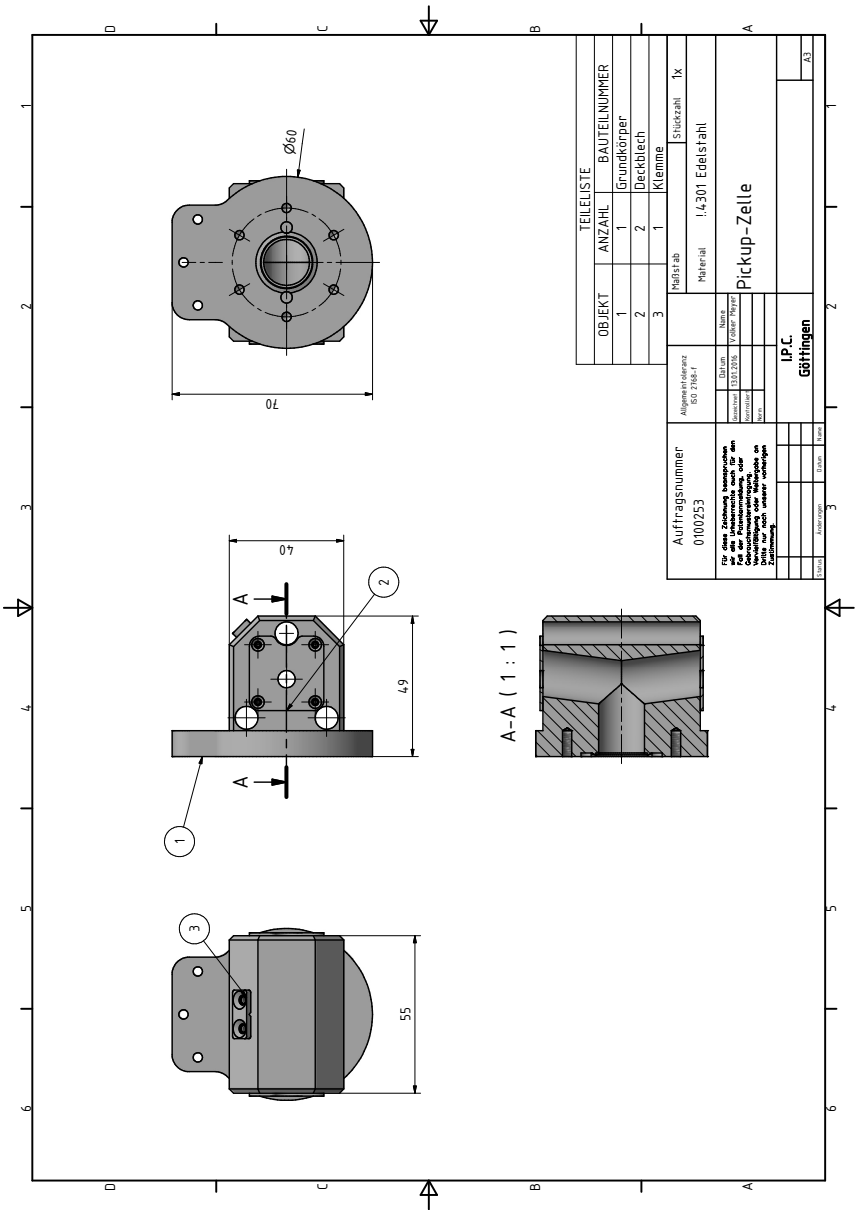

Figure A.5: Cross section of the novel pick-up cell. Properties like the internal diameter were inspired from the former model presented in references [93, 127]. The engineering drawing was provided by the Faculty of Chemistry workshop of the Georg-August university Göttingen.

A.3 Correction of the pressures of the old manometer

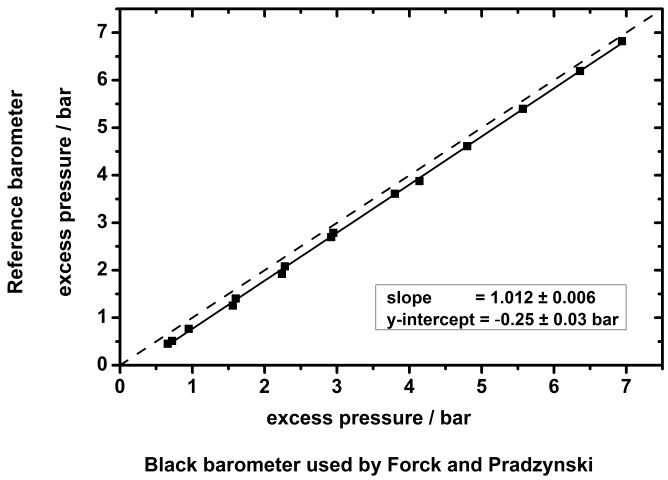

Figure A.6: Offset of the formerly used[90,139] black barometer. The dashed line corresponds to unit slope, the solid line is the obtained straight line for the correction.

A.4 List of chemicals and gases

All chemicals and gases have been used without previous purification or modification. Double-demineralized water was provided by Mr. Schlote from the Institute of Physical Chemistry at Göttingen (IPC). The laser dyes used in this work are listed in Table 3.4 on page 43.

Table A.1: List of the gases and chemicals used for the measurements.

	chemical formula	CAS number	purity	supplier
sodium	Na	7440-23-5	unknown, stored in paraffin oil	Merck
water	H_2O	7732-18-5	unknown	IPC Göttingen
helium	He	7440-59-7	$\geq 99.996\%$	Linde
neon	Ne	7440-01-9	$\geq 99.99\%$	Air Liquide
argon	Ar	7440-37-1	$\geq 99.999\%$	Air Liquide
1,4-dioxane	$C_4H_8O_2$	123-91-1	$\geq 98\%$	Th. Geyer
ethanol	C_2H_6O	64-17-5	$\geq 99.8\%$	Carl Roth
phenol	C_6H_6O	108-95-2	$\geq 99\%$	Sigma Aldrich

Table A.2: Nonlinear crystals used in the laser system described in Section 3. [90,212–215,243]

nonlinear crystal ($n_e - n_o$ or $n_z - n_{x,y}$, type)	laser system	output range in nm	nonlinear process
$\beta - BaB_2O_4$, BBO (−, II)	Panther Ex OPO	$410 - 709$	OPO
		709–2631	
$\beta - BaB_2O_4$, BBO (−, I)	Panther Ex OPO	$215 - 260$	SHG
$\beta - BaB_2O_4$, BBO (−, I)	Panther Ex OPO	$260 - 420$	SHG
$\beta - BaB_2O_4$, BBO (−, I)	Cobra-Stretch	$280 - 450$	SHG
KD_2PO_4, KD*P (−, I)	Powerlite 9010	532	SHG
KD_2PO_4, KD*P (−, II)	Powerlite 9010	355	THG/SFG
$KTiOAsO_4$, KTA (biaxial, +, II)	IR OPO/OPA	$1450 - 4000$	OPA
$KTiOPO_4$, KTP (biaxial, +, II)	IR OPO/OPA	532	SHG
$KTiOPO_4$, KTP (biaxial, +, II)	IR OPO/OPA	$710 - 845$	OPO
		$1350 - 2218$	

A.5 List of abbreviations

Abbreviation	Meaning
A	hydrogen bond acceptor
AIE	adiabatic ionization energy
aIE	appearance ionization energy, referred to as ionization threshold energy
BBO	beta-barium borate, $\beta - BaB_2O_4$
CNT	classical nucleation theory
D	hydrogen bond donor
DA	single donor, single acceptor of hydrogen bonds
DAA	single donor, double acceptor of hydrogen bonds
DDA	double donor, single acceptor of hydrogen bonds
DDAA	double donor, double acceptor of hydrogen bonds
DFT	density functional theory
dOH	dangling OH bonds
EBE	electron binding energy
EI	electron impact ionization
ESI	electrospray ionization
FT-ICR	Fourier transform ion cyclotron resonance
FTIR	Fourier transform infrared spectroscopy
FWHM	full width at half maximum
HDA	high density amorphous ice
Ic	cubic ice
ICR	ion cyclotron resonance
IE	ionization energy
Ih	hexagonal ice
IP	ionization potential, also called ionization threshold energy[61]
IPC	Institute of Physical Chemistry Göttingen
IR	infrared
IRMPD	infrared multi photon dissociation
IY	ion yield
KD*P	potassium dideuterium phosphate, KD_2PO_4
KTA	potassium titanyl arsenate, $KTiOAsO_4$

Abbreviation	Meaning
KTP	potassium titanyl phosphate, $KTiOPO_4$
LDA	low density amorphous ice
MCP	multichannel plate
MD	molecular dynamics
MS	mass spectroscopy
Nd:YAG	neodymium doped yttrium aluminium garnet, Nd:$Y_3Al_5O_{12}$
NIR	Near-infrared
OPA	optical parametric amplifier
OPO	optical parametric oscillator
PEPICO	photoelecron photoion coincidence spectroscopy
PES	photoelectron spectroscopy
PSD	post-source decay
REMPI	resonance enhanced multi photon ionization
SFG	sum frequency generation
SHG	second harmonic generation
sIE	saturation ionization energy
TAG	electronic pulse for the correct assignment of ion signal into the corresponding mass spectra, TTL shape with a duration of 10 ms at a frequency of 5 Hz [203]
THG	third harmonic generation
TOF	time-of-flight
TOF-MS	time of flight mass spectrometry
TTL	transistor-transistor logic
UV	ultra violet
VHDA	very high density amorphous ice
VIE	vertical ionization energy
Vis	visible
VUV	vacuum-ultraviolet

Bibliography

[1] M. Kulmala. How particles nucleate and grow. *Science*, 302(5647):1000–1001, 2003. doi: 10.1126/science.1090848.

[2] M. A. Tolbert. Sulfate aerosols and polar stratospheric cloud formation. *Science*, 264(5158):527–528, 1994. doi: 10.1126/science.264.5158.527.

[3] P. T. M. Carlsson and T. Zeuch. Investigation of nucleation kinetics in H_2SO_4 vapor through modeling of gas phase kinetics coupled with particle dynamics. *J. Chem. Phys.*, 148(10):104303, 2018. doi: 10.1063/1.5017037.

[4] C. S. Cockell, A. Léger, M. Fridlund, T. M. Herbst, L. Kaltenegger, O. Absil, C. Beichman, W. Benz, M. Blanc, A. Brack, A. Chelli, L. Colangeli, H. Cottin, F. Coudé du Foresto, W. C. Danchi, D. Defrère, J.-W. den Herder, C. Eiroa, J. Greaves, T. Henning, K. J. Johnston, H. Jones, L. Labadie, H. Lammer, R. Launhardt, P. Lawson, O. P. Lay, J.-M. LeDuigou, R. Liseau, F. Malbet, S. R. Martin, D. Mawet, D. Mourard, C. Moutou, L. M. Mugnier, M. Ollivier, F. Paresce, A. Quirrenbach, Y. D. Rabbia, J. A. Raven, H. J. A. Rottgering, D. Rouan, N. C. Santos, F. Selsis, E. Serabyn, H. Shibai, M. Tamura, E. Thiébaut, F. Westall, and G. J. White. Darwin—-A Mission to detect and search for life on extrasolar planets. *Astrobiology*, 9(1):1–22, 2009. doi: 10.1089/ast.2007.0227.

[5] J. K. Hillier, S. F. Green, N. McBride, J. P. Schwanethal, F. Postberg, R. Srama, S. Kempf, G. Moragas-Klostermeyer, J. A. M. McDonnell, and E. Grün. The composition of Saturn's E ring. *Mon. Not. R. Astron. Soc.*, 377 (4):1588–1596, 2007. doi: 10.1111/j.1365-2966.2007.11710.x.

[6] F. Postberg, S. Kempf, J. Schmidt, N. Brilliantov, A. Beinsen, B. Abel, U. Buck, and R. Srama. Sodium salts in E-ring ice grains from an ocean below the surface of Enceladus. *Nature*, 459(7250):1098–1101, 2009. doi: 10.1038/nature08046.

[7] S. Fornasier, S. Mottola, H. U. Keller, M. A. Barucci, B. Davidsson, C. Feller, J. D. P. Deshapriya, H. Sierks, C. Barbieri, P. L. Lamy, R. Rodrigo, D. Koschny, H. Rickman, M. A'Hearn, J. Agarwal, J.-L. Bertaux, I. Bertini, S. Besse, G. Cremonese, V. Da Deppo, S. Debei, M. De Cecco, J. Deller, M. R. El-Maarry, M. Fulle, O. Groussin, P. J. Gutierrez, C. Güttler, M. Hofmann, S. F. Hviid, W.-H. Ip, L. Jorda, J. Knollenberg, G. Kovacs, R. Kramm, E. Kührt, M. Küppers, M. L. Lara, M. Lazzarin, J. J. Lopez Moreno, F. Marzari, M. Massironi, G. Naletto, N. Oklay, M. Pajola, A. Pommerol, F. Preusker, F. Scholten, X. Shi, N. Thomas, I. Toth, C. Tubiana, and J.-B. Vincent. Rosetta's comet 67P/Churyumov-Gerasimenko sheds its dusty mantle to reveal its icy nature. *Science*, 354(6319):1566–1570, 2016. doi: 10.1126/science.aag2671.

[8] E. V. Browell, C. F. Butler, S. Ismail, P. A. Robinette, A. F. Carter, N. S. Higdon, O. B. Toon, M. R. Schroeberl, and A. F. Tuck. Airborne Lidar Observations in the Wintertime Arctic Stratosphere, Polar Stratospheric Clouds. *Geophys. Res. Lett.*, 17(4):385–388, 1990. doi: 10.1029/GL017i004p00385.

[9] M. A. Zondlo, P. K. Hudson, A. J. Prenni, and M. A. Tolbert. Chemistry and Microphysics of Polar Stratospheric Clouds and Cirrus Clouds. *Annu. Rev. Phys. Chem.*, 51(1):473–499, 2000. doi: 10.1146/annurev.physchem.51.1.473.

[10] J. H. Seinfeld and S. N. Pandis. *Atmospheric Chemistry and Physics - From Air Pollution to Climate Change*. WILEY, Hoboken, New Jersey, 2 edition, 2006. ISBN 978-0-471-72018-8.

[11] R. Ludwig. Wasser: von Clustern in die Flüssigkeit. *Angew. Chem.*, 113(10):1856–1876, 2001. doi: 10.1002/1521-3757(20010518)113:10<1856::AID-ANGE1856>3.0.CO;2-5.

[12] G. A. Cisneros, K. T. Wikfeldt, L. Ojamäe, J. Lu, Y. Xu, H. Torabifard, A. P. Bartók, G. Csányi, V. Molinero, and F. Paesani. Modeling Molecular Interactions in Water: From Pairwise to Many-Body Potential Energy Functions. *Chem. Rev.*, 116(13):7501–7528, 2016. doi: 10.1021/acs.chemrev.5b00644.

[13] W. de Heer. The physics of simple metal clusters: experimental aspects and simple models. *Rev. Mod. Phys.*, 65(3):611–676, 1993. doi: 10.1103/RevModPhys.65.611.

[14] B. von Issendorff and O. Cheshnowsky. Metal to Insulator Transitions in Clusters. *Annu. Rev. Phys. Chem.*, 56(1):549–580, 2005. doi: 10.1146/annurev.physchem.54.011002.103845.

[15] X. Xu, S. Yin, R. Moro, A. Liang, J. Bowlan, and W. A. de Heer. Metastability of Free Cobalt and Iron Clusters: A Possible Precursor to Bulk Ferromagnetism. *Phys. Rev. Lett.*, 107(5):057203, 2011. doi: 10.1103/PhysRevLett.107.057203.

[16] V. Buch, S. Bauerecker, J. P. Devlin, U. Buck, and J. K. Kazimirski. Solid water clusters in the size range of tens–thousands of H_2O: a combined computational/spectroscopic outlook. *Int. Rev. Phys. Chem.*, 23(3):375–433, 2004. doi: 10.1080/01442350412331316124.

[17] M. A. Suhm. How broad are water dimer bands? *Science*, 304(5672):823–824, 2004. doi: 10.1126/science.304.5672.823.

[18] M. Y. Tretyakov, E. A. Serov, M. A. Koshelev, V. V. Parshin, and A. F. Krupnov. Water dimer rotationally resolved millimeter-wave spectrum observation at room temperature. *Phys. Rev. Lett.*, 110(9):093001, 2013. doi: 10.1103/PhysRevLett.110.093001.

[19] C. Medcraft, D. McNaughton, C. D. Thompson, D. R. T. Appadoo, S. Bauerdecker, and E. G. Robertson. Water ice nanoparticles: size and temperature effects on the mid-infrared spectrum. *Phys. Chem. Chem. Phys.*, 15 (10):3630–3639, 2013. doi: 0.1039/c3cp43974g.

[20] K. Mizuse, N. Mikami, and A. Fujii. Infrared spectra and hydrogen-bonded network structures of large protonated water clusters $H^+(H_2O)_n$ ($n = 20 - 200$). *Angew. Chem. Int. Ed.*, 49(52):10119–10122, 2010. doi: 10.1002/anie.201003662.

[21] A. Manka, H. Pathak, S. Tanimura, J. Wölk, R. Strey, and B. E. Wyslouzil. Freezing water in no-man's land. *Phys. Chem. Chem. Phys.*, 14(13):4505–4516, 2012. doi: 10.1039/c2cp23116f.

[22] O. F. Hagena. Nucleation and growth of clusters in expanding nozzle flows. *Surf. Sci.*, 106(1–3):101–116, 1981. doi: 10.1016/0039-6028(81)90187-4.

[23] A. E. K. Sundén, K. Støchkel, S. Panja, U. Kadhane, P. Hvelplund, S. Brøndsted Nielsen, H. Zettergren, B. Dynefors, and K. Hansen. Heat capacities of freely evaporating charged water clusters. *J. Chem. Phys.*, 130(22):224308, 2009. doi: 10.1063/1.3149784.

[24] K. Hansen, P. U. Andersson, and E. Uggerud. Activation energies for evaporation from protonated and deprotonated water clusters from mass spectra. *J. Chem. Phys.*, 131(12):124303, 2009. doi: 10.1063/1.3230111.

[25] J. T. O'Brien and E. R. Williams. Effects of ions on hydrogen-bonding water networks in large aqueous nanodrops. *J. Am. Chem. Soc.*, 134(24):10228–10236, 2012. doi: 10.1021/ja303191r.

[26] L. Ma, K. Majer, F. Chirot, and B. von Issendorff. Low temperature photoelectron spectra of water cluster anions. *J. Chem. Phys.*, 131(14):144303, 2009. doi: 10.1063/1.3245859.

[27] U. Buck, I. Ettischer, M. Melzer, V. Buch, and J. Sadlej. Structure and spectra of three-dimensional $(H_2O)_n$ clusters, $n = 8$, 9, 10. *Phys. Rev. Lett.*, 80(12): 2578–2581, 1998. doi: 10.1103/physrevlett.80.2578.

[28] T. Hamashima, K. Mizuse, and A. Fujii. Spectral signatures of four-coordinated sites in water clusters: Infrared spectroscopy of phenol-$(H_2O)_n$ ($\sim 20 \leq n \leq \sim 50$). *J. Phys. Chem. A*, 115(5):620–625, 2011. doi: 10.1021/jp111586p.

[29] K. Mizuse, T. Hamashima, and A. Fujii. Infrared spectroscopy of phenol-$(H_2O)_{n>10}$: Structural strains in hydrogen bond networks of neutral water clusters. *J. Phys. Chem. A*, 113(44):12134–12141, 2009. doi: 10.1021/jp9061187.

[30] N. Okai, H. Ishikawa, and K. Fuke. Hydration process of alkaline-earth metal atoms in water clusters. *Chem. Phys. Lett.*, 415(1-3):155–160, 2005. doi: 10.1016/j.cplett.2005.08.129.

[31] C. P. Schulz, R. Haugstätter, H. U. Tittes, and I. V. Hertel. Free sodium-water clusters. *Phys. Rev. Lett.*, 57(14):1703–1706, 1986. doi: 10.1103/physrevlett.57.1703.

[32] R. Takasu, F. Misaizu, K. Hashimoto, and K. Fuke. Microscopic solvation process of alkali atoms in finite clusters: Photoelectron and photoionization

studies of $M(NH_3)_n$ and $M(H_2O)_n$ (M = Li, Li^-, Na^-). *J. Phys. Chem. A*, 101(17):3078–3087, 1997. doi: 10.1021/jp9629654.

[33] F. Misaizu, K. Tsukamoto, M. Sanekata, and K. Fuke. Photoionization of clusters of Cs atoms solvated with H_2O, NH_3 and CH_3CN. *Chem. Phys. Lett.*, 188(3–4):241–246, 1992. doi: 10.1016/0009-2614(92)90016-G.

[34] C. Bobbert, S. Schütte, C. Steinbach, and U. Buck. Fragmentation and reliable size distributions of large ammonia and water clusters. *Eur. Phys. J. D*, 19 (2):183–192, 2002. doi: 10.1140/epjd/e20020070.

[35] B. Schläppi, J. J. Ferreiro, J. H. Litman, and R. Signorell. Sodium-sizer for neutral nanosized molecular aggregates: Quantitative correction of size-dependence. *Int. J. Mass Spectrom.*, 372:13–21, 2014. doi: 10.1016/j.ijms.2014.08.021.

[36] C. Steinbach and U. Buck. Vibrational spectroscopy of size-selected sodium-doped water clusters. *J. Phys. Chem. A*, 110(9):3128–3131, 2006. doi: 10.1021/jp054502g.

[37] U. Buck, C. C. Pradzynski, T. Zeuch, J. M. Dieterich, and B. Hartke. A size resolved investigation of large water clusters. *Phys. Chem. Chem. Phys.*, 16 (15):6859–6871, 2014. doi: 10.1039/c3cp55185g.

[38] I. V. Hertel, C. Hüglin, C. Nitsch, and C. P. Schulz. Photoionization of $Na(NH_3)_n$ and $Na(H_2O)_n$ clusters: A step towards the liquid phase? *Phys. Rev. Lett.*, 67(13):1767–1770, 1991. doi: 10.1103/PhysRevLett.67.1767.

[39] C. Steinbach and U. Buck. Ionization potentials of large sodium doped ammonia clusters. *J. Chem. Phys.*, 122(13):134301, 2005. doi: 10.1063/1.1863934.

[40] A. H. C. West, B. L. Yoder, D. Luckhaus, C.-M. Saak, M. Doppelbauer, and R. Signorell. Angle-resolved photoemission of solvated electrons in sodium-doped clusters. *J. Phys. Chem. Lett.*, 6(8):1487–1492, 2015. doi: 10.1021/acs.jpclett.5b00477.

[41] I. Dauster, M. A. Suhm, U. Buck, and T. Zeuch. Experimental and theoretical study of the microsolvation of sodium atoms in methanol clusters: Differences and similarities to sodium-water and sodium-ammonia. *Phys. Chem. Chem. Phys.*, 10(1):83–95, 2008. doi: 10.1039/b711568g.

[42] R. M. Forck, I. Dauster, U. Buck, and T. Zeuch. Sodium microsolvation in ethanol: common features of Na(HO-R)$_n$ (R = H, CH_3, C_2H_5) clusters. *J. Phys. Chem. A*, 115(23):6068–6076, 2011. doi: 10.1021/jp110584s.

[43] R. M. Forck, C. C. Pradzynski, S. Wolff, M. Ončák, P. Slavíček, and T. Zeuch. Size resolved infrared spectroscopy of Na$(CH_3OH)_n$ (n=4–7) clusters in the OH stretching region: unravelling the interaction of methanol clusters with a sodium atom and the emergence of the solvated electron. *Phys. Chem. Chem. Phys.*, 14(9):3004–3016, 2012. doi: 10.1039/c2cp23301k.

[44] B. Schläppi, J. H. Litman, J. J. Ferreiro, D. Stapfer, and R. Signorell. A pulsed uniform laval expansion coupled with single photon ionization and mass spectrometric detection for the study of large molecular aggregates. *Phys. Chem. Chem. Phys.*, 17(39):25761–25771, 2015. doi: 10.1039/c5cp00061k.

[45] B. L. Yoder, J. H. Litman, P. W. Forysinski, J. L. Corbett, and R. Signorell. Sizer for neutral weakly bound ultrafine aerosol particles based on sodium doping and mass spectrometric detection. *J. Phys. Chem. Lett.*, 2(20):2623–2628, 2011. doi: 10.1021/jz201086v.

[46] S. Schütte and U. Buck. Strong fragmentation of large rare gas clusters by high energy electron impact. *Int. J. Mass Spectrom.*, 220(2):183–192, 2002. doi: 10.1016/S1387-3806(02)00670-X.

[47] J. H. Litman, B. L. Yoder, B. Schläppi, and R. Signorell. Sodium-doping as a reference to study the influence of intracluster chemistry on the fragmentation of weakly-bound clusters upon vacuum ultraviolet photoionization. *Phys. Chem. Chem. Phys.*, 15(3):940–949, 2013. doi: 10.1039/c2cp43098c.

[48] J. Lengyel, A. Pysanenko, V. Poterya, J. Kočišek, and M. Fárník. Extensive water cluster fragmentation after low energy electron ionization. *Chem. Phys. Lett.*, 612:256–261, 2014. doi: 10.1016/j.cplett.2014.08.038.

[49] M. Riera, A. W. Götz, and F. Paesani. The i-TTM model for ab initio-based ion-water interaction potentials. II. Alkali metal ion-water potential energy functions. *Phys. Chem. Chem. Phys.*, 18(44):30334–30343, 2016. doi: 10.1039/c6cp02553f.

[50] K. Hashimoto, S. He, and K. Morokuma. Structures, stabilities and ionization potentials of $Na(H_2O)_n$ and $Na(NH_3)_n$ ($n = $ l–6) clusters. An ab initio MO study. *Chem. Phys. Lett.*, 206(1-4):297–304, 1993. doi: 10.1016/0009-2614(93)85555-3.

[51] K. Hashimoto and K. Morokuma. Ab initio molecular orbital study of $Na(H_2O)_n$ ($n = 1$–6) clusters and their ions. Comparison of electronic structure of the "surface" and "interior" complexes. *J. Am. Chem. Soc.*, 116(25):11436–11443, 1994. doi: 10.1021/ja00104a024.

[52] K. Hashimoto and K. Morokuma. Ab initio MO study of $Na(NH_3)_n$ ($n = 1$–6) clusters and their ions: a systematic comparison with hydrated Na clusters. *J. Am. Chem. Soc.*, 117(14):4151–4159, 1995. doi: 10.1021/ja00119a032.

[53] K. Hashimoto and K. Daigoku. Formation and localization of a solvated electron in ground and low-lying excited states of $Li(NH_3)_n$ and $Li(H_2O)_n$ clusters: a comparison with $Na(NH_3)_n$ and $Na(H_2O)_n$. *Phys. Chem. Chem. Phys.*, 11(41):9391–9400, 2009. doi: 10.1039/b907766a.

[54] C. J. Mundy, J. Hutter, and M. Parrinello. Microsolvation and chemical reactivity of sodium and water clusters. *J. Am. Chem. Soc.*, 122(19):4837–4838, 2000. doi: 10.1021/ja994507p.

[55] L. Cwiklik, U. Buck, W. Kulig, P. Kubisiak, and P. Jungwirth. A sodium atom in a large water cluster: Electron delocalization and infrared spectra. *J. Chem. Phys.*, 128(15):154306, 2008. doi: 10.1063/1.2902970.

[56] C. J. Burnham, M. K. Petersen, T. J. F. Day, S. S. Iyengar, and G. A. Voth. The properties of ion-water clusters. II. Solvation structures of Na^+, Cl^-, and H^+ clusters as a function of temperature. *J. Chem. Phys.*, 124(2):024327, 2006. doi: 10.1063/1.2149375.

[57] J. J. Fifen and N. Agmon. Structure and spectroscopy of hydrated sodium ions at different temperatures and the cluster stability rules. *J. Chem. Theory Comput.*, 12(4):1656–1673, 2016. doi: 10.1021/acs.jctc.6b00038.

[58] Y. Ferro and A. Allouche. Sodium hydroxide formation in water clusters: The role of hydrated electrons and the influence of electric field. *J. Chem. Phys.*, 118(23):10461–10469, 2003. doi: 10.1063/1.1573178.

[59] Y. Ferro, A. Allouche, and V. Kempter. Electron solvation by highly polar molecules: Density functional theory study of atomic sodium interaction with water, ammonia, and methanol. *J. Chem. Phys.*, 120(18):8683, 2004. doi: 10.1063/1.1690238.

[60] R. N. Barnett and U. Landman. Hydration of sodium in water clusters. *Phys. Rev. Lett.*, 70(12):1775–1778, 1993. doi: 10.1103/PhysRevLett.70.1775.

[61] T. Tsurusawa and S. Iwata. Theoretical studies of structures and ionization threshold energies of water cluster complexes with a group 1 metal, $M(H_2O)_n$ (M=Li and Na). *J. Phys. Chem. A*, 103(31):6134–6141, 1999. doi: 10.1021/jp990621i.

[62] M. Ciocca, C.-E. Burkhardt, and J. J. Leventhal. Precision stark spectroscopy of sodium: Improved values for the ionization limit and bound states. *Phys. Rev. A*, 45(7):4720–4730, 1992. doi: 10.1103/PhysRevA.45.4720.

[63] C. P. Schulz, R. Haugstätter, H. U. Tittes, and I. V. Hertel. Free sodium-water clusters: photoionisation studies in a pulsed molecular beam source. *Z. Phys. D*, 67(1767):279–290, 1988. doi: 10.1007/BF01384862.

[64] O. Rodriguez and J. M. Lisy. Revisiting $Li^+(H_2O)_{3-4}Ar_1$ clusters: Evidence of high-energy conformers from infrared spectra. *J. Phys. Chem. Lett.*, 2(12):1444–1448, 2011. doi: 10.1021/jz200530v.

[65] R. S. Berry. Introductory lecture. Clusters, Melting, Freezing and Phase Transitions. *J. Chem. Soc., Faraday Trans.*, 80(13):2343–2349, 1990. doi: 10.1039/FT9908602343.

[66] R. S. Berry and B. M. Smirnov. Where macro meets micro. *Phys. Chem. Chem. Phys.*, 16(21):9747–9759, 2014. doi: 10.1039/c3cp54550d.

[67] J. R. R. Verlet, A. E. Bragg, A. Kammrath, O. Chesnovsky, and D. M. Neumark. Observation of large water-cluster anions with surface-bound excess electrons. *Science*, 307(5706):93–96, 2005. doi: 10.1126/science.1106719.

[68] R. M. Forck, J. M. Dieterich, C. C. Pradzynski, A. L. Huchting, R. A. Mata, and T. Zeuch. Structural diversity in sodium doped water trimers. *Phys. Chem. Chem. Phys.*, 14(25):9054–9057, 2012. doi: 10.1039/c2cp41066d.

[69] J.-H. Kim, Y.-K. Kim, and H. Kang. Hydrolysis of sodium atoms on water–ice films. Characterization of reaction products and interfacial distribution of sodium and hydroxide ions. *J. Phys. Chem. C*, 113(1):321–327, 2009. doi: 10.1021/jp807774v.

[70] R. M. Forck, I. Dauster, Y. Schieweck, T. Zeuch, U. Buck, M. Ončák, and P. Slavíček. Communications: Observation of two classes of isomers of hydrated electrons in sodium-water clusters. *J. Chem. Phys.*, 132(22):221102, 2010. doi: 10.1063/1.3439393.

[71] C. C. Pradzynski, R. M. Forck, T. Zeuch, P. Slavíček, and U. Buck. A fully size-resolved perspective on the crystallization of water clusters. *Science*, 337 (6101):1529–1532, 2012. doi: 10.1126/science.1225468.

[72] C. W. Dierking, F. Zurheide, T. Zeuch, J. Med, S. Parez, and P. Slavíček. Revealing isomerism in sodium-water clusters: Photoionization spectra of $Na(H_2O)_n$ $(n = 2 - 90)$. *J. Chem. Phys.*, 146(24):244303, 2017. doi: 10.1063/1.4986520.

[73] M. F. Vernon, D. J. Krajnovich, H. S. Kwok, J. M. Lisy, Y. R. Shen, and Y. T. Lee. Infrared vibrational predissociation spectroscopy of water clusters by the crossed laser-molecular beam technique. *J. Chem. Phys.*, 77(1):47–57, 1982. doi: 10.1063/1.443631.

[74] U. Buck and F. Huisken. Infrared spectroscopy of size-selected water and methanol clusters. *Chem. Rev.*, 100(11):3863–3890, 2000. doi: 10.1021/cr990054v.

[75] K. Otto, Z. Xue, P. Zielke, and M. A. Suhm. The raman spectrum of isolated water clusters. *Phys. Chem. Chem. Phys.*, 16(21):9849–9858, 2014. doi: 10.1039/c3cp54272f.

[76] J. Zischang and M. A. Suhm. The OH stretching spectrum of warm water clusters. *J. Chem. Phys.*, 140(6):064312, 2014. doi: 10.1063/1.4865130.

[77] K. R. Asmis, G. Santambrogio, J. Zhou, E. Garand, J. Headrick, D. Goebbert, M. A. Johnson, and D. M. Neumark. Vibrational spectroscopy of hydrated electron clusters $(H_2O)^-_{15-50}$ via infrared multiple photon dissociation. *J. Chem. Phys.*, 126(19):191105, 2007. doi: 10.1063/1.2741508.

[78] P. Ayotte, C. G. Bailey, J. Kim, and M. A. Johnson. Vibrational predissociation spectroscopy of the $(H_2O)_6^- \cdot Ar_n$, $n \geq 6$ clusters. *J. Chem. Phys.*, 108 (2):444–449, 1998. doi: 10.1063/1.475406.

[79] J. A. Fournier, C. J. Johnson, C. T. Wolke, G. H. Weddle, A. B. Wolk, and M. A. Johnson. Vibrational spectral signature of the proton defect in the three-dimensional $H^+(H_2O)_{21}$ cluster. *Science*, 344(6187):1009–1012, 2014. doi: 10.1126/science.1253788.

[80] M. A. Suhm. *Hydrogen Bond Dynamics in Alcohol Clusters*, volume 142 of *Adv. Chem. Phys.*, pages 1–57. Wiley-Blackwell, 2008. doi: 10.1002/9780470475935.ch1. ISBN 9780470475935.

[81] R. J. Cooper, M. J. DiTucci, T. M. Chang, and E. R. Williams. Delayed onset of crystallinity in ion-containing aqueous nanodrops. *J. Am. Chem. Soc.*, 138 (1):96–99, 2016. doi: 10.1021/jacs.5b11880.

[82] A. Kiselev, F. Bachmann, P. Pedevilla, S. J. Cox, A. Michaelides, D. Gerthsen, and T. Leisner. Active sites in heterogeneous ice nucleation—the example of K-rich feldspars. *Science*, 355(6323):367–371, 2017. doi: 10.1126/science.aai8034.

[83] P. Pedevilla, M. Fitzner, and A. Michaelides. What makes a good descriptor for heterogeneous ice nucleation on OH-patterned surfaces. *Phys. Rev. B*, 96 (11):115441, 2017. doi: 10.1103/PhysRevB.96.115441.

[84] G. Torchet, P. Schwartz, J. Farges, M. F. de Feraudy, and B. Raoult. Structure of solid water clusters formed in a free jet expansion. *J. Chem. Phys.*, 79(12): 6196–6202, 1983. doi: 10.1063/1.445803.

[85] J. P. Devlin, C. Joyce, and V. Buch. Infrared spectra and structures of large water clusters. *J. Phys. Chem. A*, 104(10):1974–1977, 2000. doi: 10.1021/jp994416e.

[86] N. Gimelshein, S. Gimelshein, C. C. Pradzynski, T. Zeuch, and U. Buck. The temperature and size distribution of large water clusters from a non-equilibrium model. *J. Chem. Phys.*, 142(24):244305, 2015. doi: 10.1063/1.4922312.

[87] B. Bandow and B. Hartke. Larger water clusters with edges and corners on their way to ice: Structural trends elucidated with an improved parallel

evolutionary algorithm. *J. Phys. Chem. A*, 110(17):5809–5822, 2006. doi: 10.1021/jp060512l.

[88] J. C. Johnston and V. Molinero. Crystallization, melting, and structure of water nanoparticles at atmospherically relevant temperatures. *J. Am. Chem. Soc.*, 134(15):6650–6659, 2012. doi: 10.1021/ja210878c.

[89] J. K. Kazimirski and V. Buch. Search for low energy structures of water clusters $(H_2O)_n$, $n = 20 - 22, 48, 123$, and 293. *J. Phys. Chem. A*, 107(46): 9762–9775, 2003. doi: 10.1021/jp0305436.

[90] C. C. Pradzynski. Größenselektive Untersuchungen zur Kristallisation und Struktur von Wasserclustern, 2015. Dissertation, Georg-August-Universität Göttingen.

[91] W. Demtröder and H.-J. Foth. Molekülspektroskopie in kalten Düsenstrahlen. *Phys. Bl.*, 43(1):7–13, 1987. doi: 10.1002/phbl.19870430104.

[92] J. B. Anderson and J. B. Fenn. Velocity Distributions in Molecular Beams from Nozzle Sources. *Phys. Fluids*, 8(5):780–787, 1965. doi: 10.1063/1.1761320.

[93] I. Dauster. Die Ionisationsdymanik in Natrium-Solvens-Clustern, 2008. Dissertation, Georg-August-Universität Göttingen.

[94] G. Scoles, editor. *Atomic and Molecular Beam Methods*, volume 1. Oxford University Press, New York, 1988. ISBN 978-0-19-504280-1.

[95] G. D. Stein. Cluster beam sources: Predictions and limitations of the nucleation theory. *Surf. Sci.*, 156:44–56, 1985. doi: 10.1016/0039-6028(85)90556-4.

[96] W. Demtröder. *Laserspektroskopie 2*. Springer, Berlin, 2013. doi: 10.1007/978-3-642-21447-9. ISBN 978-3-642-21447-9.

[97] H. Haberland, editor. *Clusters of Atoms and Molecules I – Theory, Experiment, and Clusters of Atoms*. Springer-Verlag, Heidelberg, 1994. doi: 10.1007/978-3-642-84329-7. ISBN 978-3-642-84331-0.

[98] H. Pauly. *Atom, Molecule, and Cluster Beams I*. Springer, Berlin, 2000. doi: 10.1007/978-3-662-04213-7. ISBN 978-3-540-66945-6.

[99] A. E. Beylich. Struktur von Überschall-Freistrahlen aus Schlitzblenden. *Z. Flugwiss. Weltraumforsch. 3*, 3:48–58, 1979.

[100] A. Kantrowitz and J. Grey. A High Intensity Source for the Molecular Beam. Part I. Theoretical. *Rev. Sci. Instrum.*, 22(5):328–332, 1951. doi: 10.1063/1.1745921.

[101] G. B. Kistiakowsky and W. P. Slichter. A High Intensity Source for the Molecular Beam. Part II. Experimental. *Rev. Sci. Instrum.*, 22(5):333–337, 1951. doi: 10.1063/1.1745922.

[102] J. H. Gross. *Massenspektrometrie*. Springer, Heidelberg, 2013. doi: 10.1007/978-3-8274-2981-0. ISBN 978-3-8274-2981-0.

[103] R. T. Jongma, Y. Huang, S. Shi, and A. M. Wodtke. Rapid Evaporative Cooling Suppresses Fragmentation in Mass Spectrometry: Synthesis of "Unprotonated" Water Cluster Ions. *J. Phys. Chem. A*, 102(45):8847–8854, 1998. doi: 10.1021/jp983366v.

[104] H. Shinohara, N. Nishi, and N. Washida. Photoionization of water clusters at 11.83 eV: Observation of unprotonated cluster ions $(H_2O)_n^+$ $(2 \leq n \leq 10)$. *J. Chem. Phys.*, 84(10):5561–5567, 1986. doi: 10.1063/1.449914.

[105] B. Apicella, X. Li, M. Passaro, N. Spinelli, and X. Wang. Multiphoton ionization of large water clusters. *J. Chem. Phys.*, 140(20):204313, 2014. doi: 10.1063/1.4878663.

[106] T. Zeuch and U. Buck. Sodium doped hydrogen bonded clusters: Solvated electrons and size selection. *Chem. Phys. Lett.*, 579:1–10, 2013. doi: 10.1016/j.cplett.2013.06.011.

[107] A. Halder, C. Huang, and V. V. Kresin. Photoionization yields, appearance energies, and densities of states of copper clusters. *J. Phys. Chem. C*, 119(20):11178–11183, 2015.

[108] W. E. Stephens. A pulsed mechanical mass spectrometer with time dispersion. *Phys. Rev.*, 69(11-12):691, 1946.

[109] C. Brunnée. The ideal mass analyzer: Fact or fiction? *Int. J. Mass Spectrom. Ion Process.*, 76(2):125–237, 1987. doi: 10.1016/0168-1176(87)80030-7.

[110] S. Schütte and U. Buck. Cluster sputtering: complete fragmentation of large ammonia clusters by photons and electrons. *Appl. Phys. A*, 69(1):S209–S211, 1999. doi: 10.1007/s003399900390.

[111] R. J. Cotter. Time-of-flight mass spectrometry for the structural analysis of biological molecules. *Anal. Chem.*, 64(21):1027A–1039A, 1992. doi: 10.1021/ac00045a002.

[112] U. Boesl. Time-of-flight mass spectrometry: Introduction to the basics. *Mass Spectrom. Rev.*, 36(1):86–109, 2017. doi: 10.1002/mas.21520.

[113] W. C. Wiley and I. H. McLaren. Time-of-flight mass spectrometer with improved resolution. *Rev. Sci. Instrum.*, 26(12):1150–1157, 1955. doi: 10.1063/1.1715212.

[114] U. Boesl, R. Weinkauf, and E. W. Schlag. Reflectron time-of-flight mass spectrometry and laser excitation for the analysis of neutrals, ionized molecules and secondary fragments. *Int. J. Mass Spectrom.*, 112(2-3):121–166, 1992. doi: 10.1016/0168-1176(92)80001-H.

[115] B. A. Mamyrin, V. I. Karataev, D. V. Shmikk, and V. A. Zagulin. The mass-reflectron, a new nonmagnetic time-of-flight mass spectrometer with high resolution. *Sov. Phys. JETP*, 37(1):45–48, 1973.

[116] G. Schwedt. *Analytische Chemie*. WILEY-VCH, Weinheim, 2008. ISBN 978-3-527-31206-1.

[117] M. Wolf. Multi-Channel-Plates. *Phys. Unserer Zeit*, 23(3):90–95, 1981. doi: 10.1002/piuz.19810120305.

[118] M. Wüest, D. S. Evans, and R. von Steiger. *Calibration of Particle Instruments in Space Physics*. ESA Publications Division, Noordwijk, 2007. ISBN 978-92-9221-936-9.

[119] R. Signorell, B. L. Yoder, A. H. C. West, J. J. Ferreiro, and C.-M. Saak. Angle-resolved valence shell photoelectron spectroscopy of neutral nanosized molecular aggregates. *Chem. Sci.*, 5(4):1283–1295, 2014. doi: 10.1039/C3SC53423E.

[120] T. E. Gough, M. Mengel, P. A. Rowntree, and G. Scoles. Infrared spectroscopy at the surface of clusters: SF_6 on Ar. *J. Chem. Phys.*, 83(10):4958–4961, 1985. doi: 10.1063/1.449757.

[121] I. Pócsik. Lognormal distribution as the natural statistics of cluster systems. *Z. Phys. D*, 20(1):395–397, 1990. doi: 10.1007/BF01544020.

[122] M. Lewerenz, B. Schilling, and J. P. Toennies. A new scattering deflection method for determining and selecting the size of large liquid clusters of ^{4}He. *Chem. Phys. Lett.*, 206(1):381–387, 1993. doi: 10.1016/0009-2614(93)85569-A.

[123] C.-R. Wang, R.-B. Huang, Z.-Y. Liu, and L.-S. Zheng. Lognormal-size distributions of elemental clusters. *Chem. Phys. Lett.*, 227(1):103–108, 1994. doi: 10.1016/0009-2614(94)00790-X.

[124] U. Buck, R. Krohne, and S. Schütte. Vibrational excitation of ammonia clusters by helium atom scattering. *J. Chem. Phys.*, 106(1):109–115, 1997. doi: 10.1063/1.473036.

[125] H. Chen, R.-B. Huang, X. Lu, Z.-C. Tang, X. Xu, and L.-S. Zheng. Studies on carbon/sulfur cluster anions produced by laser vaporization: Experiment (collision-induced dissociation) and theory (ab initio calculation). I. $C_2S_m^-$ ($1 \leq m \leq 11$). *J. Chem. Phys.*, 112(21):9310–9318, 2000. doi: 10.1063/1.481552.

[126] H. Pauly. *Atom, Molecule, and Cluster Beams II*. Springer, Berlin, 2000. doi: 10.1007/978-3-662-05902-9. ISBN 978-3-540-67673-7.

[127] C. Steinbach. Streuung und Spektroskopie von Wasserstoffbrückensystemen, 2000. Dissertation, Georg-August-Universität Göttingen.

[128] O. F. Hagena. Condensation in free jets: Comparison of rare gases and metals. *Z. Phys. D*, 4(3):291–299, 1987. doi: 10.1007/BF01436638.

[129] L. Bewig, U. Buck, S. Rakowsky, M. Reymann, and C. Steinbach. Reactions of sodium clusters with water clusters. *J. Phys. Chem. A*, 102(7):1124–1129, 1998. doi: 10.1021/jp9727714.

[130] N. Okai, S. Yoshida, K. Aranishi, A. Takahata, and K. Fuke. Multiphoton ionization and oxidation processes of mg-ammonia clusters. *Phys. Chem. Chem. Phys.*, 7(5):921–929, 2005. doi: 10.1039/B415964K.

[131] C. Bobbert and C. P. Schulz. Solvation and chemical reaction of sodium in water clusters. *Eur. Phys. J. D*, 16(1):95–97, 2001. doi: 10.1007/s100530170068.

[132] C. P. Schulz, C. Bobbert, T. Shimosato, K. Daigoku, N. Miura, and K. Hashimoto. Electronically excited states of sodium–water clusters. *J. Chem. Phys.*, 119(22):11620–11629, 2003. doi: 10.1063/1.1624599.

[133] R. Moro, R. Rabinovitch, and V. V. Kresin. Pick-up cell for cluster beam experiments. *Rev. Sci. Instrum.*, 76(5):056104, 2005. doi: 10.1063/1.1904243.

[134] M. Behrens, R. Frochtenicht, M. Hartmann, J.-G. Siebers, U. Buck, and F. C. Hagemeister. Vibrational spectroscopy of methanol and acetonitrile clusters in cold helium droplets. *J. Chem. Phys.*, 111(6):2436–2443, 1999. doi: 10.1063/1.479521.

[135] O. Bünermann and F. Stienkemeier. Modeling the formation of alkali clusters attached to helium nanodroplets and the abundance of high-spin states. *Eur. Phys. J. D*, 61(3):645–655, 2011. doi: 10.1140/epjd/e2011-10466-0.

[136] M. Lewerenz, B. Schilling, and J. P. Toennies. Successive capture and coagulation of atoms and molecules to small clusters in large liquid helium clusters. *J. Chem. Phys.*, 102(20):8191–8207, 1995. doi: 10.1063/1.469231.

[137] J. Fedor, V. Poterya, A. Pysanenko, and M. Fárník. Cluster cross sections from pickup measurements: Are the established methods consistent? *J. Chem. Phys.*, 135(10):104305, 2011. doi: 10.1063/1.3633474.

[138] U. Buck. Photodissociation of hydrogen halide molecules in different cluster environments. *J. Phys. Chem. A*, 106(43):10049–10062, 2002. doi: 10.1021/jp0208079.

[139] R. Forck. Strukturaufklärung von Natrium-Solvens-Clustern durch IR-anregungsmodulierte Photoionisationsspektroskopie, 2012. Dissertation, Georg-August-Universität Göttingen.

[140] P. W. Forysinski, P. Zielke, D. Luckhaus, J. Corbett, and R. Signorell. Photoionization of small sodium-doped acetic acid clusters. *J. Chem. Phys.*, 134 (9):094314, 2011. doi: 10.1063/1.3559464.

[141] J. Lengyel, A. Pysanenko, J. Kočišek, V. Poterya, C. C. Pradzynski, T. Zeuch, P. Slavíček, and M. Fárník. Nucleation of mixed nitric acid-water ice nanoparticles in molecular beams that starts with an HNO_3 molecule. *J. Phys. Chem. Lett.*, 3(21):3096–3101, 2012. doi: 10.1021/jz3013886.

[142] D. Šmídová, J. Lengyel, A. Pysanenko, J. Med, and P. Slavíček. Reactivity of Hydrated Electron in Finite Size System: Sodium Pickup on Mixed N_2O-Water Nanoparticles. *J. Phys. Chem. Lett.*, 6(15):2865–2869, 2015. doi: 10.1021/acs.jpclett.5b01269.

[143] H. Haberland, editor. *Clusters of Atoms and Molecules II – Solvation and Chemistry of Free Clusters, and Embedded, Supported and Compressed Clusters*. Springer-Verlag, Heidelberg, 1994. ISBN 978-3-642-84987-9.

[144] K. Hansen. *Statistical Physics of Nanoparticles in the Gas Phase*. Springer Science+Business, Dordrecht, 2013. doi: 10.1007/978-94-007-5839-1. ISBN 978-94-007-5839-1.

[145] C. E. Klots. Evaporative cooling. *J. Chem. Phys.*, 83(11):5854–5560, 1985. doi: 10.1063/1.449615.

[146] C. E. Klots. The evaporative ensemble. *Z. Phys. D*, 5(1):83–89, 1987. doi: 10.1007/BF01436578.

[147] C. E. Klots. Temperatures of evaporating clusters. *Nature*, 327:222–223, 1987. doi: 10.1038/327222a0.

[148] W. M. Haynes, editor. *CRC Handbook of Chemistry and Physics*. CRC Press, Boca Raton, 97 edition, 2016.

[149] C. Hock, M. Schmidt, R. Kuhnen, C. Bartels, L. Ma, H. Haberland, and B. von Issendorff. Calorimetric observation of the melting of free water nanoparticles at cryogenic temperatures. *Phys. Rev. Lett.*, 103(7):073401, 2009. doi: 10.1103/PhysRevLett.103.073401.

[150] M. Schmidt and B. von Issendorff. Gas-phase calorimetry of protonated water clusters. *J. Chem. Phys.*, 136(16):164307, 2012. doi: 10.1063/1.4705266.

[151] H. Abdoul-Carime, F. Berthias, L. Feketeová, M. Marciante, F. Calvo, V. Forquet, H. Chermette, B. Farizon, M. Farizon, and T. D. Märk. Velocity of a Molecule Evaporated from a Water Nanodroplet: Maxwell–Boltzmann Statistics versus Non-Ergodic Events. *Angew. Chem. Int. Ed.*, 54(49):14685–14689, 2015. doi: 10.1002/anie.201505890.

[152] C. Steinbach and U. Buck. Reaction and solvation of sodium in hydrogen bonded solvent clusters. *Phys. Chem. Chem. Phys.*, 7(5):986–990, 2005. doi: 10.1039/b419325n.

[153] U. Buck and C. Steinbach. Formation of sodium hydroxyde in multiple sodium-water cluster collisions. *J. Phys. Chem. A*, 102(38):7333–7336, 1998. doi: 10.1021/jp982357j.

[154] A. V. Vorontsov and Y. V. Novakovskaya. Reaction of sodium atoms with water clusters. *Phys. Scr.*, 80(4):048112, 2009. doi: 10.1088/0031-8949/80/04/048112.

[155] F. Mercuri, C. J. Mundy, and M. Parrinello. Formation of a reactive intermediate in molecular beam chemistry of sodium and water. *J. Phys. Chem. A*, 105(37):8423–8427, 2001. doi: 10.1021/jp011046x.

[156] R. N. Barnett and U. Landman. Water adsorption and reactions on small sodium chloride clusters. *J. Phys. Chem.*, 100(33):13950–13958, 1996. doi: 10.1021/jp9605764.

[157] P. E. Mason, F. Uhlig, V. Vaněk, T. Buttersack, S. Bauerecker, and P. Jungwirth. Coulomb explosion during the early stages of the reaction of alkali metals with water. *Nat. Chem.*, 7:250–254, 2015. doi: 10.1038/NCHEM.2161.

[158] S. Barth, M. Ončák, V. Ulrich, M. Mucke, T. Lischke, P. Slavíček, and U. Hergenhahn. Valence ionization of water clusters: From isolated molecules to bulk. *J. Phys. Chem. A*, 113(48):13519–13527, 2009. doi: 10.1021/jp906113e.

[159] L. Šištík, M. Ončák, and P. Slavíček. Simulations of photoemission and equilibrium redox processes of ionic liquids: the role of ion pairing and long-range polarization. *Phys. Chem. Chem. Phys.*, 13(25):11998–12007, 2011. doi: 10.1039/c1cp20570f.

[160] E. A. Gislason. Series expansions for Franck-Condon factors. I. Linear potential and the reflection approximation. *J. Chem. Phys.*, 58(9):3702–3707, 1973. doi: 10.1063/1.1679721.

[161] J. V. Coe, G. H. Lee, J. G. Eaton, S. T. Arnold, H. W. Sarkas, and K. H. Bowen. Photoelectron spectroscopy of hydrated electron cluster anions, $(H_2O)^-_{n=2-69}$. *J. Chem. Phys.*, 92(6):3980–3982, 1990. doi: 10.1063/1.457805.

[162] H. G. Limberger and T. P. Martin. Photoionization spectra of cesium and cesium oxide clusters. *J. Chem. Phys.*, 90(6):2979–2991, 1989. doi: 10.1063/1.455899.

[163] A. Halder and V. V. Kresin. Spectroscopy of metal "superatom" nanoclusters and high-T_c superconducting pairing. *Phys. Rev. B*, 92(21):214506, 2015. doi: 10.1103/PhysRevB.92.214506.

[164] K. R. Siefermann, Y. Liu, E. Lugovoy, O. Link, M. Faubel, U. Buck, B. Winter, and B. Abel. Binding energies, lifetimes and implications of bulk and interface solvated electrons in water. *Nat. Chem.*, 2:274–280, 2010. doi: 10.1038/NCHEM.580.

[165] A. Lübcke, F. Buchner, N. Heine, I. V. Hertel, and T. Schultz. Time-resolved photoelectron spectroscopy of solvated electrons in aqueous NaI solution. *Phys. Chem. Chem. Phys.*, 12(43):14629–14634, 2010. doi: 10.1039/c0cp00847h.

[166] A. T. Shreve, T. A. Yen, and D. M. Neumark. Photoelectron spectroscopy of hydrated electrons. *Chem. Phys. Lett.*, 493(4):216–219, 2010. doi: 10.1016/j.cplett.2010.05.059.

[167] P. Ayotte and M. A. Johnson. Electronic absorption spectra of size-selected hydrated electron clusters: $(H_2O)_n^-$, $n = 6 - 50$. *J. Chem. Phys.*, 106(2):811–814, 1997. doi: 10.1063/1.473167.

[168] Y. Tang, H. Shen, K. Sekiguchi, N. Kurahashi, T. Mizuni, Y.-I. Suzuki, and T. Suzuki. Direct measurement of vertical binding energy of a hydrated electron. *Phys. Chem. Chem. Phys.*, 12(15):3653–3655, 2010. doi: 10.1039/b925741a.

[169] J. M. Herbert and M. P. Coons. The Hydrated Electron. *Annu. Rev. Phys. Chem.*, 68(1):447–472, 2017. doi: 10.1146/annurev-physchem-052516-050816.

[170] J. Ceponkus, P. Uvdal, and B. Nelander. Water tetramer, pentamer, and hexamer in inert matrices. *J. Phys. Chem. A*, 116(20):4842–4850, 2012. doi: 10.1021/jp301521b.

[171] U. Buck and H. Meyer. Scattering analysis of cluster beams: formation and fragmentation of small Ar_n clusters. *Phys. Rev. Lett.*, 52(2):109–112, 1984. doi: 10.1103/PhysRevLett.52.109.

[172] U. Buck and I. Ettischer. Structure and structural transitions of size-selected clusters: $(CH_3CN)_n$ and $(CH_3OH)_6$. *Faraday Discuss.*, 97:215–228, 1994. doi: 10.1039/FD9949700215.

[173] M. F. Bush, R. J. Saykally, and E. R. Williams. Formation of hydrated triply charged metal ions from aqueous solutions using nanodrop mass spectrometry. *Int. J. Mass Spectrom.*, 253(3):256–262, 2006. doi: 10.1016/j.ijms.2006.04.009.

[174] K. Mizuse, A. Fujii, and N. Mikami. Long range influence of an excess proton on the architecture of the hydrogen bond network in large-sized water clusters. *J. Chem. Phys.*, 126(23):231101, 2007. doi: 10.1063/1.2750669.

[175] A. Fujii and K. Mizuse. Infrared spectroscopic studies on hydrogen-bonded water networks in gas phase clusters. *Int. Rev. Phys. Chem.*, 32(2):226–307, 2013. doi: 10.1080/0144235X.2012.760836.

[176] D. J. Nesbitt, T. Häber, and M. A. Suhm. *Faraday Discuss.*, 118:305–306, 2001. doi: 10.1039/b105220a.

[177] S. Kazachenko and A. J. Thakkar. Water nanodroplets: Predictions of five model potentials. *J. Chem. Phys.*, 138(19):194302, 2013. doi: 10.1063/1.4804399.

[178] F. Zurheide, C. W. Dierking, C. C. Pradzynski, R. M. Forck, F. Flüggen, U. Buck, and T. Zeuch. Size-resolved infrared spectroscopic study of structural transitions in sodium-doped $(H_2O)_n$ clusters containing 10–100 water molecules. *J. Phys. Chem. A*, 119(11):2709–2720, 2015. doi: 10.1021/jp509883m.

[179] C. Pérez, M. T. Muckle, D. P. Zaleski, N. A. Seifert, B. Temelso, G. C. Shields, Z. Kisiel, and B. H. Pate. Structures of cage, prism, and book isomers of water hexamer from broadband rotational spectroscopy. *Science*, 336(6083):897–901, 2012. doi: 10.1126/science.1220574.

[180] C. Steinbach, P. Andersson, M. Melzer, J. K. Kazimirski, U. Buck, and V. Buch. Detection of the book isomer from the OH-stretch spectroscopy of size selected water hexamers. *Phys. Chem. Chem. Phys.*, 6(13):3320–3324, 2004. doi: 10.1039/b400664j.

[181] K. Nauta and R. E. Miller. Formation of cyclic water hexamer in liquid helium: The smallest piece of ice. *Science*, 287(5451):293–295, 2000. doi: 10.1126/science.287.5451.293.

[182] R. J. Saykally and D. J. Wales. Pinning down the water hexamer. *Science*, 336(6083):814–815, 2012. doi: 10.1126/science.1222007.

[183] J. Brudermann, M. Melzer, U. Buck, J. K. Kazimirski, J. Sadlej, and V. Buch. The asymmetric cage structure of $(H_2O)_7$ from a combined spectroscopic and computational study. *J. Chem. Phys.*, 110(22):10649–10652, 1999. doi: 10.1063/1.479008.

[184] C. C. Pradzynski, C. W. Dierking, F. Zurheide, R. M. Forck, U. Buck, T. Zeuch, and S. S. Xantheas. Infrared detection of $(H_2O)_{20}$ isomers of exceptional stability: a drop-like and a face-sharing pentagonal prism cluster. *Phys. Chem. Chem. Phys.*, 16(48):26691–26696, 2014. doi: 10.1039/c4cp03642e.

[185] F. Zurheide. Größenselektive Untersuchung natriumdotierter Wassercluster durch IR-anregungsmodulierte Photoionisationsspektroskopie, 2013. Diploma thesis, Georg-August-Universität Göttingen.

[186] K. Mizuse. *Spectroscopic Investigations of Hydrogen Bond Network Structures in Water Clusters*. Springer, Tokyo, Heidelberg, 2013. doi: 10.1007/978-4-431-54312-1. ISBN 978-4-431-54312-1.

[187] A. Y. Zasetsky, A. F. Khalizov, M. E. Earle, and J. J. Sloan. Frequency dependent complex refractive indices of supercooled liquid water and ice determined from aerosol extinction spectra. *J. Phys. Chem. A*, 109(12):2760–2764, 2005. doi: 10.1021/jp044823c.

[188] U. Buck, I. Dauster, B. Gao, and Z. Liu. Infrared spectroscopy of small sodium-doped water clusters: Interaction with the solvated electron. *J. Phys. Chem. A*, 111(49):12355–12362, 2007. doi: 10.1021/jp075717o.

[189] P. Geiger, C. Dellago, M. Macher, C. Franchini, G. Kresse, J. Bernard, J. N. Stern, and T. Loerting. Proton ordering of cubic ice Ic: spectroscopy and computer simulations. *J. Phys. Chem. C*, 118(20):10989–10997, 2014. doi: 10.1021/jp500324x.

[190] A. Falenty, T. C. Hansen, and W. F. Kuhs. Formation and properties of ice XVI obtained by emptying a type sII clathrate hydrate. *Nature*, 516:231–233, 2014. doi: 10.1038/nature14014.

[191] J. E. Bertie, H. J. Labbé, and E. Whalley. Absorptivity of ice I in the range $4000 - 30\,\mathrm{cm}^{-1}$. *J. Chem. Phys.*, 50(10):4501–4520, 1969. doi: 10.1063/1.1670922.

[192] W. F. Kuhs, C. Sippel, A. Falenty, and T. C. Hansen. Extent and relevance of stacking disorder in "ice ic". *Proc. Natl. Acad. Sci. U.S.A.*, 109(52):21259–21264, 2012. doi: 10.1073/pnas.1210331110.

[193] J. Huang and L. S. Bartell. Kinetics of homogeneous nucleation in the freezing of large water clusters. *J. Phys. Chem.*, 99(12):3924–3931, 1995. doi: 10.1021/j100012a010.

[194] T. L. Malkin, B. J. Murray, A. V. Brukhno, J. Anwar, and C. G. Salzmann. Structure of ice crystallized from supercooled water. *Proc. Natl. Acad. Sci. U.S.A.*, 109(4):1041–1045, 2012. doi: 10.1073/pnas.1113059109.

[195] C. Hock, C. Bartels, S. Straßburg, M. Schmidt, H. Haberland, B. von Issendorff, and A. Aguado. Premelting and postmelting in clusters. *Phys. Rev. Lett.*, 102(4):043401, 2009. doi: 10.1103/PhysRevLett.102.043401.

[196] L. S. Bartell, L. Harsanyi, and E. J. Valente. Phases and phase changes of molecular clusters generated in supersonic flow. *J. Phys. Chem.*, 93(16):6201–6205, 1989. doi: 10.1021/j100353a047.

[197] V. Buch and J. P. Devlin. A new interpretation of the OH-stretch spectrum of ice. *J. Chem. Phys.*, 110(7):3437–3443, 1999. doi: 10.1063/1.478210.

[198] V. Molinero and E. B. Moore. Water modeled as an intermediate element between carbon and silicon. *J. Phys. Chem. B*, 113(13):4008–4016, 2009. doi: 10.1021/jp805227c.

[199] E. B. Moore and V. Molinero. Structural transformation in supercooled water controls the crystallization rate of ice. *Nature*, 479:506–508, 2011. doi: 10.1038/nature10586.

[200] E. B. Moore and V. Molinero. Is it cubic? Ice crystallization from deeply supercooled water. *Phys. Chem. Chem. Phys.*, 13(44):20008–20016, 2011. doi: 10.1039/C1CP22022E.

[201] S. Schütte. Mehrphotonen- und Elektronenstoßprozesse in Clustern, 1996. Dissertation, Georg-August-Universität Göttingen.

[202] M. Hobein. Photodissoziation und Photoionisation von Molekülclustern, 1994. Dissertation, Georg-August-Universität Göttingen.

[203] S. Wolff. Analysis of mass spectra of temporally delayed two step photoionization of sodium doped water clusters, 2014. Master's thesis, Georg-August-Universität Göttingen.

[204] F. Zurheide. *in preparation*, expected 2019. Dissertation, Georg-August-Universität Göttingen.

[205] D. Becker. Größenselektive Untersuchung zur Kristallisation natriumdotierter Wassercluster in Überschallexpansionen, 2018. Master's thesis, Georg-August-Universität Göttingen.

[206] U. Buck and H. Pauly. Dampfdruckmessungen an Alkalimetallen. *Z. Phys. Chem. N. F.*, 44:345–352, 1965.

[207] C. W. Dierking. Untersuchung der Strukturentwicklung von Wasserclustern zwischen 15 und 100 Molekülen mittels größenselektiver IR-Spektroskopie, 2013. Master's thesis, Georg-August-Universität Göttingen.

[208] H. Wollnik, U. Grüner, and G. Li. Flugzeit-Massenspektrometer mit gitterfreien Ionenspiegeln und Elektronenstoß-Ionenquellen. *Ann. Phys.*, 48:215, 1991. doi: 10.1002/andp.19915030119.

[209] B. A. Mamyrin. Laser assisted reflectron time-of-flight mass spectrometry. *Int. J. Mass Spectrom. Ion Process.*, 131:1–19, 1994. doi: 10.1016/0168-1176(93)03891-O.

[210] H. Haberland, H. Kornmeier, C. Ludewigt, A. Risch, and M. Schmidt. A double/triple time-of-flight mass spectrometer for the study of photoprocesses in clusters, or how to produce ions with different temperatures. *Rev. Sci. Instrum.*, 62(11):2621–2625, 1991. doi: 10.1063/1.1142241.

[211] *Powerlite Precision II Scientific Laser System, Manual*. Continuum, Santa Clara, CA, 2002.

[212] *Powerlite DLS Laser System, Manual*. Continuum, Santa Clara, CA, 2010.

[213] *Pulsed dye laser, User Manual*. Sirah Lasertechnik GmbH, Grevenbroich, 2012.

[214] *Panther EX OPO & EX PLUS OPO Operation and Maintenance, Manual*. Continuum, Santa Clara, CA, 2011.

[215] D. Guyer. *Broadband OPO/A System Manual*. LaserVision, Bellevue, WA, 2014.

[216] *P7887 User Manual, Version 3.03. 250 ps / 4 GHz Time-of-Flight / Multiscaler*. FAST ComTec GmbH, Oberhaching, 2009.

[217] C. A. Taatjes, O. Welz, A. J. Eskola, J. D. Savee, A. M. Scheer, D. E. Shallcross, B. Rotavera, E. P. F. Lee, J. M. Dyke, D. K. W. Mok, D. L. Osborn, and C. J. Percival. Direct measurements of conformer-dependent reactivity of the Criegee intermediate CH_3CHOO. *Science*, 340(6129):177–180, 2013. doi: 10.1126/science.1234689.

[218] A. D. Boese and J. M. L. Martin. Development of density functionals for thermochemical kinetics. *J. Chem. Phys.*, 121(8):3405–3416, 2004. doi: 10.1063/1.1774975.

[219] O. A. Vydrov and G. E. Scuseria. Assessment of a long-range corrected hybrid functional. *J. Chem. Phys.*, 125(23):234109, 2006. doi: 10.1063/1.2409292.

[220] S. Grimme, J. Antony, S. Ehrlich, and H. Krieg. A consistent and accurate ab initio parametrization of density functional dispersion correction (DFT-D) for the 94 elements H-Pu. *J. Chem. Phys.*, 132(15):154104, 2010. doi: 10.1063/1.3382344.

[221] D. Becker. Zeitabhängige IR-induzierte Wirkungsspektroskopie natriumdotierter Wassercluster, 2016. Bachelor's thesis, Georg-August-Universität Göttingen.

[222] D. Schwarzer, J. Lindner, and P. Vöhringer. OH-Stretch Vibrational Relaxation of HOD in Liquid to Supercritical D_2O. *J. Phys. Chem. A*, 110(9): 2858–2867, 2006. doi: 10.1021/jp0530350.

[223] T. Schäfer, J. Lindner, P. Vöhringer, and D. Schwarzer. OD stretch vibrational relaxation of HOD in liquid to supercritical H_2O. *J. Chem. Phys.*, 130(22): 224502, 2009. doi: 10.1063/1.3151673.

[224] H. Iglev, M. Schmeisser, K. Simeonidis, A. Thaller, and A. Laubereau. Ultrafast superheating and melting of bulk ice. *Nature*, 439:183–186, 2006. doi: 10.1038/nature04415.

[225] V. Buch and J. P. Devlin, editors. *Water in Confining Geometries*. Springer, Berlin, 2003. doi: 10.1007/978-3-662-05231-0. ISBN 978-3-540-00411-0.

[226] G. Niedner-Schatteburg and V. E. Bondybey. FT-ICR studies of solvation effect in ionic water cluster reactions. *Chem. Rev.*, 100(11):4059–4086, 2000. doi: 10.1021/cr990065o.

[227] F. Dong, S. Heinbuch, J. J. Rocca, and E. R. Bernstein. Dynamics and fragmentation of van der Waals clusters: $(H_2O)_n$, $(CH_3OH)_n$, and $(NH_3)_n$ upon ionization by a 26.5 eV soft x-ray laser. *J. Chem. Phys.*, 124(22):224319, 2006. doi: 10.1063/1.2202314.

[228] C. Caleman and D. van der Spoel. Evaporation from water clusters containing singly charged ions. *Phys. Chem. Chem. Phys.*, 9(37):5105–5111, 2007. doi: 10.1039/b706243e.

[229] C. Caleman and D. van der Spoel. Temperature and structural changes of water clusters in vacuum due to evaporation. *J. Chem. Phys.*, 125(15):154508, 2006. doi: 10.1063/1.2357591.

[230] P. Andersson, C. Steinbach, and U. Buck. Vibrational spectroscopy of large water clusters of known size. *Eur. Phys. J. D*, 24(1):53–56, 2003. doi: 10.1140/epjd/e2003-00105-x.

[231] C. Steinbach, P. Andersson, J. K. Kazimirski, U. Buck, V. Buch, and T. A. Beu. Infrared predissociation spectroscopy of large water clusters: A unique probe of cluster surfaces. *J. Phys. Chem. A*, 108(29):6165–6174, 2004. doi: 10.1021/jp049276+.

[232] J. P. Devlin and V. Buch. Surface of ice as viewed from combined spectroscopic and computer modeling studies. *J. Phys. Chem.*, 99(45):16534–16548, 1995. doi: 10.1021/j100045a010.

[233] J. Lengyel, A. Pysanenko, V. Poterya, P. Slavíček, M. Fárník, J. Kočišek, and J. Fedor. Irregular shapes of water clusters generated in supersonic expansions. *Phys. Rev. Lett.*, 223(11):113401, 2014. doi: 10.1103/PhysRevLett.112.113401.

[234] A. Y. Zasetsky, S. V. Petelina, and I. M. Svishchev. Thermodynamics of homogeneous nucleation of ice particles in the polar summer mesosphere. *Atmos. Chem. Phys.*, 9(3):965–971, 2009. doi: 10.5194/acp-9-965-2009.

[235] W. L. Jorgensen, J. Chandrasekhar, J. D. Madura, R. W. Impey, and M. L. Klein. Comparison of simple potential functions for simulating liquid water. *J. Chem. Phys.*, 79(2):926–935, 1983. doi: 10.1063/1.445869.

[236] C. J. Burnham and S. S. Xantheas. Development of transferable interaction models for water. IV. A flexible, all-atom polarizable potential (TTM2-F) based on geometry dependent charges derived from an ab initio monomer dipole moment surface. *J. Chem. Phys.*, 116(12):5115–5124, 2002. doi: 10.1063/1.1447904.

[237] V. Stert, W. Radloff, C. P. Schulz, and I. V. Hertel. Ultrafast photoelectron spectroscopy: Femtosecond pump-probe coincidence detection of ammonia cluster ions and electrons. *Eur. Phys. J. D*, 5(1):97–106, 1999. doi: 10.1007/PL00021590.

[238] V. Babin, C. Leforestier, and F. Paesani. Development of a "first principles" water potential with flexible monomers: Dimer potential energy surface, VRT spectrum, and second virial coefficient. *J. Chem. Theory Comput.*, 9(12):5395–5403, 2013. doi: 10.1021/ct400863t.

[239] V. Babin, G. R. Medders, and F. Paesani. Development of a "first principles" water potential with flexible monomers. II: trimer potential energy surface, third virial coefficient, and small clusters. *J. Chem. Theory Comput.*, 10(4):1599–1607, 2014. doi: 10.1021/ct500079y.

[240] G. R. Medders, V. Babin, and F. Paesani. Development of a "first-principles" water potential with flexible monomers. III. liquid phase properties. *J. Chem. Theory Comput.*, 10(8):2906–2910, 2014. doi: 10.1021/ct5004115.

[241] D. R. Moberg, S. C. Straight, C. Knight, and F. Paesani. Molecular origin of the vibrational structure of ice Ih. *J. Phys. Chem. Lett.*, 8(12):2579–2583, 2017. doi: 10.1021/acs.jpclett.7b01106.

[242] U. Even, J. Jortner, D. Noy, N. Lavie, and C. Cossart-Magos. Cooling of large molecules below 1 K and He clusters formation. *J. Chem. Phys.*, 112 (18):8068–8071, 2000. doi: 10.1063/1.481405.

[243] J. Wang, J. Wei, Y. Liu, X. Yin, X. Hu, Z. Shao, and M. Jiang. A survey of research on KTP and its analogue crystals. *Prog. Cryst. Growth Charact. Mater.*, 40(1–4):3–15, 2000. doi: 10.1016/S0960-8974(00)00007-3.

Danksagung

Ich möchte PD Dr. Thomas Zeuch für die Möglichkeit der Promotion im Bereich der Clusterspektroskopie und sein Vertrauen bei der Bearbeitung der Projekte danken. Die Zeuch'sche Unterstützung zeichnet sich durch viele Diskussionen aus, die in der Regel neue Denkanstöße hervorrufen. Mit dieser Diskussionsfreude und Thomas' Erfahrungsschatz mit der vorliegenden Molekularstrahlapparatur finden sich häufig neue Möglichkeiten den bestehenden Aufbau auszureizen.

Prof. Dr. Alec M. Wodtke sei herzlich für die Übernahme des Korreferates gedankt. Das technische Know-how der Mitglieder seiner Gruppe war bei diversen apparativen Hürden sehr hilfreich.

Da Forschung selten—insbesondere im Bereich der experimentellen physikalischen Chemie—ohne finanzielle Unterstützung auskommt, muss ich sowohl der Georg-August-Universität Göttingen als auch der Deutschen Forschungsgemeinschaft (Förderungen ZE 890-1-1 und ZE 890-1-2) meinen Dank aussprechen.

Prof. Petr Slavíček und seinen Mitarbeitern Jakub Med und Stanislav Parez sei gedankt für das Bereitstellen simulierter Photoionisationsspektren und eine detaillierte Analyse des Natrium Pickup-Prozesses im Rahmen der o.g. Kooperation.
Vielen Dank auch an Prof. Barbara Wyslouzil, Richard Cooper, Ph.D., Prof. Evan R. Williams und Dr. Christoph Czeslaw Pradzynski für das Bereitstellen der Originaldaten Ihrer Spektren, die dem Vergleich mit den von mir gemessenen dienten.

Dr. Christoph Czeslaw Pradzynski danke ich ferner für das Einführen in die experimentellen Gegenbenheiten und die spannende Zeit der "Wiederentdeckung" des Innenlebens der P11 während meiner Masterarbeit. Florian Zurheide sei gedankt für das Heranführen an die Bedienung der Gerätschaften des Labors wie auch für seine Hilfe bei Reparaturen. Sabine Wolff sei gedankt für die freundliche Zusammenarbeit

während ihrer Masterarbeit und das Bereitstellen des Vorauswertungsprogramms und die Einführung in selbiges. Für die angenehme Arbeitsatmosphäre und die von seinem Arbeitseifer sowie seiner Hartnäckigkeit getragene Zusammenarbeit während seiner Bachelor- und Masterarbeit danke ich Daniel Becker. Dr. Matthias Heger danke ich für seine Hilfe während der Reinstandsetzung des Setups und des Screenings der Turbomolekularpumpen im Sommer 2016.

Gedankt sei auch Clemens Heymann und Michael Schlote für Entsorgung der Laserfarbstofflösungen, Versorgung mit Gasflaschen und Bereitstellen bidestillierten Wassers. Für die Überwindung von Reparaturphasen mit Messunterbrechung danke ich herzlich den engagierten Teams der Werkstätten der Fakultät für Chemie, stellvertretend Annika von Roden, Volker Meyer, Mike Zippert und Reinhardt Hildebrandt, Hans-Joachim Heymel und Bernd Wichmann, Andreas Knorr und Andreas Erdmann.

Für das gründliche Korrekturlesen dieser Arbeit danke ich Philip Carlsson, Barbara Hubrich und Bastian Krüger. Der Arbeitsgruppe von Prof. Dr. Martin Suhm in sämtlichen von mir erlebten Zusammenstellungen danke ich für die freundliche Aufnahme der Zeuch Subgroup einschließlich mir, und für die Hilfsbereitschaft und die angenehme, kuchenreiche Arbeitsatmosphäre.

Für das Leben außerhalb der Universität möchte ich mich stellvertretend bei jenen Freunden bedanken, die regelmäßig ihre Zeit für Reisen mit mir opfern, die dem einen und jene die dem doppelten Kartenspiel mit mir fröhnen.
Meiner Familie danke ich für die sorgenfreie Zeit des Studiums und die vielfältige Unterstützung währenddessen sowie für ihre Geduld. Abschließend danke meiner Frau Gesa, die mich wann immer möglich mit gemeinsamen Abenteuern beschenkt, für ihre Geduld und Unterstützung.

Curriculum Vitae

I, Christoph Wilhelm Hansjörn Ralf Dierking, was born on 15th of June 1988 in Aachen as the first of two children of Heike Dierking (née Detmering) and Wilhelm Dierking and am a German citizen.

I was enrolled at Wilhelm-Röpke-Schule in Schwarmstedt in 1995 and changed to the Gymnasium Walsrode in 2001 where I passed the highschool diploma "Abitur" in 2008 and thus received the general university entrance qualification.

In October 2008 I enrolled for the studies of Chemistry at Georg-August-Universität Göttingen and obtained my Master degree (M. Sc. Chemistry) in November 2013. The theses, which I both prepared in the group of PD Dr. Thomas Zeuch, were "Partikel- und Produktbildung während der Gasphasenozonolyse von ungesättigten Alkoholen" (bachelor's thesis, 2011) and "Investigation on the structural development of water clusters in the size range of 15 to 100 molecules via size-selevtive IR spectroscopy" (master's thesis, 2013).
Subsequent to each thesis I did a three-and-half months lasting internship: In 2011, I worked in the research and development division in the department for acrylic polymers of tesa SE in Hamburg on the synthesis of optically clear adhesives and from December 2013 to March 2014 I joined the process analytical technology department at Lonza AG in Visp, Switzerland.

Since 2014 I did my doctorate under the supervision of PD Dr. Thomas Zeuch in DFG funded project (Grant No. ZE 890-1-1 and ZE 890-1-2). During my time in the Zeuch-Lab I contributed to the following publications of which only the first is dealt with in my dissertation:

I. C. W. Dierking, F. Zurheide, T. Zeuch, J. Med, S. Parez, and P. Slavíček, Revealing isomerism in sodium-water clusters: Photoionization spectra of

$Na(H_2O)_n$ clusters ($n = 2 - 90$), *J. Chem. Phys.*, 146(24):244303, 2017. doi: 10.1063/1.4986520.

II. F. Zurheide, C. W. Dierking, C. C. Pradzynski, R. M. Forck, F. Flüggen, U. Buck, and T. Zeuch, Size-resolved infrared spectroscopic study of structural transitions in sodium-doped $(H_2O)_n$ clusters containing $10 - 100$ water molecules, *J. Phys. Chem. A*, 119(11):2709–2720, 2015. doi: 10.1021/jp509883m.

III. C. C. Pradzynski, C. W. Dierking, F. Zurheide, R. M. Forck, U. Buck, T. Zeuch, and S. S. Xantheas, Infrared detection of $(H_2O)_{20}$ isomers of exceptional stability: a drop-like and a face-sharing pentagonal prism cluster, *Phys. Chem. Chem. Phys.*, 16(48):26691–26696, 2014. doi: 10.1039/c4cp03642e.